OCS Study
BOEM 2021-009

Assessing movements of birds using digital VHF transmitters: A validation study

US Department of the Interior
Bureau of Ocean Energy Management
Office of Renewable Energy Programs

BOEM
Bureau of Ocean Energy Management

OCS Study
BOEM 2021-009

Assessing movements of birds using digitally-coded VHF transmitters: A validation study

January 2021

Authors:

Peter W.C. Paton, Department of Natural Resources Science, University of Rhode Island
Clara Cooper-Mullin, Department of Natural Resources Science, University of Rhode Island
Soroush Kouhi, Department of Ocean Engineering, University of Rhode Island
Pamela H. Loring, US Fish and Wildlife Service (USFWS), Division of Migratory Birds
Jesse Moore, Department of Ocean Engineering, University of Rhode Island
James Miller, Department of Ocean Engineering, University of Rhode Island
Gopu Potty, Department of Ocean Engineering, University of Rhode Island

Prepared under BOEM Agreement No. M17AC00014

By
University of Rhode Island
Kingston RI 02881

US Department of the Interior
Bureau of Ocean Energy Management
Office of Renewable Energy Programs

DISCLAIMER

This study was funded, in part, by the US Department of the Interior, Bureau of Ocean Energy Management (BOEM), Environmental Studies Program, Washington, DC, through Agreement Number M17AC00014 with the University of Rhode Island, Kingston. This report has been technically reviewed by BOEM, and it has been approved for publication. The views and conclusions contained in this document are those of the authors and should not be interpreted as representing the opinions or policies of the US Government, nor does mention of trade names or commercial products constitute endorsement or recommendation for use.

REPORT AVAILABILITY

To download a PDF file of this report, go to the US Department of the Interior, Bureau of Ocean Energy Management Data and Information Systems webpage (http://www.boem.gov/Environmental-StudiesEnvData/), click on the link for the Environmental Studies Program Information System (ESPIS), and search on 2021-009. The report is also available at the National Technical Reports Library at https://ntrl.ntis.gov/NTRL/.

CITATION

Paton PWC, Cooper-Mullin, C., Kouhi, S. Loring PH, Moore J, Miller J, Potty G. 2021. Assessing movements of birds using digital VHF transmitters: A validation study. Sterling (VA): US Department of the Interior, Bureau of Ocean Energy Management. OCS Study BOEM 2021-009. 222 p.

ABOUT THE COVER

Cover photos by Peter Paton, University of Rhode Island.

ACKNOWLEDGMENTS

For study administration, guidance, and oversight, we thank the following individuals from the Bureau of Ocean Energy Management: David Bigger, Mary Boatman, and Paula Barksdale. We thank Debra Bourassa (Department of Natural Resources Science), Natalie Wesson (Sponsored Projects) and Gail Paolino (Ocean Engineering) at the University of Rhode Island for administrative support.

We thank staff from the Rhode Island National Wildlife Refuge Complex: John Veale, Jennifer White, and Charlie Vandemoer, for providing key field support for tagging and monitoring Piping Plovers in Rhode Island, as well as extensive logistical support for the tracking tower array. We thank Suzanne Paton of the USFWS Southern New England-New York Bight Coastal Program for providing staff, access to the 23'Parker boat for assistance with calibration surveys and logistical support for bird tagging and tracking tower, and to Tom Halavik (USFWS retired) for being an excellent captain under challenging conditions. We thank Susi vonOettingen, Abby Gelb, and Anne Hecht from USFWS Endangered Species for providing expertise on Roseate Terns and Piping Plovers. We thank Greg Bonynge for being such an excellent drone pilot and Chuck Labash, URI Environmental Data Center, for logistical support and access to the EDC's drone.

For field support we thank Dan Catlin and the Virginia Tech Shorebird Program for coordinating leg flag combinations of Piping Plovers, and Jeffery Spendelow from USGS Patuxent Wildlife Research Center for coordinating auxiliary markers on Roseate Terns. For tern capture, tagging, and monitoring at Falkner Island, CT, we thank Carolyn Mostello, Massachusetts Division of Fisheries & Wildlife for trapping Roseate Terns, and Kris Vagos, USFWS Stewart B. McKinney Refuge Biologist and her staff for assistance with trapping terns and monitoring the tracking station. For tern capture, tagging, and monitoring on Great Gull Island, New York we thank Helen Hays, Grace Cormons, Joe Dicostanzo, and Catherine Neal of the Great Gull Island Project, as well as the many volunteers and staff on Great Gull Island. We thank Dr. Stephen Fox for his surgical expertise to attach tags to Common Terns on Great Gull Island. We thank the following members of our field crew during the three-year study for their assistance with building and maintaining tracking towers, tagging and monitoring birds, and data management: Dr. Brett Still, Kevin Rogers, Michael Abemayor, Christine Fallon, Ryan Healey, Lesley Howard, Jesse Moore, Liam Corcoran, and Boma Kresning. We thank Lisa Nolan (Southeast Lighthouse Foundation) and Scott Comings (The Natural Conservancy) for permission to erect temporary tracking towers on their properties on Block Island. We thank the New Shoreham Town Council for permits to conduct research on Block Island. We thank John O'Keefe, Aileen Kenney, Bryan Wilson, and other staff from Deepwater Wind/Ørsted for all their assistance and hard work to place a receiver and antennas on Turbine #1 on the Block Island Wind Farm over three field seasons. For field and logistical support with automated radio

telemetry towers operated for this study, we thank our many cooperators from following entities: UMass Amherst-USGS Cooperative Fish and Wildlife Unit, USFWS Southern New England-New York Bight Coastal Program, USFWS Division of Migratory Birds, University of Rhode Island, Cape Cod National Seashore, Eastern MA National Wildlife Refuge (NWR) Complex, Waquoit Bay National Estuarine Research Reserve, US Army Corps of Engineers/Cape Cod Canal Field Office, Rhode Island NWR Complex, Shearwater Excursions, Nantucket Islands Land Bank, Nantucket Conservation Foundation, Watch Hill Conservancy, CT Department of Energy & Environmental Protection, American Museum of Natural History/Great Gull Island Project, Plum Island Animal Disease Center, Block Island Southeast Lighthouse Foundation, Camp Hero State Park, Fire Island National Seashore, Gateway National Recreation Area, Wildlife Conservation Society/New York Aquarium, Rutgers University Marine Field Station, Conserve Wildlife Foundation of New Jersey, New Jersey Division of Fish and Wildlife, Avalon Fishing Club, DE Department of Natural Resources/Cape Henlopen State Park, The Nature Conservancy Virginia Coast Reserve, Chincoteague NWR, Eastern Shore of VA NWR, Back Bay NWR, NOAA R/V Henry Bigelow, and Shearwater Excursions. We also thank the many partners operating automated radio telemetry stations throughout the Western Hemisphere as part of the Motus Wildlife Tracking System. For technical support and assistance with data management and analysis, we thank Motus Wildlife Tracking System, Bird Studies Canada and Mike Vandentillart (Lotek Wireless). This study was funded in part by the US Department of the Interior, Bureau of Ocean Energy Management, Environmental Studies Program, Washington DC, through Intra-Agency Agreement Number M17AC00014 with the University of Rhode Island.

SUMMARY

The Bureau of Ocean Energy Management (BOEM) manages renewable energy development on the US Outer Continental Shelf (OCS). The OCS extends from the boundary of each state's jurisdictional waters (generally 3 nautical miles offshore) to the outer boundary of the US Exclusive Economic Zone (~200 nautical miles offshore). In the Atlantic OCS, 1,742,252 acres are presently under lease agreement for development of commercial-scale offshore wind energy facilities (BOEM 2020). The first active offshore wind energy facility in the United States was the Block Island Wind Farm (BIWF), a five 6-MW turbine operation in Rhode Island state waters, where we focused this research project.

BOEM is concerned with the potential impact of offshore wind energy developments on wildlife that occur offshore, including migratory birds. Birds that utilize offshore habitats may be directly affected by collisions with offshore wind turbines or indirectly affected due to altered flight paths or displacement from foraging or resting areas (Drewitt and Langston 2006, Furness et al. 2013, Fox and Petersen 2019). Assessing collision risk is particularly challenging at offshore wind energy facilities (e.g., Erickson et al. 2001, Thaxter et al. 2017), versus land-based wind energy facilities where carcasses can be found on the ground (Smallwood et al. 2020). Therefore, risk assessments in offshore environments are typically based on species specific estimates of exposure to offshore wind turbines. Burger et al. (2011) categorized estimated exposure to offshore wind energy facilities at three nested spatial scales: macroscale (individuals that occur within a geographic region of interest, in this case the Block Island Wind Farm), mesoscale (occurs if individuals are exposed at the macroscale level and fly within the Rotor Swept Zone (RSZ) of wind turbines, 29 to 189 m Above Sea Level [ASL] at Block Island), and microscale (occurs if individuals of the species are exposed at the macro- and mesoscales and fly within the RSZ of wind turbines.).

In this study, we evaluated automated radio telemetry technology and modeling methods to assess bird movements at BIWF. Automated radio telemetry consists of very high frequency (VHF) transmitters ("transmitters" or "tags") that are attached ("tagged") to free-flying animals and emit digitally coded signals on a common radio frequency (i.e. 166.380 MHZ) every 3-10 seconds. Signals are received by automated radio telemetry stations ("receiving stations"), consisting of one or more antennas attached to a structure (e.g. a mast or building) and connected to a data-logger programmed to record data (including tag ID, time stamp, signal strength, and receiving antenna) of all tagged animals flying by. Automated radio telemetry studies are coordinated through the Motus Wildlife Tracking System, a centralized network that collects and disseminates data from all tagged wildlife and receiving stations across the globe (Taylor et al 2017).

In this study, we used automated radio telemetry stations to track movements of three focal species, Common Terns, Roseate Terns, and Piping Plovers, in the vicinity of BIWF from 2017-2019. Each field season (~June – October), we operated two automated telemetry stations with fixed Yagi and omnidirectional antennas at Southeast Lighthouse and Black Rock on the southern shore of Block Island. We also worked with staff at BIWF to install a receiving station with four fixed Yagi antennas on the eastern-most wind Turbine (#1) from 2017-2019. From 2017-2019, the tracking stations on Block Island detected a total of 157 unique tags from 15 species. These detections included our 3 focal species and 12 additional species tagged by biologists on the Motus network representing 6 species of shorebirds, and 6 species of passerines. Of our three focal species tagged at breeding areas in coastal RI, CT, and NY, we detected 79% of the Common Terns and 24% of the Roseate Terns, and 33% of the Piping Plovers moving past Block Island. These results concur with research on the breeding and post-breeding offshore movements of these three species by Loring et al. (2019). The telemetry station on Turbine #1 at BIWF was in place throughout the study, but it only collected limited data during the fall of 2017, and did not operate successfully in either 2018 or 2019 due to technological and logistical issues.

There was considerable annual variation in the total number of tagged individuals, species, and total detections at both the Black Rock and Southeast Lighthouse Stations from 2017 to 2019. At the Black Rock Station, the total number of tags detected varied from 8 to 40 annually, with 4 to 7 species, and total detections ranging from 339 to 5,217. At the Southeast Lighthouse Station, the total number of tags detected ranged from 6 to 70 annually from 2 to 13 species representing 232 to 2,957 total detections Reasons for the differences were possibly due to variations in tower height (3 to 12 m), differences in antenna gain due to the number of elements on the Yagi antennas (which ranged from 5 to 9-elements), type of receiver (either a Lotek or Sensorgnome), local environment conditions near the antennas, and the number of available tagged individuals passing by the towers. One factor that affected the total number of detections was the type of receiver. Sensorgnome receivers can detect signals from all antennas simultaneously, whereas Lotek receivers only detect signals from one antenna at a time, thus the receiver has to rotate among antennas. Most importantly, Sensorgnome receivers were not be as reliable as Lotek receivers and were more prone to not detecting passing birds.

One of the primary goals of this project was to conduct a series of calibration surveys to assess the detection probability of receiving stations with different configurations of antennas to track the offshore movements of digitally coded VHF transmitters. In 2017, during a calibration survey using a kite, we detected the tag 5,942 times and the model predictions averaged 4,527 m (SE = 182 m; range = 502 – 17,426 m; 25^{th}-75% = 2,065-5,476 m) from the actual location of the test tag based on a GPS track of the boat. During a 2018 kite calibration survey, the model predictions were more accurate and averaged 1,695 m (SE = 147 m; range = 229 – 4,221 m; 25^{th}-75% = 952-2,188 m) from the actual location of the test tag.

In 2019, we used quadcopter drone for all calibration surveys. Interestingly, in June 2019, calibration surveys conducted during dense fog conditions at fixed points at various altitudes (15 to 120 m) had no detections, even though the survey points were < 4 km of two functioning land-based receiving stations, indicating possible signal attenuation during dense fog conditions. A moving transect on 9 July had better results, but we found that when the drone flew at altitudes ≤60 m above sea level (asl), the accuracy of model predictions was relatively low, with a median difference between actual and predicted locations of 4,904 m (2.082 – 6,111; 25^{th} -75^{th} percentiles), whereas when the drone flew ≥ 90 m asl the median difference was 830 m (492 – 1,636 m).

Our research found that using digital VHF transmitters can provide useful information on macro-scale offshore movements of birds. The network was particularly effective at documenting regional movements of focal species. However, several technical challenges that occurred throughout the study limited data collection at finer spatial scales by telemetry stations within the Block Island network. Monitoring the receiving station on Turbine #1 at BIWF was particularly challenging because technology was not yet available to monitor the system remotely, and in-person equipment checks were limited to infrequent visits by turbine operation staff. Despite these limitations, our application of existing modeling methods to data collected by the Block Island network provided data on movements of birds passing near the Block Island Wind Farm, with model accuracy increasing with flight height of birds corresponding to an increase of simultaneous detections by receiving stations.

Based on our research, available VHF tracking technology has difficulties tracking fine-scale temporal and spatial movements of small (<200 g) volant organisms. Therefore, we also tested the functionality of a direction finding (DF) system that uses phase differences to accurately obtain bearings from a 3-element omnidirectional antenna array. We constructed a platform with three 10 dB omnidirectional antennas equally spaced by a distance of a half-wavelength (0.889 m) of the 166 MHz frequency. We used open source Software Defined Radio (SDR) software on a PC to integrate a FUNCube dongle (FCD) by setting the tuner frequency and sample rate. The FCD demodulated the received signals and converted them to a digital signal after a series of filtering steps. Once converted, the data were saved to a .wav file for post processing using MATLAB. To test the accuracy of this prototype tracking system, a series of drone flights were initiated, with a digitally coded VHF transmitter attached, to test the viability of this system. However, one receiver failed due to PC memory issues thus the results for estimating bearings were limited to two antennas. At very short ranges, bearing accuracy suffered due to the directivity of the omnidirectional antennas. The system performed best (±6°) when the transmitter was farther than 175 m from the array, relatively well (±15°) when the transmitter was over 100 m away from the array, and poorly (±50°) when within 100 m of the antenna array. The research did show it was feasible to track azimuth angles through phase measurements. With further developments to

the current design, it could be feasible to design an antenna array and continuous receiver to monitor fine-scale movements of VHF-tagged birds using phase measurements.

If regulators and biologists are interested in obtaining fine-scale spatial (microscale movements) of volant wildlife at offshore wind farms using VHF or UHF transmitters to assess exposure risk, more intensive research needs to be conducted on the methodology of triangulation to estimate locations from stations with fixed yagi antennas, and most importantly more calibration surveys need to be conducted at offshore sites. This includes establishing at least three or more automated receiving stations in relatively close proximity to assess the accuracy and precision of triangulation methods to assess the location of tagged volant wildlife in the offshore environment. This research could be focused on assessing the accuracy of location estimates when a transmitter is detected from multiple stationary yagi antennas. In addition, when we conducted our research, there were no VHF receivers available that could remotely upload data to determine if the receiver was working or gather data in a timely manner. There now is at least one model of receiver operating in the 434 MHz range that will upload data remotely that should be field tested on offshore turbines or buoys. This remote uploading of data from offshore wind energy facilities needs to be field tested. Based on our research, further calibration surveys are needed to assess the accuracy and precision of spatial estimates of transmitter locations. This is critical for estimating fine-scale movements of target species to assess exposure risk. Finally, further research could be conducted on the feasibility of using phase measurements to accurate detect bearing angles of moving transmitters, which could be used to precisely estimate locations of volant wildlife to obtain more reasonable estimates of exposure risk near active offshore wind energy facilities. These goals are also the research objectives outlined by a research group within New York State Energy Research and Development (NYSERDA) that could provide more insights into tracking technologies be used by biologists to assess exposure risk of birds to offshore wind energy facilities.

Table of Contents

List of Figures

List of Tables

List of Appendices

PART 1: ASSESSING MOVEMENTS OF BIRDS USING DIGITALLY-CODED VHF TRANSMITTERS: A VALIDATION STUDY

Authors:

Peter W.C. Paton, Department of Natural Resources Science, University of Rhode Island
Clara Cooper-Mullin, Department of Natural Resources Science, University of Rhode Island
Soroush Kouhi, Department of Ocean Engineering, University of Rhode Island
Pamela H. Loring, US Fish and Wildlife Service (USFWS), Division of Migratory Birds

1.1 INTRODUCTION

The Bureau of Ocean Energy Management (BOEM) is concerned with the potential impacts of offshore wind energy developments on wildlife, with an emphasis on birds that are federally-listed as threatened or endangered. In the northwestern Atlantic these species include a threatened Atlantic Coast population of the Piping Plover (*Charadrius melodus melodus*), a threatened population of the Red Knot (*Calidris canutus rufa*), and an endangered population of the Roseate Tern (*Sterna dougallii) (*Burger et al. 2011, Loring 2016, Loring et al. 2019). Up until December 2016, there were no operating offshore wind energy facilities in the United States until a 5-turbine 30-megawatt (MW) facility was constructed by Deepwater Wind three miles southeast (SE) of Block Island, Rhode Island, which is now operated by Ørsted (Figure 1.1).

Figure 1.1. The Block Island Wind Farm located in state waters ~5 km off the southeast corner of Block Island was the first operational offshore wind energy facility in North America (photo courtesy of Ørsted).

Birds that utilize offshore habitats may be negatively affected by offshore wind energy developments as a result of: (i) direct mortality from collision with turbine blades, (ii) turbines acting as barriers to migratory or daily movements that increase overall energy expenditure of individuals (barrier effect), or (iii) turbines displacing birds from important foraging and resting areas within the footprint of the development (Desholm and Kahlert 2005, Fox et al. 2006, Larsen and Guillemette 2007, Masden et al. 2010, Langston 2013, Furness et al. 2013, Skov et al. 2018, Fox and Petersen 2019). Yet, potential impacts of offshore wind turbines on migratory bird populations are still not thoroughly understood. Interactions between offshore wind energy facilities and migratory birds have only been studied for a limited number of species at a few sites over the past few decades since offshore wind turbines have become operational in Europe (Cook et al. 2018, Skov et al. 2018, Fox and Petersen 2019). Current empirical evidence from Europe suggests that collision and barrier effects are minimal for most marine birds and likely do not result in negative impacts to marine bird populations (Desholm and Kahlert 2005, Cook et al. 2018). However, available evidence suggests that some species of migratory birds might be vulnerable to collisions with turbines (Furness et al. 2013, Green et al. 2016), thus further investigation is warranted.

Burger et al. (2011) categorized estimated exposure to offshore wind energy facilities at three nested spatial scales: macro-scale (individuals that occur within a geographic region of interest, in this case the Block Island Wind Farm), mesoscale (occurs if individuals are exposed at the macroscale level and fly within the altitudinal span of the wind turbine blades (Rotor Swept Zone: RSZ), 29 to 189 m Above Sea Level (ASL) at Block Island), and microscale (occurs if individuals of the species are exposed at the macro- and mesoscales and fly within the RSZ) of wind turbines. The impact to avian populations at each scale varies temporally. Skov et al. (2018) defined avoidance behaviors (i.e., an action that prevents a collision (SNH 2010)) at three spatial scales: *micro* (a response to single turbine blade, <10 m from Rotor Swept Zone (RSZ), *meso* (within wind farm footprint, 10 m buffer around RSZ, see also Band et al. 2007, Cook et al. 2012, Furness et al. 2013), and *macro* (up to 3 km outside of windfarm, see Desholm and Kahlert 2005). Given these categories of exposure, we were interested how accurately we could track exposure risk of small volant wildlife.

There is increasing evidence that large-bodied birds (e.g., gannets, gulls, loons, seaducks) tend to avoid offshore wind turbines, while there much less information about how small-bodied birds respond (Cook et al. 2018, Skov et al. 2018, Fox and Petersen 2019). Monitoring the exposure risk of plovers in areas where BOEM renewable energy lease blocks occur is particularly challenging due to their small body size and nocturnal migratory behavior that renders satellite-based or survey-based methods less suitable for these species (Loring et al. 2019). Although terns will fly diurnally during foraging bouts over 40 km from breeding colonies (Loring et al. 2019) and, thus can be surveyed with boat-based or aerial surveys (Perrow et al. 2011, Thaxter et al. 2012, Harwood et al. 2017, Evans et al.

2019, Critchley et al. 2020), previous tracking studies have shown that terns move offshore at night during the post-breeding dispersal period (Loring et al. 2017) and during migration (Loring et al. 2019). Therefore, the best technology currently available to determine exposure risk for terns and plovers is automated tracking with digitally encoded very high frequency (VHF) or ultrahigh frequency (UHF) radio tags.

Wildlife biologists have been tracking organisms with radio transmitters in the VHF band since the 1950s (Cochran et al. 1965, White and Garrott 1990). VHF is the designation of radio waves with wavelengths ranging from 1 to 10 m that correspond to radio frequency electromagnetic waves that range from 30 to 300 megahertz (MHz). Tracking organisms within the VHF band requires: 1) a transmitter with a power source and antenna that emits a signal (e.g., ~166.380 MHz), 2) some type of attachment system to mount the tag on the organism of interest that minimizes impact to the organism (Barron et al. 2010, Geen et al. 2019), 3) either a Yagi, H-Adcock, dipole or loop antenna to determine the location of the tagged organism, and 4) a receiver to process the signal detection (Kenward 2001). VHF telemetry works on a "line of sight" detection, thus landscape barriers (e.g., vertical rock face) can block the emitted signal.

Radio Direction Finding (RDF) requires a passive receiving system that extracts information from passing electromagnetic radio waves from a VHF transmitter to estimate the bearing angle from the receiver to the VHF transmitter. There are three RDF approaches that researchers typically use to estimate the position of the VHF tag from two or more receiving stations: amplitude response, phase delay response, and time delay (Jenkins 1991, Kenward 2001). Most avian ecologists use the amplitude response to estimate the location of tagged individuals (White and Garrott 1990, Kenward 2001), which infers location based on a combination of signal strength and compass bearing (Desrochers et al. 2008), which is the focus of Part I of this report. Traditionally, biologists estimate the compass bearing of a VHF tag from the receiver by rotating a directional antenna, either a Yagi-Uda or H-Adock, to detect the maximum signal strength or the null signal, respectively (Cochran et al. 1965, White and Garrott 1990, Kenward 2001). The receiving stations must be known locations, but they can either be a series of temporary locations or fixed locations. In Part II of this report, we focus on estimating VHF tag locations using the phase delay response using omnidirectional antennas.

The advantage of Yagi-Uda (hereafter Yagi) antennas is that they achieve high gain (e.g., detect approximately twice the range of dipole antennas), are highly directional (i.e., the signal reception pattern has the strongest peak at the front of the antenna and has a high 'front to back' ratio), they are relatively easy to handle and maintain, waste relatively little power, and cover a broad range of frequencies, however they are prone to noise and atmospheric effects (Kenward 2001). Thus, bearings from two or more different receiving stations can be used to bi-angulate or triangulate the position of a tagged individual (White

and Garrott 1990). The other directional antenna used by many biologists is the H-Adcock antenna which has greater gain than a dipole antenna, and the reception pattern has a distinctive 'null' when the elements are equidistance from the tag - therefore the estimate of the signal bearing is more accurate than a Yagi antenna. However, just like a dipole, there is uncertainty about the true signal bearing versus the 'reverse' bearing, which can be resolved using a variety of techniques (Kenward 2001). When using the amplitude response approach, an omnidirectional antenna (i.e., either dipole antenna when horizontal or a loop antenna) can be used to detect the presence of a tag within the range the antenna (Kenward 2001).

The Motus network is an automated network of receiving stations, primarily using fixed Yagi antennas designed to monitor the movements small (<50 g) volant (flying) wildlife at local, regional, and hemispheric scales using digital VHF tags (e.g., 166.380 MHz in North America) (Taylor et al. 2017), although recently biologists have also started to use UHF tag (434 MHz). Most projects associated with the Motus network use Nanotags to track smaller species of birds or bats. Nanotags (www.lotek.com) are lightweight digital VHF transmitters that have a relatively long battery life (~70-140 days depending on tag weight and burst interval) and emit uniquely identifiable signals every 3-7 seconds on a common frequency. The automated receiver stations in this network consist of one or more fixed Yagi or omni-directional antennas on towers of various heights. Previous avian tracking studies funded by BOEM utilized receiving stations that consisted of 6 nine-element (3.3 m long) Yagi antennas horizontally mounted in a radial configuration at 60° intervals on 12.2-m tall radio antenna masts (Loring et al. 2019). Loring et al. (2019) estimated the detection range of these 12.2 m towers was up to 20 km for a bird flying at 25 m altitude and 40 km for a bird flying at 250 m altitude, while birds flying at 1,000 m could be detected at over 80 km away.

The Block Island Wind Farm provides a unique opportunity to assess exposure of migratory birds at an operating offshore wind energy facility. Due to the proximity of the Block Island Wind Farm to Block Island (~3 miles (5 km)), land-based receiving stations can be constructed on Block Island to track movements of tagged birds passing near the Block Island Wind Farm. Baseline daily movement data of Roseate and Common terns, and Piping Plovers near Block Island during the breeding, post-breeding staging period, and fall migration was collected for three field seasons prior to the construction of the Block Island Wind Farm by a network of over 30 receiving stations along in New England and New England Bight region on the Atlantic Coast (Figure 1.2; Loring 2016, Loring et al. 2019). Previous BOEM-funded studies on offshore avian movements developed spatially explicit movement models of Common and Roseate terns and Piping Plovers throughout southern New England, including movements through federal offshore energy lease blocks in the region (Loring et al. 2019). These models combined a physical model of bird movements with the electrical characteristics of the receiving arrays to predict the flight paths of birds from time series of power received sequentially from several towers and beams (Janaswamy et al. 2018).

Results from regional movement studies of terns and plovers in the Atlantic OCS indicate that these species may move through BOEM renewable energy lease blocks during post-breeding and fall migratory movements (Loring et al. 2019). Therefore, the goal of this project was to evaluate the potential to assess fine-scale movements of relatively lightweight (~150 g or smaller) volant (free-flying) organisms near offshore wind turbines (after the development of the Block Island Wind Farm), with a focus on terns and plovers. As BOEM renewable energy lease blocks currently total 1,742,252 acres along the Atlantic Outer Continental Shelf (Figure 1.2), there is a pressing need to understand in greater detail the exposure risk of these listed species and other volant wildlife to the development of these offshore renewable energy facilities (Goodale et al. 2016, Platteeuw et al. 2017, Kelsey et al. 2018, Fox and Petersen 2019) and to help to inform estimates of collision risk (Band et al. 2007, Furness et al. 2016, Masden and Cook 2016).

1.2 METHODS

1.2.1 Study Area

1.2.1.1 Atlantic OCS and Wind Energy Areas

The primary Study Area extended along the US Atlantic Coast and adjacent OCS from Cape Cod, MA to the north and Back Bay, VA to the south, with a focus on Block Island (Figure 1.2). Currently (June 2020), there are 16 BOEM Renewable Energy Lease Areas within the Study Area (Table 1.1). These BOEM Renewable Energy Lease Areas are located in Rhode Island Sound and adjacent offshore waters of Massachusetts (~908,000 acres), New York Bight (~80,000 acres km²), and adjacent waters offshore of New Jersey (344,000 acres), Delaware (~26,000 acres), Maryland (~80,000 acres), Virginia (113,000 acres), and North Carolina (~122,000 acres) In total, their combined area covers 1,742,252 acres of the Atlantic OCS. The Motus Wildlife Tracking system network extended from Nova Scotia to the coast of South America (Taylor et al. 2017), with tracking stations changing annually as new stations were brought online or older stations were decommissioned due to a lack of funding resources.

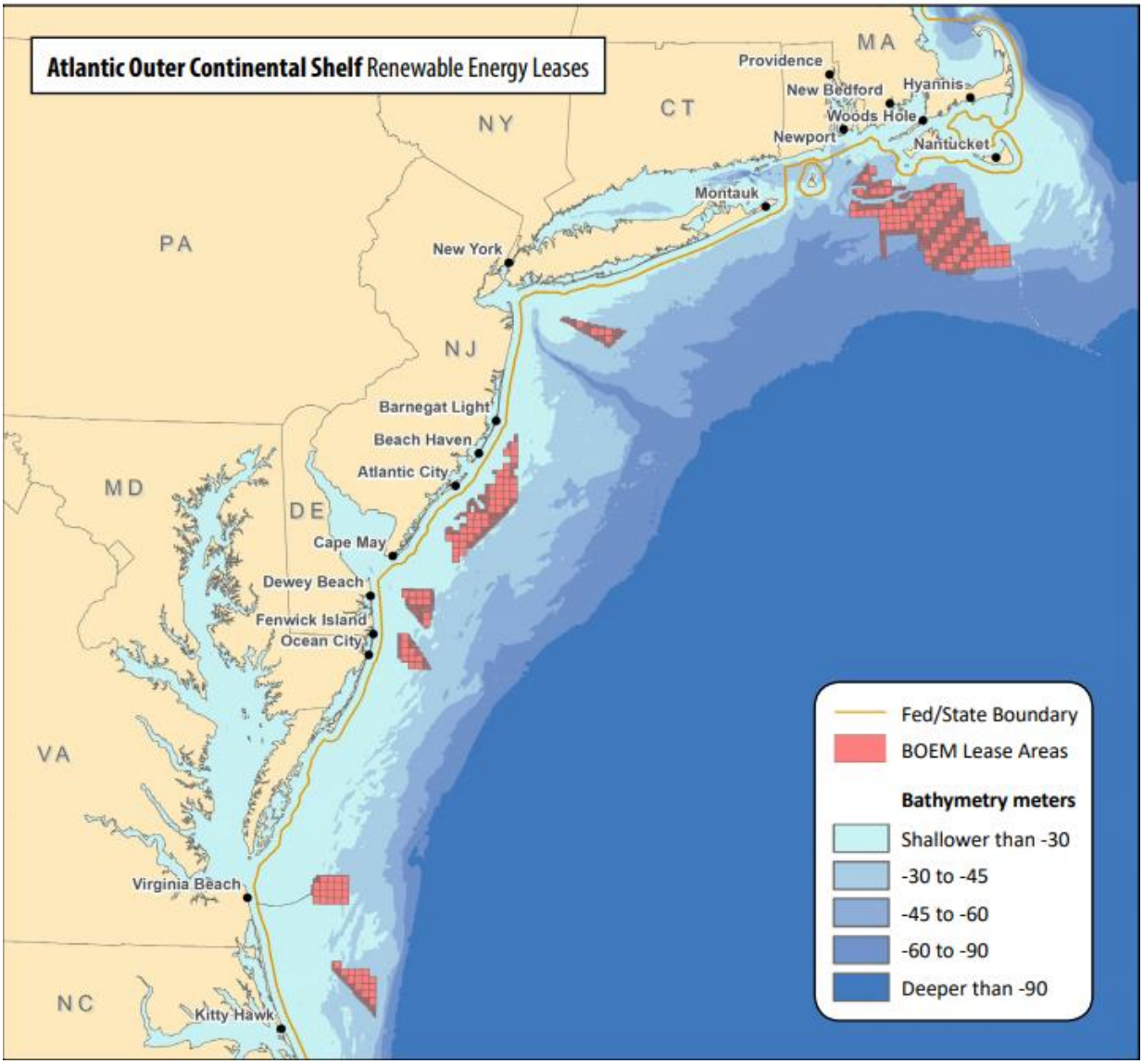

Figure 1.2. Location of BOEM renewable energy lease areas along the Atlantic Outer Continental Shelf (from BOEM 2019).

Table 1.1. Current leasing status of BOEM renewable energy lease blocks along the Atlantic Outer Continental Shelf (BOEM 2020).

Lease Number	Year	Company	Acres	State
OCS-A 0482	2012	GSOE I	70,098	DE
OCS-A 0519	2018	Skipjack Offshore Energy	26,332	DE
OCS-A 0483	2013	Virginia Electric and Power	112,799	VA
OCS-A 0486	2013	DWW REV I	83,798	RI/MA
OCS-A 0517	2013	DWW South Fork.	13,700	RI/MA
OCS-A 0487	2013	DWW NE	67,252	RI/MA
OCS-A 0490	2014	US Wind Inc.	79,707	MD
OCS-A 0498	2016	Ocean Wind	160,480	NJ
OCS-A 0499	2016	Atlantic Shores Offshore W	183,353	NJ
OCS-A 0500	2015	Bay State Wind	187,523	MA
OCS-A 0501	2015	Vineyard Wind	166,886	MA
OCS-A 0508	2017	Avangrid Renewables	122,405	NC
OCS-A 0512	2017	Equinor Wind US	79,350	NY
OCS-A 0520	2018	Equinor Wind US	128,811	MA
OCS-A 0521	2018	Mayflower Wind Energy	127,388	MA
OCS-A 0522	2018	Vineyard Wind	132,370	MA
Total			1,742,252	

1.2.2 Ecology of target species

1.2.2.1 Common Tern ecology

The Common Tern (*Sterna hirundo*)is a cosmopolitan, moderately sized (110 to 145 g) tern that nests in small to large colonies (e.g., <12,000 individuals at Monomoy, Massachusetts), near freshwater and saltwater habitats throughout the Holarctic and winters in coastal habitats in the southern hemisphere (Nisbet et al. 2017). In New England, most the population nests at offshore islands, where they usually forage for a diversity of small fish ~20 to 30 km of breeding colonies (Safina et al. 1990, Nisbet et al. 2017). In southern New England, adults arrive at their nesting sites in late April to May, initiate 2-3 egg clutches in open habitats (Burger and Gochfeld 1991) from late May through mid-July, peak hatching occurs between late June and early July, and peak fledging (~25 d after hatching) occurs from mid-July early August (Nisbet et al. 2017). After fledging, many of the adults and their accompanying chicks disperse from colonies throughout New England to stage at Cape Cod for ~one month prior to migration to South America (Nisbet and Mostello 2015, Loring et al. 2017, Nisbet et al. 2017), where birds can be found foraging far offshore (Goyet 2014). Common Terns breeding in New England tend to

winter along the east coast of South America (Nisbet et al. 2011a, 2011b; Nisbet and Mostello 2015). Common Terns breeding in Germany behave similarly, staging for about 4 weeks before migrating to West Africa where they wintered in upwelling areas; interestingly spring migration was longer ~ 2 months than fall migration of ~ 1.3 months (Becker et al. 2016). Furness et al. (2013) ranked Common Terns as low vulnerability to collision risk with offshore wind turbines because they estimated that only 7% of individuals fly within the rotor swept zone.

1.2.2.2 Roseate Tern ecology

The subspecies of the Roseate Tern (*Sterna dougallii dougallii*) nesting in New England was federally listed as endangered in 1987 (Nisbet et al. 2014). This species is slightly smaller (95 to 130 g) than similar the Common Tern (Figure 1.3). Roseate Terns nest across the Holarctic and winter in the southern hemisphere. In New England, Roseate Terns only nest on offshore islands where there are also Common Terns nesting, typically at sites that have over 1,000 nesting pairs of Common Terns. Much of the population (4,171 of 4,593 pairs (91%) in 2018) of this endangered subspecies nests at three sites in southern New England: Bird Island, MA (1,175 pairs in 2018 during peak census); Ram Island, MA (1,093 pairs in 2018), and Great Gull Island, NY (1,903 pairs in 2018) (Roseate Tern Recovery Team, unpubl. data). Adults typically exhibit high fidelity to breeding colonies, although they will disperse to other breeding colonies (Spendelow et al. 2010). The breeding chronology of Roseate Terns in southern New England is similar to the sympatric Common Tern, with adults and their young departing from breeding colonies to the primary staging site at Cape Cod, Massachusetts from mid-July to early August (Althouse et al. 2016, 2018), where they are detected foraging far offshore (Goyert 2014). This species has a more specialized diet than Common Terns, which consists primarily of sand lance (*Ammodytes* spp.) (Safina et al. 1990, Urmy and Warren 2018, Staudinger et al. 2020). Peak migration from staging sites in New England is initiated in early September (Nisbet et al. 2014), when Roseate Terns presumably migrate offshore to staging sites in Puerto Rico and the Dominican Republic and then to wintering sites along the eastern coast of South America (Mostello et al. 2014). Occasionally birds breeding in the eastern Atlantic (Azores) are detected wintering in the western Atlantic (Brazil), thus there is some transatlantic migration (Neves et al. 2016). Burger et al. (2011) suggested that Roseate Terns were likely exposed to collision risk with offshore wind energy facilities during migratory movements and the breeding season when the occur on the Atlantic Outer Continental Shelf.

Figure 1.3. Adult Roseate Terns with yellow plastic field readable (PFR) band used to aid observers and adult with sandlance (*Ammodytes* spp) which is the primary fish this species consumes and feeds to their chicks (Staudinger et al. 2020).

1.2.2.3 Piping Plover ecology

Piping Plovers are small-bodied (~50 g) migratory shorebirds (Figure 1.4), with three federally-listed populations in North America: Atlantic Coast (Threatened), Great Lakes (Endangered), and the Northern Great Plains (Threatened) (Elliott-Smith and Haig 2004). The Atlantic Coast population was estimated at 2,008 pairs in 2019, with almost 50% (980 pairs) nesting in New England (USFWS 2020a), which was the first time their population was greater than the recovery plan goal (USFWS 2020b). Piping Plovers start to arrive in southern New England in late March with nest initiation from late April to early July, with latter nesting attempts typically second or third nesting attempts. The species tends to select unvegetated microhabitats to nest (Figure 1.5), with an incubation period ~28 d and fledging takes ~25 days. The migration ecology is the "least understood part of the Piping Plovers annual cycle" (USFWS 2020b). Adults initiate migration to staging sites at Cape Hatteras in early July (Weithman et al. 2018), with most adults departing breeding sites by early August, where juveniles tend to linger into September (Elliott-Smith and Haig 2004, Loring et al. 2020). Based on resightings of banded individuals, most plovers breeding in southern New England winter in Florida and the Caribbean, with much of the population detected in the Bahamas and Turks and Caicos (Gratto-Trevor et al. 2016, P. Paton, unpubl. data). Burger et at. (2011) hypothesized that Piping Plovers were only exposed to collision risk to nearshore wind energy facilities during spring and fall migration as they believed this species migrated close to shore. However, Loring et al. (2019, 2020) found that Piping Plover often migrate far from shore.

Figure 1.4. Piping Plover with transmitter glued to back and trailing antenna; green flag with 3 alphanumeric codes were unique to each individual, which aided resighting records. Tagged plovers were regularly detected at stopover sites from New York to South Carolina and wintering areas Florida to Turks and Caicos.

Figure 1.5. Piping Plover walk-in trap at Monomoy NWR in open sandy habitat preferred by this species for nesting.

1.2.3 Tagging Sites

We conducted all tagging during the breeding period and tracking continued through post-breeding dispersal and migratory departure. We tagged Common and Roseate Terns at the largest Roseate Tern colony in the western Atlantic (Great Gull Island, NY), as well as one of the larger Common Tern colonies in the region (Falkner Island, CT) (Nisbet et al. 2014, 2017). We tagged Piping Plovers in Rhode Island track their southbound flights during fall migration (Figure 1.6). Trapping methods used for this study are described in detail in Loring et al. (2019).

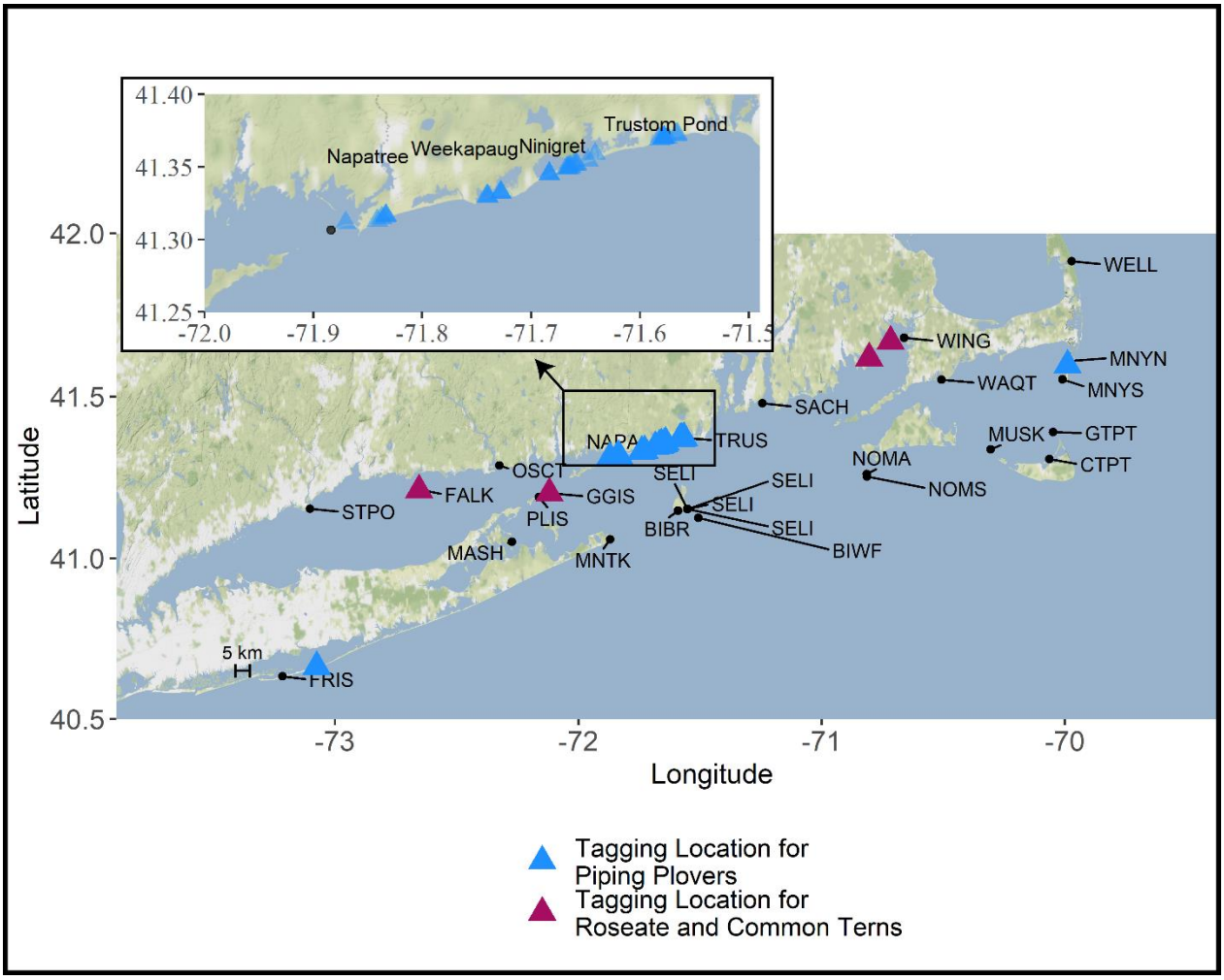

Figure 1.6. Capture and tagging locations for Roseate Terns and Common Terns (pink) and Piping Plovers (blue) from 2017-2019. Locations of automated receiving stations in the region (black circles) are labeled. The inset map shows the distribution of tagging locations for Piping Plovers along the coast of Rhode Island.

1.2.3.1 Great Gull Island, New York

Great Gull Island (GGIS; 41°12'23" N, 72°06'25" W) is a 0.08 km^2 offshore island in eastern Long Island Sound, NY, that supports one of the largest concentrations of nesting Common Terns (~9,000 pairs) and Roseate Terns (~2,000 pairs) in the Western Hemisphere (H. Hays and G. Cormons, unpubl. data). GGIS is managed by the Great Gull Island Project with the American Museum of Natural History. On GGI, we tagged 20 Common Terns in 2018 and 40 Common Terns in 2019, and 20 Roseate Terns in 2018 (Appendix 1.1).

1.2.3.2 Falkner Island, Connecticut

Falkner Island (FALK, 41°12′39″N 72°39′11″W) is a ~1.2 ha island owned and managed by the US Fish and Wildlife Service's Stewart B. McKinney NWR in Long Island Sound 5 km south of Guilford, Connecticut. Falkner Island has a small colony of Roseate Terns (~30-60 pairs) and a larger population of Common Terns (~1,500 to 2,000 pairs) (Kris Vagos, Refuge Biologist, pers. comm.). We tagged 18 Common Terns and 10 Roseate Terns on Falkner in 2018 (Appendix 1.2).

1.2.3.3 Coastal Rhode Island

We tagged 20 and 18 Piping Plovers in 2018 and 2019, respectively, at several beaches along the southern coast of Rhode Island. We planned on tagging 20 plovers in 2019, but two tags would not activate, and we were unable to obtain replacement tags in time for field efforts. Nesting Piping Plovers at Rhode Island's beaches were monitored by USFWS staff from the Rhode Island National Wildlife Refuge complex, although individual sites were owned and managed by various Federal, State, and NGO entities and have varying levels of public use and access. Across all sites in Rhode Island, the highest trapping effort for Piping Plovers was at Trustom Pond NWR (41°22'N, 71°34'W) at East Beach Watch Hill (EBWH; 41°18'N, 71°50'W). Trustom Pond NWR (13 pairs in 2019) and EBWH (15 pairs in 2019) contain the largest concentrations of the 65 of nesting pairs monitored by USFWS staff in 2019 (Durkin et al. 2019).

1.2.3.4 Buzzard's Bay, MA

In 2017, Loring et al. (2019) tagged 29 Common and 30 Roseate Terns from three islands (Bird, Ram, and Penikese) in Buzzards Bay, Massachusetts. These islands are managed by the Massachusetts Natural Heritage and Endangered Species Program and collectively supported over 6,500 Common Terns and approximately 2,600 pairs of Roseate Terns in 2016 (Mostello et al. 2018). Bird Island (41°40'10 N, 70°43'02"W) is a 0.006 km^2 island located < 2 km off the coast of Marion, MA. Ram Island (41°37'05"N, 70°48'16"W) is a 0.01 km^2 island located < 1 km off the coast of Mattapoisett, MA. Penikese Island (41°27'05"N, 70°55'03"W) is 0.3 km^2 island located near the western entrance of Buzzards Bay, within the Elizabeth Islands chain.

1.2.4 Digital VHF Transmitters

In this study, we tracked the movements of Common Terns, Roseate Terns, and Piping Plovers using digital VHF transmitters ("nanotags", Lotek Wireless, Ontario, Canada). Each Common and Roseate tern in the study was fitted with Lotek NTQB2-4-2 nanotags (Appendices 1.1 & 1.2). The transmitter body measured 1.4 g; 12 x 8 x 8 mm with an 18-cm long antenna, and a battery life of 72-92 days. The NTQB2-4-2 nanotags were sutured on the backs of terns, since they are plunge-divers, which increased tag retention rates (Loring et al. 2019). All tern tags

were coated with a waterproofing material and custom-fit with 1-mm tubes at the front and back of the transmitter body for attachment, bringing the total tag weight to 1.5 g. The transmitter and attachment materials weighed <2% of the body mass of tagged Common and Roseate terns. Detailed behavior studies found no evidence of an adverse effect of the tag on adult Common Terns (Loring 2016) or adult Roseate Terns (Paton et al. in press)

In 2017, 2018 and 2019, each Piping Plover within the study was fitted with a Lotek NTQB2-3-2 nanotag (0.67 g; 12 x 6 x 5 mm), which had a 16.5-cm long antenna (Appendix 1.3). Following Loring et al. (2019), transmitters were glued to the interscapular region. The transmitter and attachment materials weighed <2% of the body mass of tagged Piping Plovers. During prior fieldwork, we determined the tags did not affect nest success or chick survival rates when their parents were tagged (Stantial et al. 2018) or apparent survival rates of adult Piping Plovers (Stantial et al. 2019)

All transmitters in the study were programmed to continuously transmit signals on a shared frequency of 166.380 MHz from activation through the end of battery life. Burst intervals (time between transmissions) were randomly assigned and unique to each transmitter and ranged from 4 to 6 seconds. The expected life of the NTQB-3-2 nanotags ranged from 72 days (4 second burst interval) to 92 days (6 second burst interval). Tag deployment metadata for each tagged bird in this study are provided in Appendix 1.3).

1.2.5 Automated Radio Telemetry Stations: Motus Network

We tracked the signals of tagged birds using multiple automated radio telemetry stations that were part of the Motus Wildlife Tracking System, an international network of collaborative automated radio telemetry studies (Taylor et al. 2017). From 2014 to 2017, most stations in the US Atlantic coast study area consisted of a 12.2-m radio antenna mast supporting six 9-element (3.3 m long, www.Lairdconnect.com model PLC1669: 11.1 dB gain, 166 to 174 MHz) Yagi-Uda (hereafter Yagi) antennas mounted in a radial configuration at 60° intervals (Loring et al. 2019). During Fall 2017, these towers were modified to 6-m tall towers by removing two 3-m long segments, and replacing the 9-element Yagi antennas with shortened 5-element Yagi antennas (~1.5 m long, similar to a www.Lairdconnect.com PLC1666, ~7 dB gain; frequency range 166 to 174 MHz). Additional coverage throughout the Study Area was provided by Motus Network receiving stations that varied in height, number of antennas, station elevation, and type of receiver (Figures 1.7 & 1.8). To view a map of the extent of the Motus Network and how it has expanded from 2013 through 2020 visit: https://motus.org/data/receiversMap?lang=en

Figure 1.7. Example of a Motus Wildlife Tracking System station with three 9-element, 11-dB Yagi antennas located on a 6 m telescoping mast on the northcentral Puerto Rico.

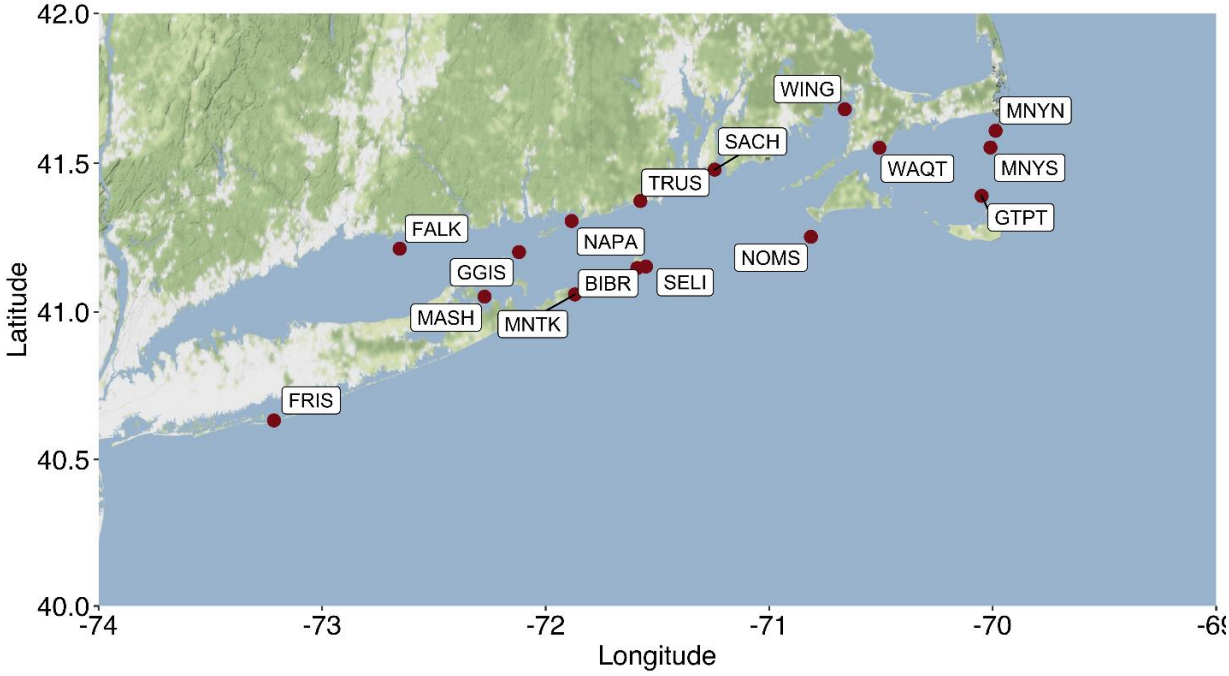

Figure 1.8. Some of the Motus Wildlife Tracking System network stations in southern New England that tracked focal bird species for this project.

In 2018 and 2019, 31 Motus stations from Nova Scotia to French Guiana detected terns and plovers tagged for this study (Table 1.2). We operated an array of eleven, land-based automated radio telemetry towers at coastal sites ranging from Cape Cod, MA to Long Island, NY. In addition, at each tern tagging site (Great Gull Island, NY, and Falkner Island, CT), we operated receiving stations that were configured to monitor to track local movements of tagged terns at the breeding colony.

Table 1.2. Motus Wildlife Tracking System automated telemetry stations that had detections of tagged Roseate Terns, Common Terns, or Piping Plovers in 2017, 2018 and 2019.

Code	Location	Latitude	Longitude	Motus Project ID	Model[1]	Years active	# of Tagged Birds Detected
TICO	Icapuí, Brazil	-4.699	-37.358	239	SG	2019	1
CAYE	Cayenne, French Guiana	4.944	-52.325	117	SG	2018	1
AWYA	Awala-Yalimapo, French Guiana	5.746	-53.935	117	SG	‘18,‘19	4
CEDI	Cedar Is. NWR, NC	34.957	-76.278	4	SG	‘17	4
PEAI	Pea Island NWR, NC	35.717	-75.493	4	SG	‘17,‘18,’19	16
BBVA	Back Bay NWR, VA	36.671	-75.915	14	Lotek	‘17	9
FISH	Fisherman Is, VA	37.098	-75.978	167	Lotek	‘19	1
SKID	Skidmore Is., DE	37.134	-75.925	14	Lotek	‘17,‘18,’19	15
PARR	Wachapreague, VA	37.573	-75.617	14	Lotek	‘18	3
CHIN	Chincoteague VA	37.862	-75.369	14	Lotek	‘17	1
ASSA	Assateauge Is. DE	38.241	-75.136	48	SG	‘17,‘18,’19	5
CHDE	Cape Henlopen State Park, DE	38.770	-75.085	14	Lotek	‘17,‘18,’19	8
DADS	Dad's, Cape May, NJ	39.028	-74.801	47	SG	‘17	2
NORB	Cape May, NJ	39.053	-74.925	47	SG	‘17	1
AVNJ	Avalon, NJ	39.092	-74.717	14	Lotek	‘19	1
NBNJ	North Brigantine NJ	39.429	-74.34	14	Lotek	‘17	6
RTNJ	Great Bay B. WMA, NJ	39.509	-74.324	14	Lotek	‘19	1
SHNJ	Sandy Hook, NJ	40.429	-73.984	14	Lotek	‘17,‘18,’19	5
CONY	Coney Island, NY	40.573	-73.977	14	Lotek	‘17	1
FRIS	Fire Is., NY	40.632	-73.215	14	Lotek	‘17,‘18,’19	6
MASH	Mashomack Preserve TNC, NY	41.052	-72.273	14	Lotek	‘18, ‘19	30
MNTK	Montauk, NY	41.059	-71.869	14	Lotek	‘17,‘18,’19	135
BIWF	Block Is. Wind Farm, RI	41.126	-71.507	14	SG	‘17	1
BIBR	Black Rock, RI	41.148	-71.59	14	SG	‘17,‘18,’19	63
SELI	SE Lighthouse, RI	41.153	-71.552	14	Lotek	‘17,‘18,’19	44
STPO	Stratford Point, CT	41.155	-73.103	84	SG	‘17	2
PLIS	Plum Island, NY	41.189	-72.163	14	Lotek	‘17	80
GGIS	Great Gull Is., NY	41.202	-72.119	14	Lotek	‘17,‘18,’19	147

Code	Location	Latitude	Longitude	Motus Project ID	Model[1]	Years active	
FALK	Falkner Is., CT	41.213	-72.653	14	Lotek	‘18, ‘19	51
NOMS	South Nomans Is., MA	41.253	-70.813	14	Lotek	‘17,‘18,’19	18
NOMA	North Nomans Is., MA	41.261	-70.815	14	Lotek	‘17	63
OSCT	Old Lyme, CT	41.287	-72.324	14	Lotek	‘17, ‘18	2
NAPA	Napatree, RI	41.306	-71.883	14	Lotek	‘17,‘18,’19	36
CTPT	Coatue Beach, MA	41.307	-70.063	14	Lotek	‘17, ‘18	36
MUSK	Muskeget Is, MA	41.337	-70.304	14	Lotek	‘17	61
TRUS	Trustom Pond NWR, RI	41.373	-71.576	14	Lotek	‘17,‘18,’19	71
GTPT	Great Pt Light, MA	41.390	-70.049	14	Lotek	‘17, ‘18	48
SACH	Sachuest Pt NWR, RI	41.479	-71.243	14	Lotek	‘17,‘18,’19	10
WAQT	Waquoit Bay NERR, MA	41.551	-70.506	14	Lotek	‘17,‘18,’19	84
MNYS	S Monomoy NWR, MA	41.553	-70.01	14	Lotek	‘17, ‘18,	29
MNYN	N Monomoy NWR, MA	41.609	-69.986	14	Lotek	‘17,‘18,’19	51
WING	Wings Neck, MA	41.680	-70.661	14	Lotek	‘17, ‘18	6
WELL	Wellfleet, MA	41.915	-69.972	14	Lotek	‘17	1
RCPT	Race Point Lighthouse, MA	42.065	-70.243	14	Lotek	‘17	11
PKRS	Parker River NWR, MA	42.780	-70.808	9	SG	‘19	2
WNER	Rachel Carson NWR, ME	43.349	-70.523	25	SG	‘19	1

[1]Sensorgnome (SG) or Lotek receiver

1.2.5.1 Stations on Block Island: Black Rock and Southeast Lighthouse

On and near Block Island, we operated three receiving stations from 2017 to 2019, one at Southeast Lighthouse (on land owned by the Southeast Lighthouse Foundation) and one at Black Rock (land owned by the Natural Conservancy), and the eastern-most turbine (#1) on the Block Island Wind Farm (owned and operated by Deepwater Wind, which is now operated by Ørsted; www.us.Orsted.com/wind-projects). Our permits from the town of New Shoreham required that Black Rock and Southeast Lighthouse receiving stations were temporary structures, therefore they had to be deconstructed around November each year, stored on the mainland, and transported back to Block Island each spring to be reconstructed by a crew of 3-5 people.
At the two land-based receiving stations on Block Island, we tested a variety of hardware and software configurations to assess effects to detection rates throughout the project (Table 1.3).

In 2017, the receiving station at Southeast Lighthouse was operated by Loring et al. (2019). It consisted of four 3-m long triangular tower sections (www.rohnnet.com; 25G), with six 9-element 11-dB antennas mounted in a radial configuration at 60° intervals (Table 1.3). The station at Black Rock consisted of a portable telescoping mast extended to a height of 6.1 m. This station had three 9-element 11-dB Yagi antennas, a Sensorgnome receiver with a beaglebone black processer, a 140-watt solar panel, two 12-volt deep-cycle batteries, and a lockable tool case for the receiver, the marine batteries, and a solar charge controller (Figure 1.9). Antenna bearings for these three Yagi antennas are given in Table 1.3, with two antennas facing south towards the Block Island Wind Farm.

Figure 1.9. Telescoping mast (~6 m tall) used at Black Rock and Southeast Lighthouse, Block Island, RI during 2017 field season. This photo is the Black Rock station with three 9-element 3.3 m long, 11-dB Yagi antennas, a 140-watt solar panel used as power source, and metal lockable tool case that contained the receiver, solar charge controller and 2 marine batteries.

In 2018 at Black Rock, we constructed a 6.1 m tall tower using two 3-m long triangular tower sections (www.rohnnet.com; 25G), with three 5-element 8-dB Yagi antennas constructed from the terminal end of a 9-element Yagi antenna (i.e., 3 directors, one driven element and one reflector) and one 6.4 m tall 10-dB omnidirectional antenna (Shakespeare model 476 VHF antenna; www.Shakespeare.ce.com); the latest model Sensorgnome receiver with a newer model raspberry pi processor constructed by Compudata.ca to collect data, and same power supply and lock box as in 2017 (Figures 1.9 & 1.10). At Southeast Lighthouse in 2018, the station consisted of a 6.1 m pop-up mast, one 5-element 8-dB Yagi antenna, one 10-dB omnidirectional antenna, a Sensorgnome receiver with a raspberry pi processor, and associated supplies to power the station (Figure 1.12). Antenna bearings for 2018 are given in Table 1.3.

Table 1.3. Summary of automated VHF telemetry stations operated by this project on Block Island and vicinity from 2017 – 2019. The stations included Block Island Wind Farm (BIWF), Black Rock (TNC property) and Southeast Lighthouse (SE Lighthouse Foundation).

Station (tower height in m)	Year	Antenna bearing	Receiver[1]	Begin Date	End Date	Motus Deploy ID
BIWF (33 m)	2017	166°*	SG-BBK	08-03	09-14	4488
BIWF (33 m)	2017	256°*	SG-BBK	08-03	09-14	4488
BIWF (33 m)	2017	346°*	SG-BBK	08-03	09-14	4488
BIWF (33 m)	2017	76°*	SG-BBK	08-03	09-14	4488
BIWF (33 m)	2018	166°*	SG-BBK	05-16	10-01	5004
BIWF (33 m)	2018	256°*	SG-BBK	05-16	10-01	5004
BIWF (33 m)	2018	346°*	SG-BBK	05-16	10-01	5004
BIWF (33 m)	2018	76°*	SG-BBK	05-16	10-01	5004
BIWF (33 m)	2019	346°*	L-800-D1	06-26	10-24	5375
BIWF (33 m)	2019	76°*	L-800-D1	06-26	10-24	5375
BIWF (33 m)	2019	256°*	L-800-D1	06-26	10-24	5375
BIWF (33 m)	2019	166°*	L-800-D1	06-26	10-24	5375
Black Rock (6 m)	2017	102°**	SG-BBK	07-01	12-28	4483
Black Rock (6 m)	2017	152°*	SG-BBK	07-01	12-28	4483
Black Rock (6 m)	2017	201°**	SG-BBK	07-01	12-28	4483
Black Rock (6 m)	2018	130°*	SG-RPI	05-15	10-01	4998
Black Rock (6 m)	2018	250°*	SG-RPI	05-15	10-01	4998
Black Rock (6 m)	2018	10°*	SG-RPI	05-15	10-01	4998
Black Rock (6 m)	2018	OMNI°*	SG-RPI	05-15	10-01	4998
Black Rock (6 m)	2019	234°*	L-SRX800	06-03	08-31	5374, 6035
Black Rock (6 m)	2019	114°*	L-SRX800	06-03	08-31	5374, 6035
Black Rock (6 m)	2019	336°*	L-SRX800	06-03	08-31	5374, 6035
Black Rock (6 m)	2019	OMNI	L-SRX800	06-03	08-31	5374, 6035
SE Light (12 m')	2017	60° int[2]**	L-SRX800	01-01	10-18	3271
SE Light (6 m)	2018	166°*	SG-RPI	05-15	10-15	4994
SE Light (6 m)	2018	OMNI	SG-RPI	05-15	10-15	4994
SE Light (3.3 m)	2019	98°*	L-SRX800	06-03	12-31	5372
SE Light (3.3 m)	2019	338°*	L-SRX800	06-03	12-31	5372
SE Light (3.3 m)	2019	178°*	L-SRX800	06-03	12-31	5372
SE Light (3.3 m)	2019	OMNI	L-SRX800	06-03	12-31	5372

[1] Receiver models: sensorgnome beaglebone black (SG -BBK), sensorgnome raspberry pi (SG-RPI), Lotek model SRX800MD2 (L-SRX800), or Lotek model SRX800D1 (L-800-D1)

[2]6 antennas at 60° intervals: bearings: 0°, 60°, 120°, 180°, 240°, 300°,

*5-element 8-dB Yagi antenna, **9-element 11-dB Yagi antenna

Figure 1.10. Tower array at Black Rock, Block Island used during 2018 field season, which consisted of two 3.3 m tower segments with three 5-element 8-dB Yagi antennas and one 6.4 m tall 10-dB tall omnidirectional antenna.

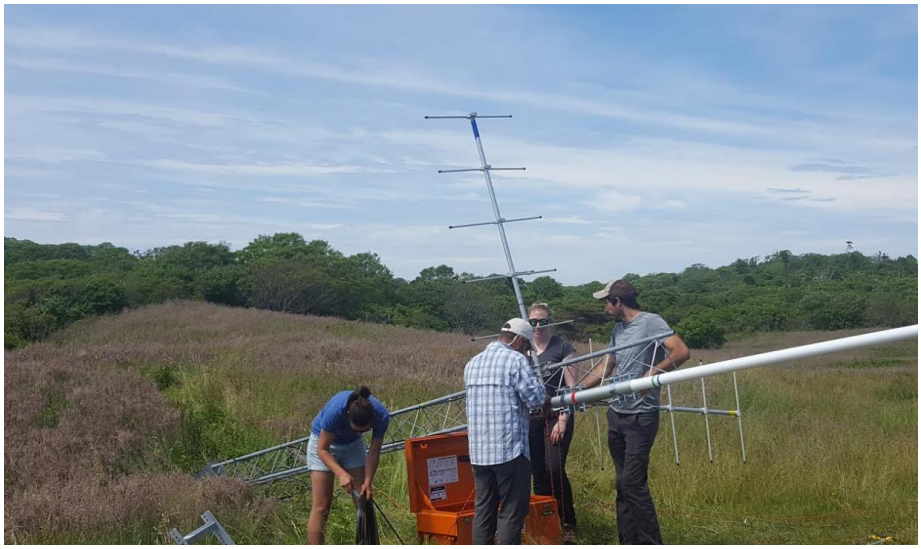

Figure 1.11. Tower being constructed at Black Rock, Block Island in June 2018. This 20 ft tall tower had 3 5-element 8-dB Yagi antennas and a 6.4 m tall 10-dB omnidirectional antenna.

Figure 1.12. Tower being constructed for the 2018 field season at Southeast Lighthouse. Tower was built on 4 m tall pop-mast and included 1 5-element 8-dB Yagi antenna and one 6.4 m tall 10-dB omnidirectional antenna. The lighthouse was north of the tower array and another omnidirectional antenna for another project is in the foreground on the left. The solar panel was covered as the array was not operational when this photo was taken.

In 2019 at Black Rock and Southeast Lighthouse, we used one 3-m tall triangular Rohn tower section to support three 5-element Yagi antennas, one 6.4 m tall omnidirectional antenna, and Lotek SRX800-D1, as well as the usual power supplies and lock cases (Figures 1.13, 1.14 & 1.15).

All receivers were programmed to automatically log several types of data from each antenna including: tag ID number, date, time stamp, antenna (defined by monitoring station and bearing), and signal strength (Lotek receivers: linear scale = 0 to 255; Sensorgnomes: linear scale = -104 to-40). Sensorgnome receivers monitor multiple antennas simultaneously, whereas Lotek receivers cycled sequentially among antennas (6.5 s dwell time) with a switchbox (Taylor et al. 2017).

Figure 1.13. Tower array (3 m tall tower) at Southeast Lighthouse in June 2019, showing 3 5-element Yagi 8-dB antennas, a 6.m tall, 10-dB omnidirectional antenna, with Lotek SRX800 receiver.

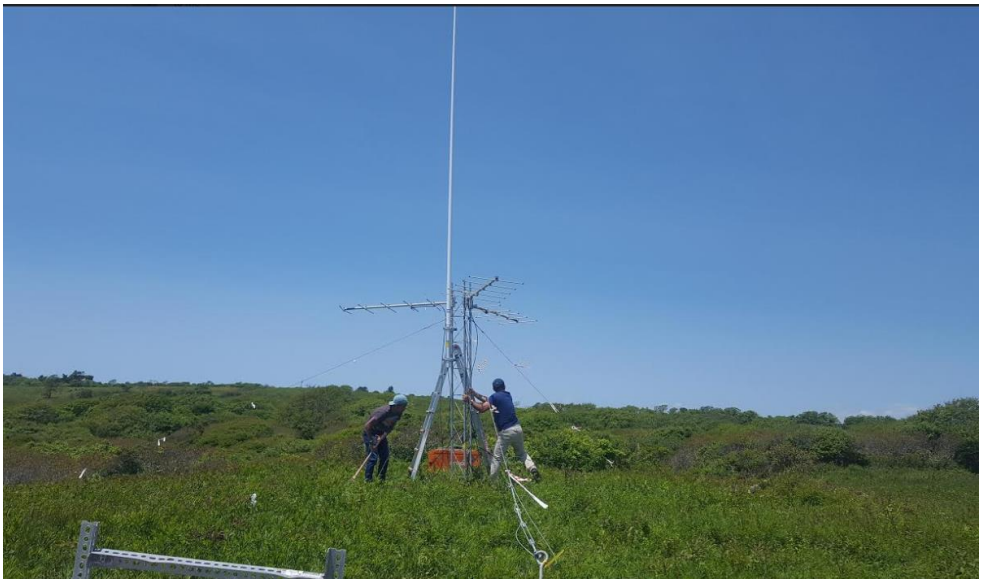

Figure 1.14. Constructing 3-m tall tower at Black Rock. Block Island, Rhode Island with three 5-element Yagi 8-dB antennas and one 6.1-m tall, 10-dB omnidirectional antenna for the 2019 field season.

Figure 1.15. Station supplies loaded into a truck to transport to Block Island

1.2.5.2 Station on Block Island Wind Farm

The Block Island Wind Farm was the first operational offshore wind energy facility in North America. In 2015 and 2016, Deepwater Wind (DWW) constructed the wind farm in state waters ~3 miles offshore from the southeast corner of Block Island, Rhode Island (Figure 1.1). Block Island Wind Farm consisted of five 6-MW, 180-m tall Haliade 150 wind turbines (151 m rotor diameter) that became operational in December 2016. We were able to enter into a research collaboration with DWW for the 2017 and 2018 field seasons (Appendix 1.4), and Ørsted (which acquired Deepwater Wind) in 2019 to operate a VHF receiving station at the Block Island Wind Farm on Turbine #1 (the eastern most turbine)(Figures 1.16, 1.17, & 1.18. Due to stringent OSHA regulations, we (URI or USFWS staff) could not install or directly monitor the VHF telemetry station on this offshore wind energy facility, therefore only DWW or Ørsted OSHA-certified staff could work on the platform.

A Hold Harmless agreement was signed in July 2017 which allowed the receiver and antennas to be installed on the turbine platform by DWW staff on 4 August 2017 (Appendix 1.4). DWW staff, led by John O'Keefe installed a Sensorgnome receiver with a beaglebone black processer, which was located in a water-resistant, insulated cooler (Yeti tundra 65 cooler, www.yeti.com, Figure 1.16). The turbine had a 110-volt AC power outlet, which was the power source for the receiver. There were 6-element 7.1-dB Yagi antennas installed on railings of the platform pointing in approximately the four cardinal directions.

Figure 1.16. VHF telemetry station on Turbine #1, Block Island Wind Farm, installed on 3 August 2017 by Deepwater Wind with 4 6-element 7.1-dB Yagi antennas installed. Block Island can be seen in background. Photo by J. O'Keefe DWW.

Figure 1.17. Block Island Wind Farm, five 6-MW turbines ~5 km off Block Island, started operations were initiated on 12 December 2016. Since 2015, an automated radio telemetry station at SE Lighthouse (red star) has tracked birds with digital VHF transmitters. Turbine #1 (far right turbine) had a VHF telemetry receiving station in 2017 to 2019. Photo courtesy of dwwind.com

Figure 1.18. Block Island Wind Farm Turbine #1 (eastern most turbine) showing 3 of 4 6-element (7.1-dB) antennas (red arrows) mounted on railings ~ 33 m above ocean.

In 2018, DWW staff re-installed the 4 6-element Yagi antennas and we had them replace the receiver used in 2017 with a new Sensorgnome receiver with a newer model raspberry pi processor. This receiver frequently had technical issues resulting in data gaps during most of 2018 (see Results), so it was replaced in 2019 with a Lotek SRX800-D1, installed on 24 June 2019. Our original agreement with DWW was to use a receiver that transmits data remotely via cellular stick. However, technology for remote data acquisition was not yet available for offshore locations including the Block Island Wind Farm due to limited cellular data coverage. Therefore, we instead requested that DWW staff download data from the receiver when feasible during summer maintenance trips.

The detection range of each station varied with the height of the antennas on the tower, height of the station above sea level (asl), terrain surrounding tower, altitude of the transmitting bird, and the antenna type (White and Garrott 1990, Kenward 2001, Taylor et al. 2017). Directional antennas, such as 3-5 element Yagis have an estimated detection range of 2-5 km, whereas 9-element Yagis can detect tags >3 km or farther, with tags often detected 20 km or farther (Taylor et al. 2017). Omnidirectional antennas have a 360-degree detection radius but a much more limited range, typically around 500 m (Taylor et al. 2017).

1.2.6 Calibration Surveys

1.2.6.1 Kite along moving transect: 13 Sept 2017

Using the USFWS Coastal Program's 23' Parker boat with Tom Halavik as captain, Pam Loring and another technician conducted a series of moving transects off the southern coast of Block Island. Two Lotek nanotags were taped to the upper surface of a large kite and the kite was flown on a 122 m long string at a 30° angle resulting in a flight altitude of ~20-25 m altitude above the ocean surface as the boat motored at approximately 10 knots. A Lotek SRX800 receiver with GPS attached was activated to monitor the track of the boat and ensure the tags were active during these trials. The transect was ~ 3-12 km from receiving stations.

1.2.6.2 Kite along moving transect: 9 July 2018

Using the USFWS Coastal Program's 23' Parker boat with Tom Halavik as captain, Kevin Rogers and another technician conducted a series of moving transects off the southern coast of Block Island. A Lotek nanotag was taped to the upper surface of a large kite and the kite was flown on a 122 m long string at a 30° angle resulting in a flight altitude of ~20-25 m altitude above the ocean surface as the boat motored at approximately 10 knots. A Lotek SRX800 receiver with GPS attached was activated to monitor the track of the boat and ensure the tag was active during these trials. The transect was ~ 2 -7 km from receiving stations.

1.2.6.3 Kite along moving transect: 16 July 2018

With Tom Halavik as captain, Peter Paton and an assistant attempted a calibration survey off Block Island. However, due to extreme fog, the mission had to be aborted due to dangerous conditions. The transect was ~ 2-11 km from receiving stations.

1.2.6.4 Kite along moving transects: 9 Aug 2018

Using the USFWS Coastal Program's 7 m Parker boat with Tom Halavik as captain, Kevin Rogers and another technician conducted a series of moving transects off the southern coast of Block Island. A Lotek nanotag was taped to the upper surface of a large kite and the kite was flown at approximately 20 m altitude above the ocean surface as the boat motored at approximately 10 knots. A Lotek SRX800 receiver with GPS attached was activated to monitor the track of the boat and ensure the tag was active during these trials. The transect was ~ 2-9 km from receiving stations.

1.2.6.5 Drone 5 Fixed locations, 5 altitudes: 10 June 2019

Using the USFWS Coastal Program's 7 m Parker boat with Tom Halavik as captain, Peter Paton and Greg Bonynge, certified FAA pilot, flew a Phantom3 drone with a test tag (#4) attached to drone strut at 5 fixed points at 5 altitudes (15 m, 30.5 m, 61 m, 91 m, and 122 m) for 2 min at each altitude. At each altitude the drone would remain stationary for 2 min

(Figures 1.19 & 1.20). The start times and latitude-longitude coordinates were: 1) Start time= 09:37; 41.137077, -71.514584, 2) Start time = 10:01, 41.122023, -71.502009, 3) Start time = 10:24, 41.100499, 71.533742; 4) Start time = 10:40, 41.105742, -71.544638; 5) Start time= 11:07, 41.118533, -71.541893 (Figure 1.20). We used 4 batteries for the drone to complete these flights. Between fixed points the drone Pilot Bonynge would land the drone in the boat, the boat would move to the next fixed point and relaunch the drone. The points were ~ 3-6 km from receiving stations.

1.2.6.6 Drone 3 fixed locations 30 m altitude - 27 June 2019

Using the USFWS Coastal Program's 7 m Parker boat with Tom Halavik as captain, Peter Paton, Soroush Kouhi and Greg Bonynge attempted a series of moving transects with a test tag attached to the landing strut of a DJI Phantom 3 drone. However, it was so foggy off the southern coast of Block Island, we had to alter flight plans to make sure we could keep track of the drone. Therefore, we flew stationary flights at three fixed point, 30 m altitude, for 15 min at each point. The flight times and latitude- longitude for each point are: 1) Flight time = 9:52 – 10:08; 41.1331, -71.5241; 2) Flight Time: 10:22-10:33; 41.1252, -71534; 3) Flight Time: 10:50 – 11:00; 41.1331, -71.4241 (Figure 1.20). The data were downloaded from the Block Island stations on 28 June. Points were 3-5 km from receiving stations.

Figure 1.19. Quadcopter drone during calibration surveys within 1 km of the Block Island Wind Farm. Right panel: Nanotag was taped to right lower strut of quadcopter.

Figure 1.20. Captain Tom Halavik, USFWS retired, piloted the USFWS's 7 m Parker boat near the Block Island Wind Farm for drone and kite calibration surveys.

1.2.6.7 Drone along moving transect - 9 July 2019

The goal of this survey was to mimic the direct flight pattern of a bird by flying the drone at a fixed speed similar to the flight speed of a tern (10 m per sec) based on estimated tern flight speed of 10 m per second (Wakeling and Hodgson 1992) and a Piping Plover at 12 m per second (Hedenström et al. 2013, Stantial and Cohen 2015; see also Anderson et al. 2019). Greg Bonynge programmed the flight plan of the drone to fly the 3-km long transect from east to west, and then return along the same transect from west to east. Each 6-km route was flown at 4 altitudes (100' (30.5 m), 200' (61 m), 300' (91.5 m), and 400' (122 m)). This transect was ~1,600 m NW of the Block Island Wind Farm and 3 – 4 km from receiving stations.

The drone was programmed to start at a fixed point (Figure 1.21) by hovering for 30 seconds and taking a GPS referenced photo. The photo was taken to document the latitude and longitude (± ~ 10 m accuracy, G. Bonynge, pers. comm.) as well as the time and date. Points associated with location #1 effectively documented the start time of each transect. The drone then shifted ~2 meters to location #2, took a picture, then hovered 30 seconds. The drone had to shift because the app, *DJI Ground Station Pro*, used by Greg Bonynge to program the flight did not allow him to stack two waypoints on top of each other, and it did not allow hovering for longer than 30 seconds at a single waypoint. Next, the drone started the transect by accelerating to 10 meters per

second (approximate flight speed of a tern) on the outbound east to west leg, pausing briefly at locations #3 and #4" to take a photo and collect GPS coordinates.

These two waypoints were necessary because the app would let not the pilot program a flight with any given leg longer than ~1000m. The outbound leg ended at location #5, taken another photo, hover for 30 seconds, shift 2 m to location #6 and hover for 30 seconds, take a photo, hover 30 sec, small shift to location "6", photo, hover 30 sec. The inbound leg (west to east) also flew at 10 m per second, with brief stops at locations #7 and #8 for a photo, and ended at location #9, take a photo, hover for 30 sec, shift 2 m to location #10, take a final photo and hover for 30

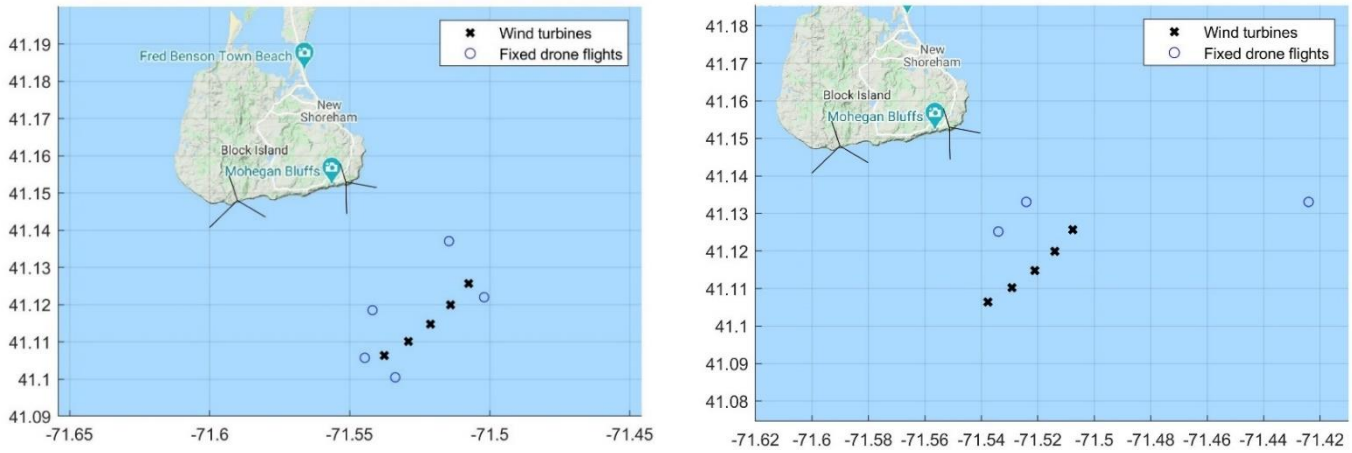

Figure 1.21. Locations of calibration surveys using a quadcopter drone with a test tag attached to a strut on 10 June 2019 (left panel) at 5 fixed locations (blue circles) SE of Block Island and 27 June 2019 (right panel) at 3 fixed locations (blue circles). The drone was at least 400 m from closest turbine in the Block Island Wind Farm (black X's) and 4 to 10 km from automated receiving stations.

sec. After each outbound-inbound flight, the pilot flew the drone back to the waiting motorboat, changed the drone's battery and conducted another flight that was 30.5 m higher. According to FAA rules, the maximum altitude the pilot was allowed to fly was 122 m asl with the drone.

1.2.7 Analysis of data

We based analyses of bird movements using components of models and code developed by Janaswamy et al. (2018) as explained in section 1.2.6.3.

1.2.7.1 Post-processing of tag data

Raw detection data, and tag metadata, were sent to the Motus Wildlife Tracking System for centralized processing (Taylor et al. 2017). Processed tag detections were downloaded from the Motus database using R Core Team version 3.6.3 (2020) and the Motus package in one of two

ways. Data associated with the automated receiving stations at Black Rock, Southeast Lighthouse, and the Block Island Wind Farm were downloaded using the unique ID for a given receiver (Table 1.4). This dataset included any Common Tern, Piping Plover, and Roseate Tern detected by the Block Island Towers, as well as detections of any other species passing by these towers. To obtain detections of Common Tern, Piping Plover, and Roseate Tern nanotags by other automated receiving stations in the Motus network, we downloaded the data using our unique Motus project ID number (#14). For all detections by Yagi antennas, we filtered the data following recommendations by Taylor et al. (2017) and Crewe et al. (2019). Primarily, we used "run lengths" of a tag to filter our data. A run length indicates a sequence of hits at a tower of a given Nanotag ID that are within the time interval expected by the burst length of that tag. A run includes hits that differ by the tag's unique period between bursts, and is allowed have a given missing time gap between hits of that tag. Noise in the environment around a tower from interference can create bursts that seem like a tag detection, so it is important to apply filters to the data to remove those false positives. In general, the likelihood of a tag detection being false decreases as a run length increases. Therefore, we first excluded any detections with a run length of 3 or less, as those detections have a higher probability of being a false positive detection, and we allowed for a maximum of 20 consecutive missing bursts of a given tag within each run.

Additionally, we excluded detections that were more than four milliseconds from a tag's unique burst interval between each consecutive burst. Using the traditional filtering algorithm, omnidirectional antennas attached to Lotek receivers returned very few detections. Since this result was likely due to the time intervals that Lotek receivers cycled through antennas (compared to Sensorgnome receivers that are capable of detecting all antennas simultaneously), we applied a slightly different filtering process for those omnidirectional antennas described in (Appendix 1.8; note code will be inserted in next draft). Once data were downloaded, we created a dataframe on our local computer so that we could more easily work with dates and times, and, importantly, transform timestamps from coordinated universal time to easten standard times. We were also careful to examine detections of a given tag over time and space to further discard any implausible detections based on a given species flight speed or ecology. Once we obtained a clean dataset for each year, we subset out tags associated with the calibration surveys, and joined the Motus data with our banding dataset. All R code associated with this initial filtering process, as well as any figures and tables can be found in Appendix 1.8).

Table 1.4 – Unique receiver IDs used to download datasets from Motus.org.

Automated Receiving Station	Year	Receiver ID
SELI	2017	Lotek-6448
	2018	SG-30B8RPI3AB49
	2019	Lotek-225
BIBR	2017	SG-4001BBBK2230
	2018	SG-B4B4RPI36D28
	2019	Lotek-380
BIWF	2017	SG-2616BBBK1111
	2018	SG-2616BBBK1111
	2019	Lotek-D000793

The Motus.org network provides several helpful tools that quickly summarize detection data for each receiver associated with the project. This includes a graph showing timeline of a given receiver per year of operation and a graph illustrating the timeline of a given receiver deployment. The receiver deployment timeline illustrates the number of tags detected by the receiver (although a rough estimate) as well as the amount of time the station was active illustrated by the time a GPS unit associated with a given receiver was active, and activity patterns associated with the antennas. Therefore, we used the deployment timeline to estimate when the receiver was on and powered (GPS unit = On) and the associated antenna activity patterns. The antenna activity patterns indicate when the antenna was detecting any noise or tags in the area. We assumed for Sensorgnome receivers, but not Lotek receivers, the lack of antenna activity indicated when an antenna was not powered, although more analysis is needed.

1.2.7.2 Converting signal strength between Lotek and Sensorgnome receivers

The signal strength from the tags are recorded on a unitless scale of 1 - 255 from Lotek receivers (www.lotek.com). Although most receiving stations during this study were equipped with Lotek receivers, some stations used Sensorgnome receivers (www.compudata.ca). For the Sensorgnome receivers, the received signal strength ranges from -104 dB to -40 dB, thus needed to the Lotek range using the following simple linear relationship (J. Bruzowski, pers comm.):

$$Z = (40G_0 + 44dBm + 4565)/11 \quad (1)$$

where Z is the signal strength from the Lotek range, G_0 is the Sensorgnome receiver gain, and *dBm* is the signal strength from the Sensorgnome. In this study the receiver gain, G_0, was assumed zero as it had the best compatibility with the signal range (1 - 255) from Lotek receivers.

1.2.7.3 Analysis of movements during calibration surveys

First, we looked at all detections of a test tag during a given calibration survey and assigned each detection to a known GPS location of the drone or kite by matching the time of the detection to the nearest timepoint of the survey.

We then used the modeling approach developed by Janaswamy (2018) to estimate the locations of tags. Predicting the location of the tag requires converting the received signal from the receiver to the actual signal strength accurately. We used data from the calibration surveys to adjust the parameters in the conversion equation used by Janaswamy et al. (2018). The following equation was used to convert the received signal strength to the actual power:

$$tanh^{-1}\left(\frac{Z-Z_m}{Z_M-Z_m}\right) = b.\ln\left(\frac{\xi^2}{P_0}+1\right) \quad (2)$$

where $Z_m = 0$ and $Z_M = 255$ show the lower and upper limits of the received signal, Z is the displayed signal from receiver, ξ^2 is the expected received power in the noiseless environment, P_0 is environmental noise, and b is a constant value. The value of b and P_0 were adjusted during the calibration surveys: that is the kite surveys in 2017 and 2018, and drone flight in 2019. The value of b was set to 0.3013, and the value of P_0 was set to 4.89 x 10^{-11} , 4 x 10^{-12}, and 10 x 10^{-10} for the simulations regarding to 2017, 2018, and 2019, respectively. Results of the calibration will be presented in the next sections.

1.2.7.3.1 Estimating the radiation pattern of Yagi antennas

In order to find the intersection of the radiation pattern contours, we needed to be able to estimate the radiation pattern of each Yagi antenna. We changed antenna annually (e.g., bearings and number of elements, as well as the number of antenna) at each station on Block Island at Black Rock and Southeast Lighthouse stations. For this study, we used either 5-, 6- or 9- element Yagi arrays which had an estimated gain of 8-dB, 7.1, and 11.1 dB, respectively. All antennas were tuned to a frequency band that overlapped the frequency of nanotags (166.380 MHz) based on half a wavelength in free-space (λ_0 = 1.8 m). We estimated the radiation pattern, $g(\theta)$ of each antenna based on Janaswamy et al. (2018):

$$g(\theta) = \frac{\cos(\pi/2\sin\theta)}{\cos\theta}\,\frac{\sin(p+q\cos\theta)}{(p+q\cos\theta)} \quad (5)$$

in which p and q are calculated by

$$p = \beta_0 L_e/2 \qquad q = \beta_0 L_e/2 \quad (6)$$

where β_0 is the phase per unit length ($\beta_0 = -\left(k_0 + \frac{2.94}{L_e}\right)$), k_0 the wave number ($k_0 = 2\pi/\lambda_0$), and L_e is the effective length of the antenna. For the 9-element Yagi-antenna, L_e = 4.6 m and for

the 5-element Yagi-antenna $L_e = 2\ m$ [3]. When these parameters are estimated, Eq 4. is used to project these patterns on a horizontal plane at each desired altitude. If the tag is in the direction of the main beam, $\theta = 0$, and Eq. (5) reduces to Eq (7) that can be simply used for the single detections:

$$g(0) = \frac{\sin(p+q)}{(p+q)} \quad (7)$$

All Matlab code for calculating antenna bearings are provided in Appendix 1.7.

1.2.7.3.2 Static model

The actual received power ξ^2 depends on the distance and direction of the tagged bird and the gain of the Yagi antenna. The relation between the received power and the location of the bird can be expressed as

$$\xi^2 = g^2(\theta)\frac{sin^2(k.H.\frac{z}{R})}{(k.R)^2} \quad (3)$$

where $g(\theta)$ is the radiation pattern of the directional beam of the receiving antenna, θ is the angle made by a bird location and direction of the antenna in the local coordinate system, k represents the wave number, z represents the flight altitude, H is the height of the station, and R is the horizontal distance between the bird and the station. The radiation pattern will be described in the next section. For bird and tower heights much smaller than the horizontal bird range to tower, (i.e. $k.H.z \ll R$), it can be approximated that R = r (distance between tower and the bird) and $\sin(k.H.z) = k_0 Hz$ which result in the following form of Eq. (3)

$$r^2 = g(\theta)\frac{H.z}{\xi} \quad (4)$$

In Eq. (4), θ , z, and R are the unknowns of the equation. Eq. 4 is the basis formula to calculate the bird location using the received signal and antenna pattern. With a single value of received signal, Eq. 4 results in multiple locations from the same signal strength that makes the prediction of the bird non-unique. Therefore, we used data from single antenna detections and Simultaneous detections among antennas to estimate the location of the bird (or test tag) and reduce the associated uncertainties.

In this method, triangulation is used to estimate the bird location in which the distance between the bird and at least two simultaneous detections from separate antennas at two or more receiving stations is calculated. As there are usually limited number of simultaneous detections, we used a time window with a specific length (within the range of 30 to 100 seconds). We assumed the detections within the time window were near-simultaneous detections. If the time window is too large, the movements of the bird between detections cannot be ignored. In this study, we assumed a specified altitude for the calibration surveys and several specified altitudes (20, 30,

60, and 90m) for the bird movement in Eq. 3. The intersection of projected antenna pattern contours on the horizontal coordinates for the corresponding signals in that specified altitude predicts the approximate location of the bird with the assumption that bird is not moving during the time window (Figure 1.22). This method can be applied to different antennas at the same station or using different antennas at different station. Even though the uncertainty in the estimated location is reduced with near simultaneous detections, predicating of the bird's location with near-simultaneous can still be inaccurate because of the uncertainty in the estimated altitude (Janaswamy et al. 2018). Within each time window, there might only be single detections. For these single detections, we assumed that the bird was along the main beam of the received antenna.

All Matlab code for estimating tag locations during calibration surveys from 2017-2019 are provided in Appendix 1.6.

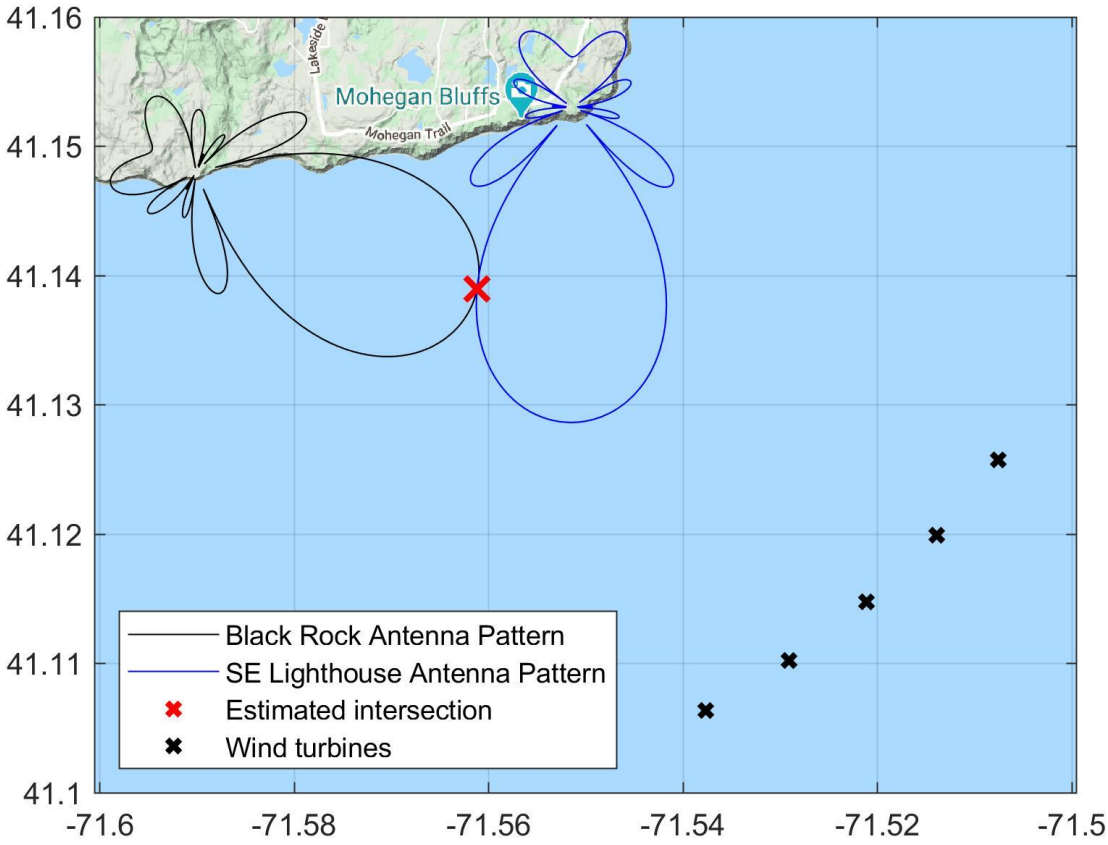

Figure 1.22. Example of the intersection the simultaneous/near simultaneous detections from two separate towers which represents the approximate location of the bird (red x).

1.3.0 RESULTS

The following section summarizes detections of tagged birds from automated telemetry stations on Block Island:

1.3.1 Black Rock station: 2017

The Black Rock station was active from 29 Aug to 8 Dec in 2017 (Figure 1.23). A total of 6 unique tags were detected at Black Rock in 2017 from four different species (3 species of shorebirds and Tree Swallows) (Table 1.4). Presumably because the station became active after Common and Roseate terns had dispersed from breeding colonies to staging sites, and after tagged adult Piping Plovers migrated from the region, these focal species were not detected at this station in 2017. There were no time periods when the station was inactive and most antennas detected environmental noise and/or tags 24 hours per day. There were no detections after Oct 3.

In 2017, we had relatively few detections using three 9-element Yagi antennas, with no terns or plovers we tagged detected out of the 339 detections, with relatively similar detection rates among each of the antennas: 102°: 134 detections; 152°: 76 detections, and 201°: 129 detections (Table 1.4). We detected a total of 6 tags in 2017 at Black Rock, with from 4 different species including 2 Semipalmated Plovers, 2 Semipalmated Sandpipers, 1 Tree Swallows, and 1 White-rumped Sandpiper.

Table 1. 4. Total number of detections for four species at three 9-element 11-dB antennas at Black Rock station during the 2017 season.

	Antenna bearing			
Species – Tag ID	**101.8°**	**151.8°**	**200.8°**	**Total**
Semipalmated Plover				
39	38	29	73	140
96	19			19
Semipalmated Sandpiper				
297.1	19			19
337	30	29	35	94
Tree Swallow				
146	16	18	21	55
White-rumped Sandpiper				
153	12			12
Total	**134**	**76**	**129**	**339**

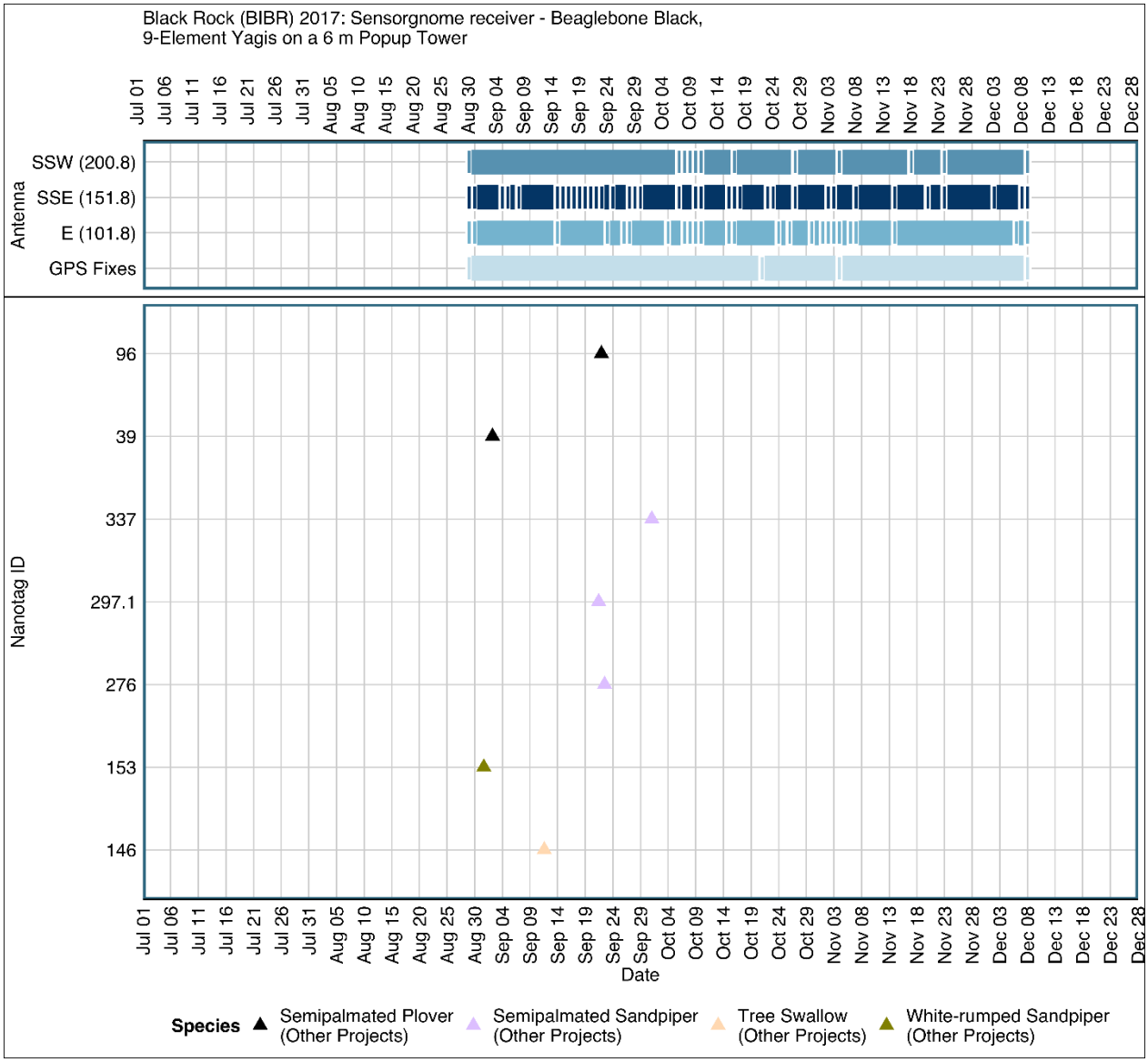

Figure 1.23. Chronology of 6 tags detected at Black Rock station from 30 Aug to 8 Dec 2017. The receiver was a Sensorgnome with beaglebone black processor. Tags associated with this project (Project 14) are circles and tags registered to other Motus projects are triangles. Blue boxes for each antenna at the top represent days when each 5-element 8-dB antenna, the 10-dB omnidirectional were active and reciving information (tags or environmental noise) and when the GPS at the station was active indicating that the station was powered on; smaller boxes are days when receiver or antennas were not receiving data for the full24 hrs in a day, and no blue box indicates the GPS or antennas was not active or receiving data that date.

In 2017 at Black Rock, estimates of run length were under 10 min (median = 6.2 min, 25-75th percentiles = 3.1 to 7.7 min, N = 7) including for 2 Semipalmated Plovers (SEPL) (1.6 to 6.2 min), 2 Semipalmated Sandpipers (SESA) (7.8 to 8.2 min), 1 White-rumped Sandpiper (WRSA) (3.1 min) and one Tree Swallow (TRES)(6.7 min) (Figure 1.24). The total number of detections per run ranged from 12 – 102 detections (average = 48.4, SD = 36.8), with an average of 8.9 detections per min (SD = 4.9).

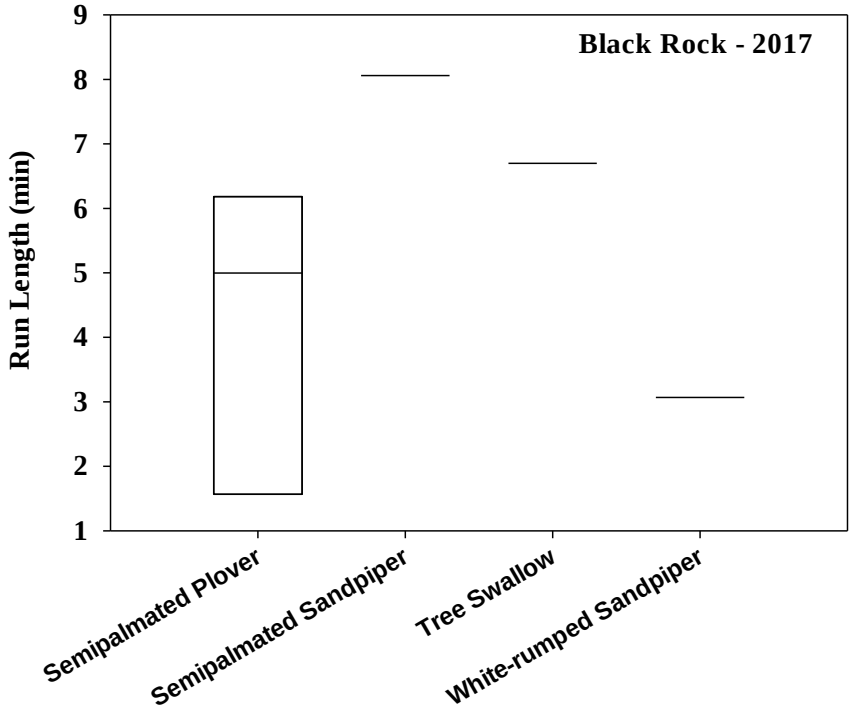

Figure 1.24. Run length (min) that tagged birds that were continuously tracked at Black Rock station in 2017.

1.3.2 Black Rock station: 2018

The Black Rock station in 2018 was active from 20 June to 22 Aug, with the exception of ~ 1 week from 2 July to 10 July (Figure 1.25). Peak detections occurred from 13 – 24 July, which was when most Common and Roseate terns were detected.

In 2018, with three 5-element Yagi antennas and one 6.4 m omnidirectional antenna. we had a total of 5,127 detections from a total of 36 tagged individuals, with most tags (29 tags) detected on the antenna facing 166° (Table 1.5). A total of seven species were detected including 14 Common Terns (3 from Falkner Is, CT; 11 from Great Gull Is, NY), 5 Piping Plovers (all from Trustom Pond NWR, RI), 11 Roseate Terns (3 from Falkner Is, CT; 8 from Great Gull Is, NY), and 2 Red Knots, 1 Sanderling, 1 Semipalmated Plover, and 2 Semipalmated Sandpipers tagged by other projects. The antennas facing 136° (1,123 detections of 12 tags) and 196° (462

detections of 7 tags) and omnidirectional antenna (788 detections 12 tags) tended to have fewer detections than the antenna facing 166° (2,754 detections of 29 tags).

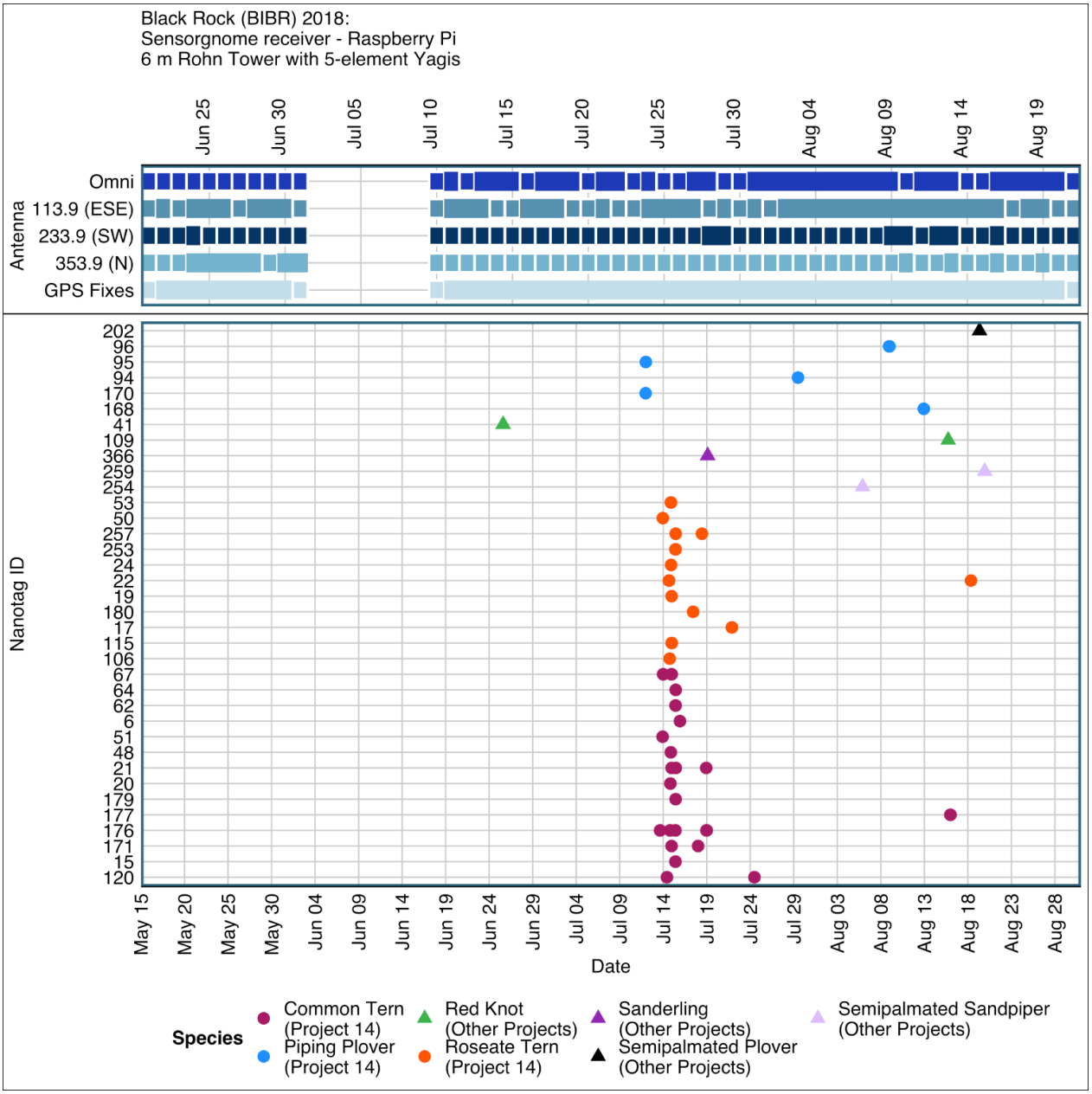

Figure 1.25. Chronology of tags detected at Black Rock station from 20 Jun to 22 Aug 2018. The receiver was a Sensorgnome with a raspberry pi processor. Tags associated with this project (Project 14) are circles and tags registered to other Motus projects are triangles. Blue boxes at the top represent days when the GPS at the station was active and when each antenna was detecting either tag bursts or noise in the environment; smaller boxes are days when receiver detecting any data for the full 24 hrs of a day, and no box indicates the receiver was not active (if the GPS) or was not detecting any data (if an antenna) on a given date.

Table 1.5. Total number of detections on each of the 5-element 8-dB Yagi antennas or a 10-omnidirectional antenna at the Black Rock station in 2018.

	Antenna Bearing				
Species – Tag ID (capture location)	**354°**	**234°**	**114°**	**Omni**	**Grand Total**
Common Tern	**387**	**1670**	**353**	**533**	**2943**
6 (Falkner Is, CT)		18			18
15 (Falkner Is, CT)	7	301	34	71	413
20 (Great Gull Is, NY)				37	37
21 (Great Gull Is, NY)	19	150	43	10	222
48 (Great Gull Is, NY)		63			63
51 (Great Gull Is, NY)		24			24
62 (Great Gull Is, NY)		118			118
64 (Great Gull Is, NY)	6	52	19	55	132
67 (Great Gull Is, NY)		165			165
120 (Falkner Is, CT)		144		42	186
171 (Great Gull Is, NY)		23			23
176 (Great Gull Is, NY)	203	521	257	318	1299
177 (Great Gull Is, NY)	152	44			196
179 (Great Gull Is, NY)		47			47
Piping Plover	**379**	**183**		**30**	**592**
94 Trustom NWR, RI		30			30
95 Trustom NWR, RI				30	30
96 Trustom NWR, RI	379	112			491
168 Trustom NWR, RI		37			37
170 Trustom NWR, RI		4			4
Red Knot	**69**	**21**			**90**
41	69				69
109		21			21
Roseate Tern	**27**	**880**	**109**	**176**	**1192**
17 (Great Gull Is, NY)	15	43	16	36	110
19 (Great Gull Is, NY)		25			25
22 (Great Gull Is, NY)		71			71
50 (Great Gull Is, NY)		17			17
53 (Great Gull Is, NY)		11			11
106 (Great Gull Is, NY)		28			28
115 (Falkner Is, CT)		320			320
180 (Great Gull Is, NY)		35			35
253 (Falkner Is, CT)	12	247	79	108	446
257 (Falkner Is, CT)		28		32	60
Sanderling	**52**			**17**	**69**
366	52			17	69

Species – Tag ID	354°	234°	114°	Omni	Grand Total
Semipalmated Plover	**68**				**68**
202	68				68
Semipalmated Sandpiper	**141**			**32**	**173**
254	141				141
259				32	32
Total	**1123**	**2754**	**462**	**788**	**5127**

The run lengths for individuals, regardless of species, detected at Black Rock averaged 13.0 min (median = 6.9 min, 25%-75% = 2.8 – 16.4 min) (Figure 1.26). Common Terns (COTE) and Roseate Terns (ROST) tended to be detected by the Black Rock station in 2018 for similar lengths of time (median (25-75th percentiles) = COTE: 5.8 min (3.1 – 16.7 min); ROST: 6.4 min (1.4 – 8.3 min), which was not different from the length of detections for Piping Plovers (PIPL): 4.4 min (2.4 – 33.1 min) (Kruskal-Wallis H = 0.30 *P* = 0.861)(Figure 1.26). Sanderlings (SAND) (median = 14.2 min), Semipalmated Plover (7.0 min) and Semipalmated Sandpipers (SESA) (20.1 min) were all detected for relatively long run lengths. For the three focal species we tagged, the median (range) of detections per run was similar: COTE: 60 (13-137 detection per flight segment), PIPL: 30 (17-264), and ROST; 28 (6-60), where we defined a flight segment as continuous detections with no detections over 10 min apart (only 2 of 46 flight segments were on the same day).

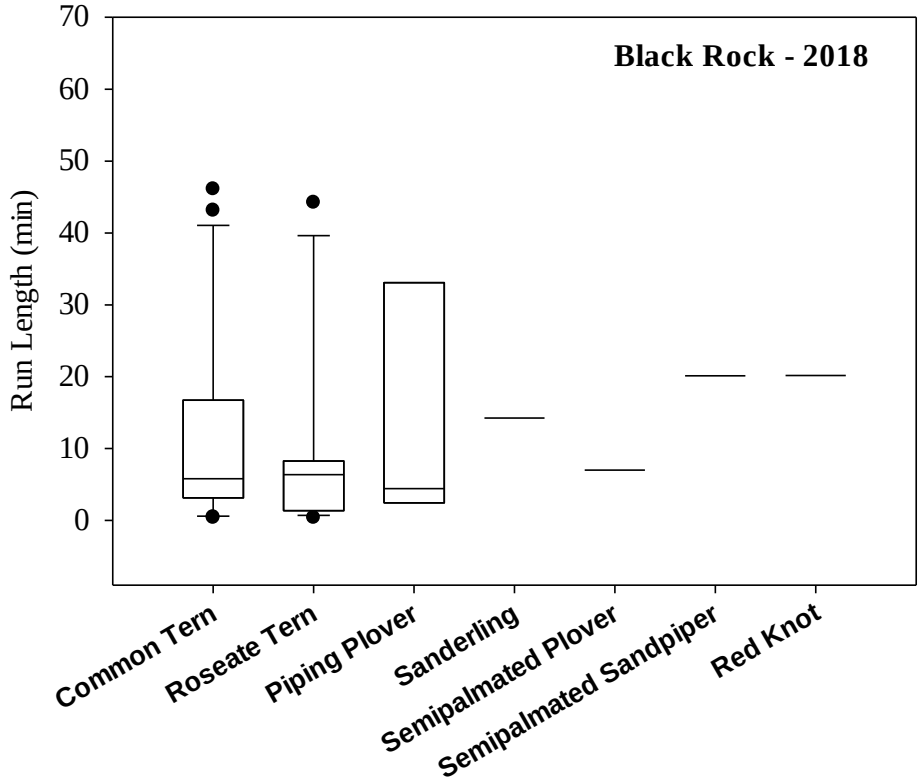

Figure 1.26. Run length (min) for 7 species of tagged birds that were detected from the Black Rock station in 2018.

1.3.3 Black Rock station: 2019

The Black Rock station was operational from 9 Jun to 1 Sep in 2019, although there were no detections after 10 Aug 2019 (Figure 1.27). There were no days when the station was inactive, although there might have been some power issues between 11-17 June based on GPS data (Figure 1.27). There was a total of 40 unique tags, of which 33 were Common Terns (2,507 total detections). We also detected 3 Piping Plovers (29 detections), in addition to 3 Red Knots (49 detections) and 1 Semipalmated Plover (4 detections). Most Common Terns were detected from 24 Jun to 29 Jul.

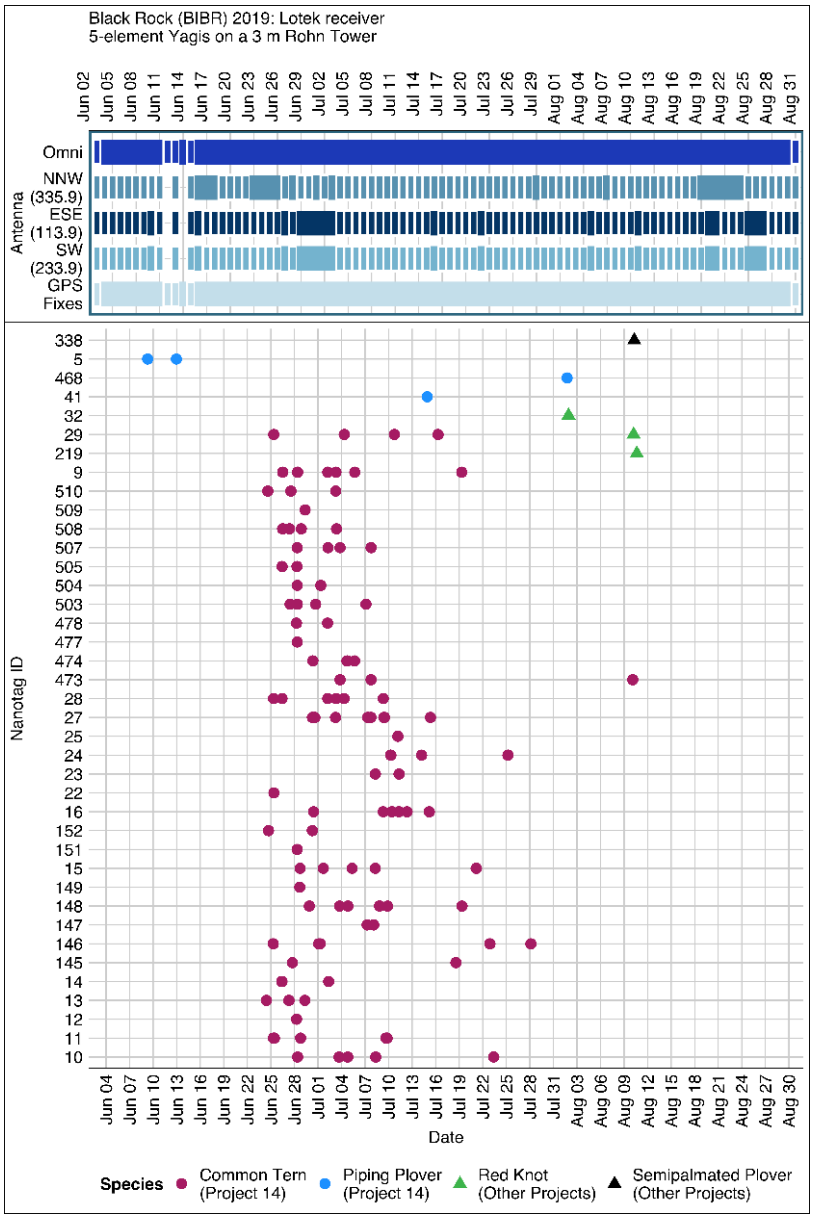

Figure 1.27. Chronology of tags detected at Black Rock station from 16 Jun to 1 Sep 2019. The receiver was a Lotek SRX800 receiver. Tags associated with this project (Project 14) are circles and tags registered to other Motus projects are triangles. Blue boxes at the top represent days when the GPS at the station was active and when each 5-element 8-dB antenna or a 10 dB omnidirectional antenna was detecting either tag bursts or noise in the environment; smaller boxes are days when receiver detecting any data for the full 24 hrs of a day, and no box indicates the receiver was not active (if the GPS) or was not detecting any data (if an antenna) on a given date.

In 2019, there was considerable variation among 5-element Yagi antennas in the total number of unique tag detections, with antenna facing SW (234°) having 81% of the 2,589 detections at this station, while the antenna facing SE (114°) with 14.6% and NW (336°) had only 3.7% for all detections; the omnidirectional antenna had only 0.5% of total detections (Table 1.6).

Table 1.6. Total number of detections on each of the three 5-element 8-dB Yagi antennas and one 10-dB omnidirectional antenna at the Black Rock station in 2019. All Common Terns were tagged by us on Great Gull Island, and Piping Plovers in coastal Rhode Island.

	Antenna Bearing				
Species- tag ID	**114°**	**234°**	**336°**	**Omni**	**Total**
Common Tern	**366**	**2049**	**92**		**2507**
9	48	125	20		193
10	34	107	10		151
11		83			83
12		11			11
13	25	108	13		146
14	5	129	7		141
15		140			140
16	97	110			207
22		7			7
23	15	21			36
24	40	74	4		118
25	7	9	20		36
27	12	76			88
28		118			118
29		38			38
145		43			43
146	31	107			138
147		72			72
148	27	55	8		90
149		24			24
151		21			21
152		34			34
473		36			36
474	15	33			48
477		9			9
478		25			25
503		83	10		93
504		20			20
505		100			100
507		31			31
508		126			126
509		24			24
510	10	50			60
Piping Plover		**13**	**4**	**12**	**29**
5				12	12
41		7			7

Species- tag ID	114°	234°	336°	Omni	Total
41		7			7
468		6	4		10
Red Knot	**12**	**37**			**49**
29		24			24
32	8	13			21
219	4				4
Semipalmated Plover		**4**			**4**
338		4			4
Total	**378**	**2103**	**96**	**12**	**2589**

In 2019, a total of 40 unique tags from 4 species that were detected at Black Rock station (Table 1.6). We detected a high percentage, 33 of 40 (82.5%) of the Common Terns we tagged on Great Gull Island, NY for this project, which is ~45 km west of Block Island. We also detected 3 of 18 Piping Plovers we tagged in 2019 in Rhode Island, which were tagged on Ninigret Beach, in contrast to 2018 when we only detected plover tagged at Trustom Pond NWR. We detected 2 species from other projects, 3 Red Knots and 1 Semipalmated Plover.

In 2019, there were 115 runs for 4 species (median = 7.1 min sec; 25-75th percentiles 3.5 to 13.0 min) (Figure 1.28). For Common Terns, we had 106 runs for 33 individual tagged birds (median = 7.2 min (range 3.5 to 12.8 min). For Piping Plovers, we had 4 runs from 3 different tagged birds (range 1.4 to 15.9 min), 4 runs of 3 tagged Red Knots (range 6.0 – 23.6 min), and 1 Semipalmated Plover (4.0 min).

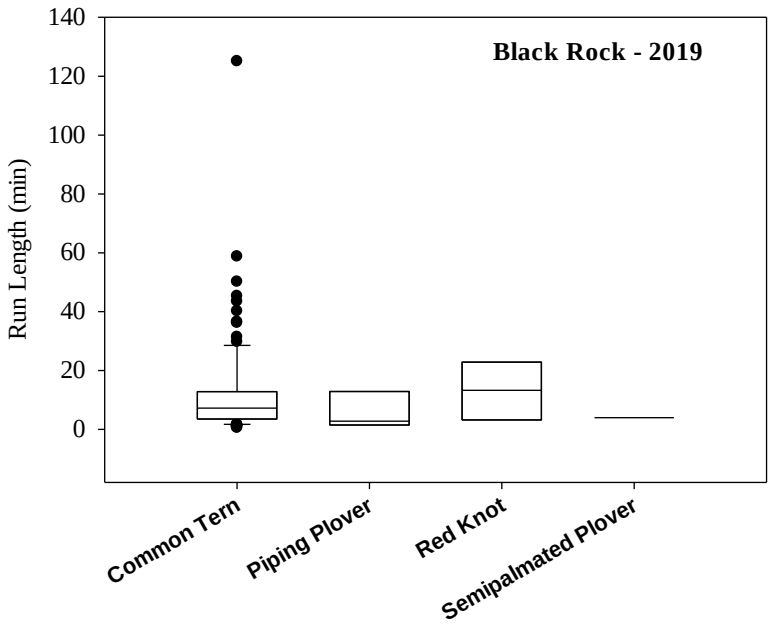

Figure 1.28. Run length (min) of tagged birds were detected at Black Rock station in 2019.

1.3.4 Southeast Lighthouse – 2017

The Southeast Lighthouse station was operational from 10 May to 20 Oct in 2017 and part of a previously funded BOEM study stations (Loring et al. 2019; Figure 1.29). We provide a summary of detections from this tower, as it was 12 m tall and had 9-element 11-dB Yagi antennas, rather than shorter (3 m or 6 m tall tower) used in 2018 and 2019 for this study. There was a total of 70 unique tags, with 2,957 detections (Table 1.7) of which 16 were Common Terns (1,822 total detections). We also detected 10 Piping Plovers (125 detections), 2 Roseate Terns (88 detections), 6 species of shorebirds tagged by other researchers (Least Sandpiper, Red Knot, Sanderling, Semipalmated Plover, Semipalmated Sandpiper, and White-rumped Sandpiper) and four species of passerines from other research projects (Gray-cheeked Thrush, Nelson's Sparrow, Saltmarsh Sparrow, and Tree Swallow) (Table 1.7).

In 2017 at Southeast Lighthouse which had antennas on a 12-m tall tower, the antennas facing N (bearing = 0°), NE (60°), and SW (240°) had the greatest detection rates (31, 29, and 33 individual tags, respectively; 510, 648, and 945 total detections, respectively). In contrast, the antennas facing S (180°) and NW (240°) had much lower detection rates (8 and 12 individual tags, respectively; 141 and 96 detections, respectively) (Table 1.7).

Median run lengths, regardless of species, for detections at Southeast Lighthouse in 2017 were 8.6 min (25^{th}% to 75^{th}% = 3.3 – 19.0 min; N = 137). The three focal species had similar run lengths: Common Terns (median = 10.3 min; 3.4 – 22.2 min; max = 110 min), Roseate Terns (10.6 min; 4.0 – 18.9 min), and Piping Plovers (6.0 min; 4.0 – 9.3 min)(Figure 1.30)(Kruskal-Wallis H = 1.6, P = 0.44). Run lengths for shorebirds tended to be slighter longer (e.g., Sanderling: median = 22.4 min, Least Sandpiper = 11.2 min, Red Knot = 9.4 min, Semipalmated Plover = 12.2 min, Semipalmated Sandpiper = 6.6 min, White-rumped Sandpiper = 2.6 min) (Figure 1.31), whereas passerines tended to be detected for slightly shorter runs (Saltmarsh Sparrow = 8.6 min, Tree Swallow = 5.5 min, Gray-cheeked Thrush = 8.7 min)(Figure 1.32).

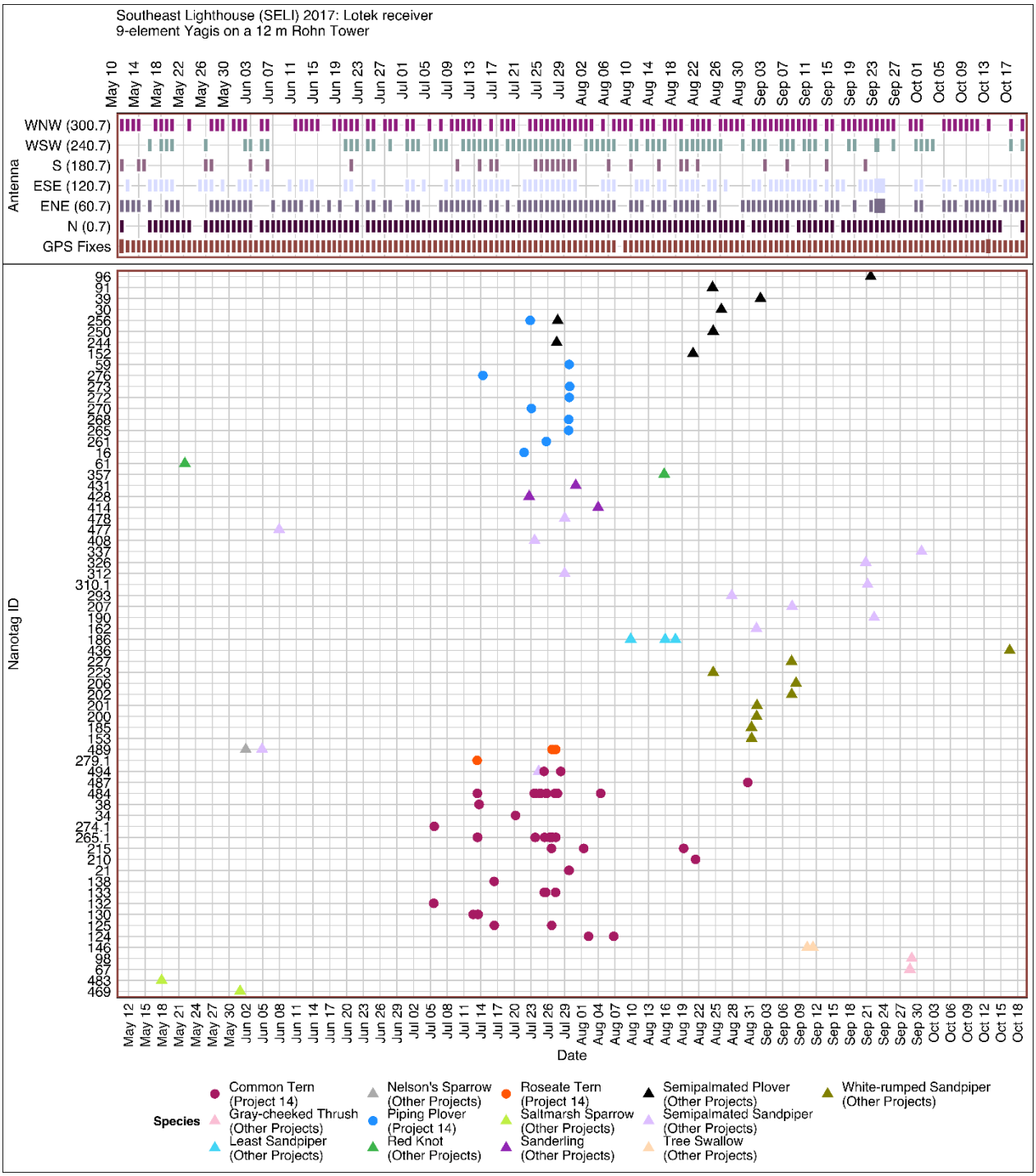

Figure 1.29. Chronology of tags detected at the Southeast Lighthouse station from 10 May to 20 Oct 2017 with a Lotek SRX800 receiver. Tags associated with this project (Project 14) are circles and tags registered to other Motus projects are triangles. Boxes at the top represent days when the GPS at the station was active (orange boxes) and when each 5-element 8-dB antenna or a 10 dB omnidirectional antenna (purple or green boxes) were detecting either tag bursts or noise in the environment; smaller boxes are days when receiver detecting any data for the full 24 hrs of a day, and no box indicates the receiver was not active (if the GPS) or was not detecting any data (if an antenna) on a given date.

Table 1.7. Total number of detections on each of the six 9-element 11-dB Yagi antennas at Southeast Lighthouse in 2017.

	Antenna Bearings						
Species – Tag ID	**0**	**60**	**120**	**180**	**240**	**300**	**Total**
Common Tern	**209**	**400**	**419**	**141**	**645**	**8**	**1822**
21	36				67	4	107
34		5					5
38		49	23	9	12		93
124	18	5	15				38
125					9		9
130	8	14	28	5	81		136
132					59		59
133	13	11	4		66		94
138					5		5
210		7			8		15
215	5	21		4	27		57
265.1	16	103	184	28	133		464
274.1						4	4
484	113	185	156	85	166		705
487			9				9
494				10	12		22
Gray-cheeked Thrush	**37**					**16**	**53**
67	27					9	36
98	10					7	17
Least Sandpiper	**46**	**54**	**10**		**16**	**9**	**135**
186	46	54	10		16	9	135
Nelson's Sparrow	**4**						**4**
489	4						4
Piping Plover	**7**		**55**		**63**		**125**
16			12				12
59					9		9
256			22				22
261			14				14
265			7				7
268					5		5
270					10		10
272					5		5
273					34		34
276	7						7
Red Knot	**16**	**5**				**16**	**37**
61	16						16
357		5				16	21

	Antenna Bearings						
Species – Tag ID	**0**	**60**	**120**	**180**	**240**	**300**	**Total**
Roseate Tern		**14**	**15**	**4**	**55**		**88**
279.1					28		28
489		14	15	4	27		60
Saltmarsh Sparrow	**5**				**32**		**37**
469	5				10		15
483					22		22
Sanderling	**22**	**17**	**7**		**24**	**16**	**86**
414					9		9
428	6	17	7				30
431	16				15	16	47
Semipalmated Plover	**46**	**56**	**76**		**11**	**8**	**197**
30			41				41
39	23	26			7	4	60
91	6	7	17				30
96		8	4				12
152	7						7
244	10	10				4	24
250		5	14				19
256					4		4
Semipalmated Sandpiper	**109**	**52**	**17**	**6**	**41**	**19**	**244**
162		5					5
190	10						10
207	10	14					24
293	4						4
310.1			4				4
312	13						13
326			9				9
337		6	4		18		28
408	4					8	12
477	7						7
478	31	9		6	23	11	80
489	15	10					25
494	15	8					23
Tree Swallow	**4**				**8**	**4**	**16**
146	4				8	4	16
White-rumped Sandpiper	**5**	**50**	**8**		**50**		**113**
153		5					5
185					22		22
200	5	10					15
201					4		4
202		4					4
206		22	8				30

	Antenna Bearings						
Species – Tag ID	**0**	**60**	**120**	**180**	**240**	**300**	total
223					20		20
227		9					9
436					4		4
Total	**510**	**648**	**607**	**151**	**945**	**96**	**2957**

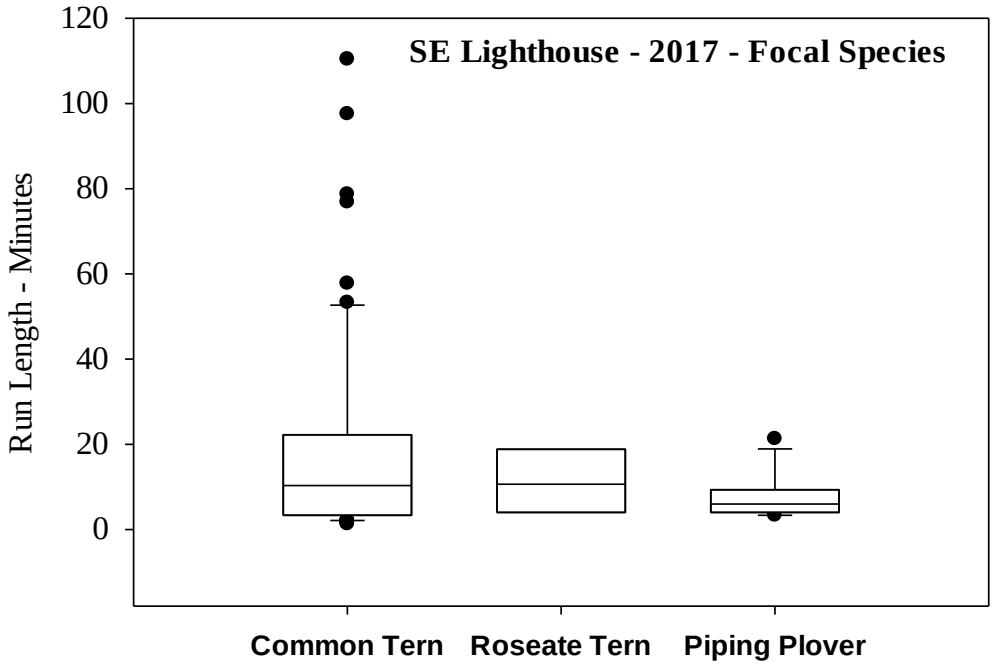

Figure 1.30. Run length of detections (minutes) for focal species tracked by the Southeast Lighthouse station in 2017, which was a Lotek receiver and a 40’ tall tower with 6 9-element Yagi antennas. A run was defined as continuous, sequential detections <10 min apart.

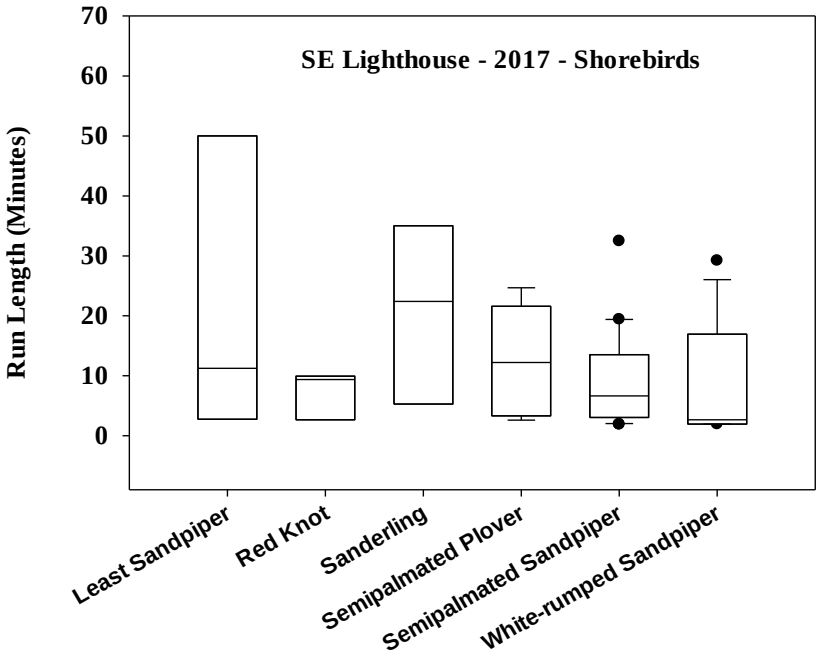

Figure 1.31. Run length of detections (minutes) of shorebirds from other projects tracked by the Southeast Lighthouse station in 2017, which was a Lotek receiver and a 40' tall tower with 6 9-element Yagi antennas.

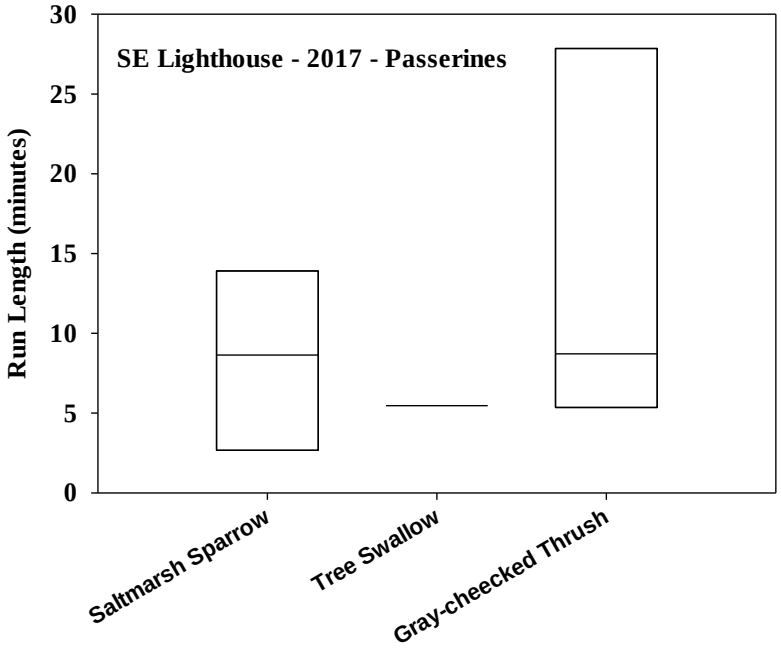

Figure 1.32. Run length of detections (minutes) of songbirds tracked by the Southeast Lighthouse station in 2017, which was a Lotek receiver and a 40' tall tower with 6 9-element Yagi antennas.

1.3.5 Southeast Lighthouse: 2018

A Sensorgnome receiver with a raspberry pi processor was active at Southeast Lighthouse station from 14 Jul to 17 Aug 2018 (Figure 1.33). We initially attempted to start the receiver on 20 Jun, but hardware issues delayed the start date until 14 Jul. However, there were major problems with the receiver this field season starting the end of July, when the receiver was only occasionally active. There were only 6 tags that were detected this field season, 4 Common Terns and 2 Roseate Terns. On 15 Aug, attempt to reboot and repower the system were only successful for ~1 day, and we also had major issues downloading data off the raspberry pi system, which was a common problem for Motus users with this Sensorgnome system

Tags were only detected on the 5-element 8-dB antenna with a south bearing (166°), as there were no detections of any tags from the omnidirectional antenna (Table 1.8). There was a total of 315 detections from 6 different tags from 14 July to 17 Aug 2018. This station only had two antennas this field season. In 2018, there were only two species detected at Southeast Lighthouse, 2 unique Roseate Terns (53 total detections) and 4 Common Terns (262 total detections), which were both detected on the 5-element Yagi antenna with a south bearing (Table 1.8). Of the four Common Terns, we tagged three ~ 45 km away at Great Gull, NY and we tagged one ~ 90 km away Falkner Island, CT. Interestingly, the Roseate Tern from Falkner Island was detected on three different days between 15 July to 25 July.

Table 1.8. Total number of detections on a 5-element 8-dB Yagi antenna at Southeast Lighthouse from 14 Jul to 17 Aug 2018. The 10-dB omnidirectional antenna in 2018 had no detections.

Species – Tag ID	Antenna bearing- 166°
Common Tern	**262**
15	62
20	79
120	94
176	27
Roseate Tern	**53**
17	23
253	30
Total	**315**

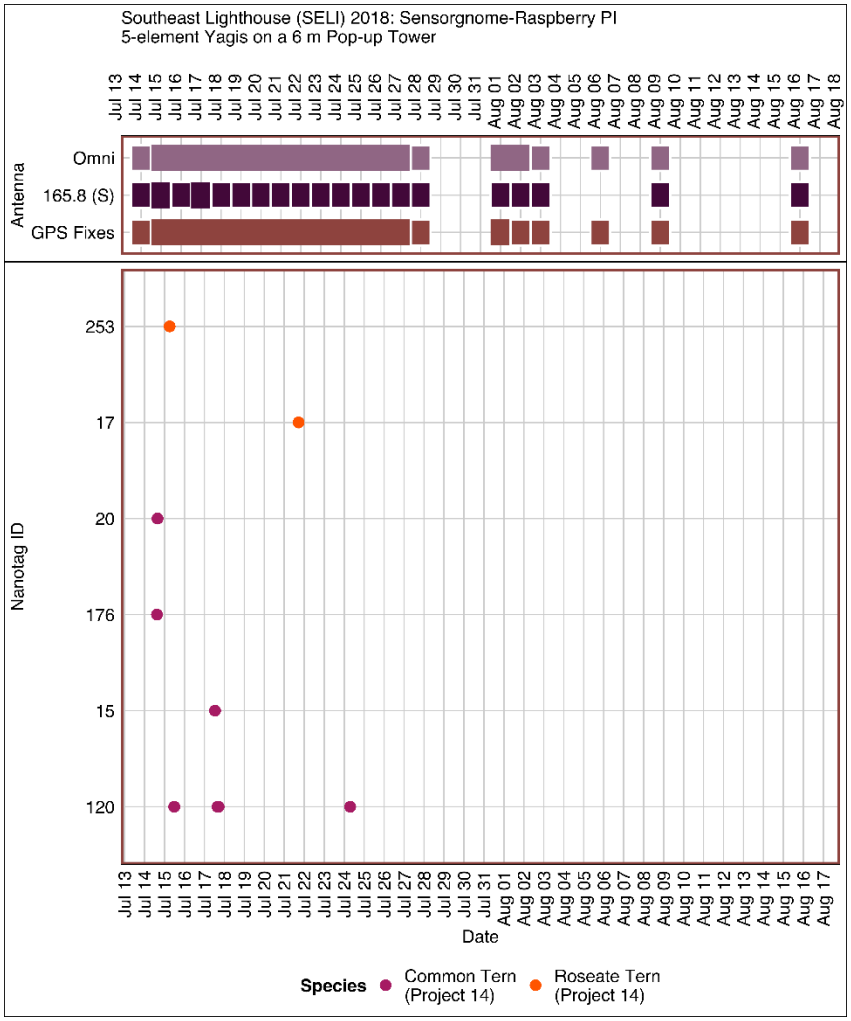

Figure 1.33. Chronology of tags detected at Southeast Lighthouse from 14 Jul to 17 Aug 2018. The Sensorgnome receiver had a beaglebone black processor. Tags associated with this project (Project 14) are circles and other Motus projects are triangles. Boxes at the top represent days when the station GPS (brown boxes) 5-element 8-dB antenna or 10 dB omnidirectional antenna (purple boxes) were detecting either tag bursts or noise in the environment; smaller boxes are days when receiver detected any data for the full 24 hrs of a day, and no box indicates the receiver was not active (if the GPS) or was not detecting any data (if an antenna) on a given date.

Due to few detections at Southeast Lighthouse in 2018, there were few runs (9 total) (Figure 1.34). For Common Terns, median run length = 2.2 min (range 1.6 – 8.8 min, N = 7), while runs were shorter for Roseate Terns (range = 2.4 – 2.6 min, N = 2) (Figure 1.34).

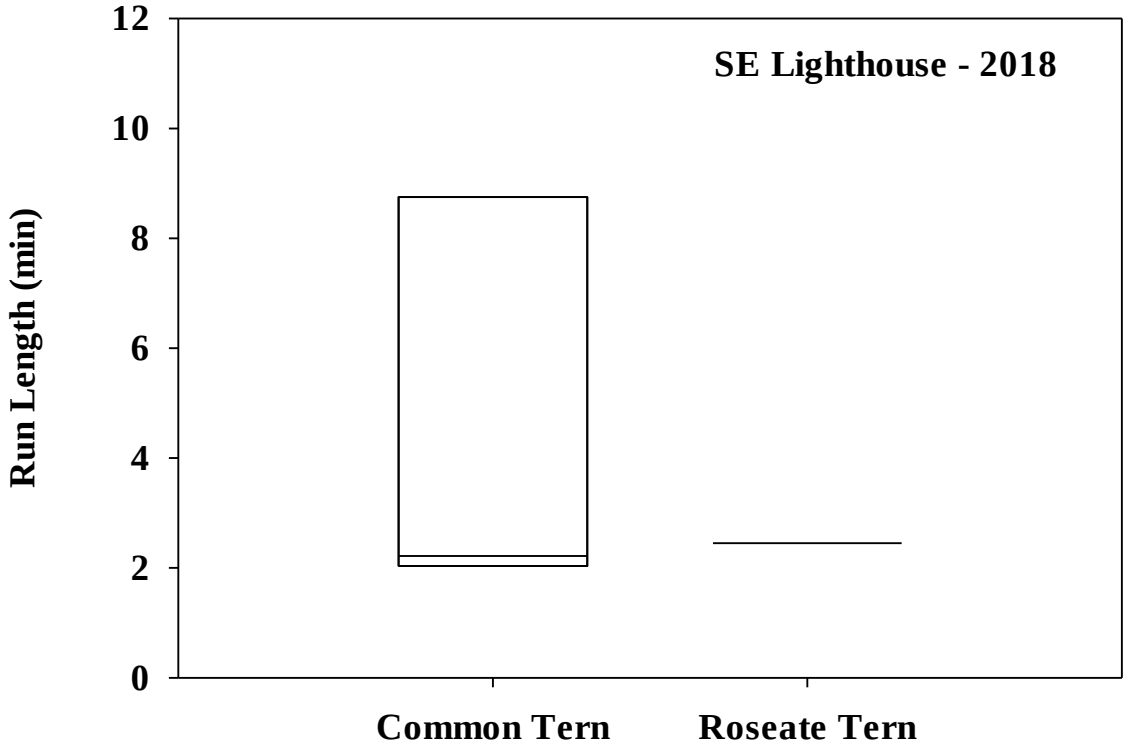

Figure 1.34. Run length (min) of birds tracked by the Southeast Lighthouse station in 2018, which was a Sensorgnome receiver and a 20' tall tower with 3 5-element Yagi antennas.

1.3.6 Southeast Lighthouse: 2019

Due to the poor performance of the Sensorgnome receiver in 2018, we switched to a Lotek receiver in 2019 which was active at Southeast Lighthouse station from 3 Jun to 30 Dec 2019 (Figure 1.35). We had detections from 29 June to 29 October 2019. There was a one-month period when the receiver was inactive (31.5% of days station was deployed) and there appeared to be power issues at this station throughout 2019, as indicated by gaps in GPS fixes (Figure 1.32). We detected 21 individual tags from 6 different species. We detected 9 Common Terns, 1 Piping Plover that we had tagged for this project (Table 1.9). In addition, we detected 1 Red Knot, 3 Semipalmated Plovers, 5 Blackpoll Warblers, and 1 Savannah Sparrow from other Motus projects.

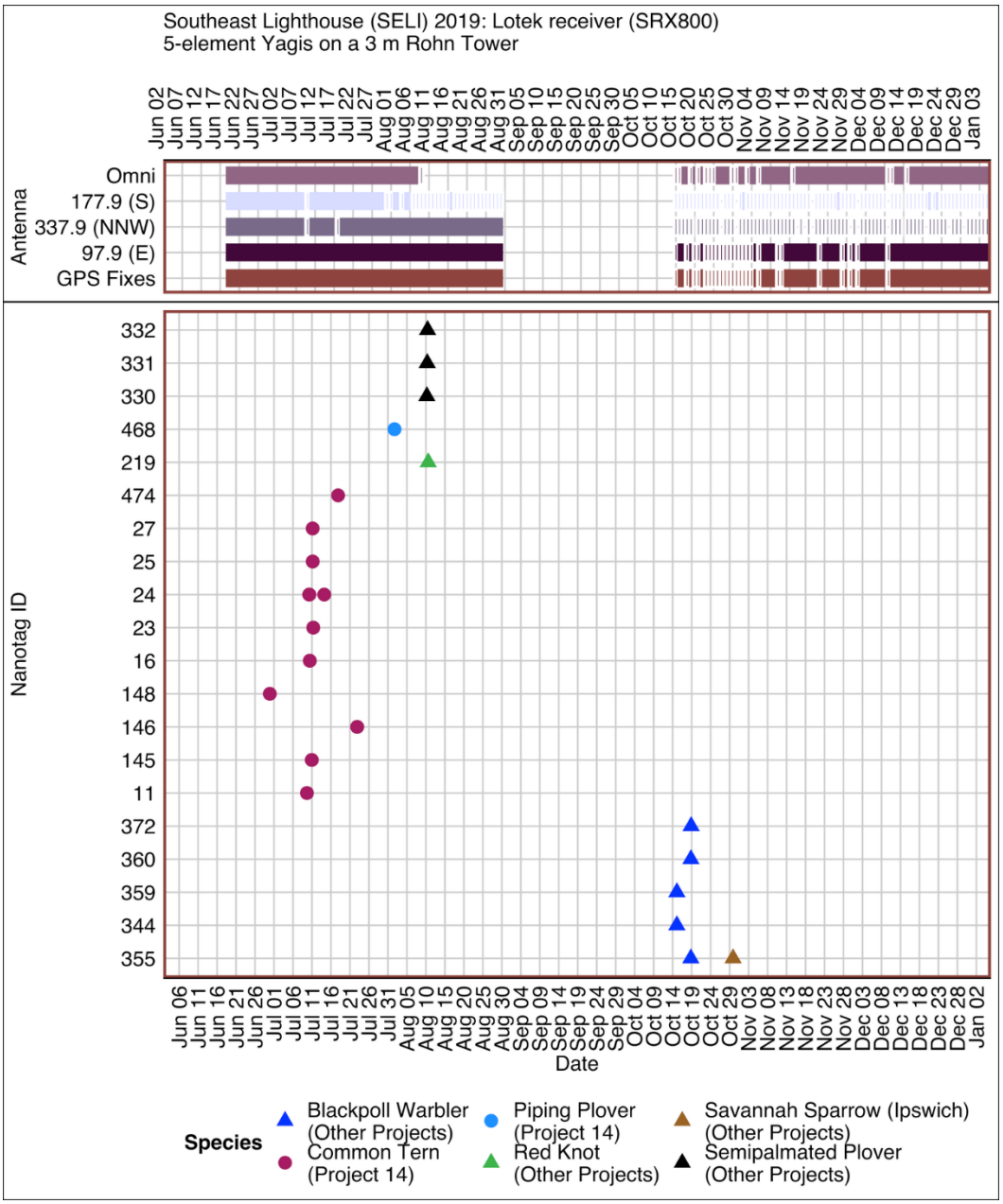

Figure 1.35. Chronology of tags detected at Southeast Lighthouse station from 3 Jun to 30 Dec 2019. The receiver was a Lotek SRX800. Tags associated with this project (Project 14) are circles and tags registered to other Motus projects are triangles. Boxes at the top represent days when the GPS at the station was active (brown boxes) and when the 5-element 8-dB antenna or a 10 dB omnidirectional antenna (purple boxes) were detecting either tag bursts or noise in the environment; smaller boxes are days when receiver detecting any data for the full 24 hrs of a day, and no box indicates the receiver was not active (if the GPS) or was not detecting any data (if an antenna) on a given date.

We had a total of 232 detections of 21 unique tags at Southeast Lighthouse in 2019 (Table 1.9). Birds were more likely be detected by the 5-element Yagi antennas facing 98° (ESE (13 tags;

48% of 232 detection) or 178° (S)(8 tags; 38%) compared to the Yagi facing 338° (NNW) (5 tags; 12%). The 10-dB omnidirectional only detected one Common Tern (1.4% of detections).

In 2019, there were 6 species detected at the Southeast Lighthouse station (Table 1.9) All 9 of the Common Terns we detected were tagged by us at Great Gull Island, NY, which is ~ 47 km away; all these tags were also detected by the Black Rock station in 2019. The one Piping Plover was tagged at Ninigret, Rhode Island in 2019 and also detected at Black Rock station. Birds from other Motus projects include passerines (Blackpoll Warbler and Ipswich Savannah Sparrow) and shorebirds (Red Knot and Semipalmated Plover).

Table 1.9. Total number of detections on three 5-element 8-dB Yagi antennas and one 10-dB omnidirectional antenna at Southeast Lighthouse station from 3 June to 31 Dec 2019.

	Antenna Bearing				
Species – Tag ID	**98°**	**178°**	**338°**	**Omni**	**Total**
Blackpoll Warbler	**29**	**10**	**6**		**45**
344	9				9
355	6	4			10
359		6	6		12
360	5				5
372	9				9
Common Tern	**60**	**70**	**10**	**3**	**143**
11		22			22
16	8	7			15
23		7			7
24	14	16	6		36
25	7				7
27	5				5
145	11				11
146	15	18			33
148				3	3
474			4		4
Piping Plover			**8**		**8**
468			8		8
Red Knot	**8**				**8**
219	8				8
Savannah Sparrow (Ipswich)			**5**		**5**
355			5		5
Semipalmated Plover	**14**	**9**			**23**
330	4				4
331		9			9
332	10				10
Grand Total	**111**	**89**	**29**	**3**	**232**

There was a total of 23 runs detected at Southeast Lighthouse in 2019, with a median length of 5.3 min (range = 2.1 – 22.7 min) (Figure 1.36). Run lengths for Common Terns (median = 4.4 min; range = 2.1 min to 19. 8 min; N = 12) and Semipalmated Plovers (median = 18.7 min, range = 3.6 min – 22.7 min; N = 3) were variable (Figure 1.36).

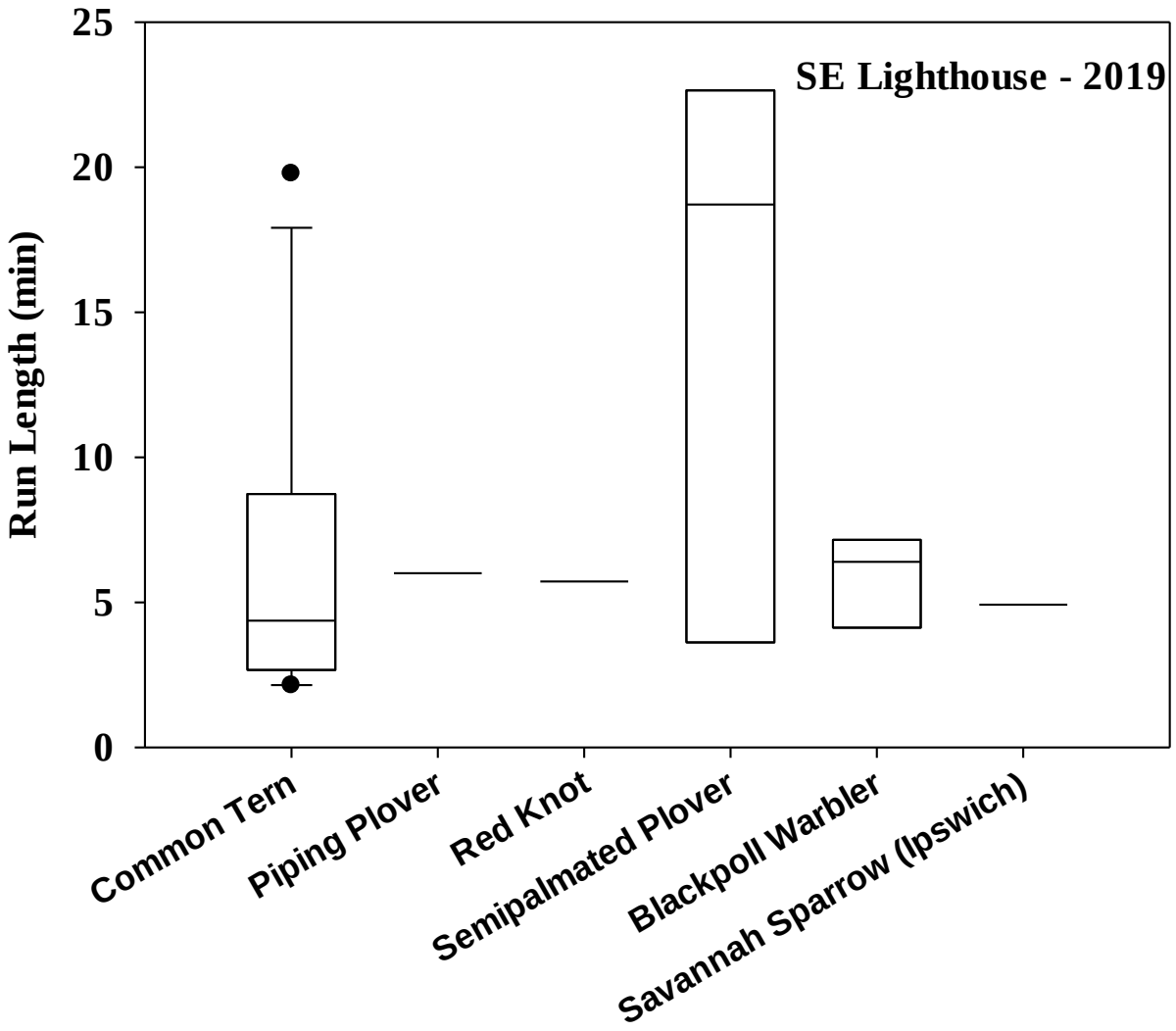

Figure 1.36. Run length for 6 species of birds detected at Southeast Lighthouse in 2019.

1.3.7 Block Island Wind Farm – Turbine #1: 2017

Deepwater Wind staff deployed a receiver and 4 antennas on 4 Aug 2017, with the receiver remaining on the Turbine until 12 Oct 2017 when the SD card was picked up (Figure 1.37), with a total of 93 detections of 2 tags (1 Common Tern and 1 Least Sandpiper)(Table 1.10). There

were power issues with the receiver from ~ 20 Aug to Aug 27 for unknown reasons (11% of the days the station was active), as the antennas had no evidence of activity although the GPS was still active (Figure 1.37).

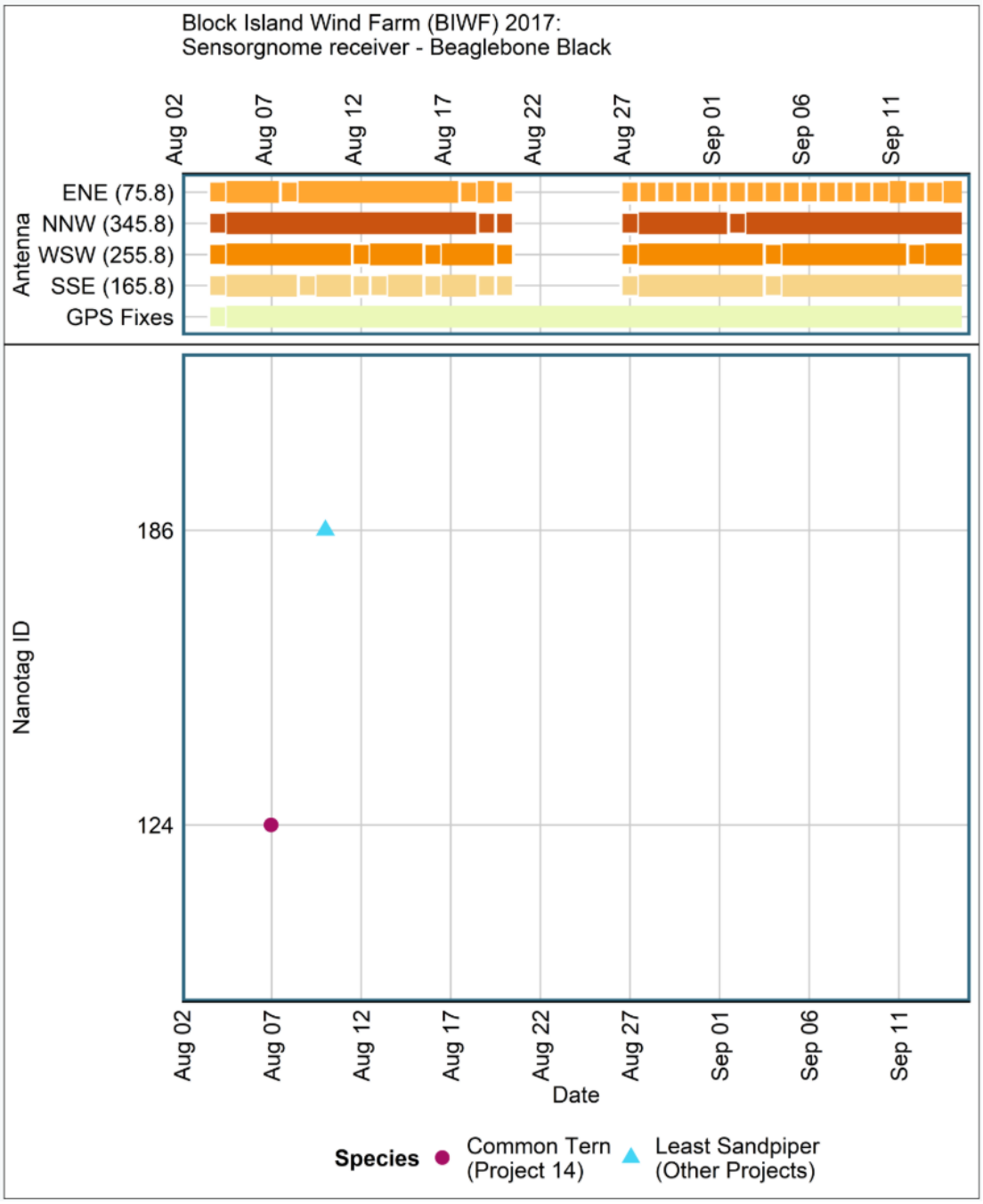

Figure 1.37. Summary of tagged birds that were detected by the station located on Turbine #1 on the Block Island Wind Farm from early Aug to mid-Oct 2017. Boxes at the top represent days when the GPS at the station was active (yellow boxes) and when the yagi antennas (orange boxes) were detecting either tag bursts or noise in the environment; smaller boxes are days when receiver detecting any data for the full 24 hrs of a day, and no box indicates the receiver was not active (if the GPS) or was not detecting any data (if an antenna) on a given date.

The station was activated after most Piping Plovers had initiated their southward migration and most Common or Roseate Terns probably had moved to staging sites (Loring et al. 2019), which explains why there were few detections of focal species. The one Common Tern we detected was tracked for 9.0 min (93 total detections), whereas a Least Sandpiper was tracked for 25.4 min (145 total detections). The Common Tern (ID#124) was detected by all four antennas, whereas the Least Sandpiper was only detected the antenna facing east (Table 1.10).

Table 1.10. Total number of detections on four 5-element Yagi antennas located on Turbine #1 of the Block Island Wind Farm from early Aug to mid-Oct 2017.

	Antenna Bearing				
Species - tag ID	**76°**	**166°**	**256°**	**345°**	Total
Common Tern	15	44	7	27	93
124	15	44	7	27	93
Least Sandpiper	145				145
186	145				145
Total	160	44	7	27	238

1.3.8 Block Island Wind Farm – Turbine #1: 2018

A new Sensorgnome receiver was installed on Turbine #1 on 7 June 2018 and the receiver was apparently active for one day, then failed until late July when it was active for another week before failing again, the station was not operations for 88% of the days it was deployed (Figure 1.38; upper panel). There were no data on the SD card, thus there were no detections to report for this station for 2018. Reasons for the failure of the Sensorgnome to collect data are unclear but were probably related to technical issues with the receiver, but we cannot rule out interference from other equiptment at the station. Unfortunately, because we cannot monitor data acquisition in the real-time with this receiver (e.g., there is no WIFI or Bluetooth connection), we could not determine if there were data acquisition issues until after data were downloaded.

1.3.9 Block Island Wind Farm – Turbine #1: 2019

DWW staff installed a new Lotek receiver on 24 June 2019, and the receiver appeared to collect data for ~1 month (Figure 1.38, lower panel), and there were no detections of tagged birds during this 1-month period. However, after 25 June the receiver became inactive with no GPS signal or antenna activity (72.5% of the days it was deployed. We hoped the Lotek receiver would be more reliable than the Sensorgnome that had major data acquisition issues in 2018, but this receiver was not capable of remote data acquisition creating logistical challenges for data access.

Again unfortunately, there were no detections of tagged birds collected from Turbine #1 in 2019. Reasons for the lack of detections remain unclear.

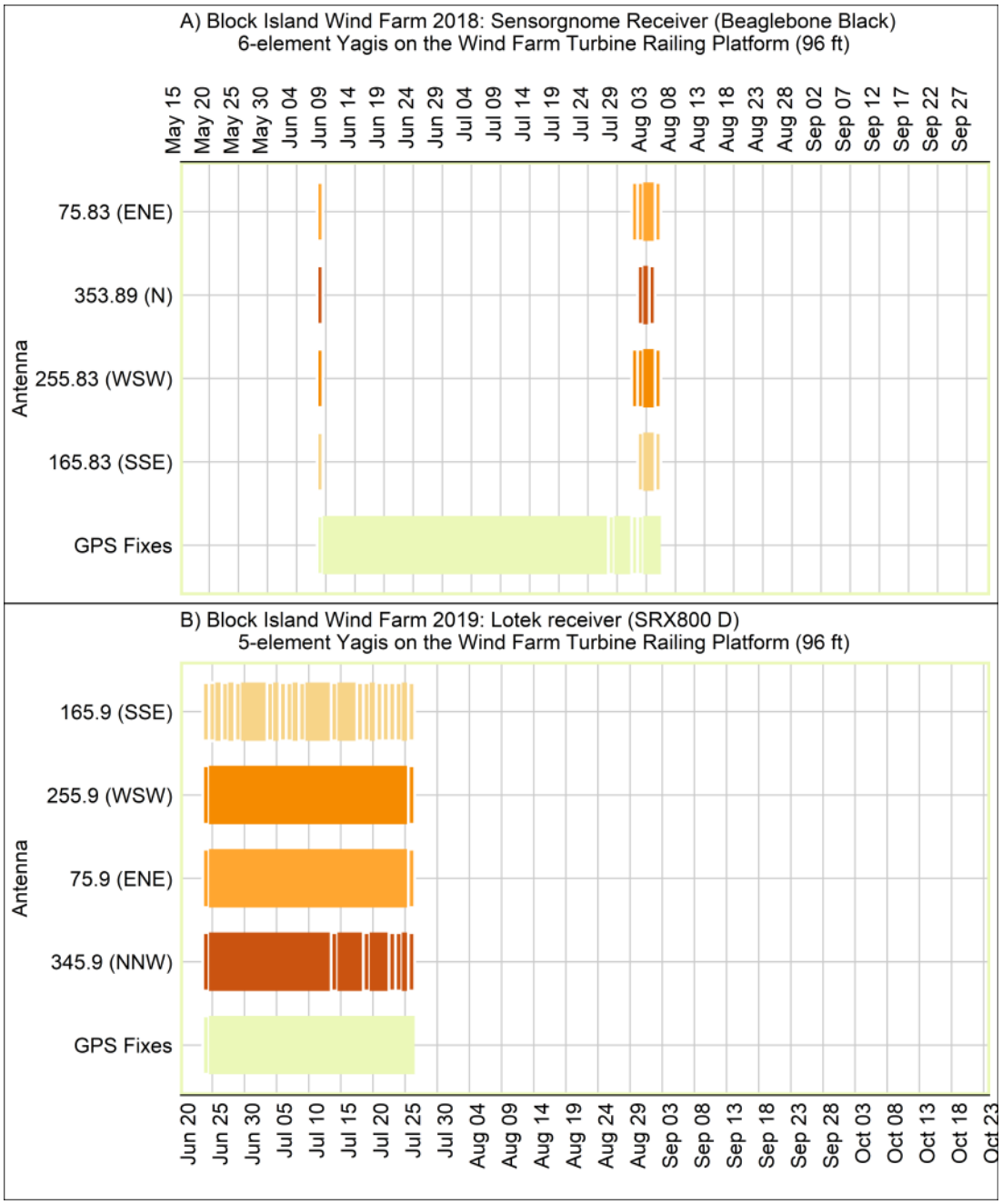

Figure 1.38. Summary of receiver activity patterns on the Block Island Wind Farm turbine #1. A Sensorgnome receiver was used in 2018 (upper panel) and a Lotek receiver in 2019 (lower panel). No tagged birds were detected either year. The yellow/orange lines represent when each antenna was active, and the white indicates inactivity. Days with partial activity are surrounded by white rectangles. Yellow boxes indicate when the GPS at the station was active and receiving

power. The orange boxes indicate when each antenna was detecting either unregistered tag bursts or noise in the environment; smaller boxes are days when receiver detecting any data for the full 24 hrs of a day, and no box indicates the receiver was not active (if the GPS) or was not detecting any data (if an antenna) on a given date.

1.3.10 Run lengths

We defined a "***run***" as sequential detections from a receiver that were <10 min (600 sec) apart, thus a run could contain detections from multiple antennas on the same receiver, but not continuous detections from the different receivers. This differs from the Motus definition of a run, "a consecutive series of detections (hits) of a single tag on the same antennas" (https://github.com/MotusWTS/motusServer/blob/master/inst/doc/motus_data_overview.md) that we previously used to filter the data (see 1.2.6.1). Overall, when data for all individuals were pooled, the average run length was 11.9 min (SE = 0.8 min; median = 6.9 min, 25^{th}-75^{th} percentiles – 3.2 – 14.3 min, range = 0.4 to 110.5 min; N = 335 runs; Figure 1.39). We pooled data from both stations on Block Island from 2017-2019 to investigate differences in run length among species. Somewhat surprisingly, we did not detect statistically significant differences in run length among species groups (Kruskal Wallis: H = 3.9, P = 0.41). Median (25^{th}%-75^{th}%) run lengths were similar among species (e.g., Common Tern: 7.4 min (3.3-15.9); Roseate Tern: 5.9 min (2.1-12.6); Piping Plover: 4.8 min (3.5-8.7), Shorebirds: 7.1 min (2.9-18.6); and Passerines; 6.5 min (4.9-8.6)) (Figure 1.40). Two Common Terns tracked for >100 min were outliers.

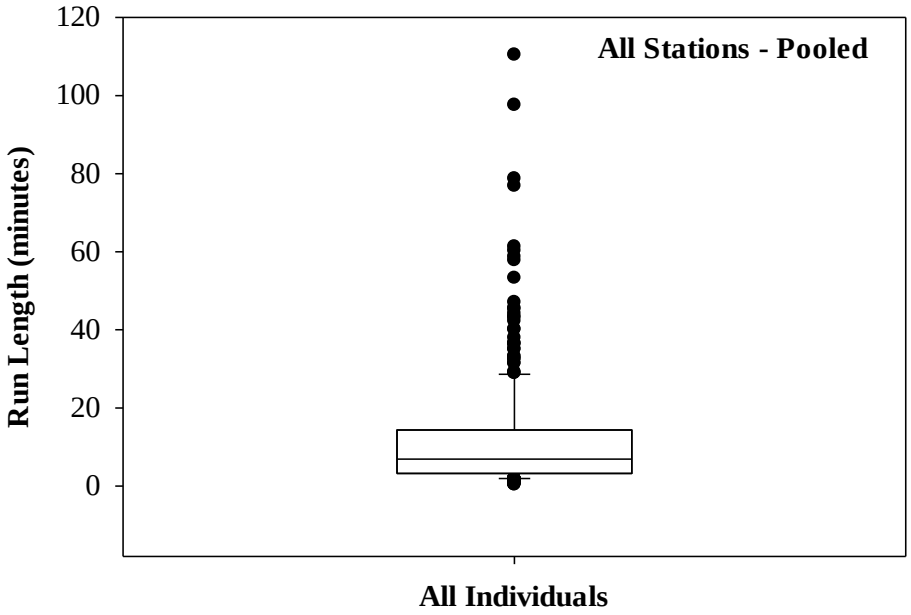

Figure 1.39. Summary of run lengths (min) for all individuals tracked by automated telemetry stations on Block Island, Rhode Island from 2017-2019.

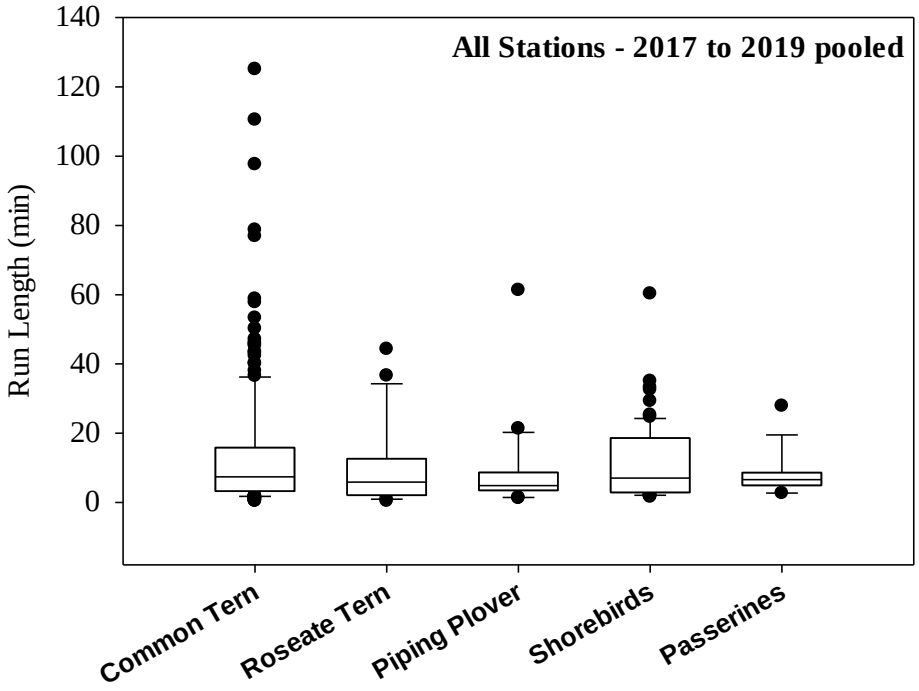

Figure 1.40. Run length for species based on a data pooled from all towers on Block Island from 2017-2019.

We compared two detection metrics (run length and total number of detections per run) for tagged birds detected by the 12 m tall station at Southeast Lighthouse (SELI) in 2017 to the other stations that we operated on Block Island from 2017-2019 that were either 6 m tall or 3 m tall. These shorter (≤6 m tall stations) also typically had 5-element 8-dB Yagi antennas rather than the 9-element 11-dB Yagi antenna that was located on Southeast Lighthouse in 2017, with the one exception was Black Rock in 2018 which also had 3 9-element Yagi antennas. We compared the run length for different stations each year, as we expected that Southeast Lighthouse in 2017 with a 12-m tall tower could detect tags for longer runs than shorter stations (Figure 1.41). However, there was no difference among stations when comparing run lengths among stations ($H = 9.4$, $P = 0.09$). We detected a significant difference in the run length of terns (Common and Roseate terns), which were tracked for 22.6 min (7.4 to 48.9 min; median, 25-75 percentiles) by SELI in 2017 compared to 6.9 min (2.4 to 12.6 min) by all other stations (Mann-Whitney $U = 1637$, $P < 0.001$). There was no difference between shorebirds tracked at Southeast Lighthouse in 2017 (10.9 min (2.9 – 25.7 min)) compared to other stations (7.4 min (4.2 min – 20.1 min) (Mann-Whitney U – 361.0, $P = 0.55$), Piping Plovers (Southeast Lighthouse in 2017 = 6.0 min (3.5 – 9.1 min)) compared to other stations (4.6 min (3.7 to 13.4 min)) (Mann-Whitney $U = 44$, $P = 0.79$), or songbirds (Southeast Lighthouse in 2017 = 5.5 min (2.1 = 22.9 min)) compared to other stations (6.5 min (4.7 to 6.9 min))(Mann-Whitney $U = 12$, $P = 1.0$).

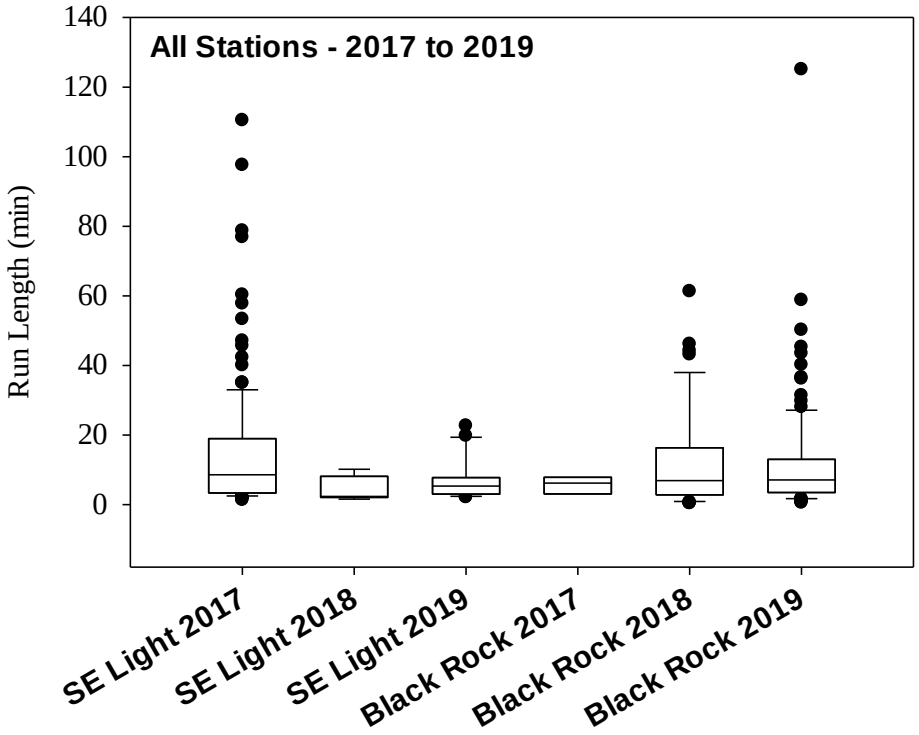

Figure 1.41. Differences in run length (min) among tracking stations on Block Island from 2017 to 2019. Southeast Lighthouse in 2017 had antennas constructed on a 12-m tall tower, whereas all other station had 3 m or 6 m tall towers (Table 1.3). There was no statistically significant difference in run lengths among stations.

1.3.10.1 Run patterns

A key aspect of runs is not only the length of the run, but variation in signal strength between contiguous detections. The variation in signal strength throughout the run can help determine the probable behavior of the bird. We provide some examples to highlight differences in probable flight characteristics. At one end of the spectrum is a Common Tern that was detected for ~50 min by the Black Rock Station on 18 July 2018 (Fig. 1.42). This individual was being tracked by a Sensorgnome receiver, and there was considerable variation in signal strength (-75 dB to –42 dB suggesting this bird was foraging off the nearshore southern coast of Block Island. Two other terns, a Roseate and Common tern, show similar movement patterns (Figure 1.43). In contrast, the runs of two shorebirds, a Sanderling and a Piping Plover, exhibit much less variation in signal strength between contiguous detections (Figure 1.44) suggesting a steady, directed flight. Presumably these birds were migrating in relatively straight direction and variation in signal strength reflects the angle of the direction of arrival of the signals from their transmitters.

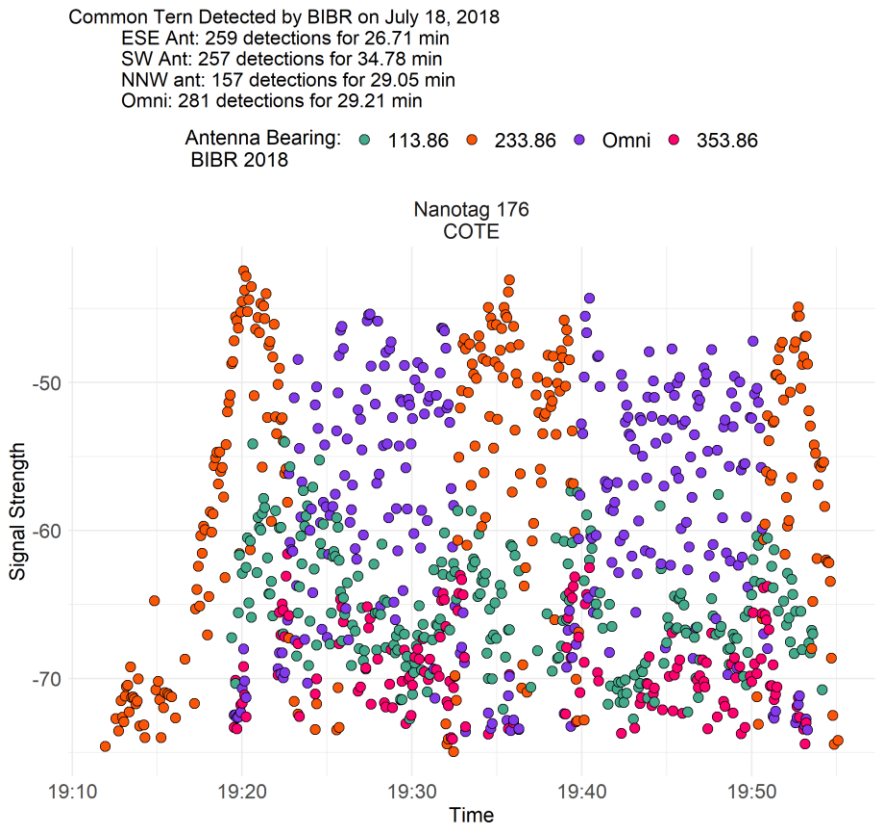

Figure 1.42. Example run of a Common Tern detected by the Black Rock Station on 18 July 2018. This tagged tern was detected by 3 5-element Yagi antennas and 1 omnidirectional antenna for ~50 min. Based on variation in signal strength, this individual was presumably foraging south of Block Island.

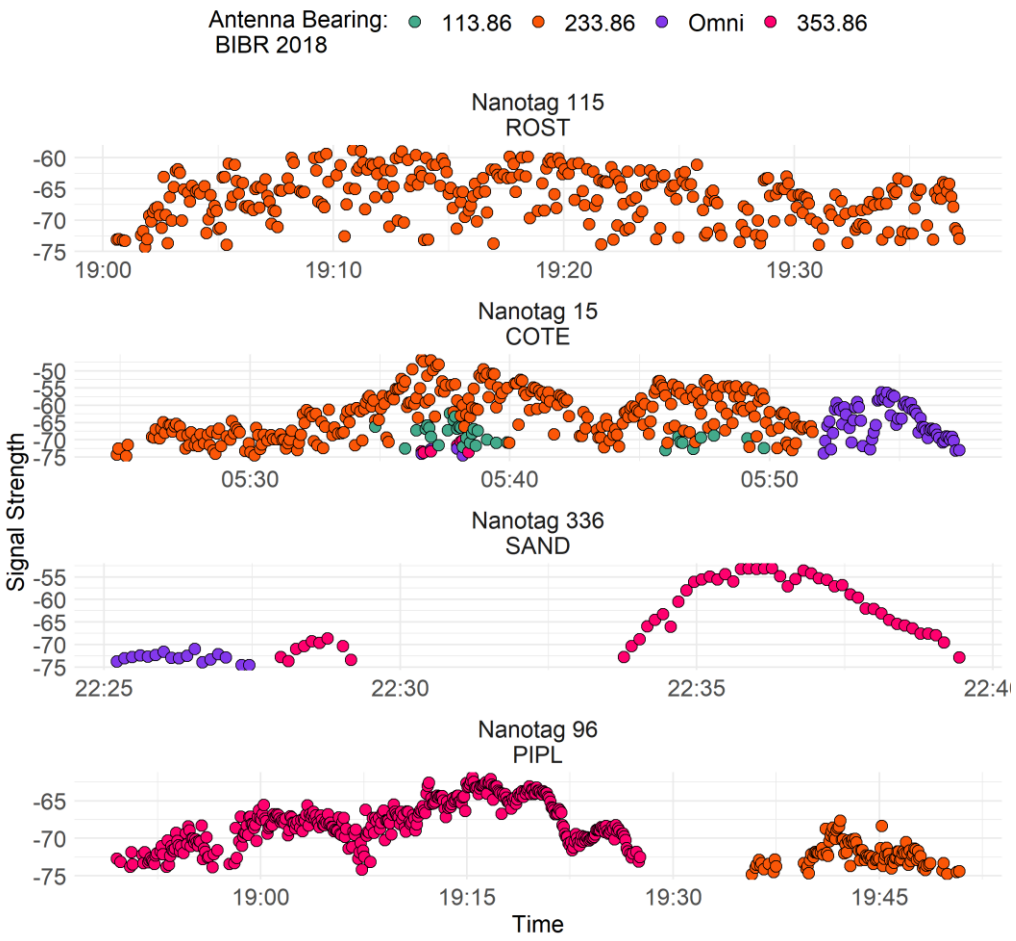

Figure 1.43. Example runs for four tagged birds flying past Block Island based on variation in signal strength. Shown are runs for a Roseate Tern (ROTE; upper panel), Common Tern (COTE), Sanderling (SAND) and Piping Plover (PIPL; bottom panel).

1.3.11 Comparing Sensorgnome vs Lotek receivers

We also compared the run length between sequential detections of individually tagged birds at stations on Block Island from 2017-2019 (Figure 1.44). Sensorgnome receivers are designed to gather incoming signals simultaneously from all antennas attached to the receiver, whereas Lotek receivers are set to scan sequentially among antennas (6.5 seconds of dwell time), thus with three antennas attached to a Lotek receiver it takes ~20 seconds for the receiver to complete a rotation among all three antennas. These differences in the ability of these receiver models are reflected in length of sequential detections, with Sensorgnome receivers reflecting the burst interval of nanotags (5 sec (4 – 6 sec; median (25^{th} – 75^{th} percentiles), whereas Lotek receivers reflected the rotation interval among antennas (29 sec (21 – 41 sec) (Figures 1.45 and 1.46). This difference in length of sequential detections was significant between Lotek and Sensorgnome receivers (Mann-Whitney U-test = 4441093, $P < 0.001$).

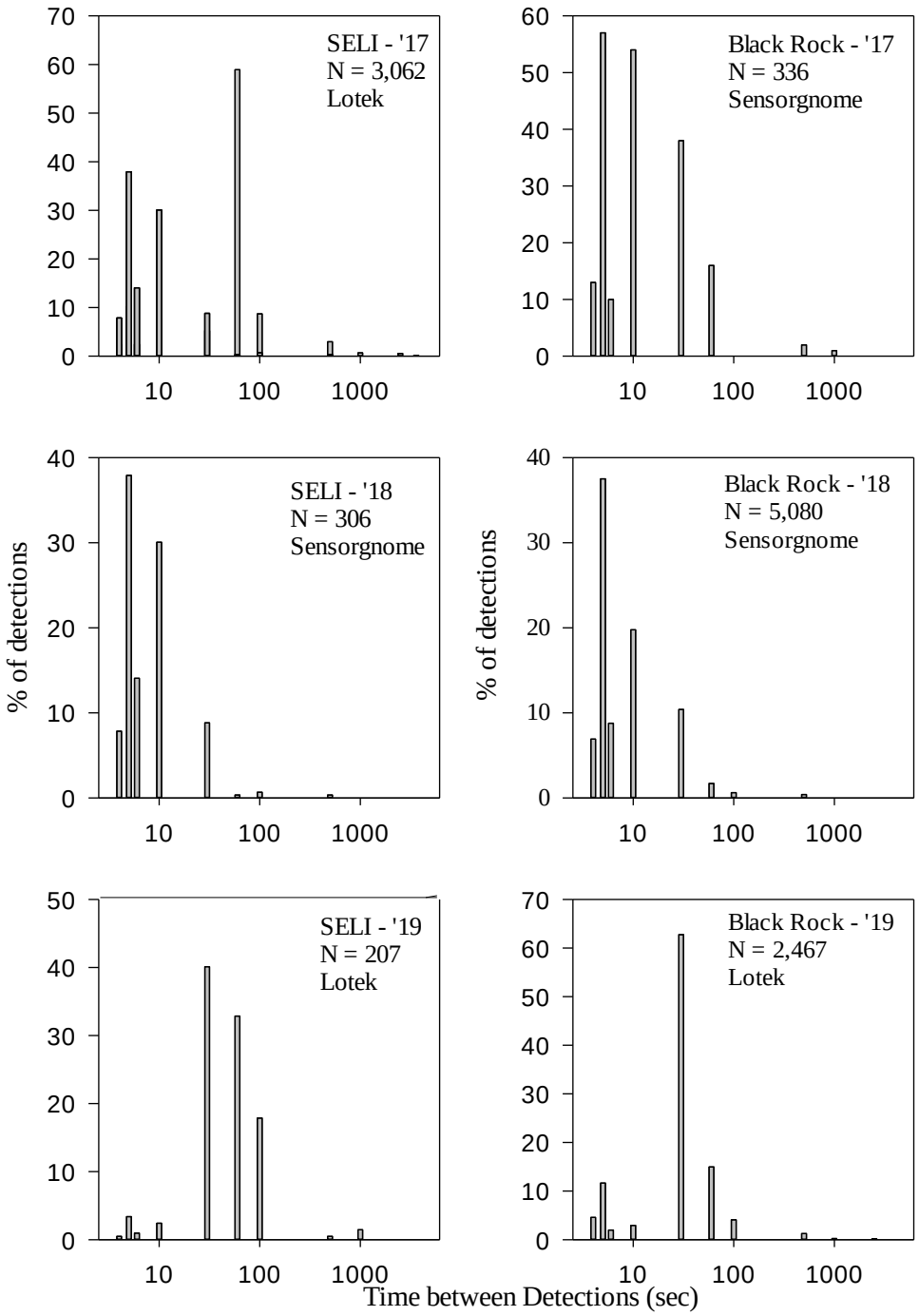

Figure 1.44. Time between sequential detections at two tracking stations on Block Island in 2017-2019. Lotek receivers monitor only one antenna at a time, while Sensorgnome can monitor all antennas simultaneously.

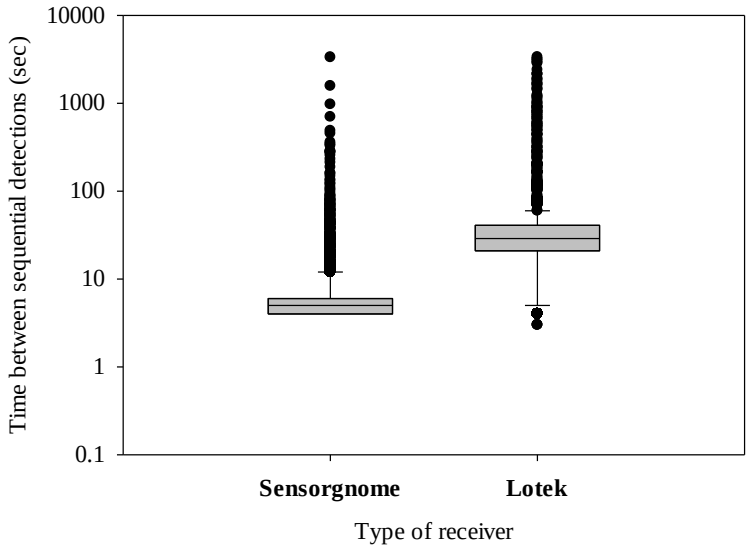

Figure 1.45. Time between sequential detections (sec) for Sensorgnome (N = 5,721) and Lotek receivers (N = 5,860) monitored at stations on Block Island from 2017- 2019.

One approach to assess differences between Lotek and Sensorgnome receivers is to compare the relationship between run length and the total number of detections per run. When a Lotek receiver is used at a station, there are a mean of 1.96 detections per min (SE = 0.05, range 0.44 – 7.5 per min, N = 269 runs) compared to a Sensorgnome with a mean of 7.98 detections per min (SE = 0.48, range = 2.1 – 22.1 detections per min, N = 66 runs) (T = 19493, P < 0.001) (Fig. 1.46). Another way to look at this is the total number of detections per run, with a median of 12.0 (6 – 24 detections) for Lotek receivers compared to a median of 37.5 detections per run (25^{th}-75^{th} percentiles = 18.7 – 96 detections) for Sensorgnome receivers (Figure 1.47).

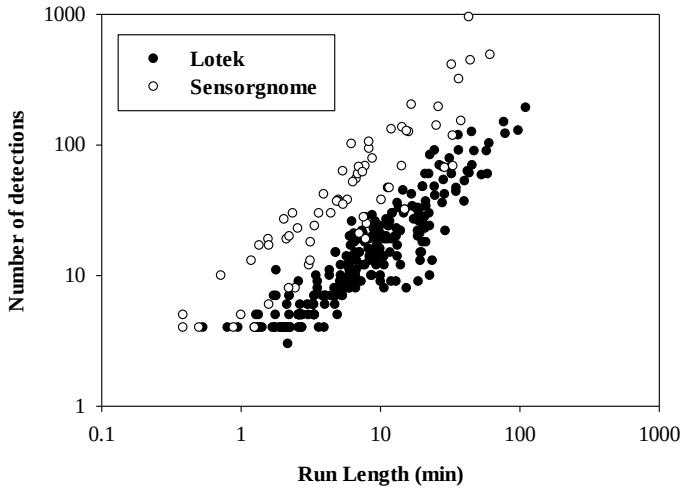

Figure 1.46. Differences between Lotek and Sensorgnome receivers in the relationship between run length and total number of detections within a run.

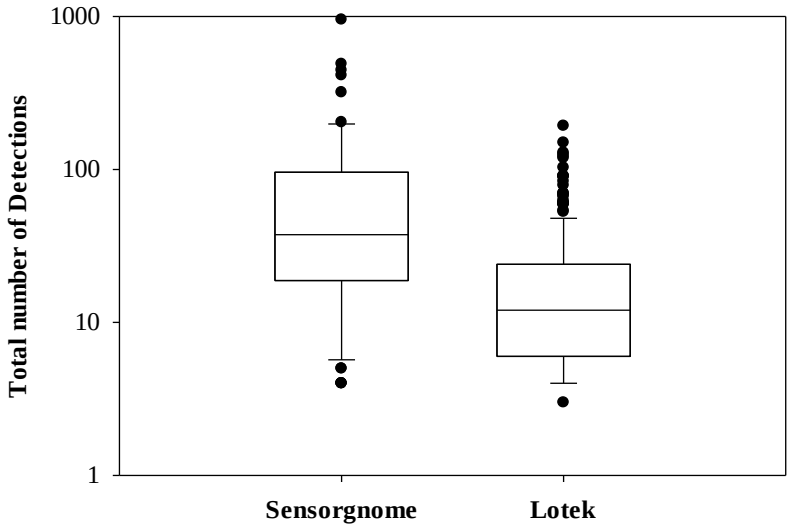

Figure 1.3. Differences between receivers in the total number of detections within a run for Sensorgnome compared to Lotek receivers. Note y-axis is in a $\log_{10}$ scale. This difference was significant ($P<0.001$).

1.3.12 Receiver Signal Strength

Another distinction between Sensorgnome and Lotek receivers were differences in estimated signal strength. Lotek receivers display values ranging from 1-255, whereas Sensorgnome values range from -104 dB to -40 dB. Only the Lotek receiver located at Southeast Lighthouse in 2017 detected signal strength values that covered the entire spectrum of potential values (mean = 95, SD = 55; median = 80, 25th% - 75% = 52-130; range = 16-255; Figure 1.48). In contrast, Sensorgnome receivers generally detected a much narrow range of values (e.g., Black Rock in 2017 and 2018, Southeast Lighthouse in 2018) or Lotek receivers in 2019 (Figure 1.48). Reasons for these differences in signal strength remain unclear.

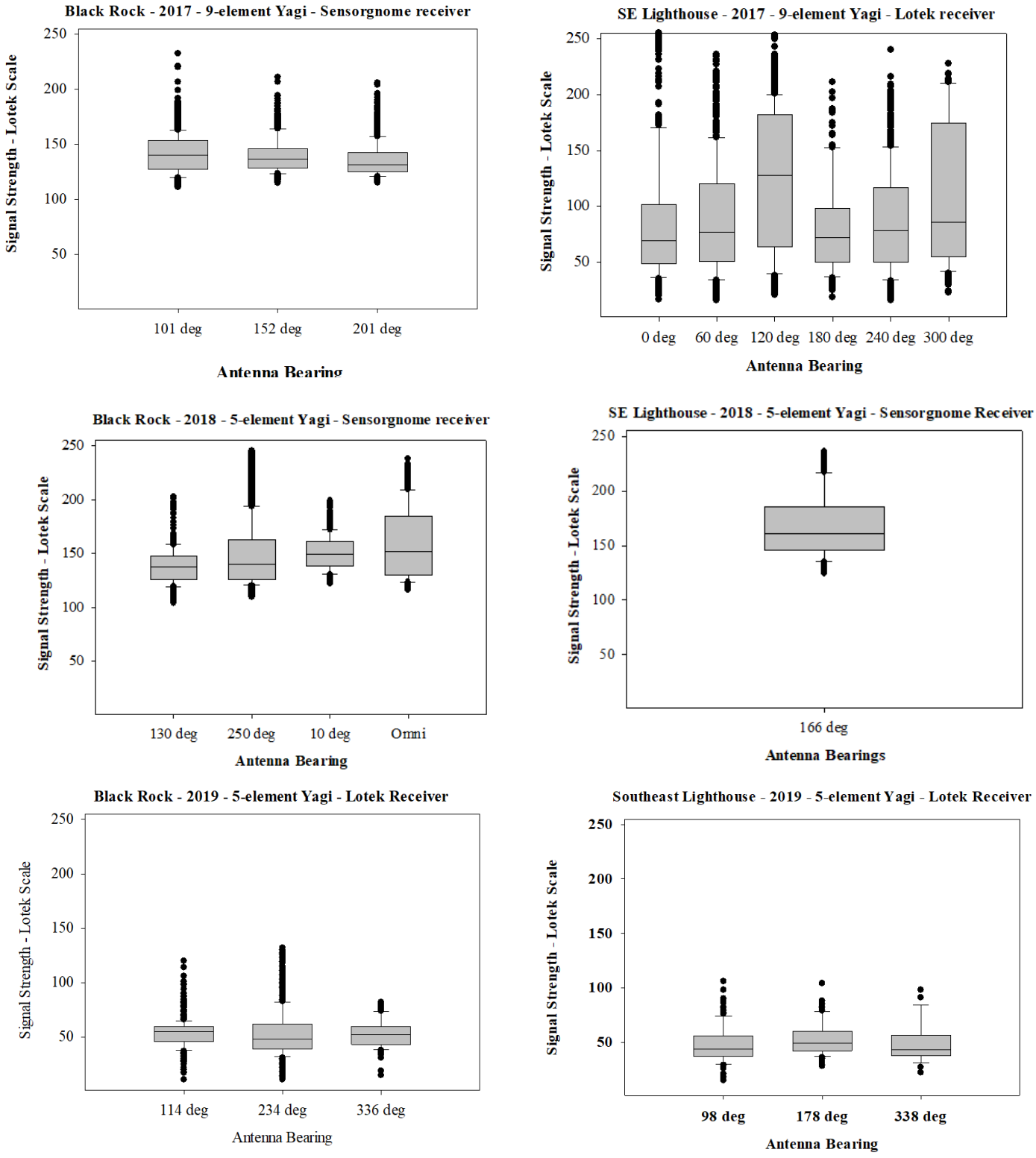

Figure 1.48. Variation among stations among years in signal strength between Lotek and Sensorgnome receivers. Stations had either 5-element or 9-element Yagi antenna and a Sensorgnome or Lotek receiver. Signal strength is shown on the Lotek receiver (1-250 scale), which for Sensorgnome receivers was based on a conversion (see Methods).

1.4.1 Regional movements of terns and plovers

A major strength of having access to the Motus network is the ability to track regional movements of our focal species. Thanks to the hard efforts of Pam Loring, there was an extensive network of towers in southern New England (project 14 stations). The number of active automated radio telemetry stations in the Motus Network (Taylor et al. 2017) varied annually, as various investigators initiated new stations and decommissioned stations (Figures 1.49, 1.50, 1.51). Obviously, this had a major impact on where our focal birds could be detected annually. The network of stations was thorough from Cape Cod to North Carolina (Figure 1.46). In 2018, new stations were added in coastal South America to begin to assess long-distance continental-scale movements (Figures 1.50 and 1.51; Table 1.2).

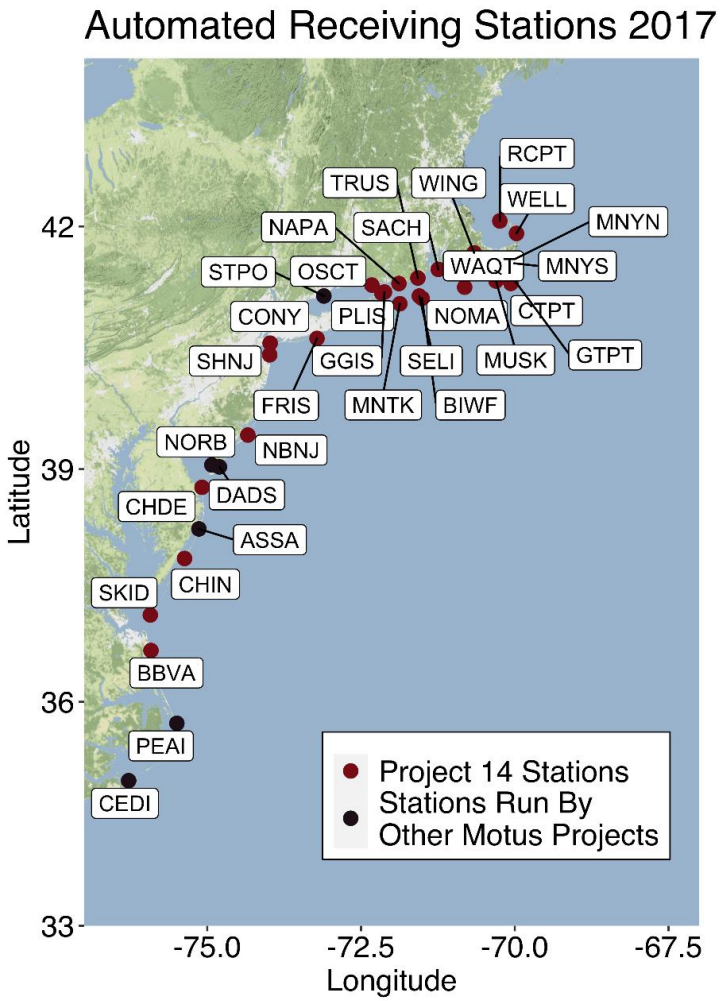

Figure 1.49. Locations of active automated radio telemetry stations active during 2017 along the Atlantic Coast that detected at least one nanotag from Project 14

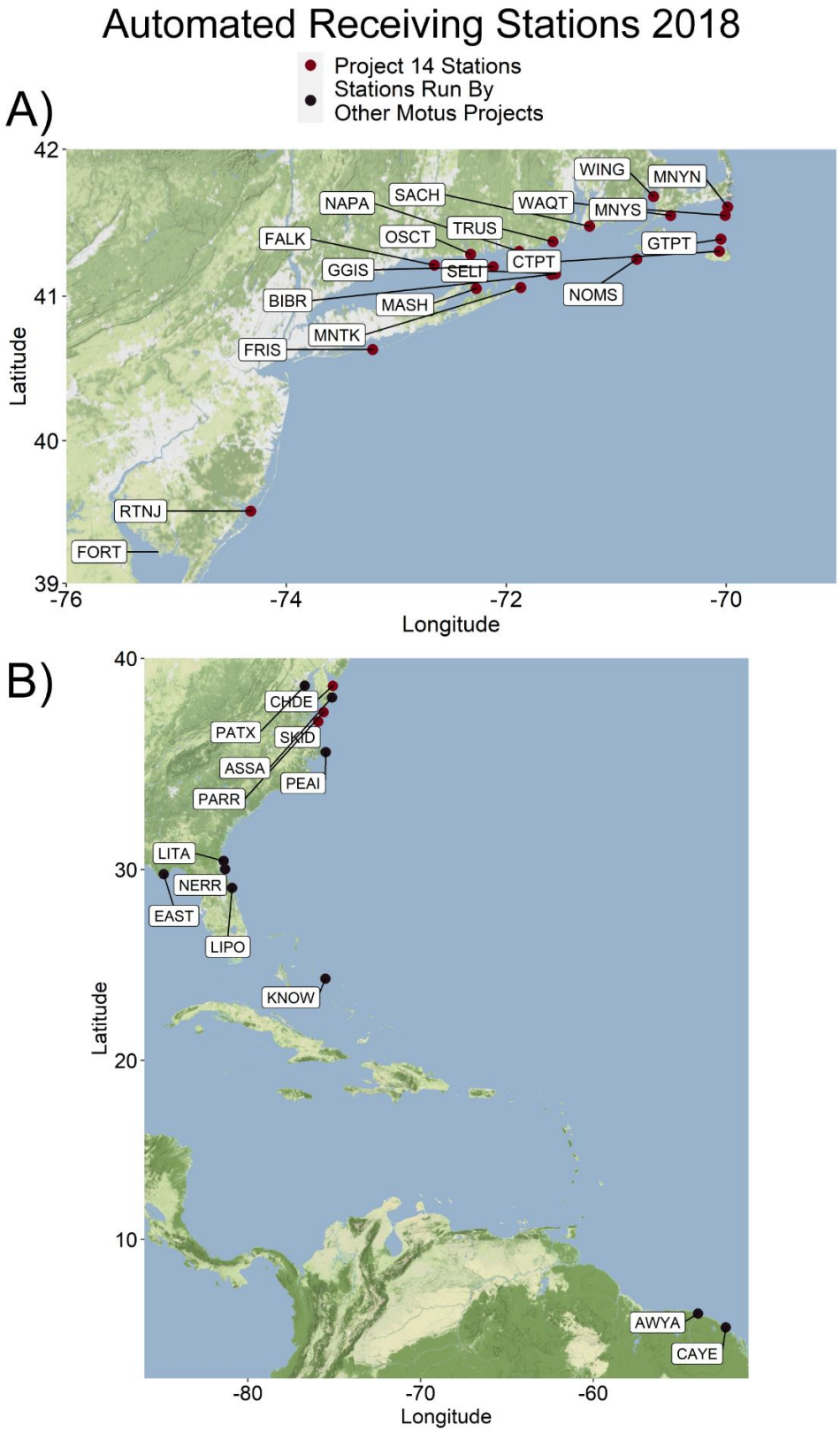

Figure 1.50. Locations of active automated radio telemetry stations active during 2018 along the Atlantic Coast that detected at least one nanotag from Project 14.

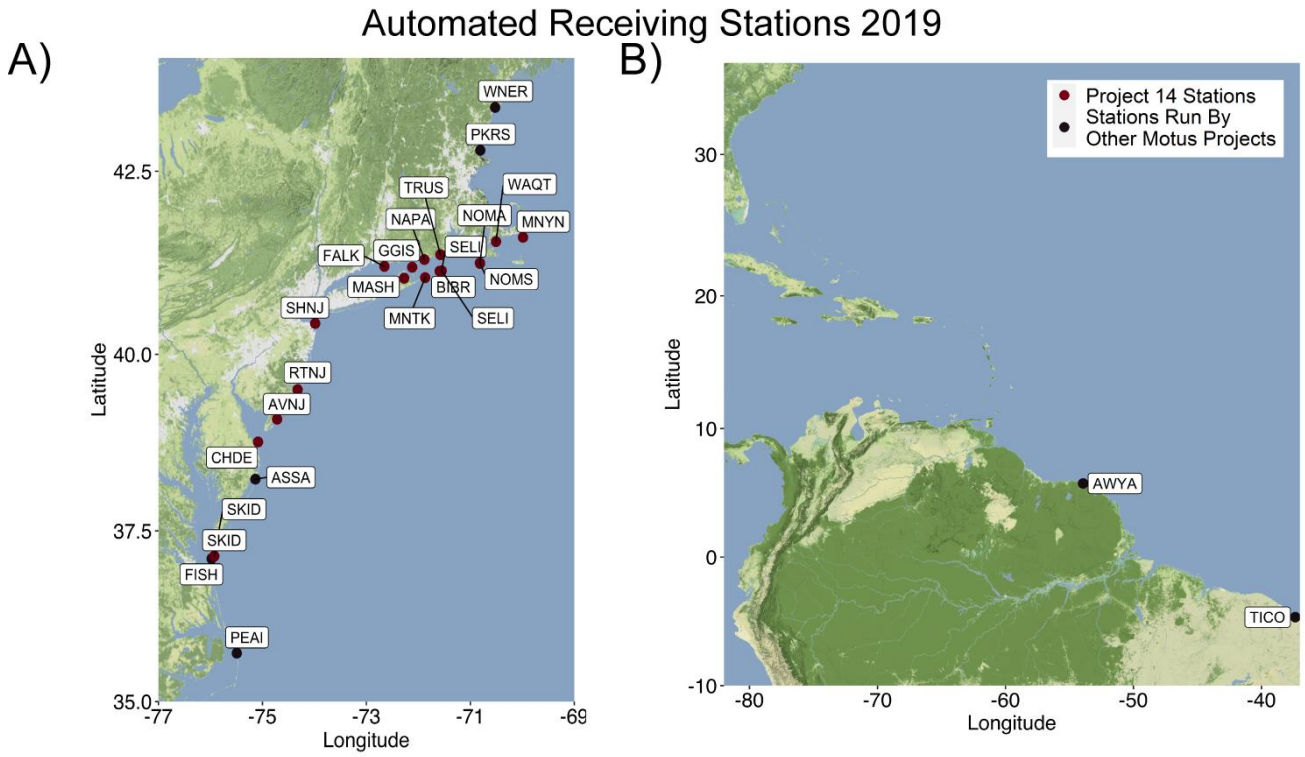

Figure 1.51. Locations of active automated radio telemetry stations active during 2019 along the Atlantic Coast that detected at least one nanotag from Project 14.

1.4.1.1 Common Tern regional movements

The key strength of the Motus network of stations is the ability of the stations to clearly document the chronology and spatial extent of movements of focal species. Of course, documenting movements is clearly dependent on the locations of stations and detection radii of each automated telemetry station given the limitations of the small VHF transmitters. From 2017-2019, the network recorded 1,646,506 detections of Common Terns we tagged, with 78% of total detections recorded at the station at Great Gull Island where we tagged most of the Common Terns we monitored (Table 1.11). We detected 124 of 134 birds we tagged (91%) at some point during the tracking season (ranging from 89% to 93% per breeding colony per year). Tracking detections of birds at Great Gull, we were able to assess the chronology of movements around the region (e.g., Figure 1.52 and 1.53).

We did occasionally detect Common Terns at Motus stations south of Rhode Island, but it was unusual (Table 1.11), presumably because most Common Terns tend to migrate farther offshore when migrating to non-breeding grounds in South America. An exciting finding was documenting detections of Common Terns in coastal South America, with detections of one individual in 2018 and three individuals at a station at Awala-Yalimapo, French Guiana

(AWYA) in late Aug 2019, and one of those same birds being detected at Icapuí, Brazil (TICO) in mid-September 2019. These areas were also identified by Nisbet et al. (2011) and Nisbet and Mostello (2015) as important stopover sites for Common Terns based on locations of Common terns tagged with geolocators.

We were much more likely to document intra-regional movements between breeding colonies in Long Island Sound (e.g., Great Gull Island NY or Falkner Island, CT) and stations farther east in Rhode Island Sound or Cape Cod and the Islands (Martha's Vineyard and Nantucket)(Figures 1.54, 1.55, 1.56, Table 1.11). What is striking looking at these examples of movements is how much Common Terns readily move between Block Island and Rhode Island Sounds to Cape Cod, and then back to Long Island Sound (e.g., ID24 in Fig 1.54, or ID25 in Fig. 1.55), or even to the New York City area and back to southern New England (Fig. 1.56). Interestingly occasionally Common Terns would disperse farther north into northern Massachusetts (Parker River NWR) or even Rachel Carson NWR, Maine (Figure 1.56).

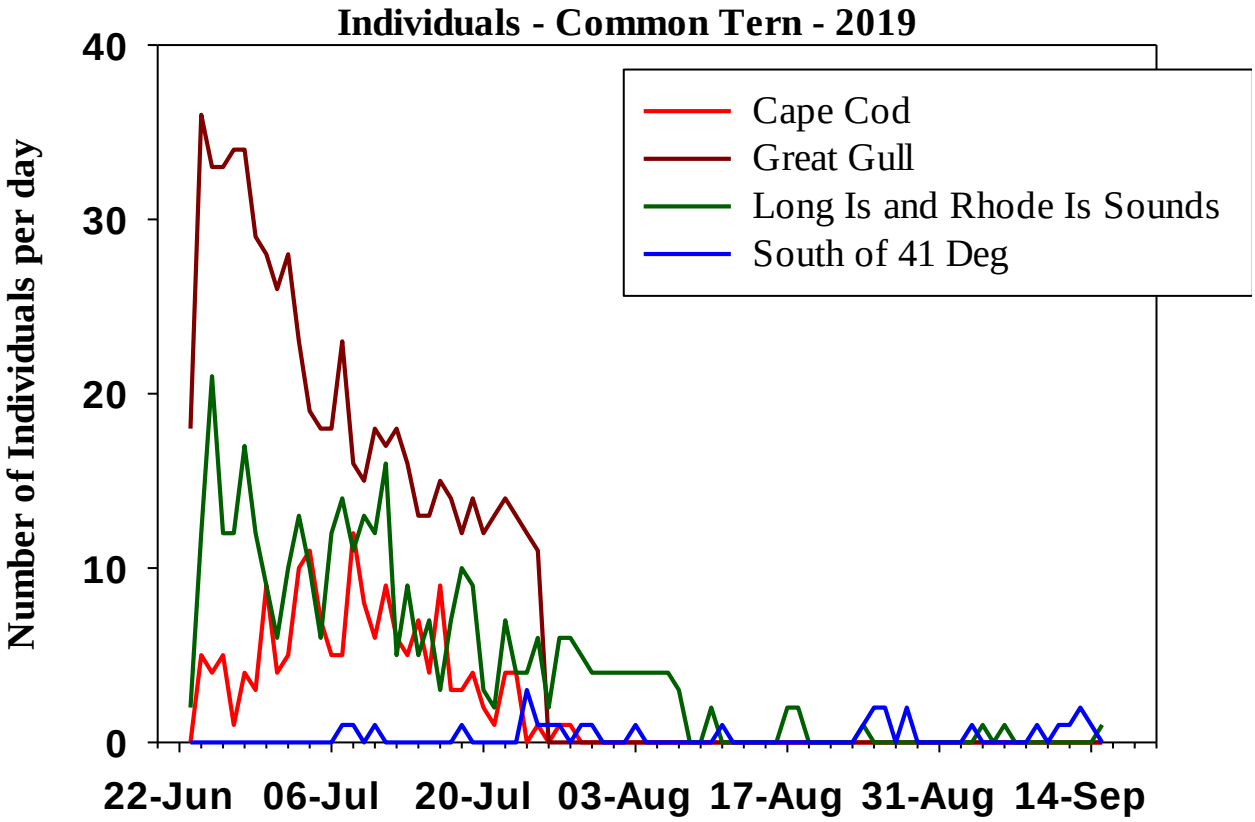

Figure 1.52. Summary of daily detection rates of individual Common Terns tagged on Great Gull Island, NY during 2019 field season (n = 40). We pooled data into 4 areas: the station on Great Gull Island (note: the station at Great Gull ceased on 28 July), stations located throughout Long Island and Rhode Island Sounds, stations on Cape Cod and the Islands (Nantucket and Martha's Vineyard) and south of southern New England (41° latitude).

Table 1.11. Cumulative detections (Detect) and number of individual (Ind) Common Terns at stations from 2017-2019 (see Fig 1.48 – 1.50 for station locations).

		2017				2018				2019	
		Great Gull (N = 30)		Buzzard's Bay (N =29)		Falkner (N = 18)		Great Gull (N = 20)		Great Gull (N = 40)	
Latitude	**Station**	**Detect**	**Ind**	**Detect**	**Ind**	**Detect**	**Ind**	**Detect**	**Ind**	**Detect**	**Ind**
-4.688	TICO									24	1
5.746	AWAY							89	1	818	3
34.957	CEDI			11	1						
35.717	PEAI			39	1					244	2
37.098	FISH									18	1
37.138	SKID									57	2
38.241	ASSA			40	1					31	1
38.770	CHDE									39	1
39.092	AVNJ									15	1
39.509	RTNJ									13	1
40.430	SHNJ									29	2
40.633	FRIS			41	1	20	1				
41.052	MASH					68	3	4869	10	280	6
41.059	MNTK	10566	25	77	1	709	8	7371	14	3110	22
41.148	**BIBR**					599	3	1894	10	2468	32
41.126	BIWF	88	1								
41.153	**SELI**	1701	13	121	3	156	2	106	2	127	9
41.153	STOP	86	2	45	1						
41.189	PLIS	49295	27	205	3						
41.202	GGIS	318156	27			1752	5	254340	18	715039	37
41.213	FALK					146783	16	13979	5	68616	18
41.253	NOMS							101	1	948	16
41.261	NOMA	269	2	7043	19					1142	23
41.306	NAPA	9	1							6538	25
41.307	CTPT	29	1	278	8						
41.337	MUSK	140	2	5773	20						
41.373	TRUS	46	3	40	1	6	1	3566	5	4964	23
41.391	GTPT	39	2	894	10	8	1				
41.479	SACH	12	1	7	1			60	3		
41.552	WAQT	455	3	4183	22	16	1	129	1	820	18
41.553	MNYS	109	2	149	7	34	1	13	1		
41.609	MNYN	4	1	37	6			13		2028	21
41.681	WING			59	2			236	1		
42.066	RCPT			1927	6						
42.780	PRKS									202	2
Overall		381,004	27	20,969	26	150,151	16	286,766	18	807,616	37

Because we had >1.3 million detections of 82 Common Terns at Great Gull, we were able to begin to assess inter-annual variation in post-breeding departure of adults from their breeding colonies (Figure 1.52). It appears that the timing of adult emigration from Great Gull was similar in 2017 and 2019, while in 2018 there was somewhat protracted emigration. The receiver at Falkner went offline twice in July and the receiver ceased at Great Gull on 28 July 2019, thus data were incomplete for those two sites.

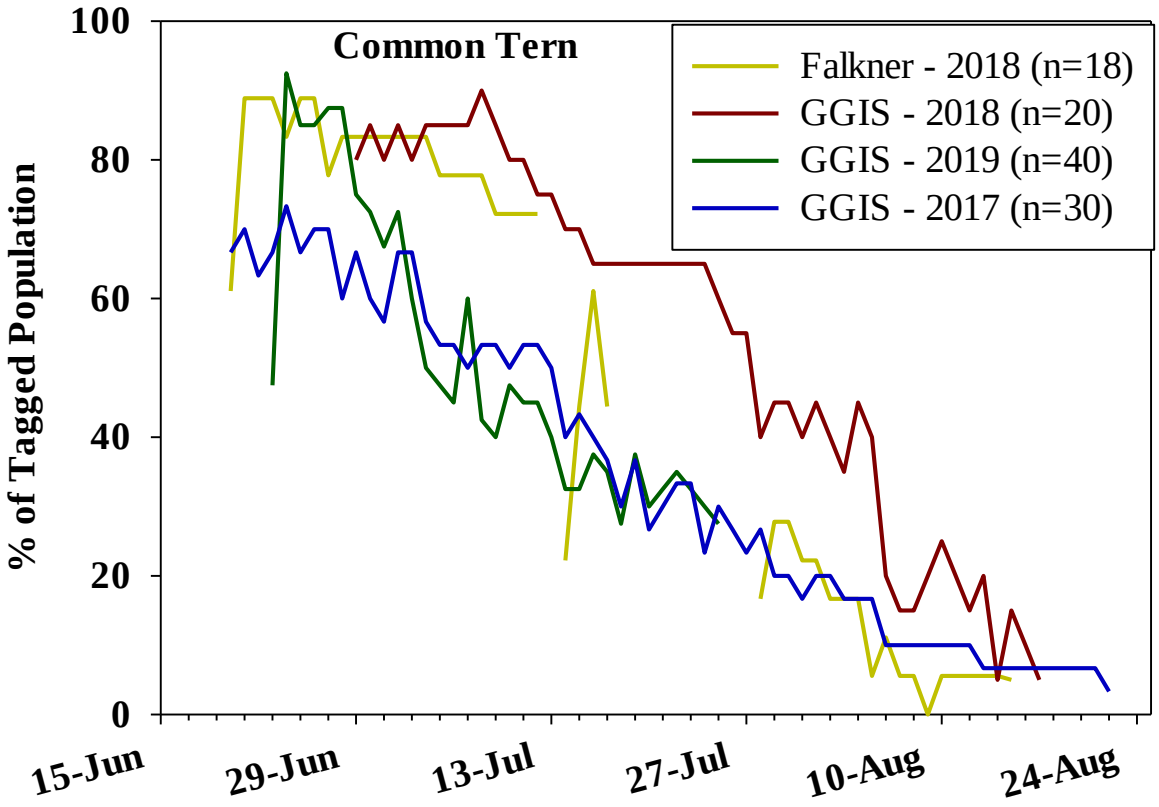

Figure 1.53. Seasonal variation in daily detection rates (% of tagged population detected) of Common Terns at Great Gull Island, NY from 2017-2019 and Falkner Island, CT in 2018. The receiver failed occasionally in July on Falkner and July 28, 2019 on Great Gull.

We were able to quantify the regional movements of Common Terns breeding on Great Gull Island in 2017 (Fig. 1.54), 2018 (Fig. 1.56) and 2019 (Fig. 1.58). It was evident that Common Terns breeding at Great Gull regularly visited other areas in Long Island Sound throughout July and Aug, with some local movements documented into September in 2018 (Fig. 1.56). Common Terns from Great Gull often ventured to coastal Rhode Island throughout the breeding season in

2018 and 2019. Individuals typically started to disperse farther from the Great Gull colony to Cape Cod and the islands in mid-August.

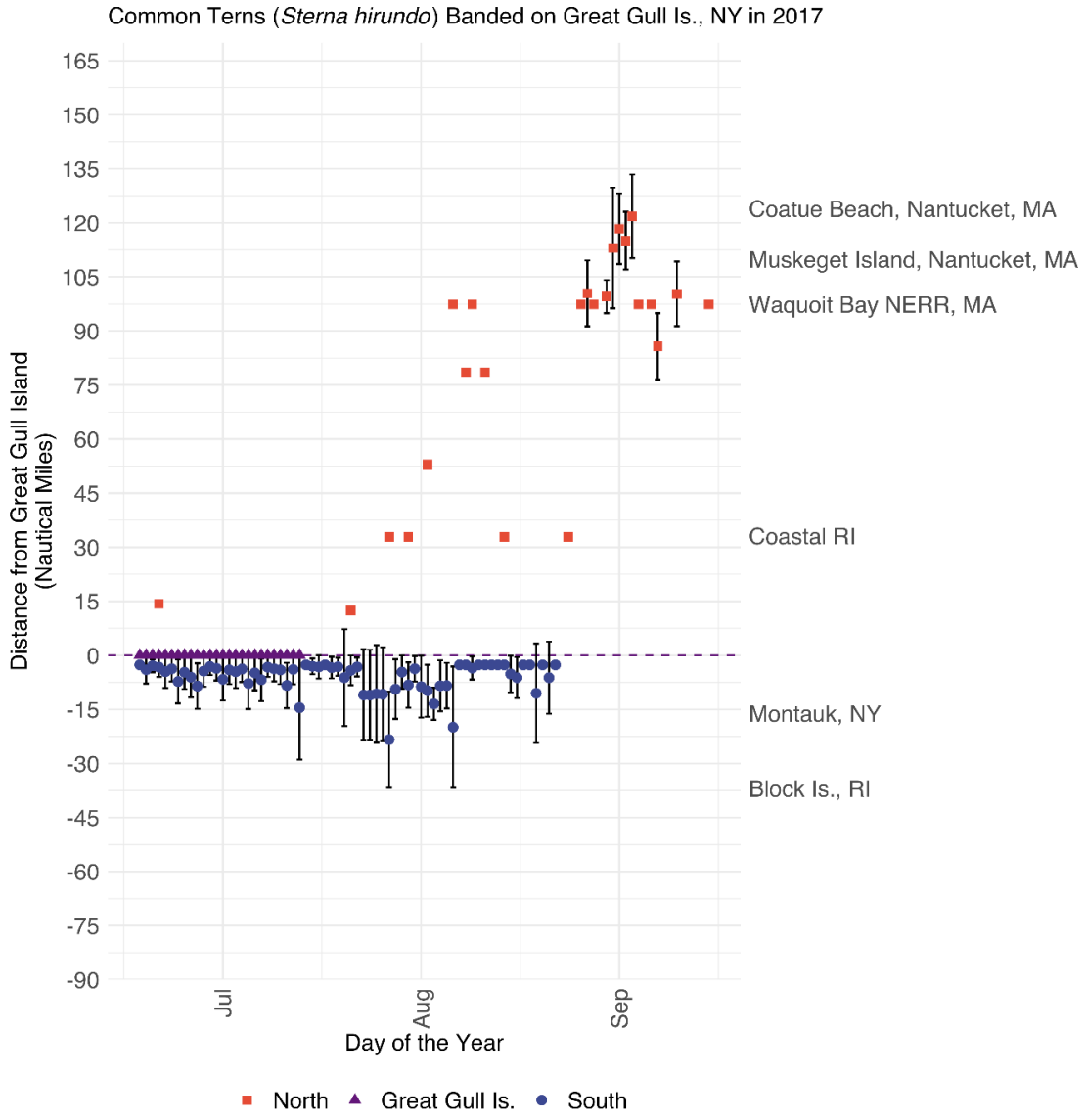

Figure 1.4. Distance traveled north (nautical miles, orange squares), south (nautical miles, blue circles) or on GGIS (purple triangles) by Common Terns tagged on Great Gull Island, NY (purple dotted line) in 2017. Data are presented as mean ± standard deviation. Representative locations for a given distance from the breeding colony are to the right for context.

The chronology of movements of Common Terns breeding in Buzzard's Bay, MA in 2017 (Figure 1.55) appeared like Common Terns nesting in Long Island Sound. There were no automated telemetry stations adjacent to nesting colonies at Bird, Ram, or Penikese Islands, so information of local movements at breeding colonies was limited. However, birds breeding at Buzzard's Bay colonies were much more likely to be detected at stations in Nantucket Sound and

Cape Cod and the islands (Martha's Vineyard and Nantucket) than terns nesting on Great Gull Island. Common Terns from Buzzard's Bay were regularly detected at stations on Cape Cod from mid-July through early-September, with some individuals detected until 1 October. Terns breeding at Buzzard's Bay colonies occasionally were detected in Long Island Sound from mid-July to early September, and a few individuals were detected in coastal regions from Delaware and farther south from late July to mid-September.

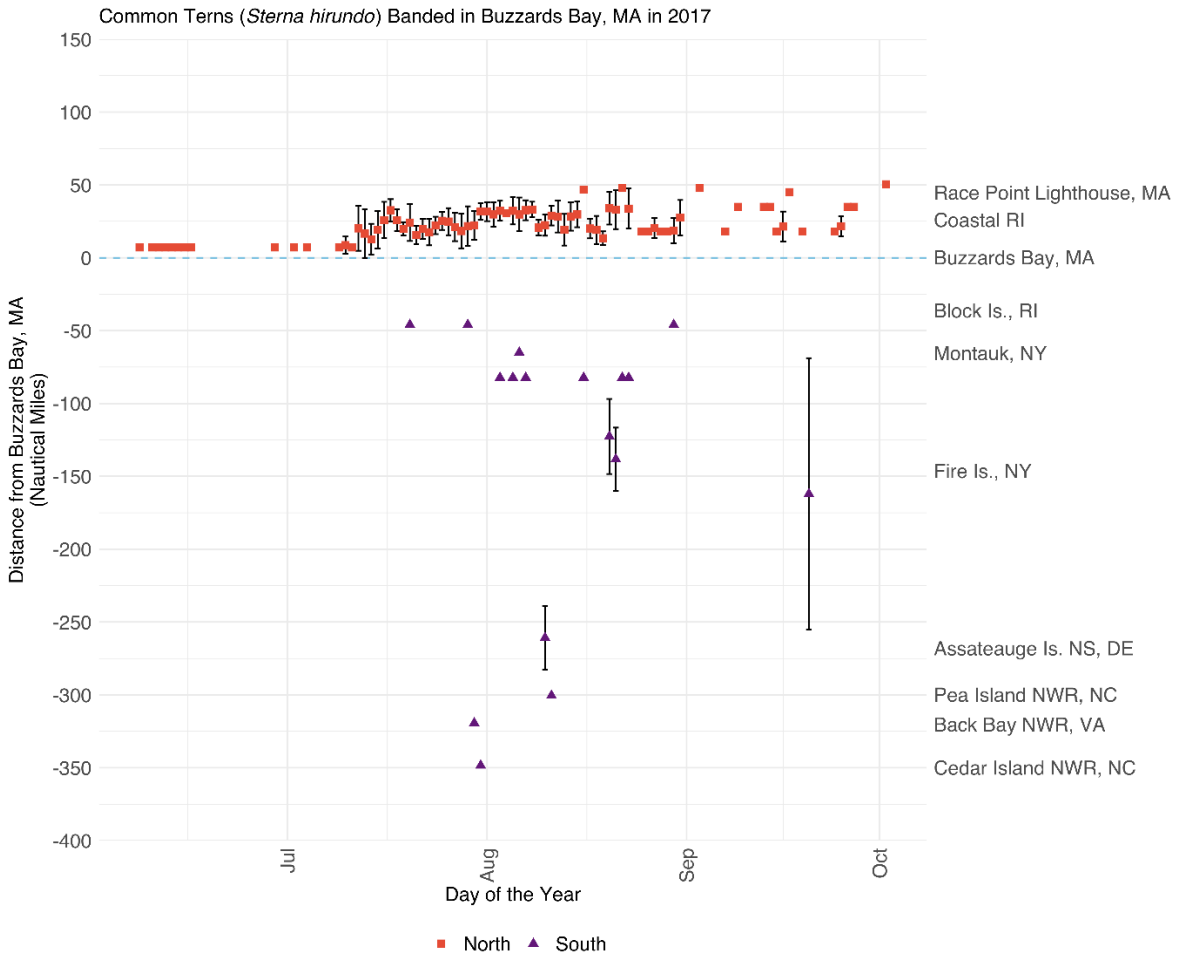

Figure 1.55. Distance traveled north (nautical miles, orange squares) or south (nautical miles, purple triangles) by Common Terns tagged at colonies in Buzzard's Bay, Massachusetts (blue dotted line) in 2017. Data are presented as mean ± standard deviation. Representative locations for a given distance from the breeding colony are to the right for context.

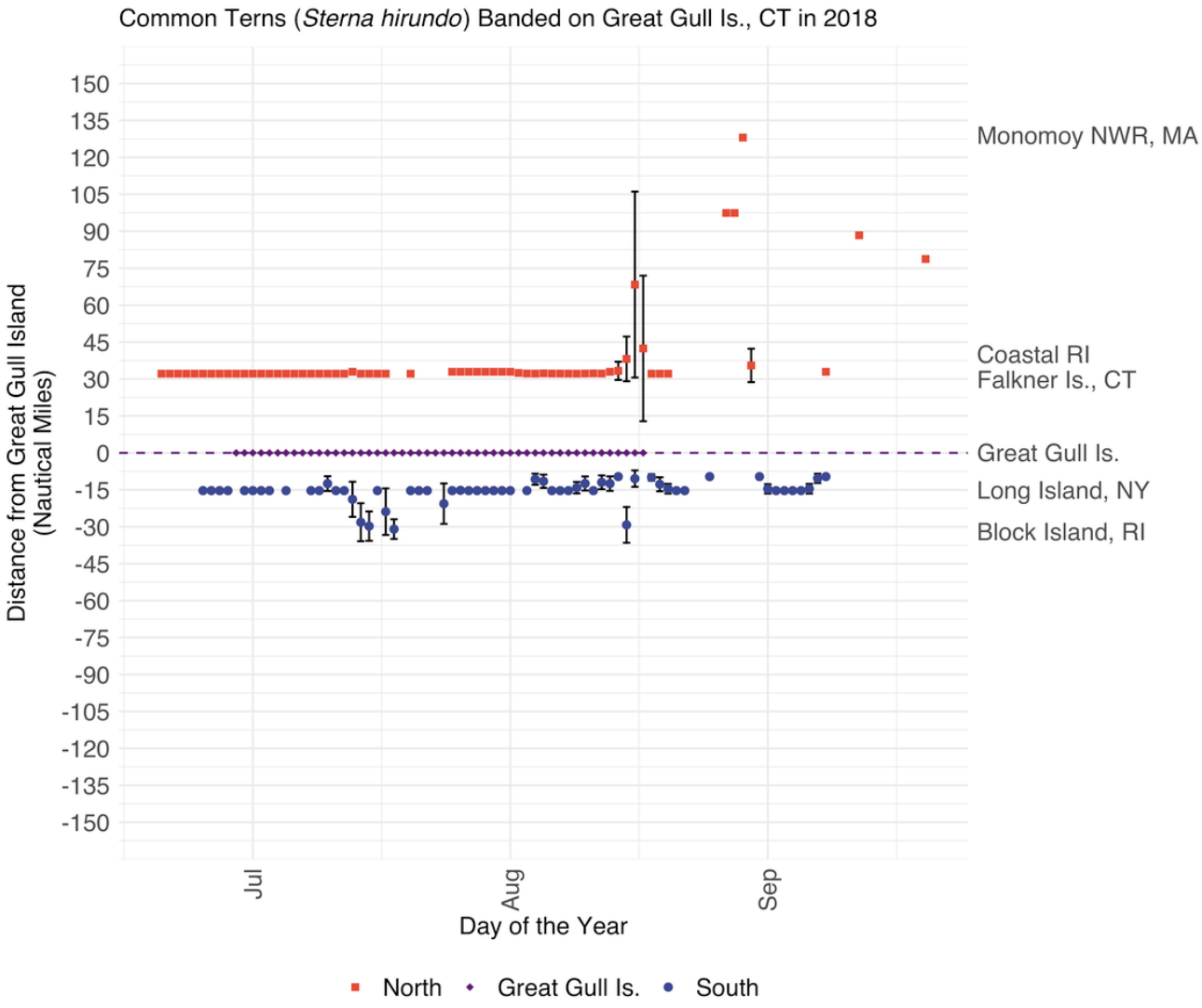

Figure 1.56. Distance traveled north (nautical miles, orange squares), south (nautical miles, blue circles) or on GGIS (purple diamonds) by Common Terns tagged on Great Gull Island, NY (purple dotted line) in 2018. Data are presented as mean ± standard deviation. Representative locations for a given distance from the breeding colony are to the right for context.

We were able to track Common Terns nesting on Falkner Island, CT in 2018 (Fig. 1.57). Unfortunately, there was a limited number of stations in Long Island Sound to track local movements of Common Terns nesting on Falkner besides Great Gull Island and Montauk. Some Common Terns nesting on Falkner regularly were detected near Great Gull Island during July into mid-August (n = 5, Table 1.11). In addition, 8 of 18 (44%) were detected as far away as Montauk, NY off the eastern end of Long Island, and 3 birds were detected off the southern shore of Block Island. There was some post-breeding dispersal of Common Tern from Falkner to Cape Cod in mid-Aug, with 4 different individuals detected at various stations on Cape Cod.

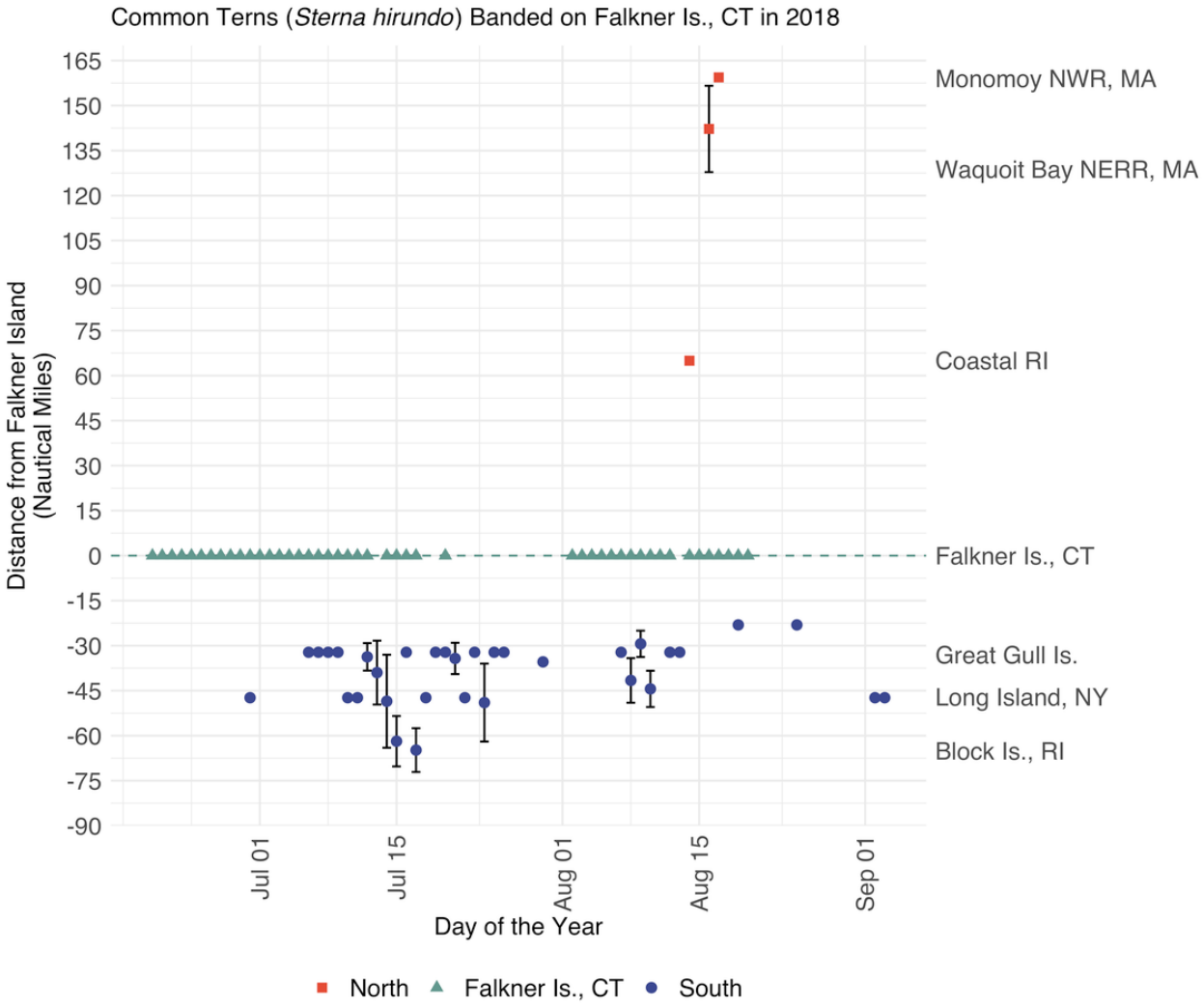

Figure 1.57. Distance traveled north (nautical miles, orange squares), south (nautical miles, blue circles) or on FALK (green triangles) by Common Terns tagged at Falkner Island, CT (green dotted line) in 2018. Data are presented as mean ± standard deviation. Representative locations for a given distance from the breeding colony are to the right for context.

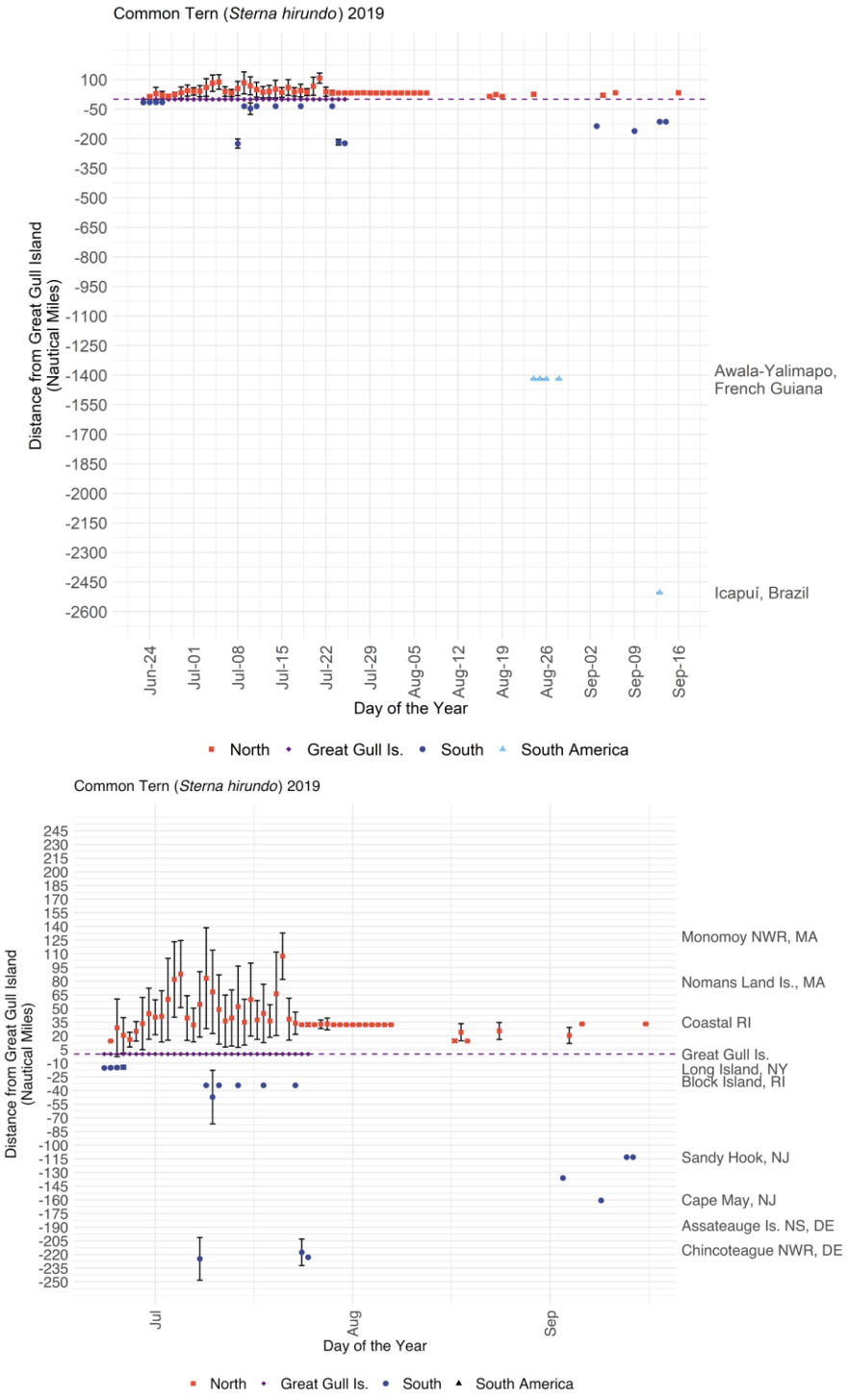

Figure 1.58. Movement chronology of Common Terns tagged on Great Gull Island, NY (purple dotted line) in 2019, with regional movements and international movements (blue triangles). Distances traveled north (nautical miles, orange squares), south (nautical miles, blue circles) or on GGIS (purple diamonds) are presented as mean ± standard deviation. Representative locations for a given distance from the breeding colony are to the right for context.

Looking at tracks of individual tagged Common Terns gives on a clearer sense of the movement patterns of this species. Individuals nesting on Great Gull Island were often detected moving throughout Long Island Sound into Nantucket Sound and then back to eastern Long Island Sound, thus not all dispersal events were focused eastward from Great Gull towards Cape Cod or sites farther north (Figures 1.59, 1.60 & 1.61).

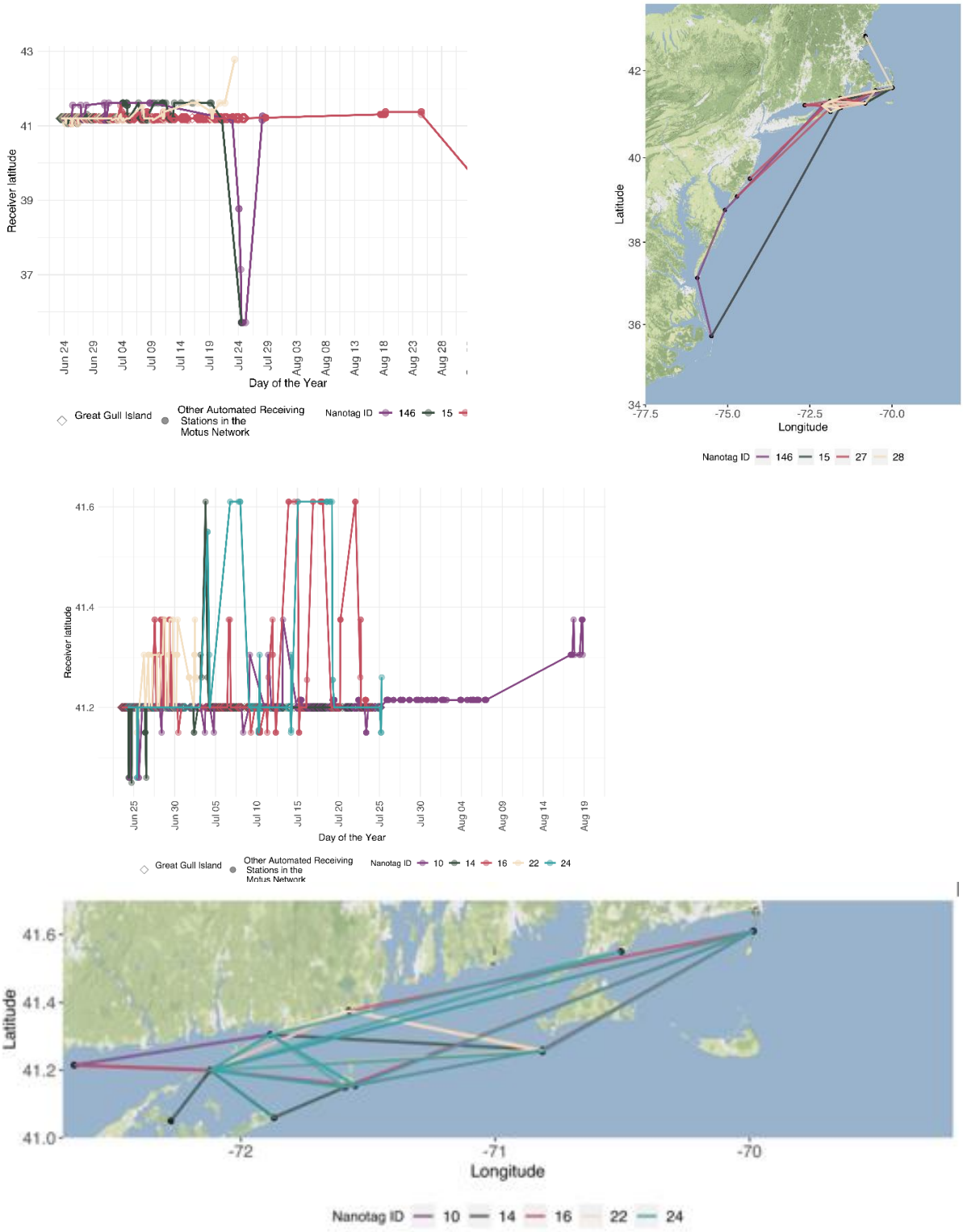

Figure 1.59. Examples of the chronology (upper panel) and spatial extent (lower panels) of regional movements of Common Terns tagged on Great Gull Island in 2019.

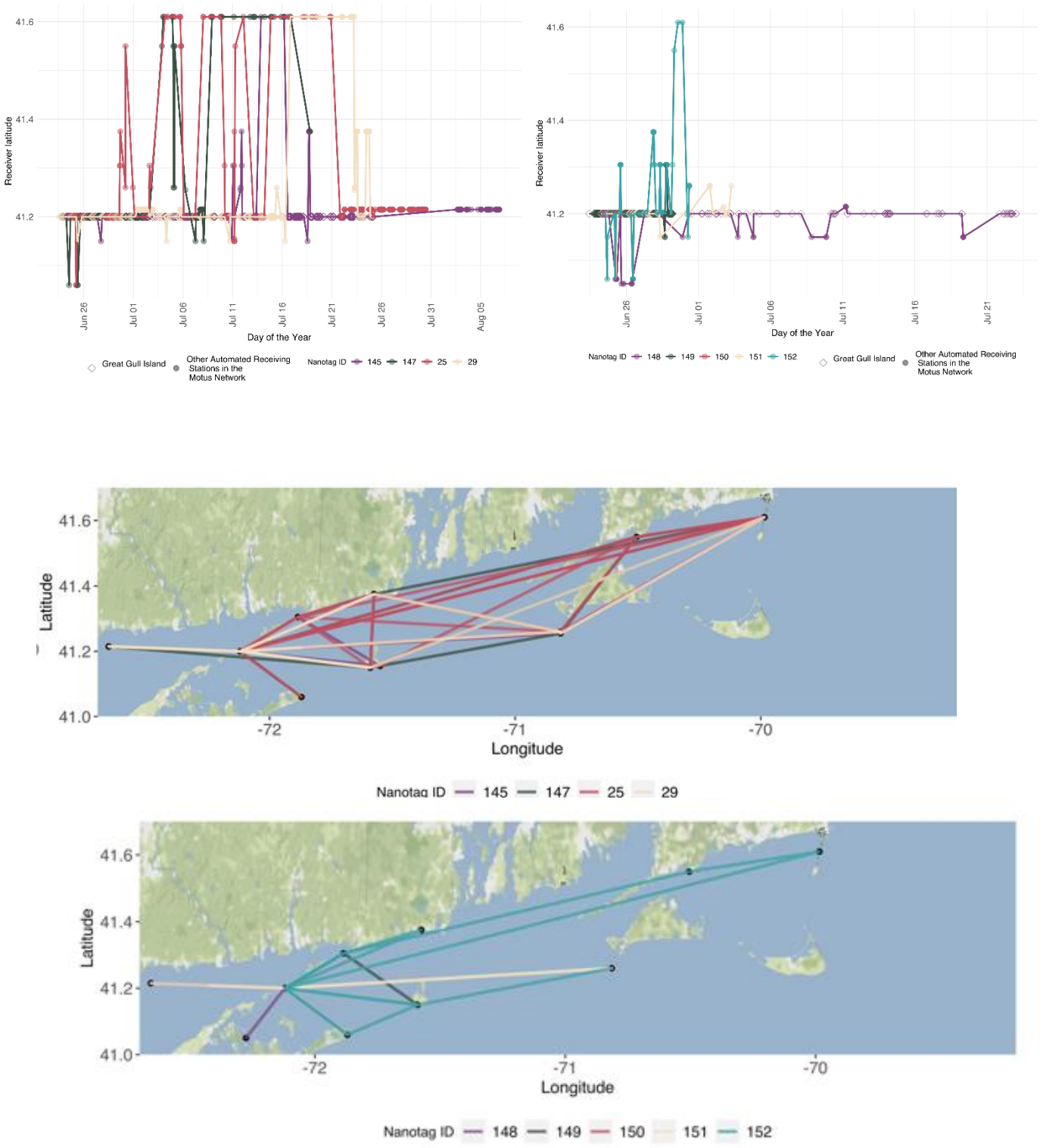

Figure 1.60. Examples of the chronology (upper panels) and spatial extent (lower panels) of regional movements of Common Terns tagged on Great Gull Island in 2019.

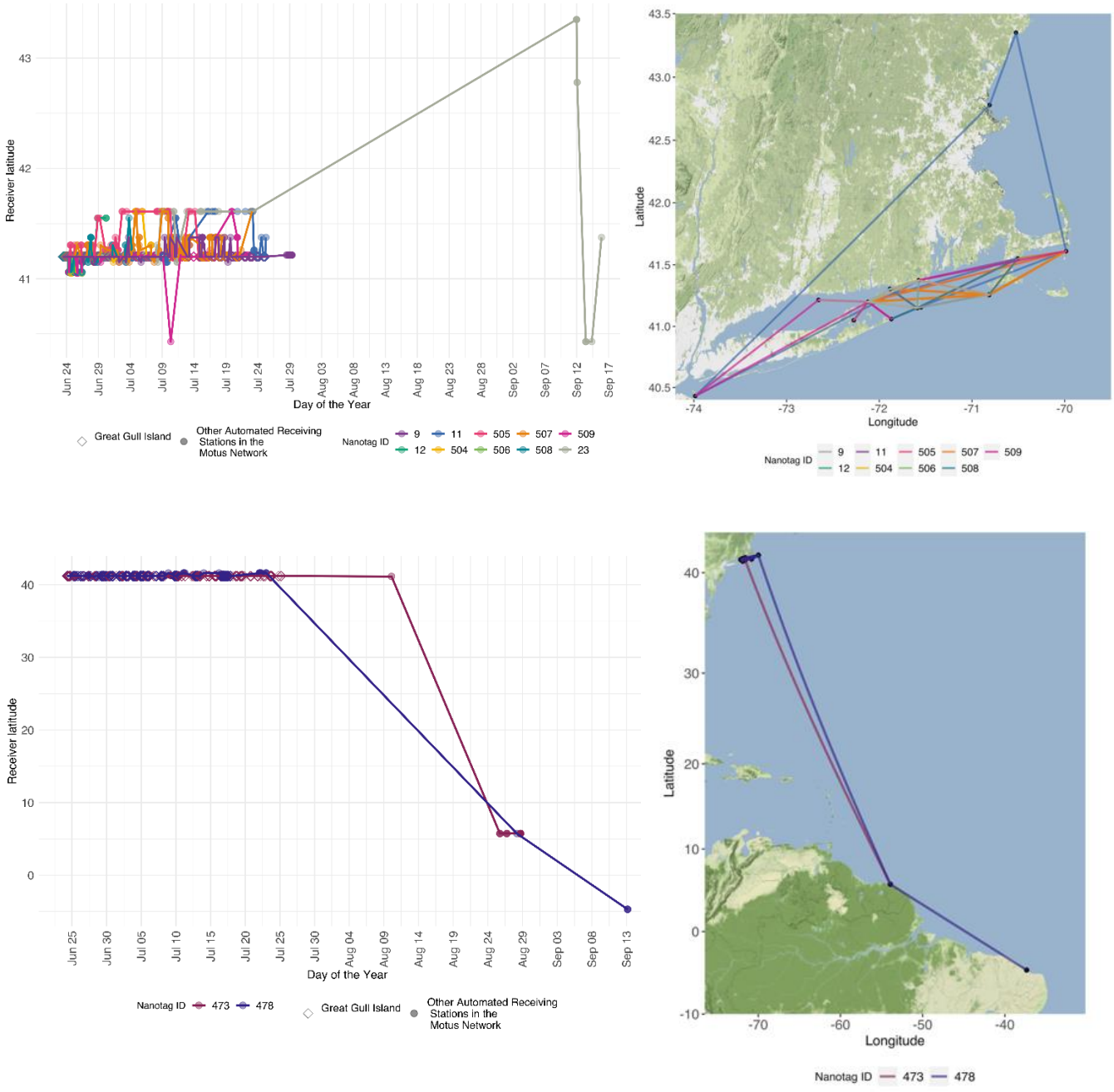

Figure 1.61. Examples of the chronology of post-breeding long-distance movements of Common Terns tagged on Great Gull Island in 2019 including to Maine (upper panel) and to northeastern South America (lower panel).

1.4.1.2 Roseate Tern regional movements

We tagged a total of 90 Roseate Terns in 2017 (Great Gull Island, NY (GGIS): 30; Bird and Ram Islands, MA: 29) and 2018 (GGIS: 20, Falkner Island, CT: 10) and made of total of 542,300 detections of 84 individuals (Table 1.12). In 2017, for birds tagged at GGIS, most detections were from Plum Island, NY (72%) or from GGIS (24%). Plum Island is located ~4 km west of GGIS and detects birds as they depart or return on GGIS, which apparently does a better job of detecting movements of this species that primarily nests under large rocks or in nest boxes where the signal is difficult to detect. Most (77%) terns from GGIS regularly flew towards Montauk, NY (MNTK), presumably to forage. Two tagged terns from GGIS spent considerable time on or near Falkner Island, CT (Falk) based on the large number of detections at Falkner, suggesting they might have dispersed from GGIS to Falkner to nest. Roseate Terns tagged in Buzzard's Bay appeared to be more likely to be detected at staging sites on Cape Cod.

Most adult Roseate Terns nesting on Great Gull Island, NY or Falkner Island, CT tended to stay on the island until early July, where there was a gradual emigration of adults from the island through early August (Figure 1.59, 1.60, 1.61). During late June through early August, adults from Great Gull and Falkner Island were regularly detected at other stations in Long Island Sound (Montauk) or Block Island Sound (Napatree), presumably to forage. There also appeared to be regular movements of some birds from Falkner to Great Gull and vice versa, although we are uncertain if it was to land on islands or forage in waters near each island (Table 1.11). In 2017, only 2 tagged adult Roseate Terns were detected during the post-breeding season by stations on Cape Cod or the islands (Nantucket or Martha's Vineyard). In contrast, Roseate Terns nesting on Bird and Ram Island, MA were regularly detected at stations at Cape Cod and the islands from mid- July through 20 Sept (Table 1.11).

Table 1.12. Total number of detections (det) and tagged individual (tags) for Roseate Terns detected from 2017 to 2019. Data are separated by year and banding location (either near Monomoy NWR in Massachusetts or coastal Rhode Island (RI). Station descriptions are given in Table 1.2.

		Number of detections				Number of tagged birds			
		2017	2018	2017	2018	2017	2018	2017	2018
						N=30		N=30	N=10
Latitude	Station	GGIS	GGIS	Mass	Falk	GGIS	GGIS	Mass	Falk
41.148	**BIBR**		**342**		**800**		**7**		**3**
41.307	CTPT		4897	890			5	9	0
41.213	FALK		53,275		77989		2		10
41.202	GGIS	30,638	249,534	433	1509	28	20	2	6
41.391	GTPT	5	638	2088	70	1	5	13	3
41.052	MASH		36				3		0
41.059	MNTK	5311	2577	27	281	23	17	1	4
41.609	MNYN		271	100	4		5	6	1
41.553	MNYS		541	884	58		4	11	1
41.337	MUSK	13		3850		2		22	
41.306	NAPA			53	5			2	1
41.261	NOMA			4960				17	
41.253	NOMS		99				1		0
41.288	OSCT				10				1
41.189	PLIS	93,859		720		29		7	
42.066	RCPT			2079				5	
41.479	SACH		148				3		
41.153	**SELI**	**88**	**23**		**30**	**2**	**1**	**0**	**1**
41.373	TRUS	121	77	50	16	3	1	2	2
41.552	WAQT	63	1048	1547	40	2	6	22	1
41.681	WING	11	56	136		1	1	1	
Overall		130,109	313,562	17,817	80,812	29	20	25	10

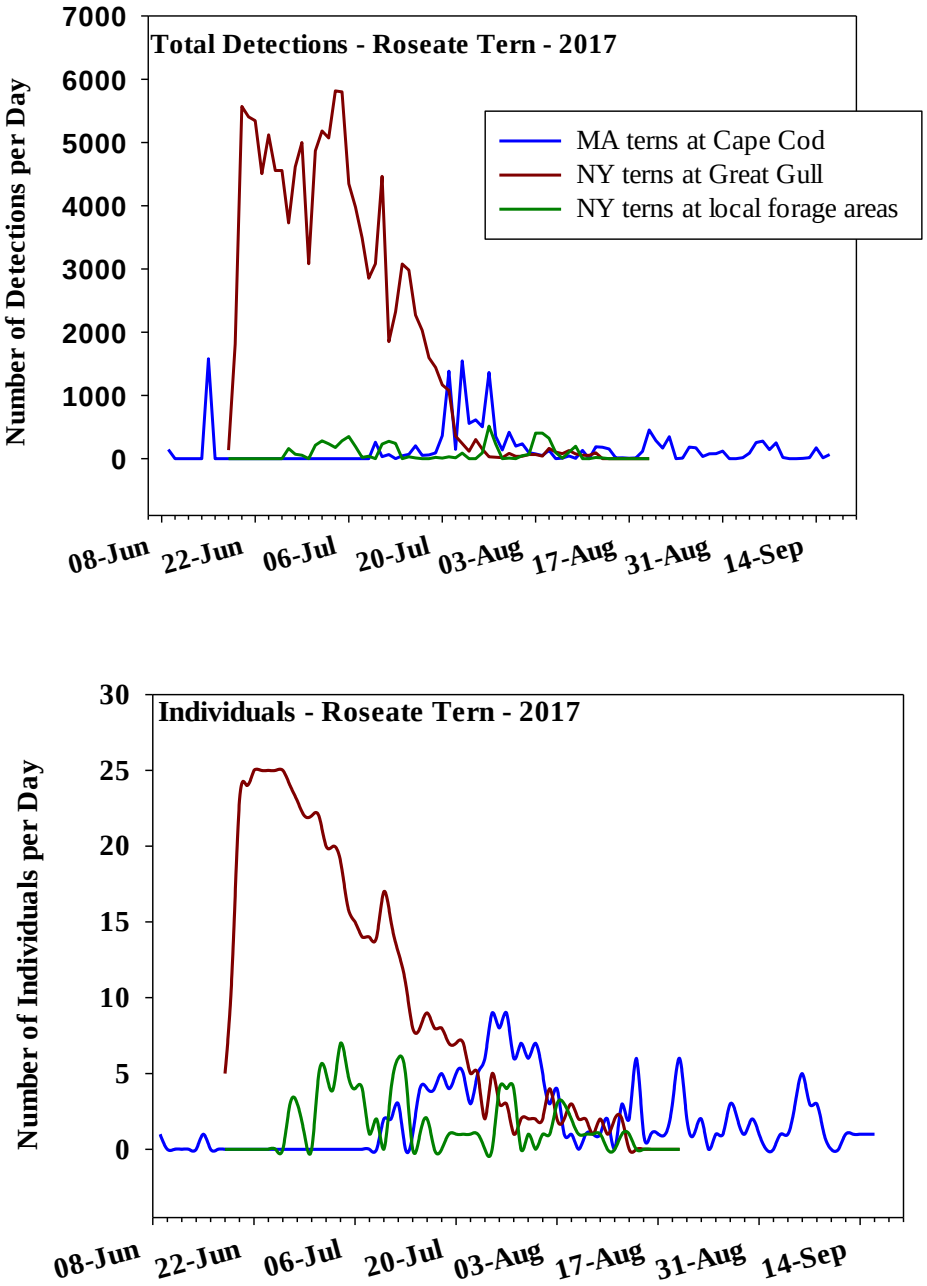

Figure 1.62. Movement chronology of Roseate Terns tagged at Great Gull Island, NY (NY terns) and colonies in Buzzard's Bay, MA (MA terns) in 2017. Shown are the total number of detections (upper panel) and number of individual tagged terns (lower panel).

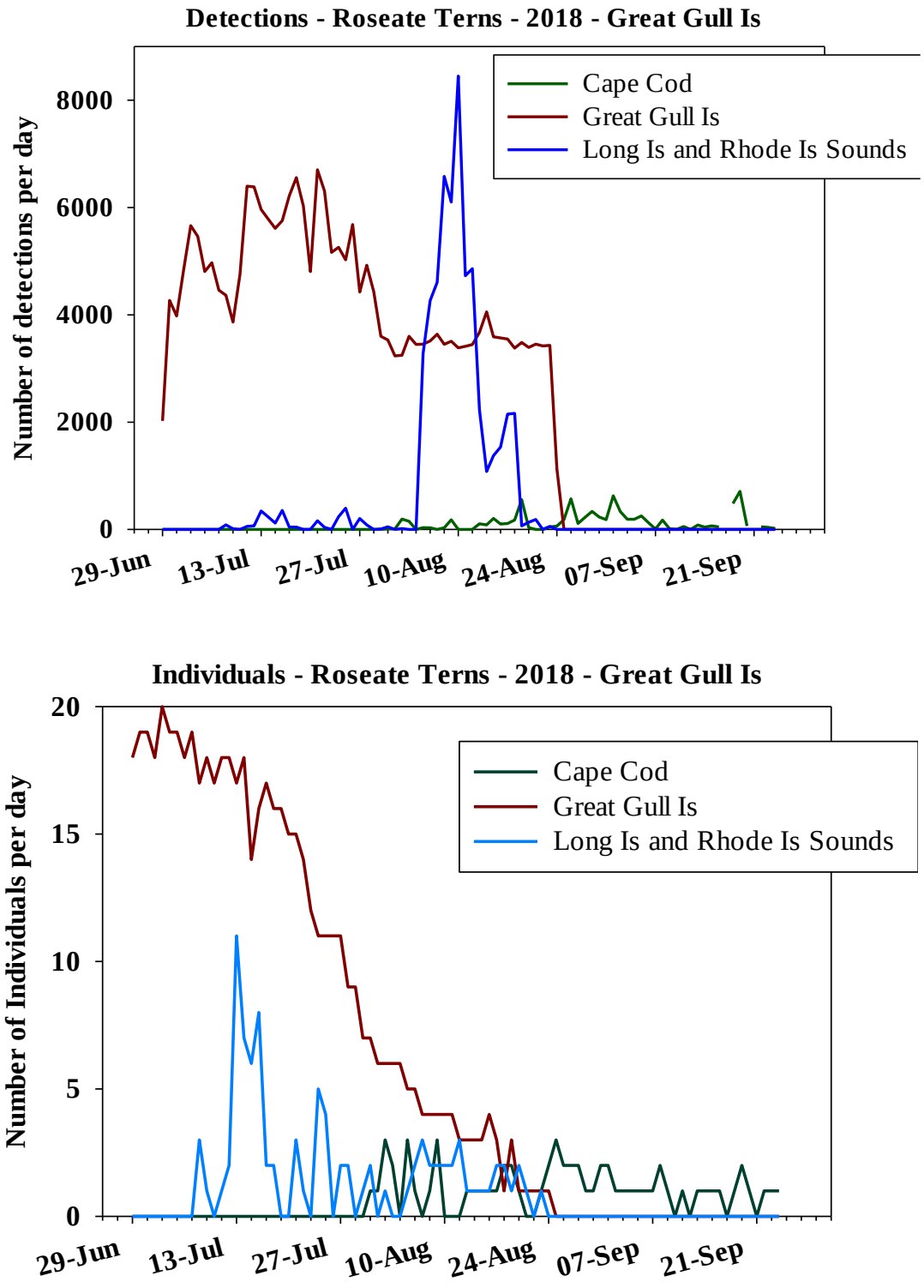

Figure 1.63. Movement chronology of Roseate Terns tagged at Great Gull Island, NY in 2018. Shown are the total number of detections (upper panel) and number of individual tagged terns (lower panel). Terns were detected by stations at Great Gull Is, elsewhere in Long Island and Rhode Island sounds, or at Cape Cod and adjacent islands.

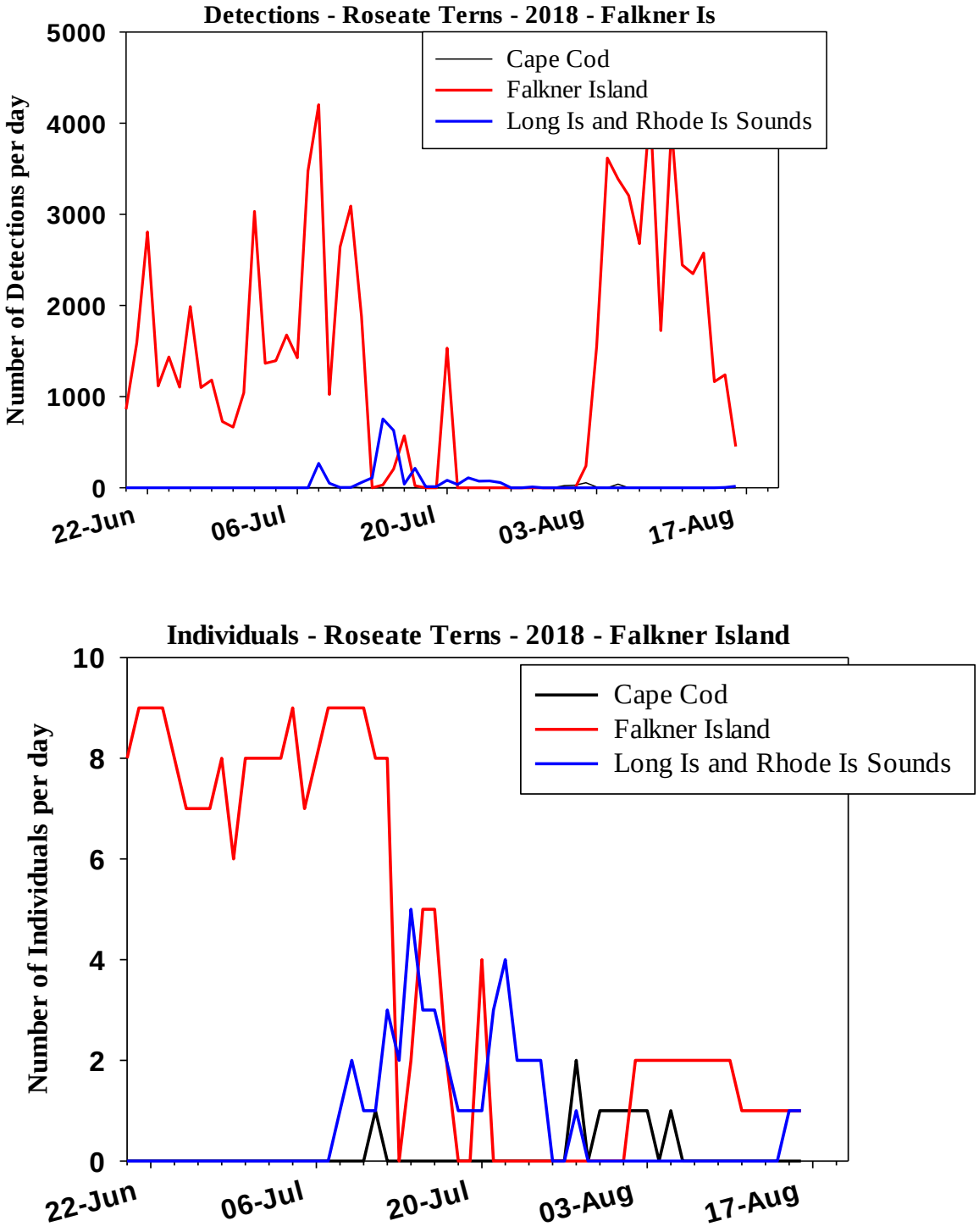

Figure 1.64. Movement chronology of Roseate Terns tagged at Falkner, NY in 2018. Shown are the total number of detections (upper panel) and number of individual tagged terns (lower panel). Terns were detected by stations at Great Gull Is, elsewhere in Long Island and Rhode Island sounds, or at Cape Cod and adjacent islands.

Looking at a more detailed assessment of the movements of Roseate Terns throughout the region, several patterns emerge. First, Roseate Terns nesting on Great Gull Island regularly flew toward Montauk, NY at the east tip of Long Island in 2017 (Fig. 1.62) and 2018 (Fig. 1.64). Second, there were occasional movements of Roseate Terns to coastal Rhode Island from Great Gull Island in 2017 but less evidence in 2018 when the station at Napatree was inactive. Adults from Great Gull Island regularly visited Falkner Island, CT farther to the west and north in Long Island Sound. Finally, some birds from Great Gull Island visited staging sites on Cape Cod from mid-Aug through Sept (Fig. 1.62 and 1.64).

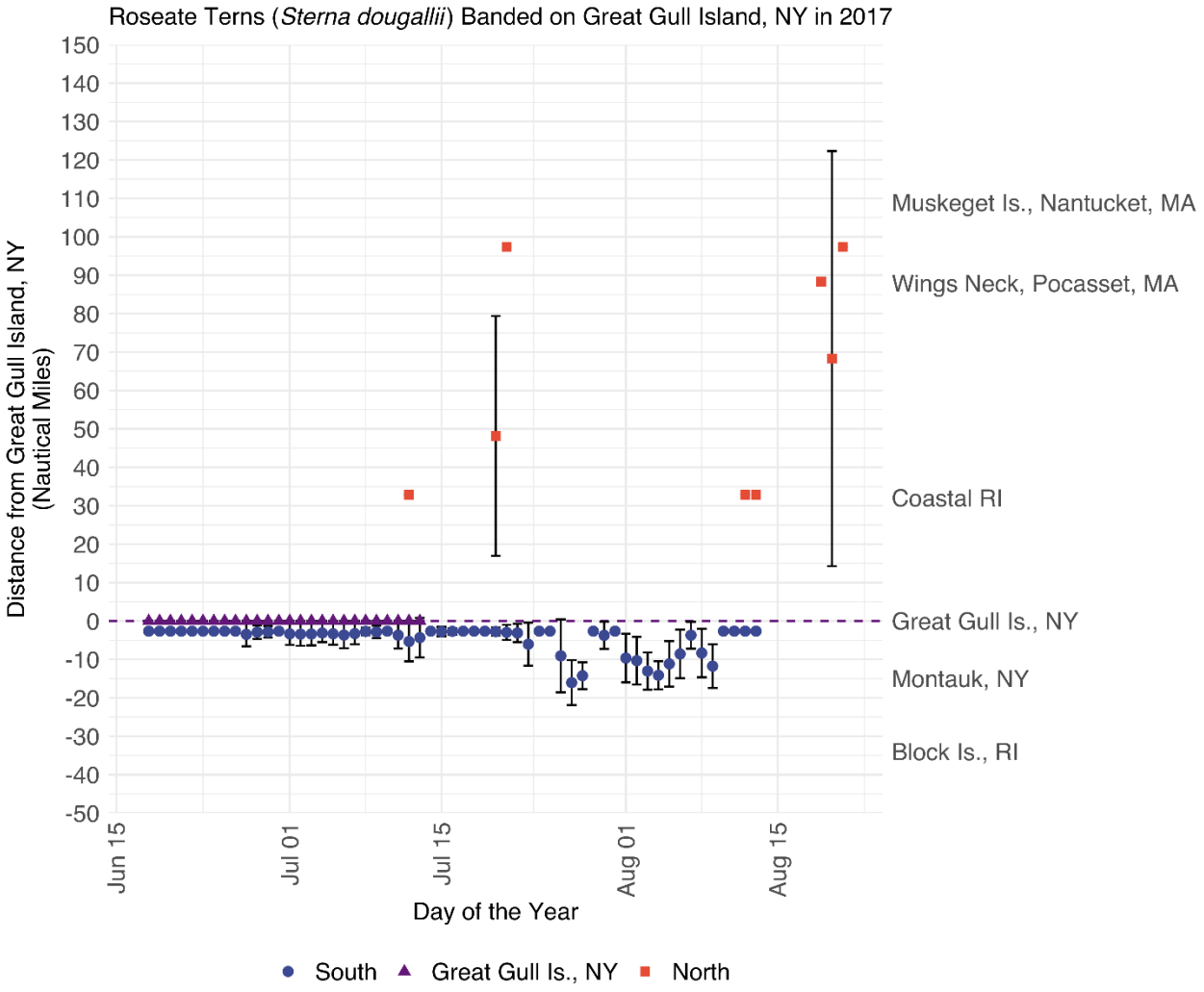

Figure 1.65. Movement chronology of Roseate Terns tagged at nesting colony on Great Gull Island, NY in 2017.

Roseate Terns nesting in colonies in Buzzard's Bay, MA tended to disperse to the Nantucket Sound and Cape Cod from mid-July to mid-Sept (Fig. 1.66). Some birds ventured as far north as Race Point, but most tended to use areas between Waquoit Bay and Monomoy NWR. Occasionally some Roseate Tern during the post-breeding season explored eastern Long Island Sound in the Great Gull Island – Montauk area.

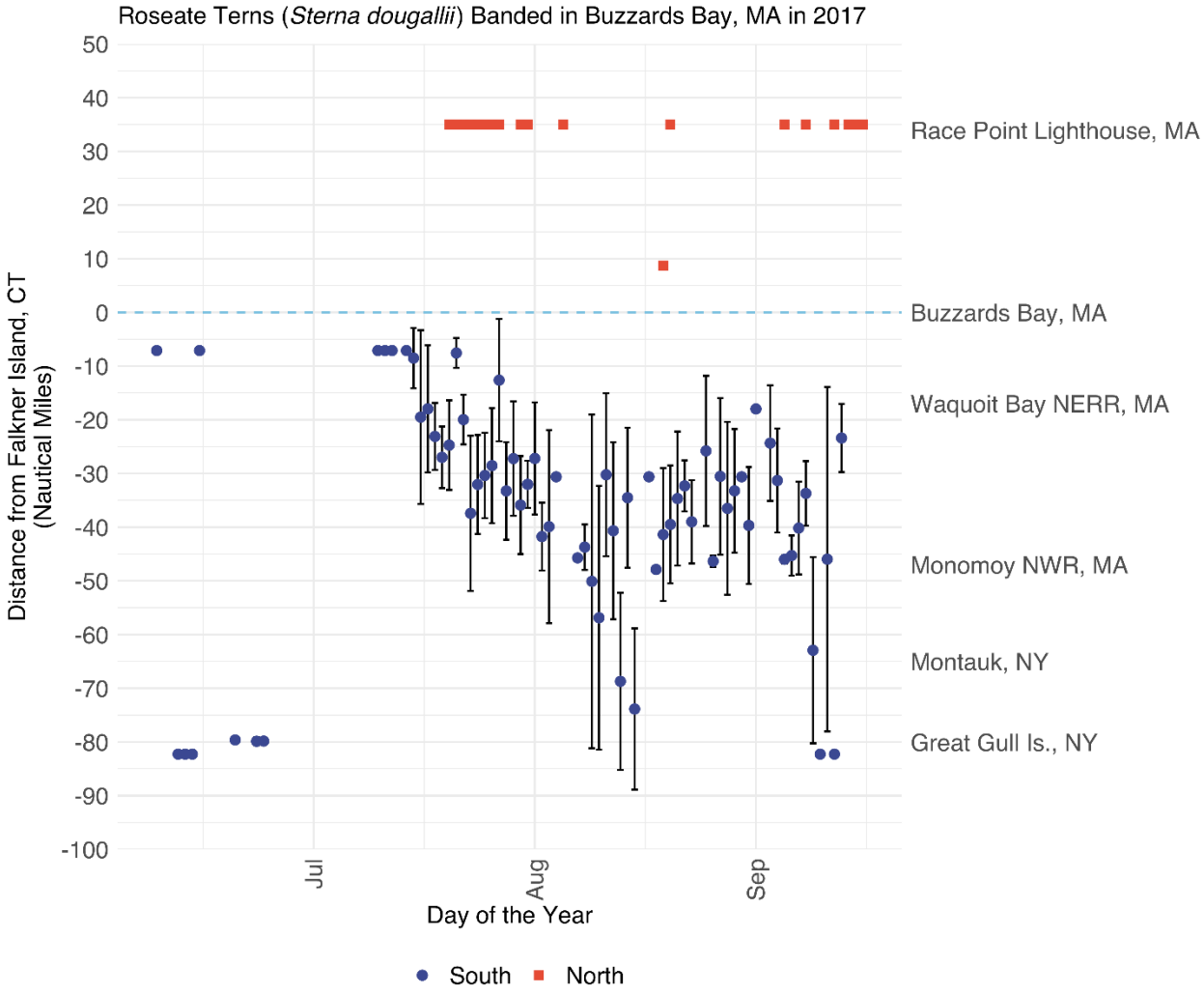

Figure 1.66. Movement chronology of Roseate Terns tagged at nesting colonies in Buzzard's Bay, MA in 2017.

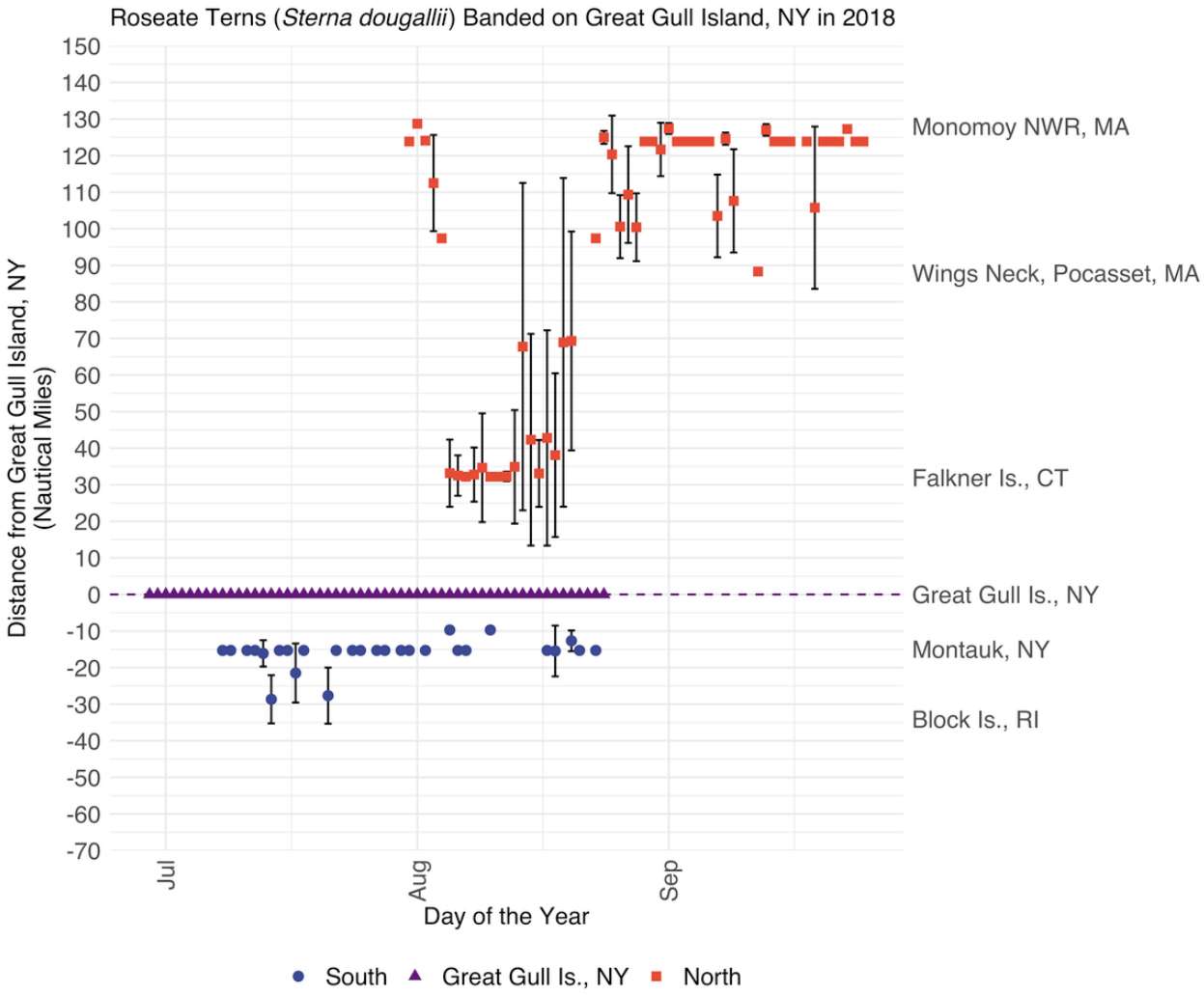

Figure 1.67. Movement chronology of Roseate Terns tagged at nesting colony on Great Gull Island, NY in 2018.

The movement chronology of adult Roseate Terns nesting on Falkner Island, CT was like Great Gull Island, NY (Fig. 1.68). Some birds regularly were detected at Great Gull Island, which is about 30 miles southeast of Falkner throughout the chick rearing period into the middle of Aug. Starting early Aug, which is when adults emigrate from nesting colonies with their chicks, birds from Falkner were detected in Nantucket Sound through the end of Sept, presumably staging at key stopover sites before initiating their migration to South America (Althouse et al. 2019)

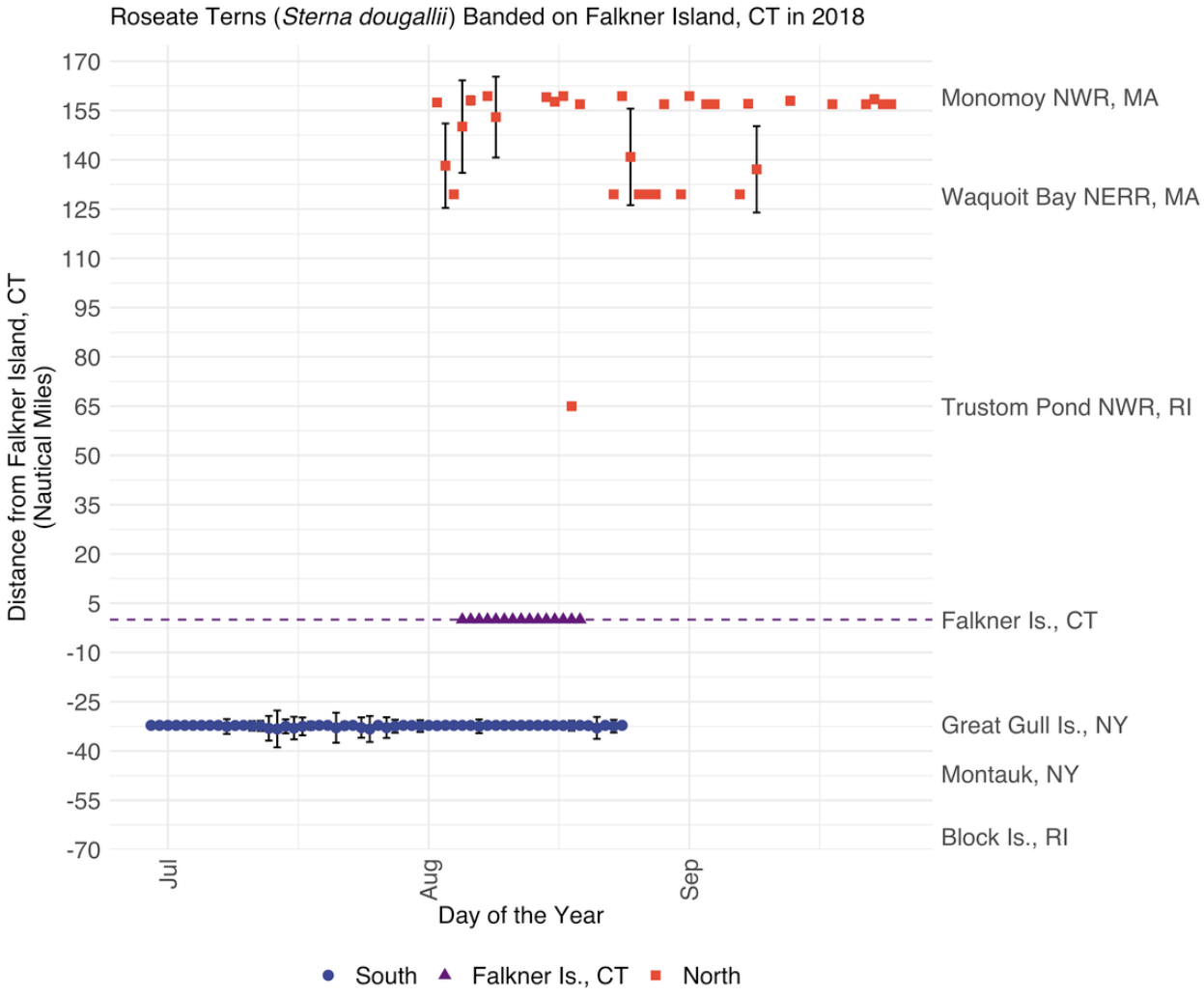

Figure 1.68. Movement chronology of Roseate Terns tagged at nesting colony on Falkner Island, CT in 2018.

The movements on individual tagged Roseate Terns gives a different perspective to their regional movement patterns (Fig. 1.69 to 1.71). Roseate Tern movements appeared to be much more directed, and they appeared to be less likely to fly from their nesting colony in Long Island Sound towards Cape Cod (Fig. 1.69) and then return back to Great Gull, as Common Terns regularly did (e.g. Figs. 1.61 and 1.62). Roseate Terns often were detected flying between Great Gull Island and Montauk, NY (Fig 1.69 and 1.73). Birds nesting in Buzzard's Bay occasionally dispersed westward, but it appeared to be uncommon (Fig. 1.70, 1.72). However, Roseate Terns from Buzzard's Bay appeared to regularly move throughout Nantucket Sound, presumable to various foraging and staging sites.

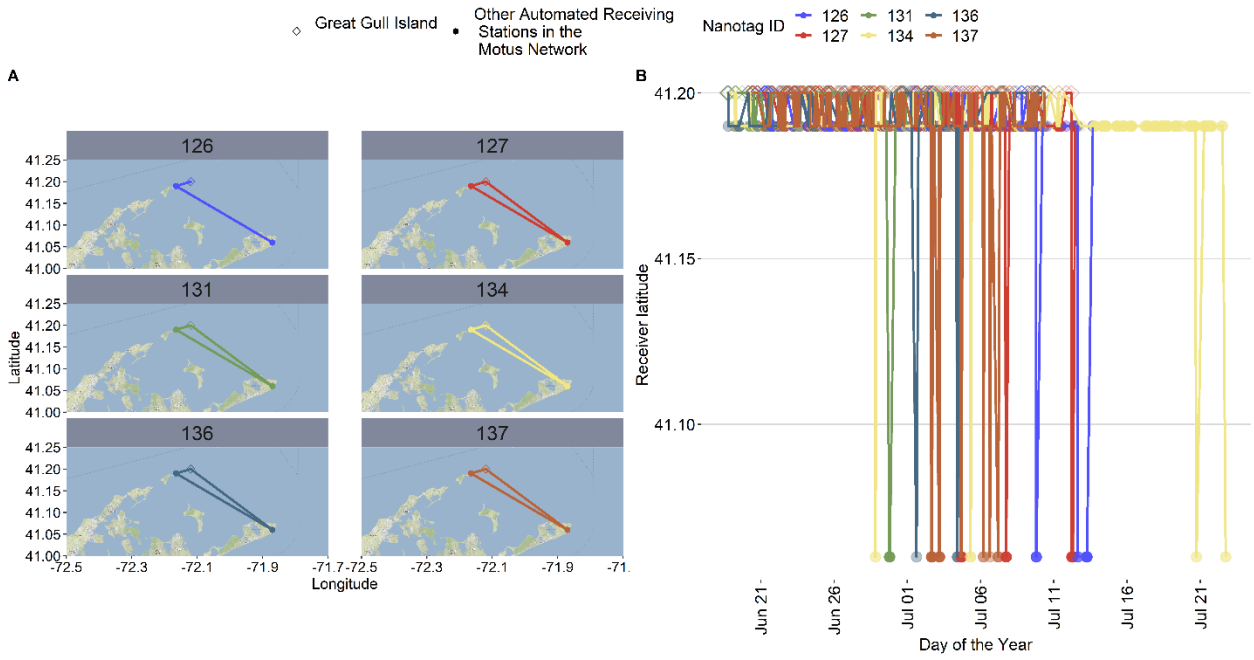

Figure 1.69. Examples of movement chronology throughout Long Island Sound of Roseate Terns tagged on Great Gull Island, NY in 2017. A) Map depicting tag movements from Great Gull Island to other automated receiving stations in the Motus Network. Each panel shows the track of a given tag. Points represent the tower locations. B) Latitude of the automated receiving station where each nanotag was detected over time. Colors represent individual movements.

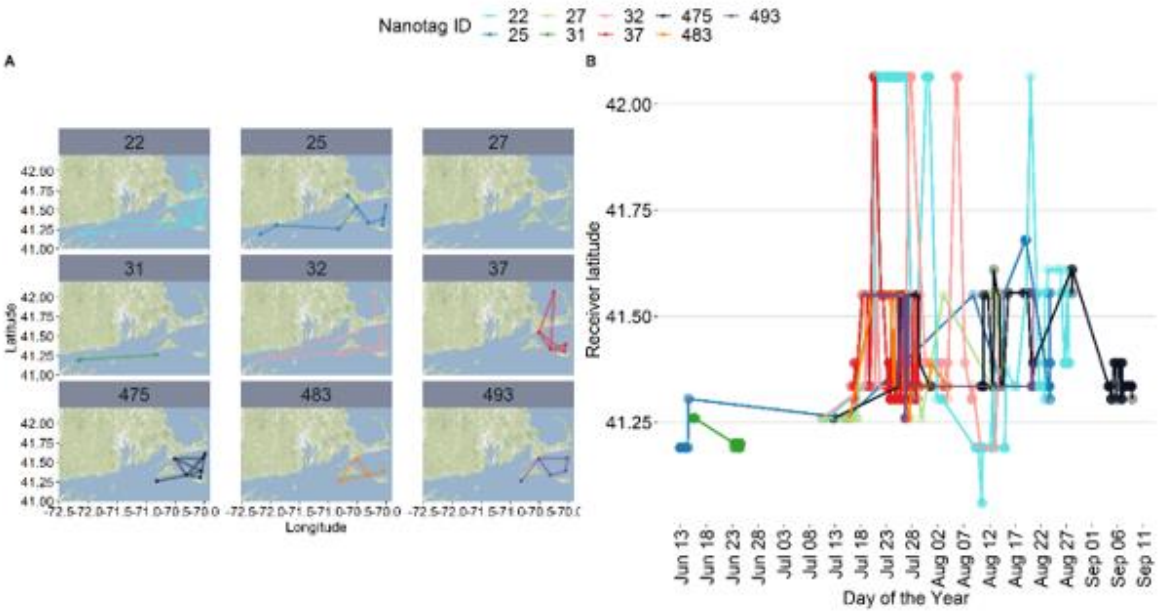

Figure 1.70. Examples of movement chronology throughout southern New England of Roseate Terns tagged on colonies in Buzzard's Bay in 2017. A) Map depicting Roseate Tern movements throughout southern New England. Each panel shows the track of a given tag. Points represent the tower locations. B) Latitude of the automated receiving station where each nanotag was detected over time. Colors represent individual movements.

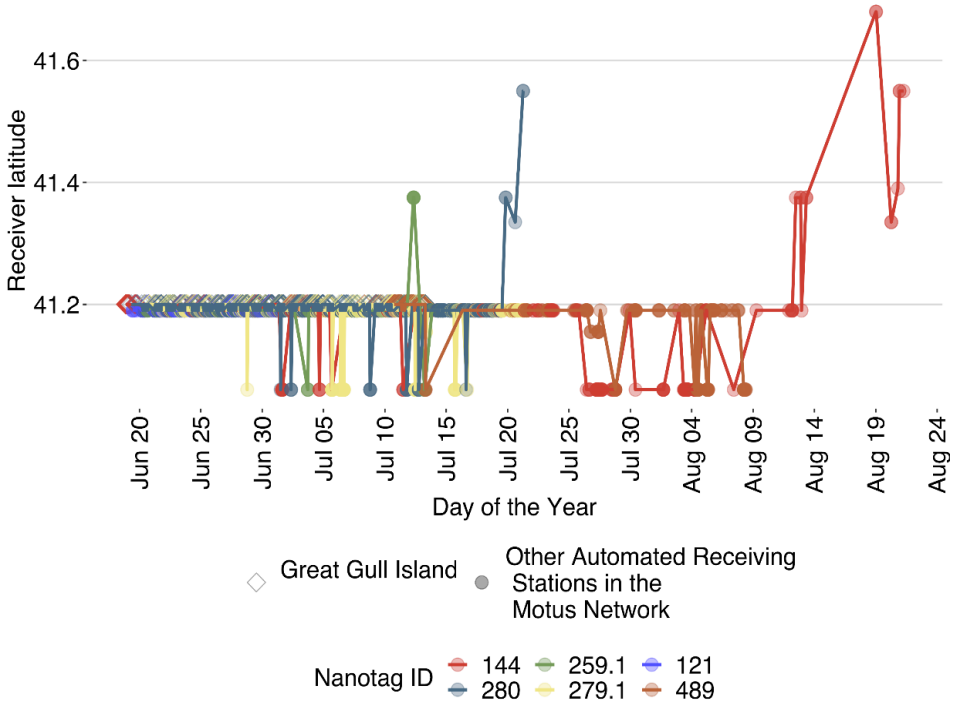

Figure 1.71. Examples of movement chronology throughout southern New England of Roseate Terns tagged on Great Gull Island in 2017.

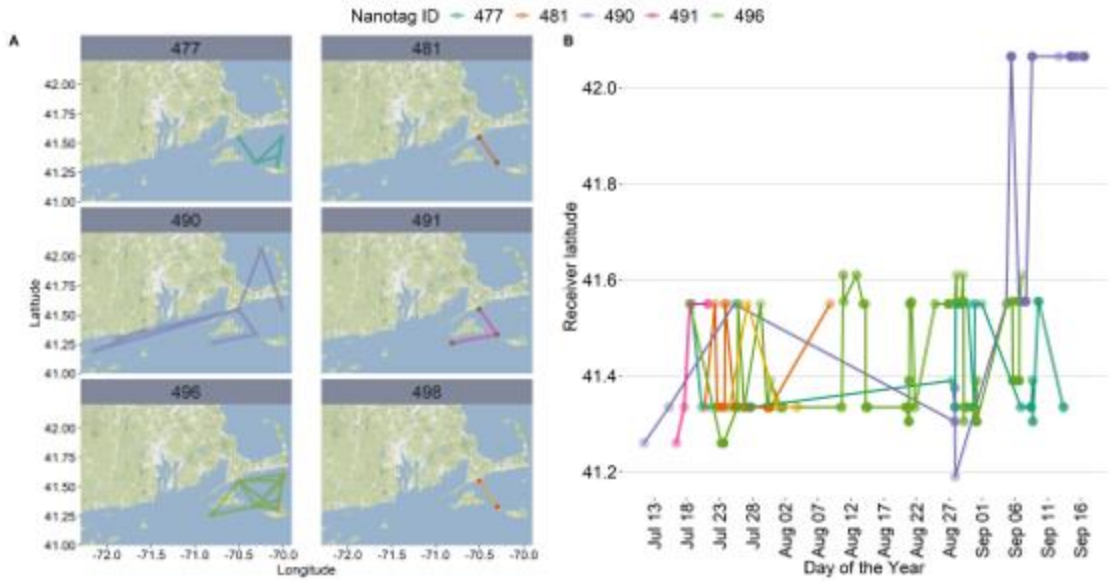

Figure 1.72. Examples of movement chronology throughout southern New England of Roseate Terns tagged on colonies in Buzzard's Bay in 2017. A) Map depicting Roseate Tern movements throughout southern New England. Each panel shows the track of a given tag. Points represent the tower locations. B) Latitude of the automated receiving station where each nanotag was detected over time. Colors represent individual movements.

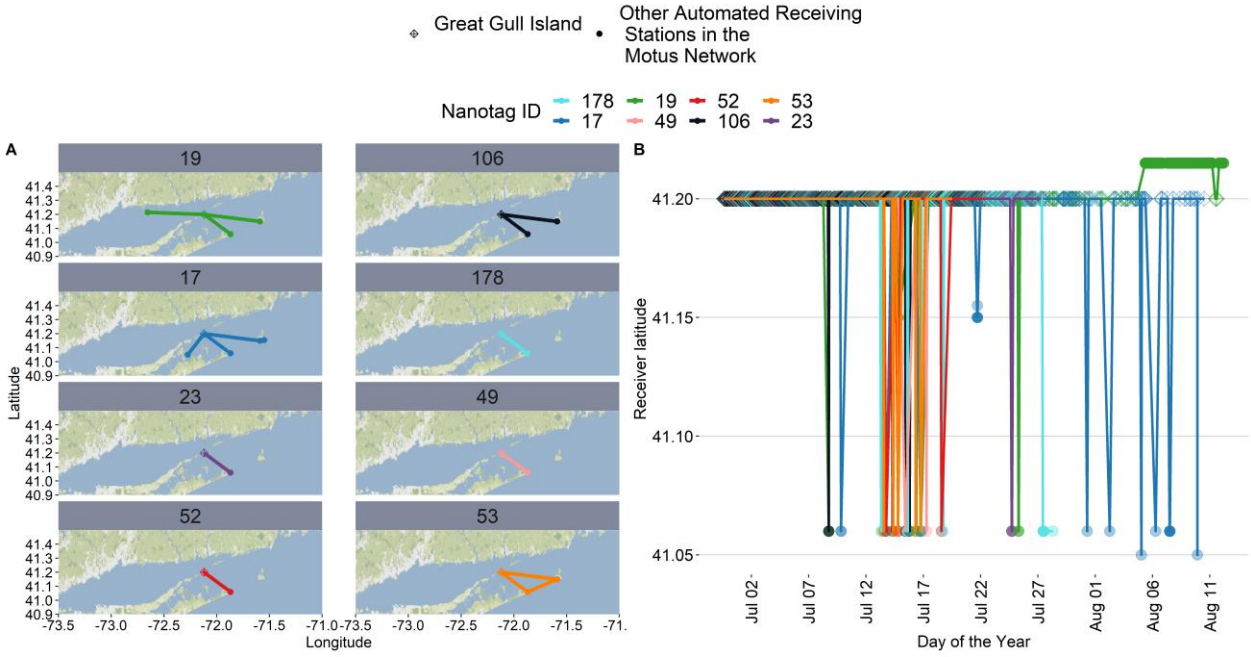

Figure 1.73. Examples of Roseate Terns tagged on Great Gull Island, NY in 2018 that were only detected by GGIS and nearby automated receiving stations. A) Map depicting Roseate Tern movements in southern New England. Each panel shows the track of a given tag. Points represent the tower locations. B) Latitude of the automated receiving station where each nanotag was detected over time. Colors represent individual movements.

1.4.1.3. Piping Plover regional movements

We tracked a total of 78 Piping Plovers including 20 tagged near Monomoy NWR, MA in 2017, and 58 in coastal Rhode Island (20, 20, and 18 from 2017 – 2019, respectfully (Table 1.13).

Table 1.13. Total number of detections (det) and tagged individual (tags) for Piping Plovers detected from 2017 to 2019. Data are separated by year and banding location (either near Monomoy NWR in Massachusetts (Mass) or coastal Rhode Island (RI).

		Mass 2017 N=20		**RI 2017 N=20**		**RI 2018 N=20**		**RI 2019 N=18**		**Overall**	
Latitude	**Station**	**Det**	**Tags**	**Det**	**Tags**	**Det**	**Tags**	**Det**	**Tags**	**Det**	**Tags**
34.957	CEDI	22	1	40	2					62	3
35.717	PEAI	50	3	237	1	746	5	139	3	1172	12
36.672	BBVA	74	4	69	4					143	8
37.134	SKID	149	5	183	4	187	2	219	2	738	13
37.574	PARR					78	3			78	3
38.241	ASSA	5	1	31	1	18	1			54	3
38.770	CHDE	8	1	104	3	32	2	75	1	219	7
39.028	DADS			24	2					24	2
39.053	NORB			65	1					65	1
39.429	NBNJ	39	2	173	4					212	6
40.430	SHNJ	22	1					8	1	30	2
40.574	CONY			9	1					9	1
40.633	FRIS			26	2	21	1	239	3	47	3
41.052	MASH					469	8			469	8
41.059	MNTK			219	10	990	10			1209	20
41.148	**BIBR**					**592**	**5**	**17**	**2**	**609**	**7**
41.153	**SELI**	**43**	**3**	**82**	**7**			**8**	**1**	**133**	**11**
41.189	PLIS			550	12					550	12
41.202	GGIS					19	1			258	4
41.261	NOMA	65	2							65	2
41.306	NAPA					3655	2	13667	5	17322	7
41.307	CTPT	827	13							827	13
41.337	MUSK	527	15							627	15
41.373	TRUS			124089	9	184061	13	17934	8	326084	28
41.391	GTPT	641	13							641	13
41.479	SACH										
41.552	WAQT	244	8							244	8
41.553	MNYS	708	3							708	3
41.609	MNYN	353	12							353	12
	OVERALL	3877	16	125901	20	190917	17	32306	13	353001	67

The Motus and Block Island networks detected 67 (86%) of tagged individuals, with a cumulative total of >350,000 detections. The station with 92% of all detections was Trustom Pond NWR, where we tagged many of the plovers and there was a station close to the primary foraging and nesting beach. The two Block Island Network stations (Black Rock (BIBR) and Southeast Lighthouse (SELI) had 7 and 11 individuals, respectively, detected (Table 1.12).

At nesting beaches, adult Piping Plovers tended to remain in the nesting areas until early July when birds-initiated emigration to areas farther south (Fig. 1.74). There appeared to be an influx of adults to nesting areas in early to mid-July, which presumably was pre-migration staging movements of adults (Fig. 1.74). We documented a rapid decline in the number of adults at nesting sites by mid-July, with some stragglers remaining until late August.

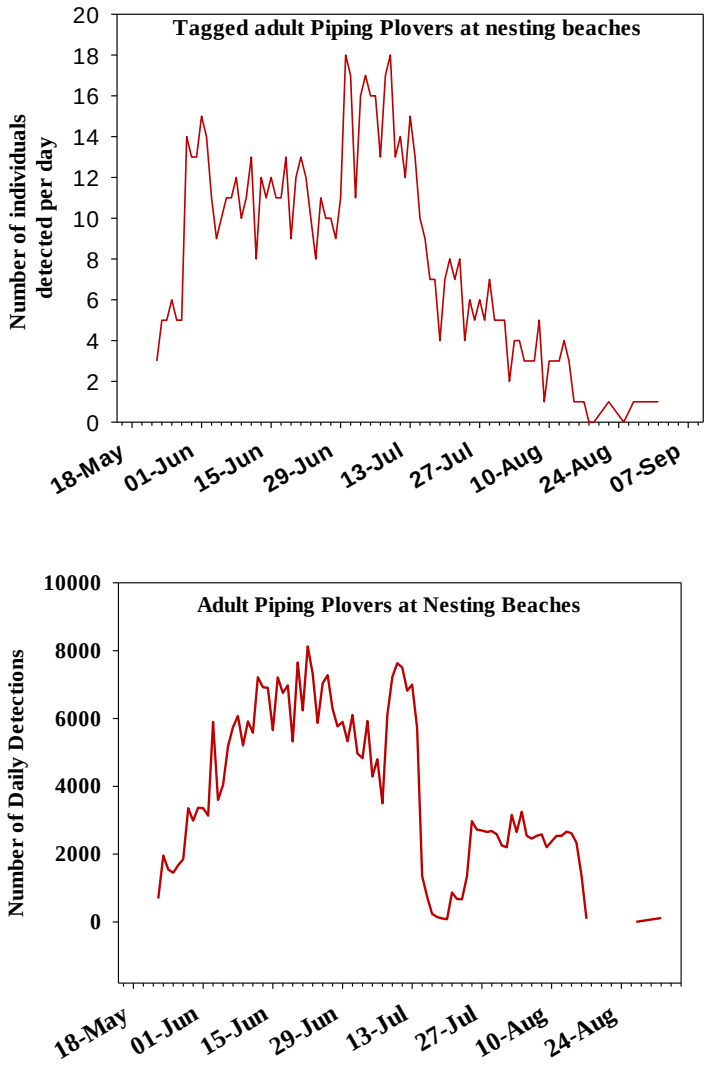

Figure 1.74. Movement phenology of tagged adult Piping Plovers near nesting beaches based on daily detection rates of tagged individuals (upper panel) and the total number of detections (lower panel) at automated radio telemetry station located at Napatree (NAPA) and Trustom NWR (TRUS), RI, and Monomoy (MNYS and MNYN), MA from 2017-2019.

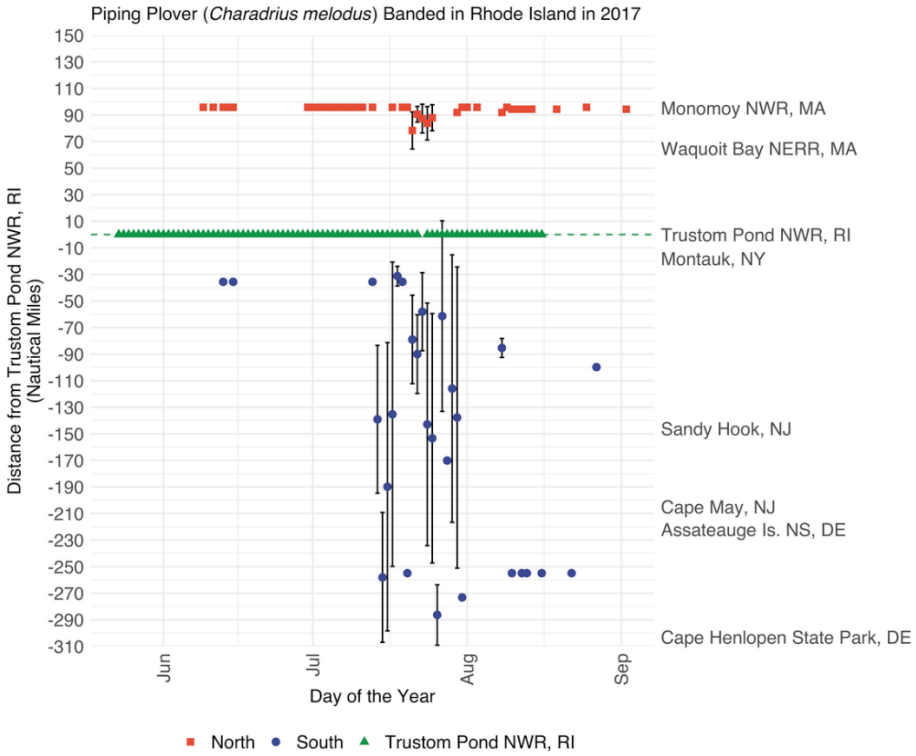

Figure 1.75. Movement chronology of adult Piping Plover nesting in coastal Rhode Island and near Monomoy NWR, MA in 2017.

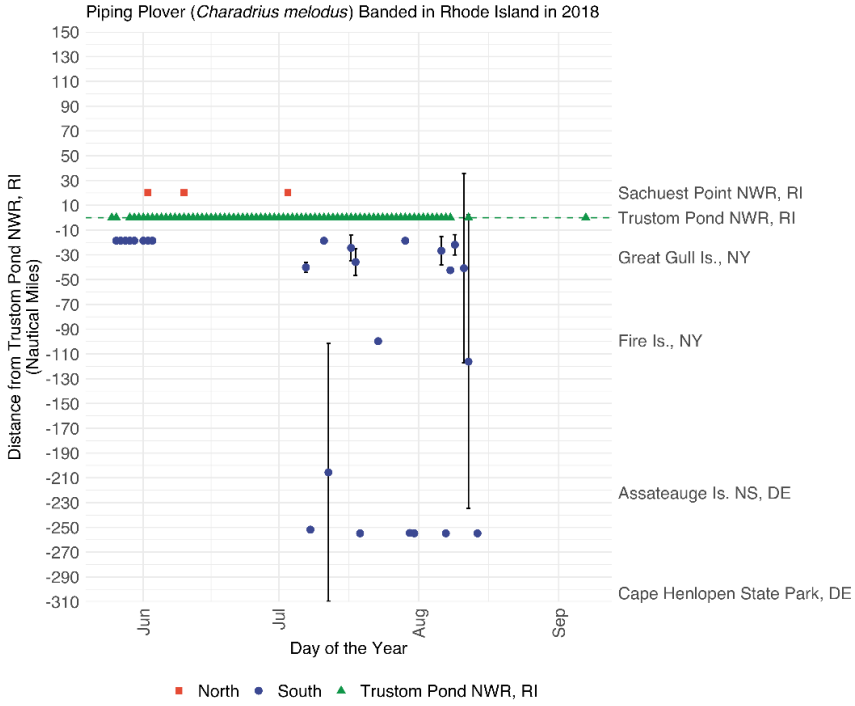

Figure 1.76. Movement chronology of adult Piping Plover nesting in coastal Rhode Island in 2018.

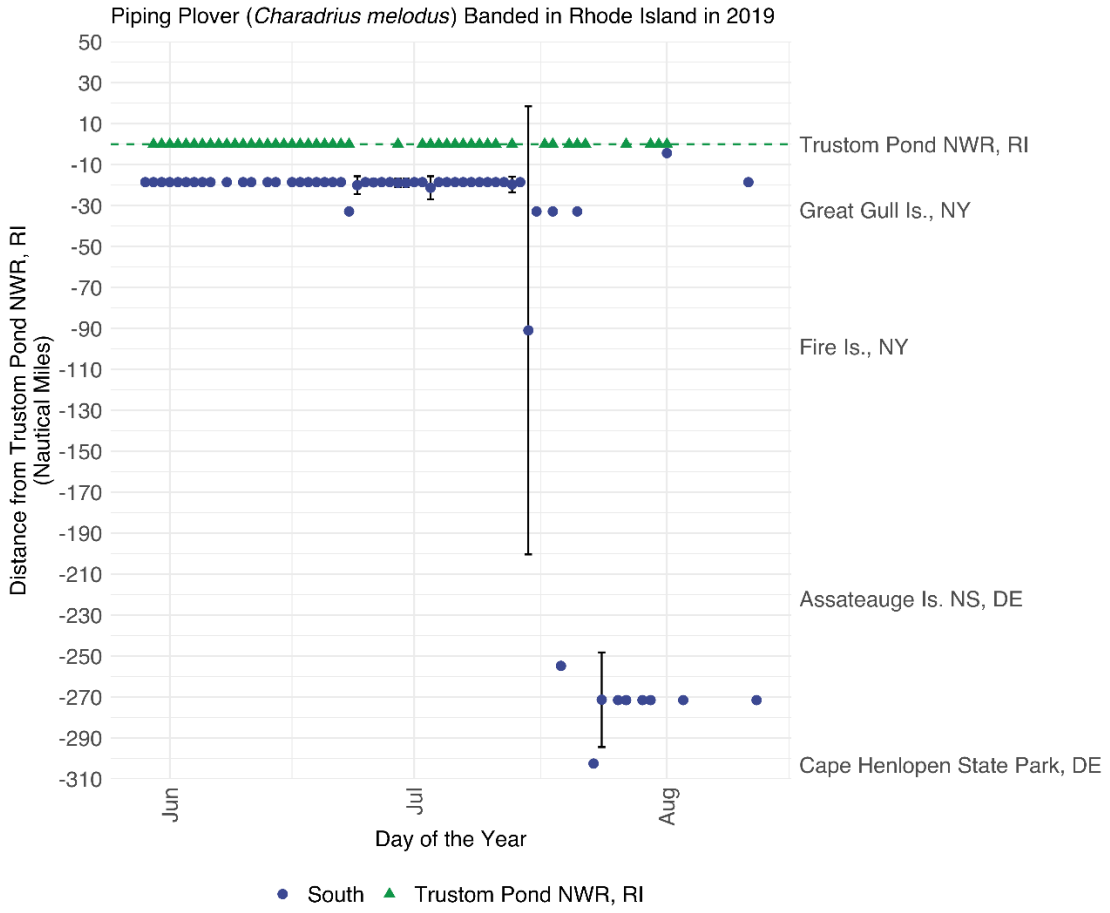

Figure 1.77. Movement chronology of adult Piping Plover nesting in coastal Rhode Island in 2019.

We summarized chronology and spatial extent of local and regional movements of Piping Plovers nesting at Mon3moy NWR, MA in 2017 (Fig. 1.72) and in coastal Rhode Island from 2017-19 (Fig. 1.75, 1.76, 1.77). The overall timing of major emigration events was similar each year, with most long-distance dispersal events conducted from mid-July to mid-Aug. Detection rates of tagged Piping Plovers tended to be highest in 2017 when Loring et al. (2019) had a network of 12 m tall towers dispersed along the Atlantic Coast, whereas there were fewer tall towers in 2018 and 2019. Plovers were regularly documented dispersing as far south as Cape Henlopen State Park, DE which is ~300 km south of coastal Rhode Island (see also Figures 1.78 and 1.79).

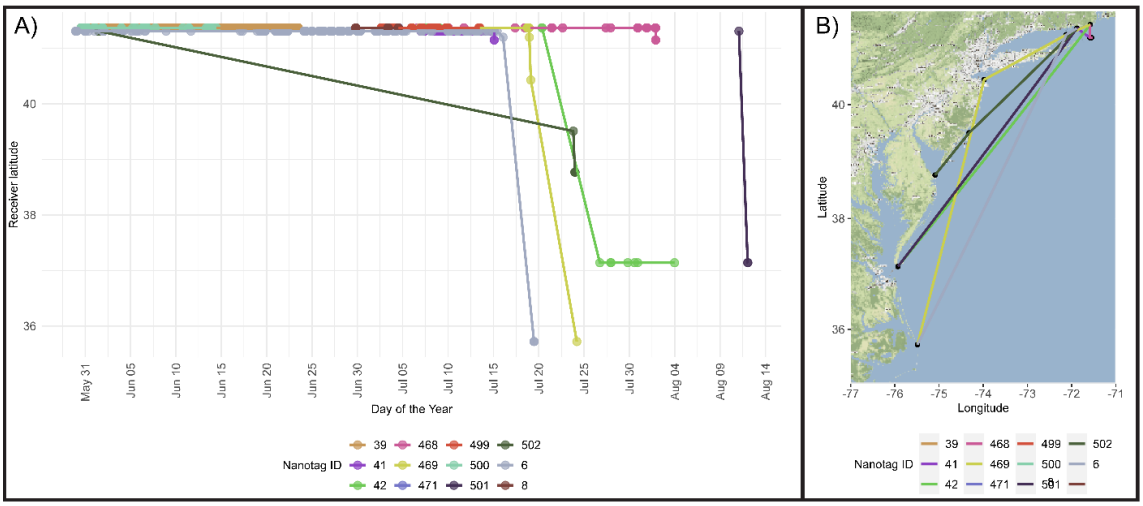

Figure 1.78. Chronology of 13 adult Piping Plover movements (left panel) in relationship to spatially explicit movements (right panel) in 2019.

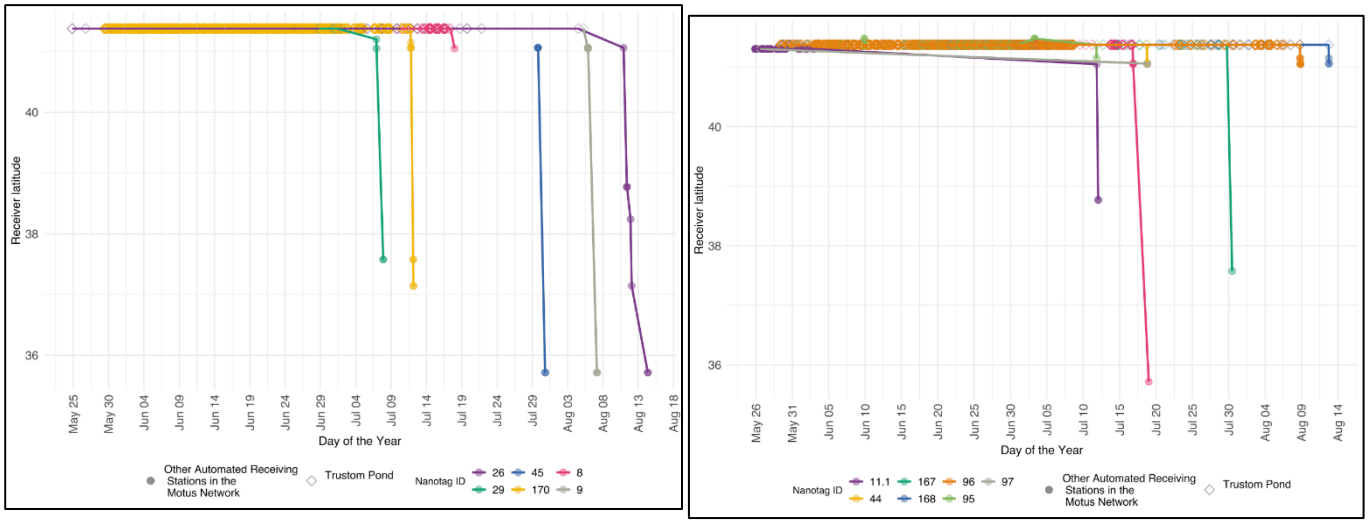

Figure 1.79. Examples of migration chronology for Piping Plovers tagged in Rhode Island.

1.5.1 Calibration Surveys: Predications of tag location based on calibration flights

The following section summarizes results from calibration surveys conducted throughout the project.

1.5.1.1 Kite survey - 13 September 2017

The kite was towed behind the boat from 10:08 AM to 14:51 PM (203 min) at an estimated altitude of 25 m at distances from 3-12 km from receiving stations. There was a total of 5,942 detections (BI Wind Farm – 615 detections; Black Rock – 4,929 detections, and Southeast Lighthouse – 398 detections) (Table 1.14)

Table 1.14. Summary of total number of detections at three Block Island tracking stations of a test tag during calibration survey on 13 September 2017.

Station – antenna bearing	Number of detections
BI Wind Farm	
75° deg	587
255° deg	16
345° deg	12
Black Rock	
101° deg	1,935
151° deg	1,305
200° deg	1,689
Southeast Lighthouse	
60° deg	84
120° deg	229
180° deg	34
240° deg	51
Grand Total	5,942

As you can see in Figure 1.80, at the Black Rock station, the antenna facing SE (101.8°) generally detected the test tag when it was located east of station (green detections – left-most panel), while the antenna facing SSE (152°) detected the tag S of Block Island (light blue detections), as did the SSW (201°) antenna (dark blue detections). Given the estimated radiation patterns for 5-element Yagi antenna (Figure 1.74), these detection patterns were expected.

Similar detection (Figure 1.81) and radiation patterns (Figure 1.82) are evident at Southeast Lighthouse. The actual detection pattern for the ENE antenna at SE Lighthouse was unexpected (upper left panel, Fig 1.82), as this antenna detected the test tag to the south and east of the tower (Figure 1.82, pink lines). Also, surprisingly, the antenna facing due south had a low detection rate, and the beam radiation pattern suggests the tag should have been detected more often when traversing space south of Block Island (see Figure 1.83, SELI-4 panel). The detections by the WSW antenna (Fig. 1.84) show width of the detection beam radiating from each antenna.

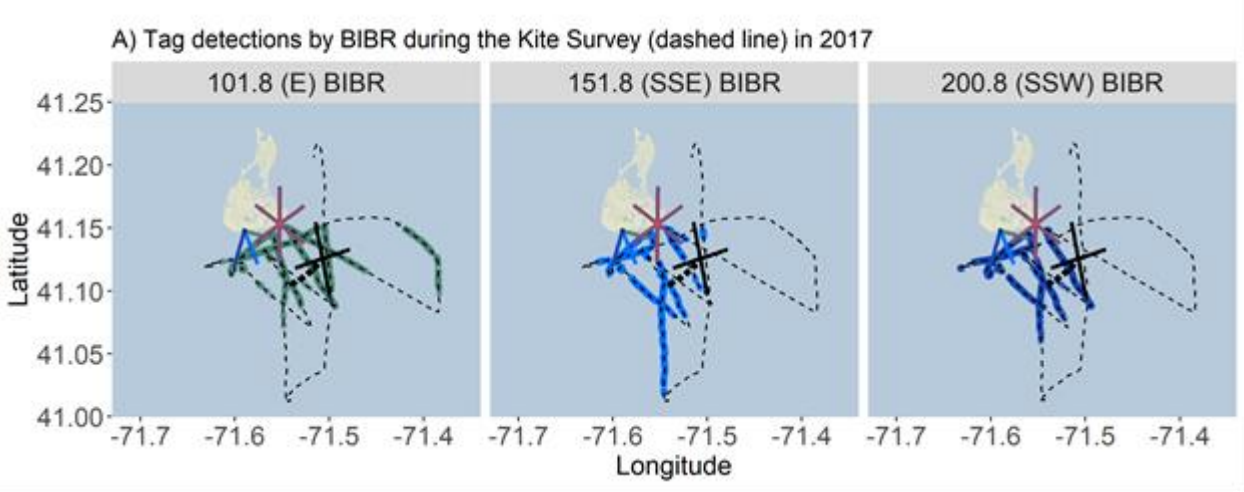

Figure 1.80. Locations of detections from 3 9-element 11-dB antennas of a test tag from a 6 m tall station at Black Rock, Block Island, RI during a calibration survey on 13 September 2017. A kite was flown behind a boat (dotted line for 203 min) at altitude of ~25-60 m.

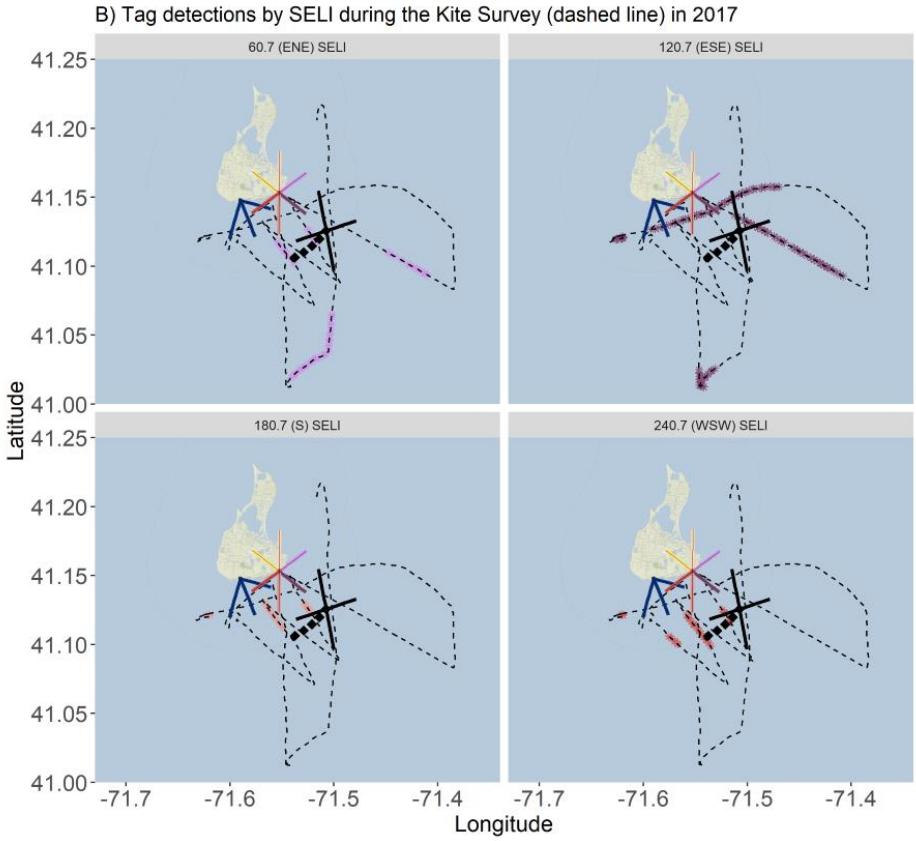

Figure 1.81. Summary of detections at 4 9-element 11-dB antennas of a test tag from a 12 m tall station at Southeast Lighthouse, Block Island, RI during a calibration survey on 13 September 2017. A kite was flown behind a boat (dotted line for 203 min) at altitude of ~20 m. Antennas facing 300 deg and due north (0 deg) had no detections. Detections for the antenna facing 60.7 deg (pink segments) in upper left panel, 120.7 deg (purple segments) in

upper right panel, 180.7 deg (orange segments) in lower left panel, and 240.7 deg (red segments) in lower right panel. BI Wind Farm turbines are black squares.

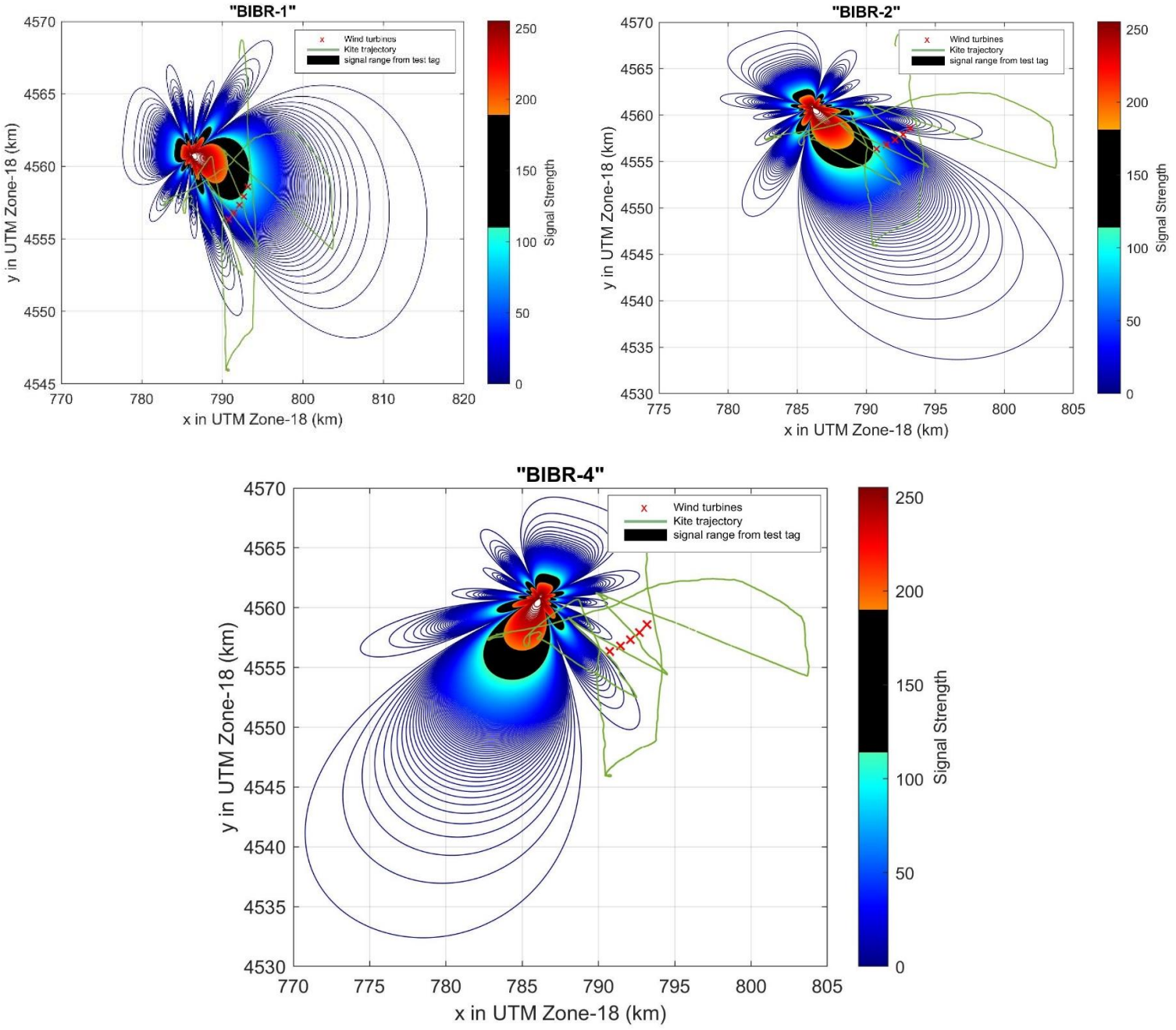

Figure 1.82. Estimated signal strength radiation pattern for 3 9-element Yagi antennas at the Black Rock station in 2017 assuming the test tag was flying at 20 m altitude. Based on signal strength (between ~110 to 190) of the test tag, it was assumed to be located within the black zone. The transect the kite was flown on is shown as the green line. The 5 turbines at the Block Island Wind Farm (red X's). For scale, UTM grid cells at 1 km by 1 km.

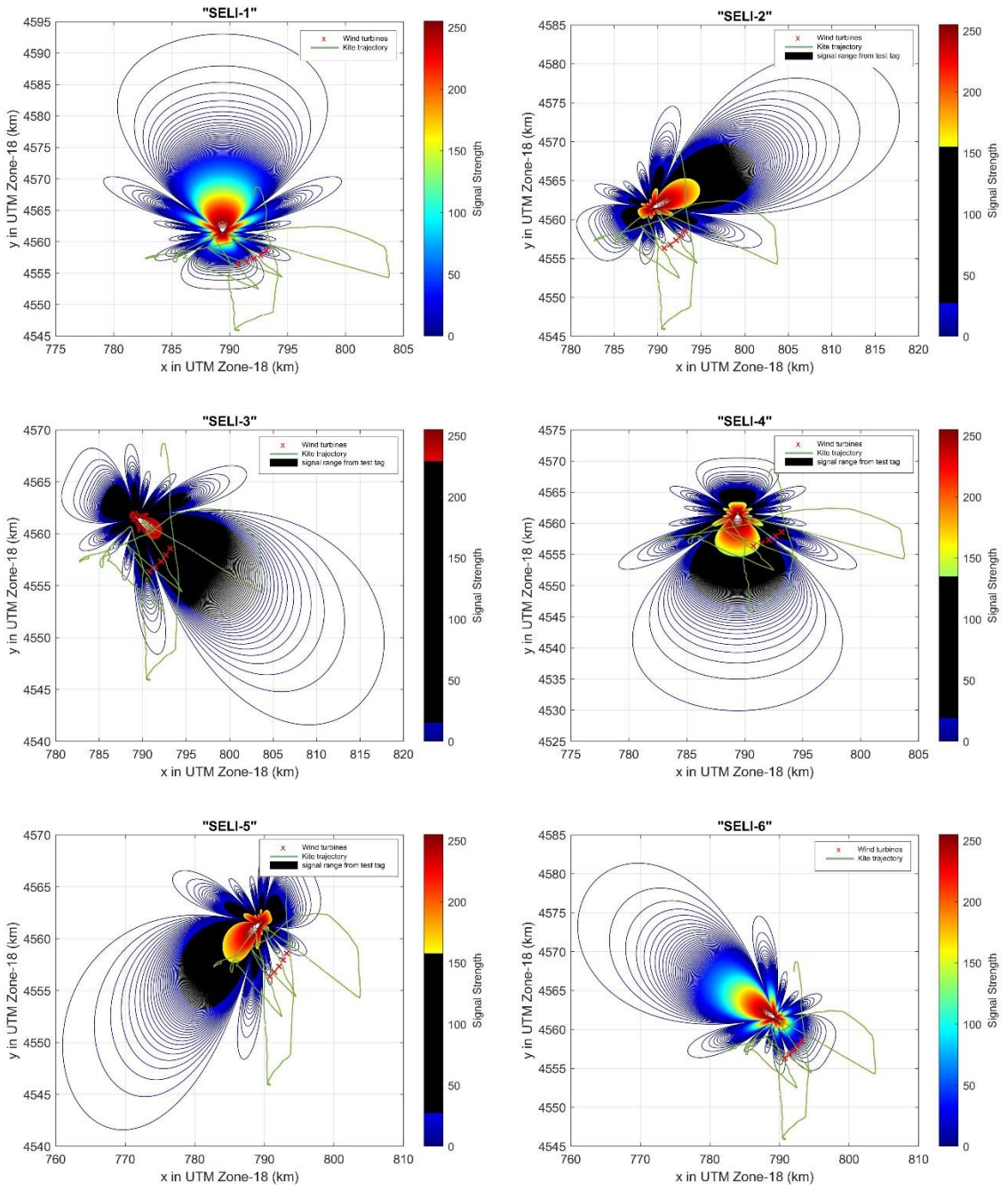

Figure 1.83. Estimated signal strength radiation pattern for 6 9-element Yagi antennas at the Southeast Lighthouse station in 2017 assuming the test tag was flying at 20 m altitude. Based on signal strength (between 20 to 240) of the test tag, it was assumed to be located within the black zone. The transect the kite was flown on is shown as the green line. The 5 turbines at the Block Island Wind Farm as shown as red X's. For scale, UTM grid cells are 1 km by 1 km.

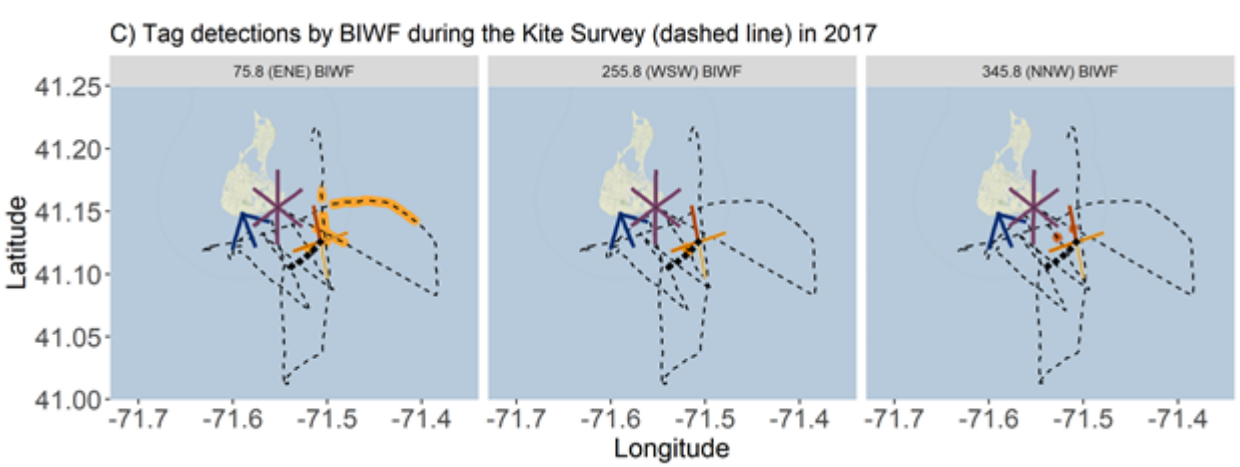

Figure 1.84. Summary of test tag detections at 5-element 8-dB antennas from turbine #1 on the Block Island Wind Farm during a calibration survey on 13 Sept 2017. A kite was behind a boat (dotted line for 203 min) at altitude of ~25 m. The S-facing antenna had no detections.

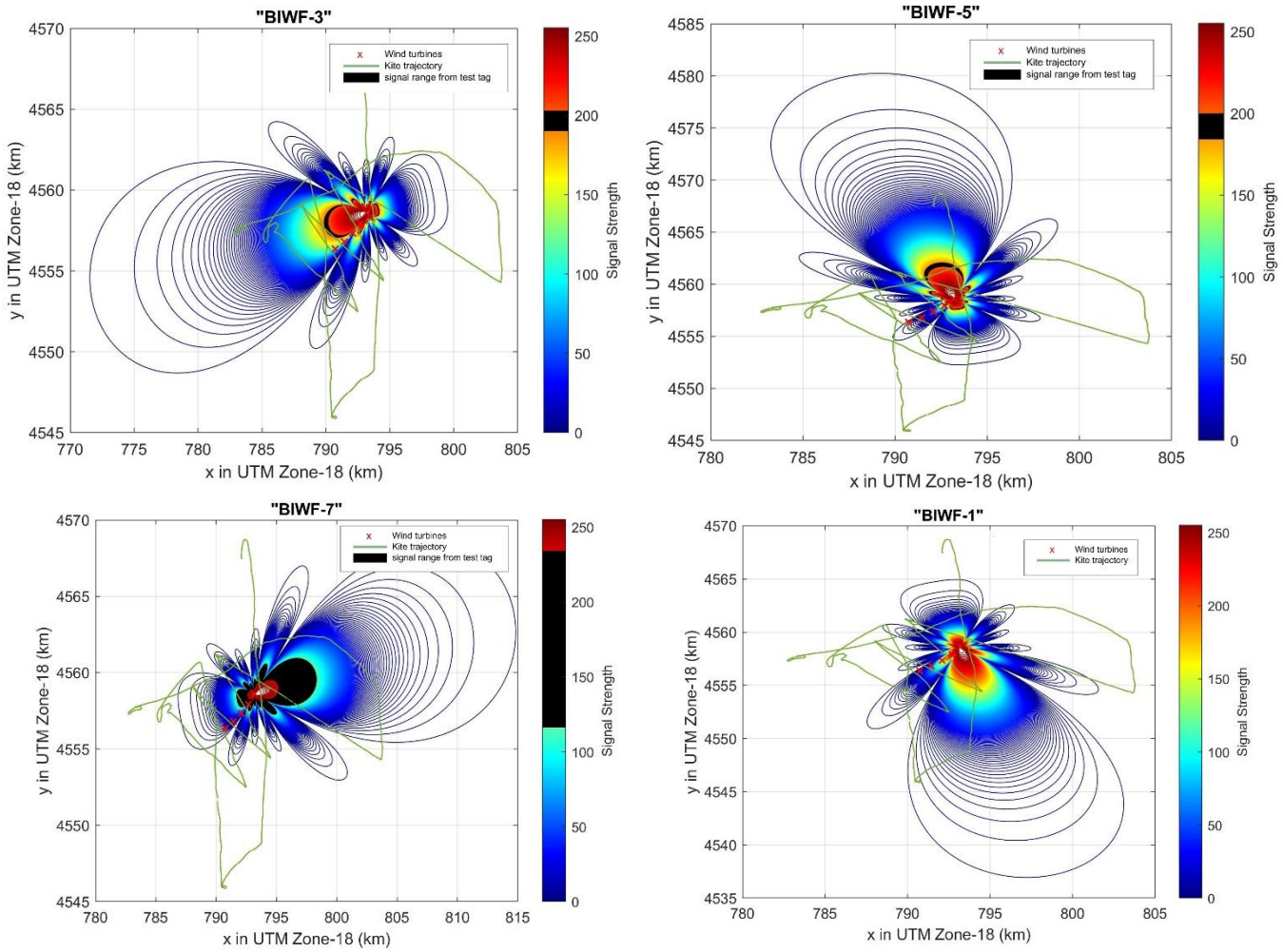

Figure 1.85. Estimated signal strength radiation pattern for 5-element Yagi antennas at the Turbine #1 at Block Island Wind Farm on 13 Sept 2017 assuming the test tag was flying at 20 m altitude. For scale, UTM grid cells are 1 km by 1 km.

Actual detections of the test tag were limited for antennas located on Turbine #1 on the Block Island Wind Farm (Figure 1.84). The antenna facing ENE(BIWF-7) was the most effective, which concurs with estimated radiation patterns of each antenna (Fig 1.85).

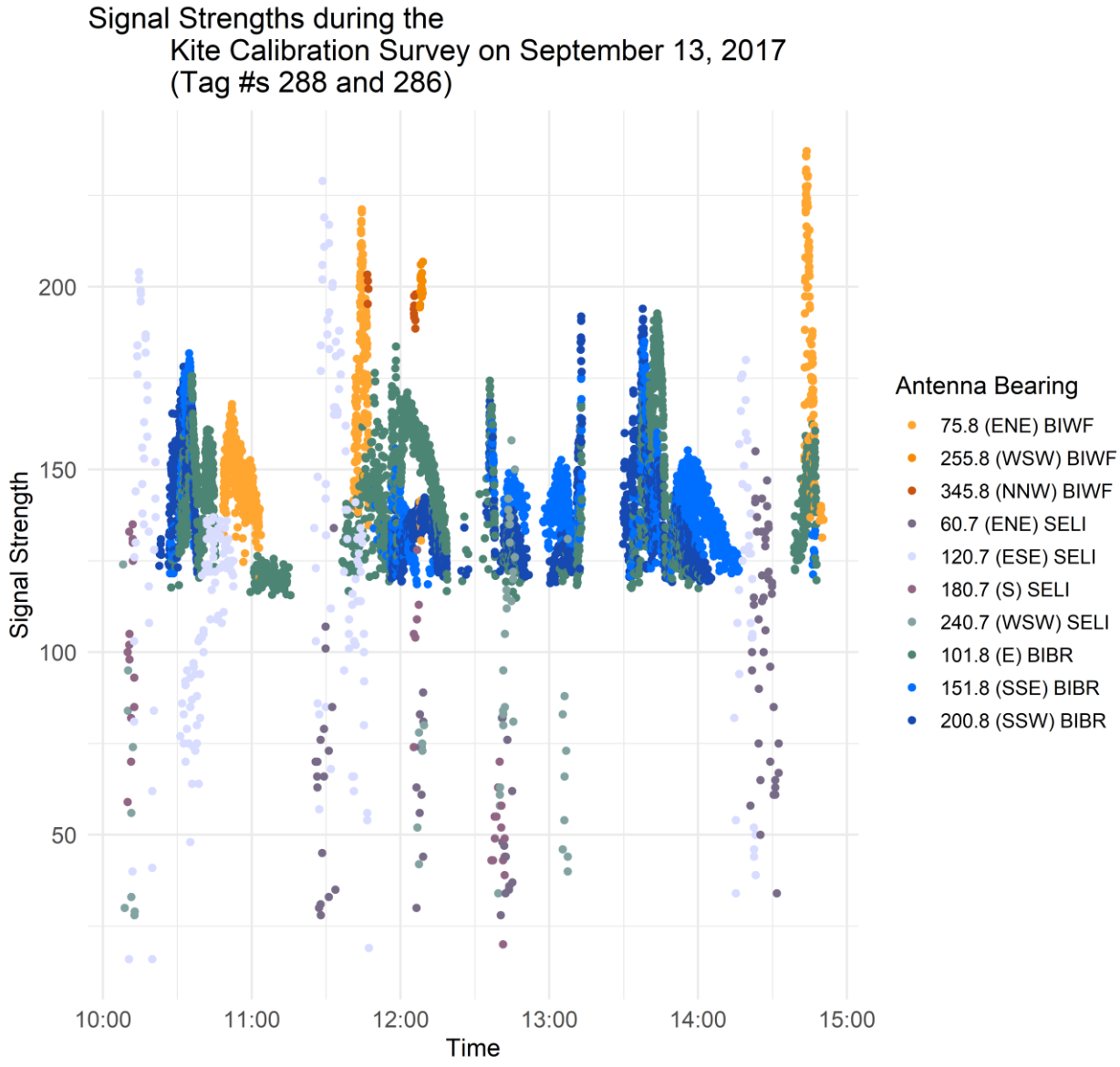

Figure 1.86. Signal strength values (Lotek receiver = raw values, Sensorgnome receivers = transformed values) of the test tag per automated receiving station and antenna during a calibration survey in 2017.

1.5.1.1.1 Model results: Kite moving transect - 13 Sept 2017

Predicted locations tended to be located due south of Block Island. The model prediction averaged 4,527 m (SE = 182 m; range = 502 – 17,426 m; 25th-75% = 2,065-5,476 m) from the actual location of the test tag (Figures 1.87 and 1.88).

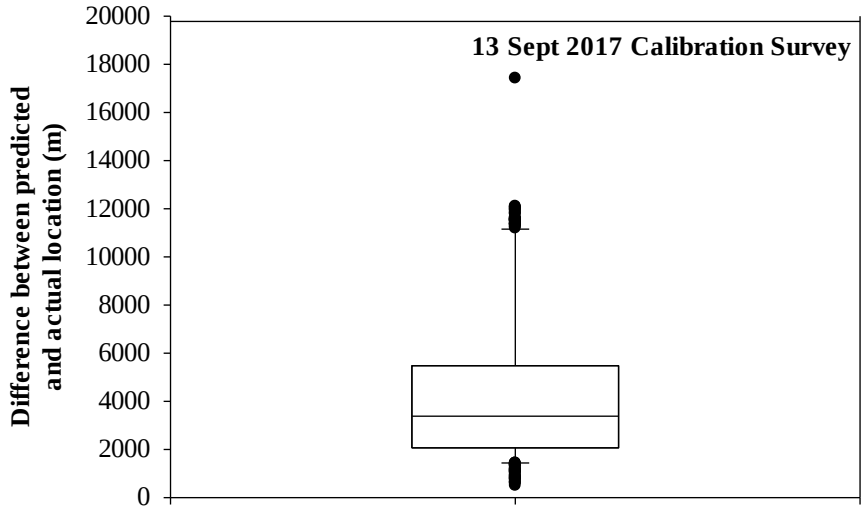

Figure 1.87. Summary of difference between actual and predicted locations of a test tag flown on a kite behind a moving boat on 13 September 2017 (see also Figure 1.85).

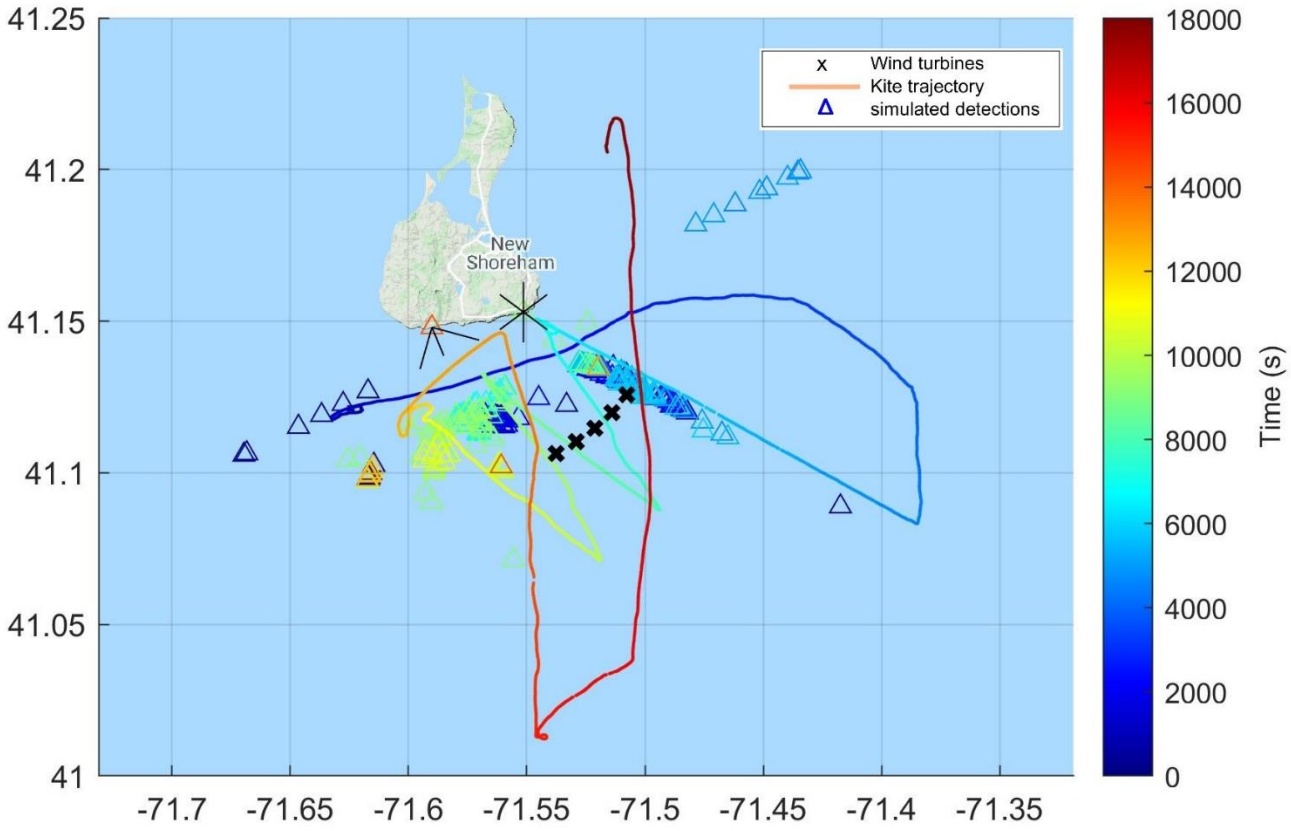

Figure 1.88. Predicted locations of the test tag (triangles) flown attached to a kite being towed by a boat (colored line) in 13 Sept 2017. Colors of the transect and predicted locations are related to the time during the survey (in seconds) from the starting point of the transect (blue segments) to the end of the transect (red segments). The model best predicted locations when the test tag was simultaneously detected from two antennas at different stations, as detections from one antenna were predicted along the main beam of the antenna.

1.5.1.2 Kite survey- moving transect – 19 July 2018

A similar calibration survey to the 13 Sept 2017 calibration survey was conducted on 19 July 2018. Again, a kite was towed behind the boat from 9:06 to 10:54 (108 min) at an estimated altitude of ~25 m. There was a total of 1,769 detections (Black Rock – 1,212 detections, and Southeast Lighthouse – 165 detections) during this calibration survey (Table 1.15), which total coverage of the entire transect by at least one antenna (Figure 1.80) with considerable variation among antennas in their coverage (Figure 1.89, 1.90 and 1.91) as would be expected based on radiation patterns (Figure 1.92). Unfortunately, the receiver at the Block Island Wind Farm was not operating during this survey, which we did not learn until September 2019 when information from the receiver was finally downloaded.

Interestingly, the omni antenna at Black Rock (but not the omni at SE Lighthouse) did

detect the test tag, but only when the tag was southeast of Black Rock (Figure 1.89, Figure 1.91 - lower left panel) and never detected the tag due south or west of Black Rock, suggesting some landscape features potentially blocked detections from those bearings.

Table 1.15. Summary of total number of detections at two stations of a test tag during a calibration survey on 19 July 2018 off the southeastern coast of Block Island.

Station-antenna bearing	**Number of detections**
Black Rock	
113° deg	946
233° deg	266
Omnidirectional	339
Southeast Lighthouse	
218° deg	165
Total	1,769

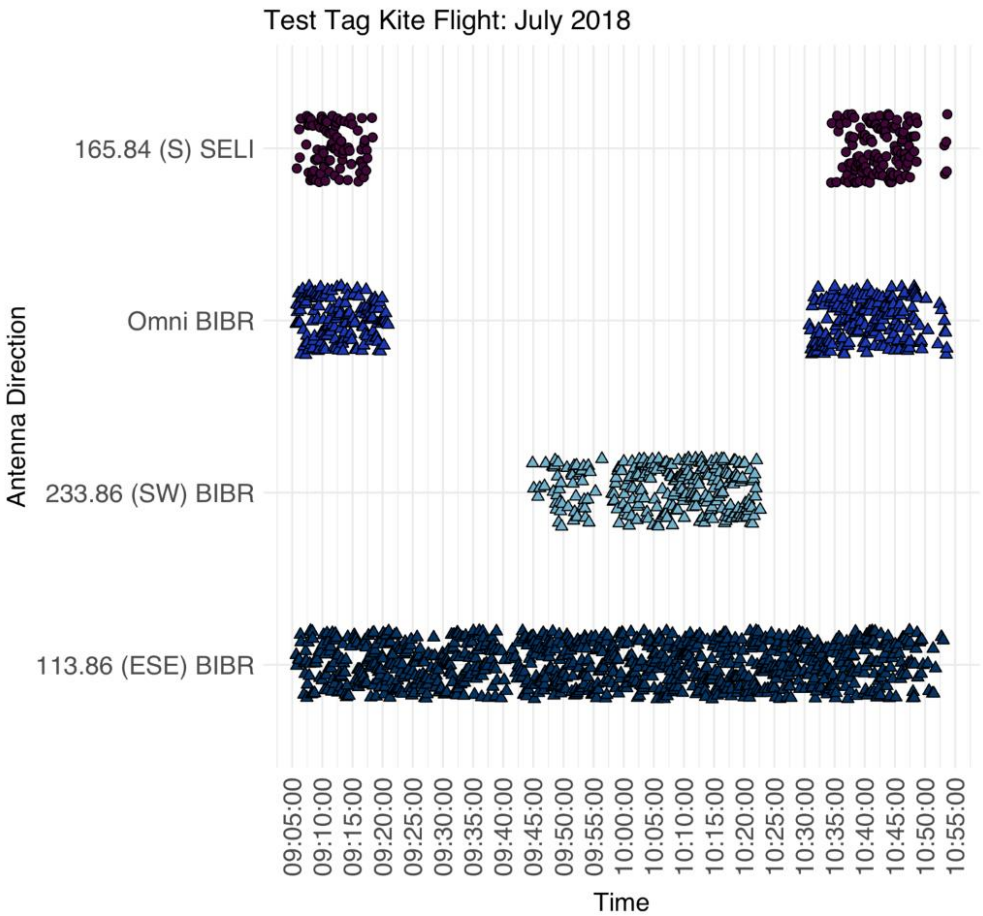

Figure 1.89. Temporal variation in detections of a test tag attached to a kite flown during a calibration survey off the southern coast of Block Island on 19 July 2018. The tag was detected by one antenna at the Southeast Lighthouse (SELI) station and three antennas from the Black Rock (BIBR) station.

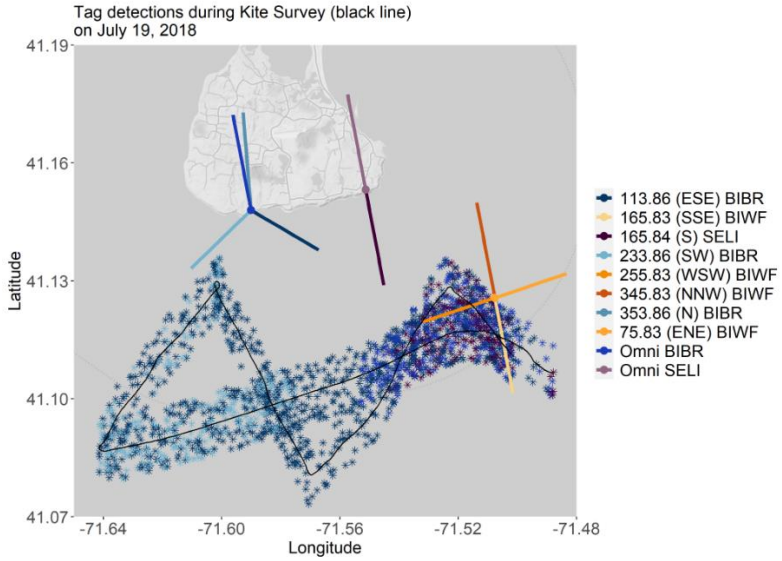

Figure 1.90. Spatial variation in detections of a test tag attached to a kite towed behind a boat (black line) during a calibration survey off the southern coast of Block Island on 19 July 2018. The tag was detected by one antenna at the Southeast Lighthouse (SELI) station and three antennas at the Black Rock (BIBR) station. The receiver on Block Island Wind Farm was not functioning in 2018. Points are shown away from transect line so they can be displayed.

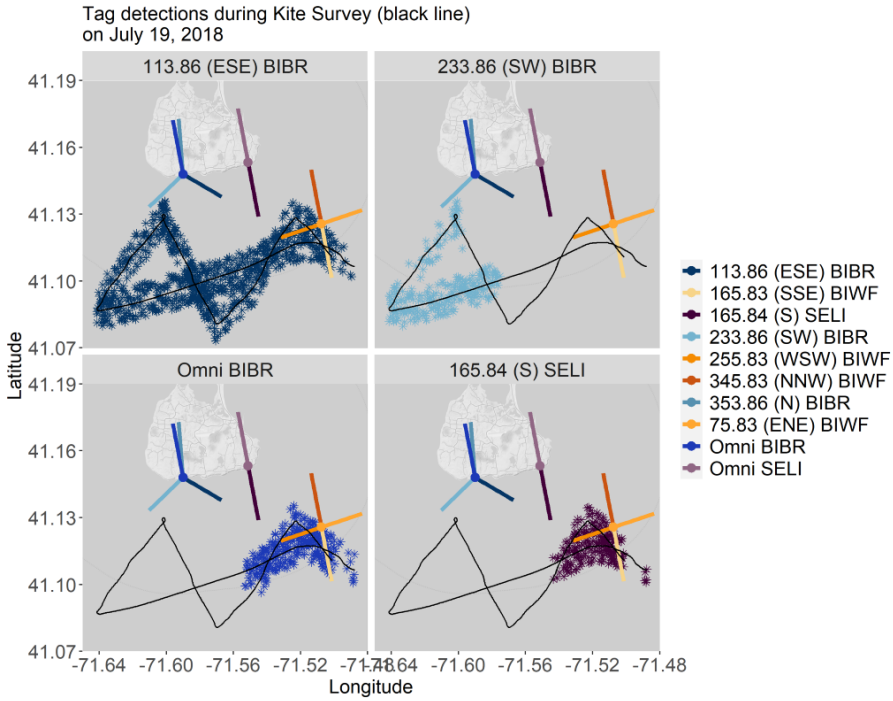

Figure 1.91. Spatial variation in detection of a test tag attached to a kite towed behind a boat (black line) during a calibration survey off the southern coast of Block Island on 19 July 2018. The tag was detected by one antenna at the Southeast Lighthouse station (SELI) and three antennas from Black Rock (BIBR) station.

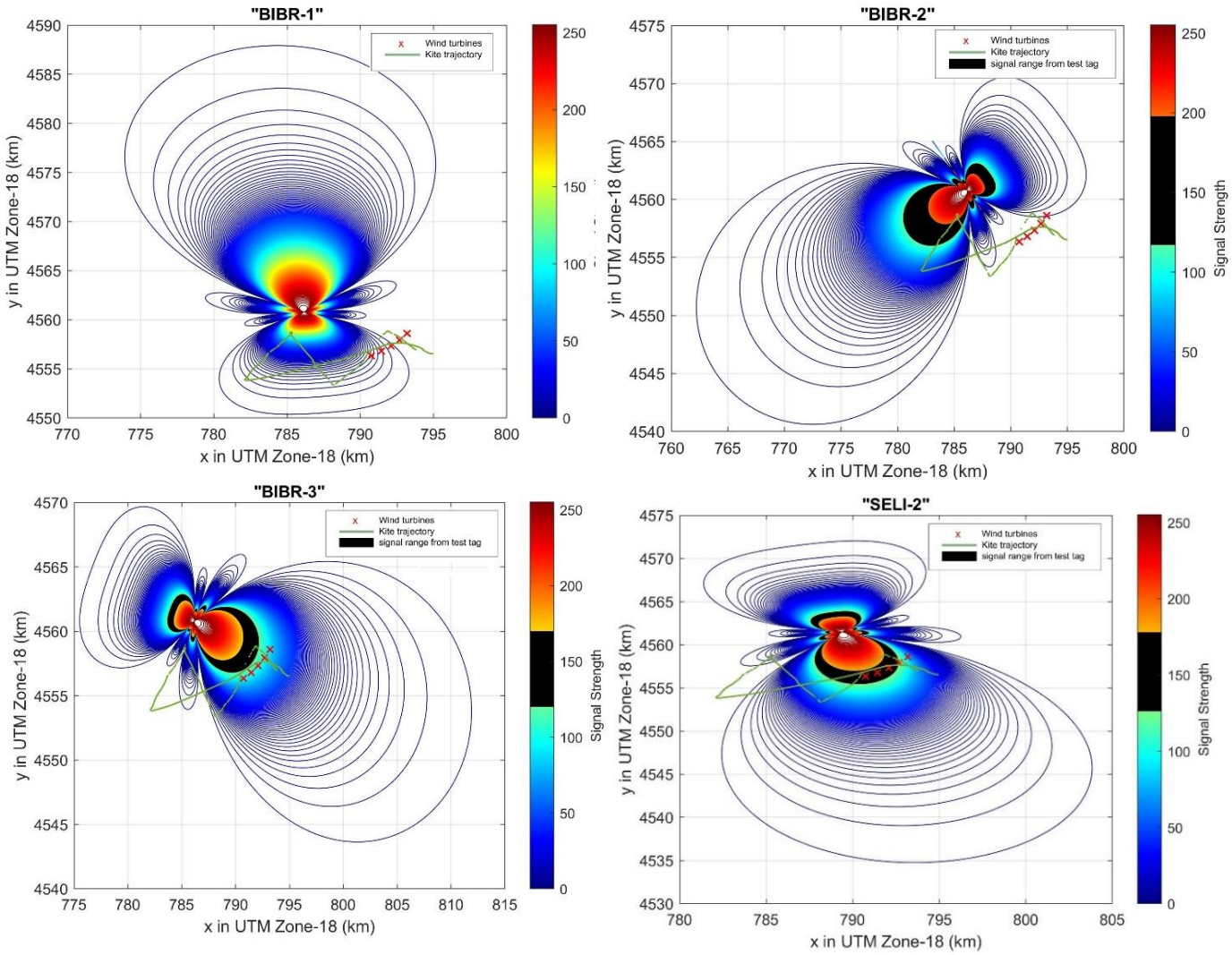

Figure 1.92. Estimated signal strength radiation pattern for 5-element Yagi antennas at Black Rock (BIBR) and the Southeast Lighthouse station (SELI) in 19 July 2018 assuming the test tag was flying at 20 m altitude. Based on signal strength (between ~110-170) of the test tag, the test tag was assumed to be located within the black zone. The transect the kite was flown is shown as the green line. The 5 turbines at the Block Island Wind Farm (red X's). UTM grid cells are 1 km by 1 km

1.5.1.2.1 Model Results, Kite survey- 19 July 2018

The model only predicted locations when there were simultaneous detections from different receivers, so the test tag had to be detected by simultaneously by both the Black Rock and Southeast Lighthouse stations. Therefore, predicted locations tended to be located due southeast of Block Island. The model prediction averaged 1,695 m (SE = 147 m; range = 229 – 4,221 m; 25th-75% = 952-2,188 m) from the actual location of the test tag (Figures 1.93 and 1.94).

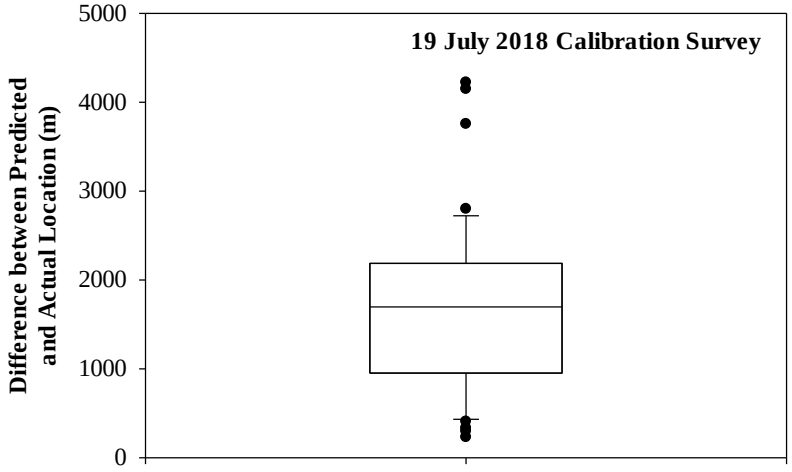

Figure 1.93. Summary of differences between actual and predicted locations of a test tag attached to a kite flown behind a moving boat on 19 July 2018 (see Figure 1.65).

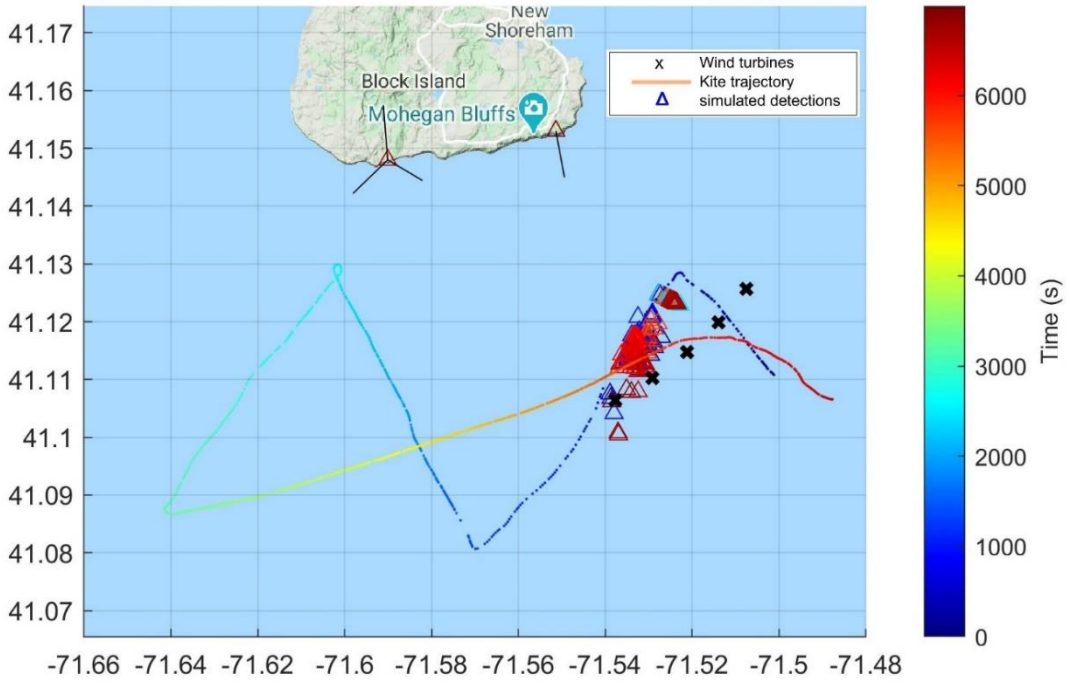

Figure 1.94**.** Predicted locations of a test tag (colored triangles) attached to a kite being towed by a boat (colored line) in 19 July 2018. Colors are related to the time during the survey (in seconds) from the start point (blue line) to the end point (red line). The model best predicted locations when the test tag was simultaneously detected from two antennas on different stations. The black X's are the 5 turbines on the Block Island Wind Farm. The color of the triangles is related to the timing of the simultaneous detection.

1.5.1.3 Kite moving transect - 9 Aug 2018

The test tag was glued to a kite that was towed behind the boat from 13:38 to 14:27 (49 min) at

an estimated altitude of 25 m. There was a total of 351 detections, all from the Black Rock station (Table 1.16). The omni antenna tended to detect the test tag early in the survey, whereas the SW and ESE antennas at the Black Rock station detected the test tag later during the survey, and two antennas detected the test tag late in the survey (Figures 1.95, 1.96, and 1.97).

Unfortunately, after survey was completed, we learned that the Southeast Lighthouse – and the receiver at the Block Island Wind Farm were not operating during this survey. Thus, no simultaneous detections from two different towers were obtained, which limited the ability to model the relationship between predicted and actual locations. However, this survey did provide further spatially explicit information on when the Black Rock station was detecting the test tag (Figure 1.97).

Table 1.16. Summary of detections at station at Black Rock, Block Island, RI of a test tag during calibration survey on 9 August 2018 off the southeastern coast of Block Island

Station – antenna bearing	Number of detections
Black Rock	
113°	178
233°	130
Omnidirectional	43
Total	351

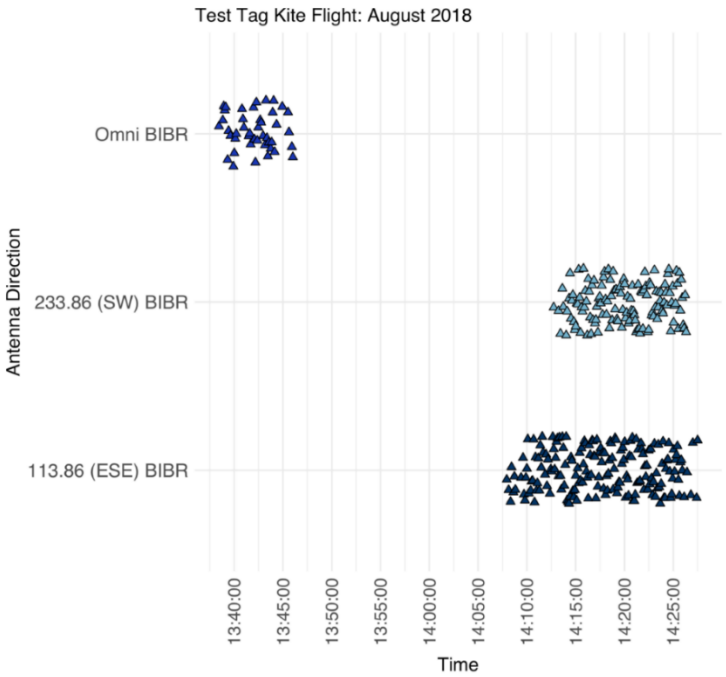

Figure 1.95. Temporal variation in detection of a test tag flown on a kite during a calibration survey off the southern coast of Block Island on 9 August 2018. The tag was detected by three antennas from a station at Black Rock (BIBR).

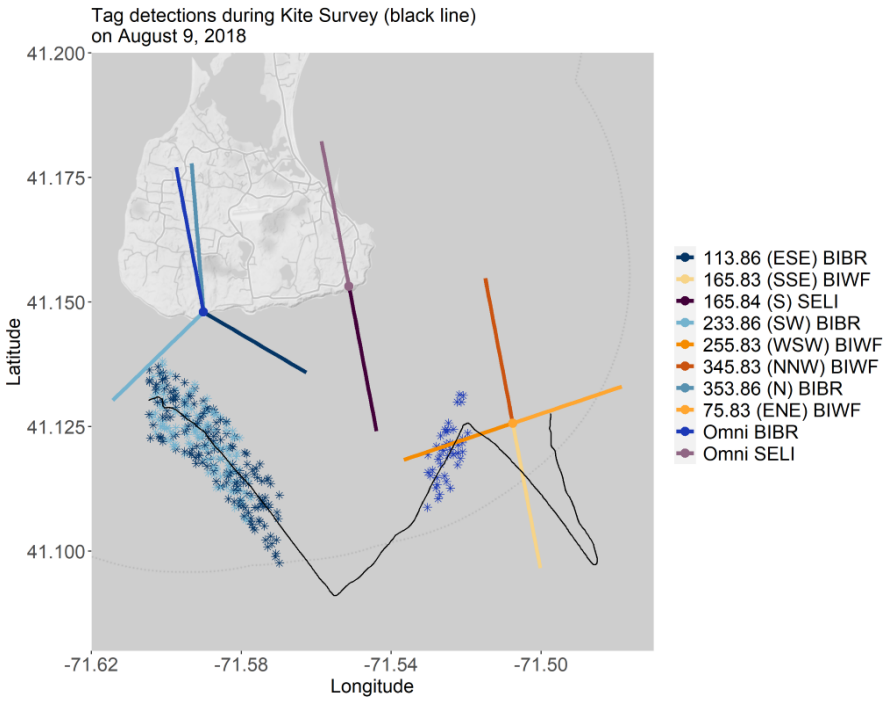

Figure 1.96. Spatial variation in detections of a test tag flown on a kite towed behind a boat (black line) during a calibration survey off the southern coast of Block Island on 9 August 2018. The tag was detected by three antennas from a station at Black Rock (BIBR). The receivers at the SE Lighthouse and Block Island Wind Farm were not operating.

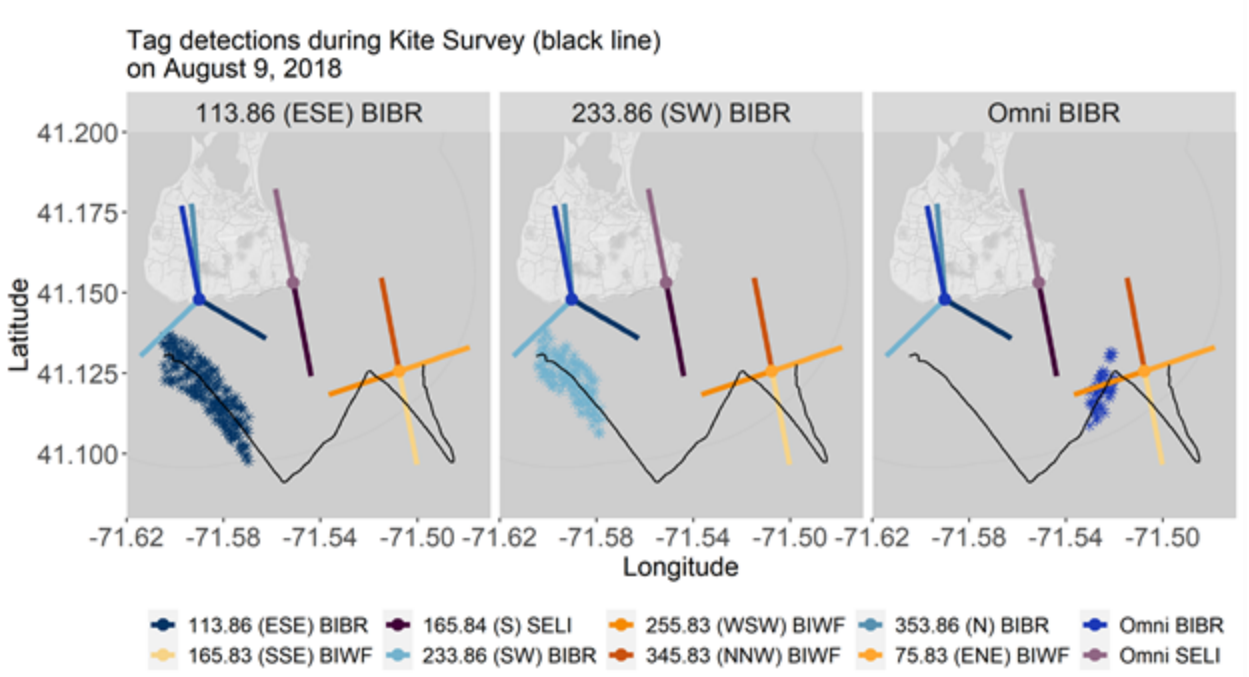

Figure 1.97. Spatial variation in detection of a test tag flown on a kite towed behind a boat (black line) during a calibration survey off the southern coast of Block Island on 19 August 2018. The tag was detected by three antennas from a station at Black Rock (BIBR).

1.5.1.3.1 9 Aug 2018 Kite Model Results

The model only predicted locations based on detections late in survey when there were detections from the 133° and 233°bearing antennas at the Black Rock Station (Figure 1.98). Model accuracy was moderate with a median difference between actual and predicted locations of 1,629 m (25th to 75th percentiles = 1,466 to 2,078 m, N = 20) (Figure 1.99).

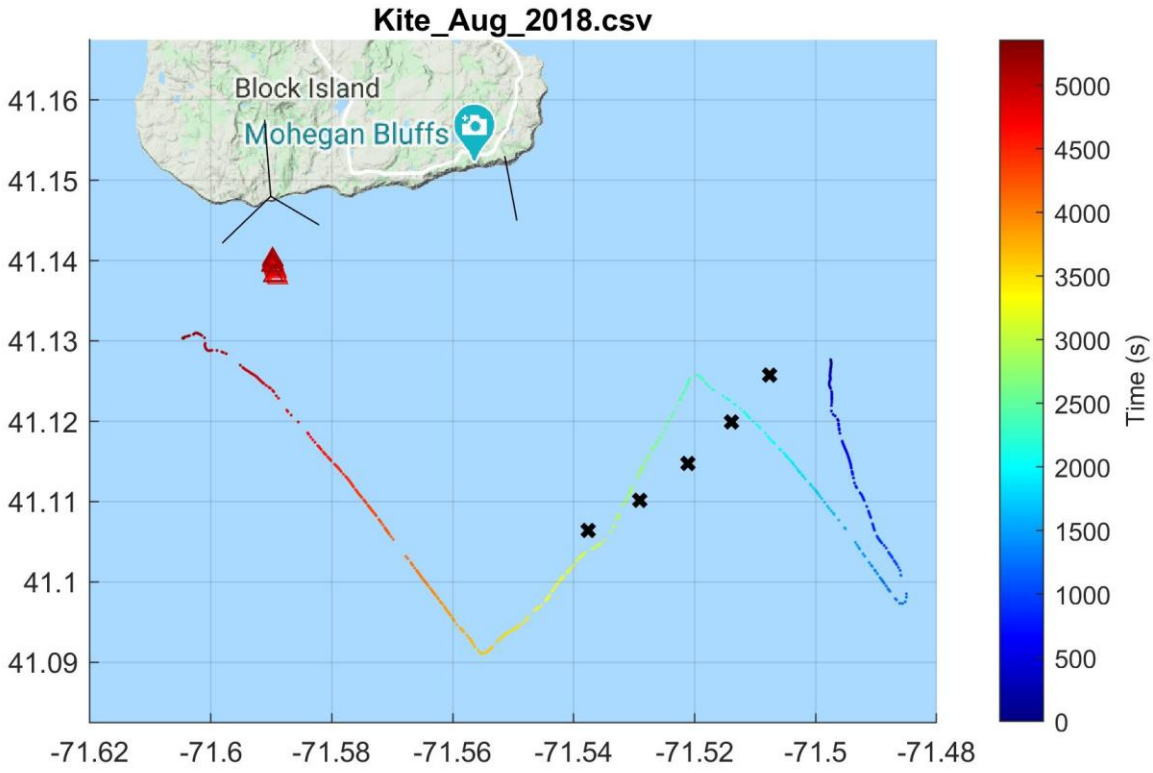

Figure 1.98. Predicted locations of a test tag (colored triangles) attached to a kite being towed by a boat (colored line) in 9 Aug 2018. Colors are related to the time during the survey (in seconds) from the start point (blue segments of line) to the end point (red segments of line). The model best predicted locations when the test tag was simultaneously detected from two antennas on different stations. The black X's are the 5 turbines on the Block Island Wind Farm. The color of the triangles is related to the timing of the simultaneous detection.

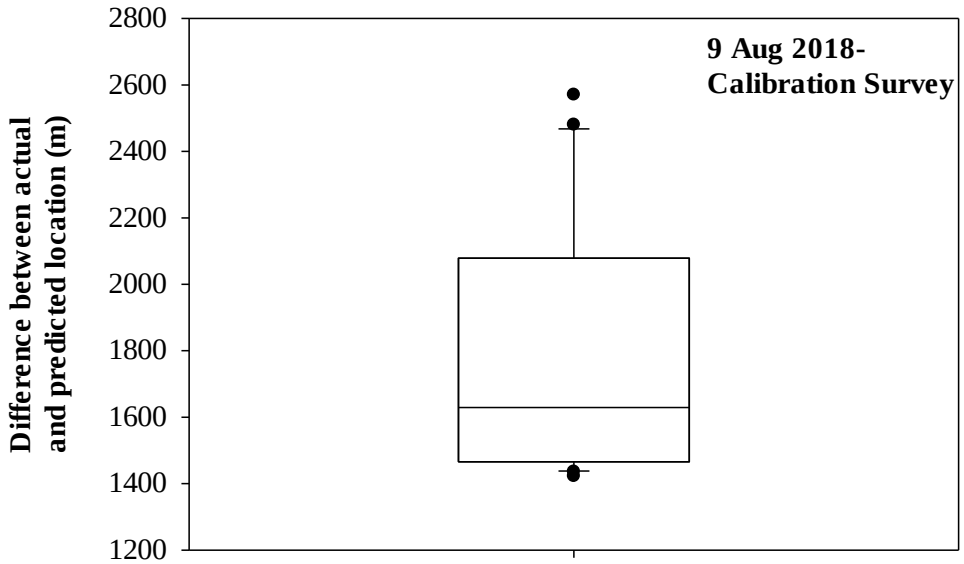

Figure 1.99. Summary of differences between actual and predicted locations of a test tag attached to a kite flown behind a moving boat on 9 July 2018 (see Figure 1.98).

1.5.1.4 10 June 2019: 5 Fixed locations, 5 altitudes

The test tag was only detected at the first point (northeast most point, Figure 1.97) by the Black Rock station with the antenna bearing 113° for 8 detections from 9:36 to 9:42 at 15 m, 30 m, and 60 m (Figure 1.100), and not detected at any altitude at the other four points (Table 1.17). Weather conditions were clear on this day.

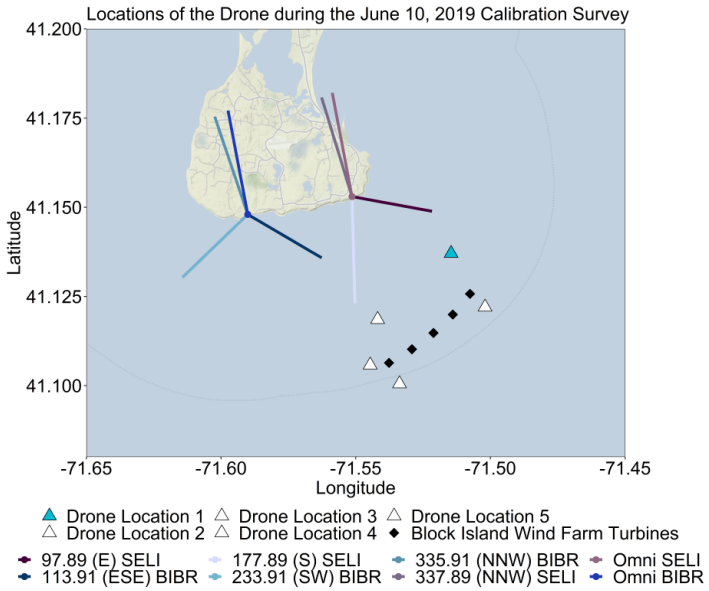

Figure 1.100. Results of calibration survey on 10 June 2019, with detections of the test tag at only one (blue triangle) of five fixed points (white triangles). Surveys centered around the Block Island Wind Farm (black diamonds). The drone flew at 5 altitudes at each point.

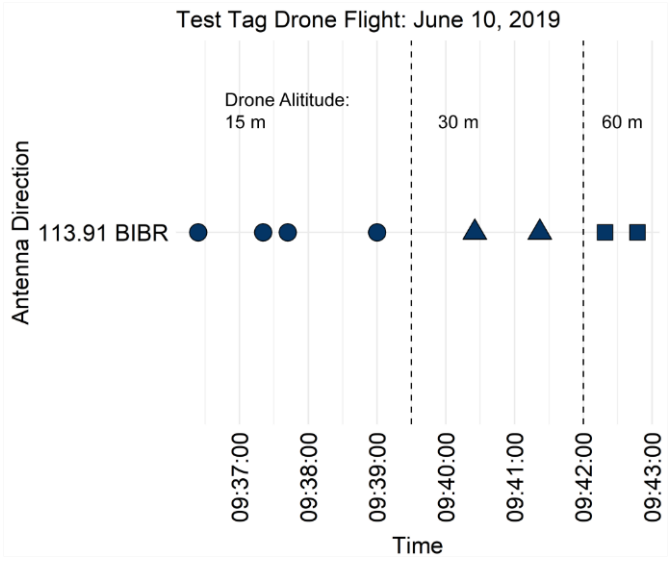

Figure 1.101. Temporal variation in detections of test tag at point #1 on 10 June 2019 calibration survey.

Table 1.17. Total number of detections of a test tag flown on 10 June 2019 south of Block Island at 5 fixed points (see Figure 1.20) for 15 min at 5 altitudes.

Fixed	Flight altitude of drone				
Point	15 m	30 m	60 m	90 m	120 m
1	4	2	2	0	0
2	0	0	0	0	0
3	0	0	0	0	0
4	0	0	0	0	0
5	0	0	0	0	0

1.5.1.4 27 June 2019: 3 fixed locations, 30 m altitude

Although test tag was in the radiation range of the antennas at Black Rock and Southeast Lighthouse (see Figures 1.85 and 1.92), the test tag was never detected by either receiver. The tag was flown at 30 m altitude for 15 min at each of the three points (Figure 1.20). We assumed the tag should have been detected given the flight altitude and duration of each flight. The flight conditions were in heavy fog, which we assume affected detection rates of the tags, although a similar survey on 10 June 2019 on a clear day also had low detection rates.

1.5.1.5 9 July 2019: Moving transect

We successfully completed a calibration survey on 9 July 2019 (Figure 1.102), with Greg

Bonynge piloting 4 6-km long transects (3 km outbound: east to west; 3 km inbound: west to east) at 4 altitudes (30 m, 60 m, 90 m, and 120 m). The drone flew at 10 m per sec and stopped at fixed points along the transect to gather latitude-longitude information. The test tag was much more likely to be detected by the Black Rock station than Southeast Lighthouse, which was probably due to antenna bearings, as well as interference at Southeast Lighthouse from terrain as well as other structures. Black Rock had 252 total detections vs 93 from Southeast Lighthouse (Figure 1.103). All detections at Black Rock were from the antenna facing 114° deg (SE), while at SE Light, 12 detections (at 30 m altitude) were from the antenna facing while most (81 detections) were for the antenna facing northwest when the drone was 90 to 120 m asl, thus the backlobe was apparently detecting the drone at higher altitudes.

During the calibration surveys on 9 July 2019, signal strength, based on the Lotek receivers 1 - 255 scale, varied from ~35 to 65, and tended to be lower during the 30 m altitude flight than flights at altitudes of 60 m or 90 m (Fig. 1.103 and 1.104). When the drone was flying at 120 m altitude, signal strength tended to decline again.

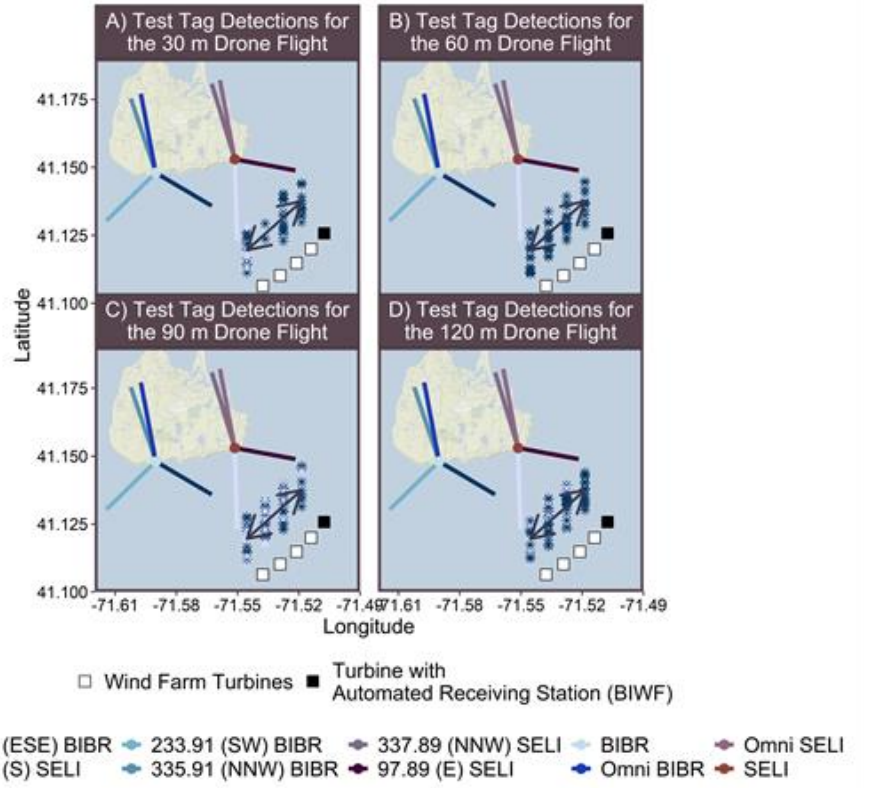

Figure 1.102. Results of calibration survey on 9 July 2019. The test tag was flown on strut of quadcopter. Station on Block Island Wind Farm (white squares) located on Turbine #1 (black square) was inactive. Black Rock station (blue Yagi antenna bearings) and Southeast Lighthouse station (red Yagi antenna bearings) detections are shown with blue (*) or purple (*) asterisks but are not spatially accurate to show all detections.

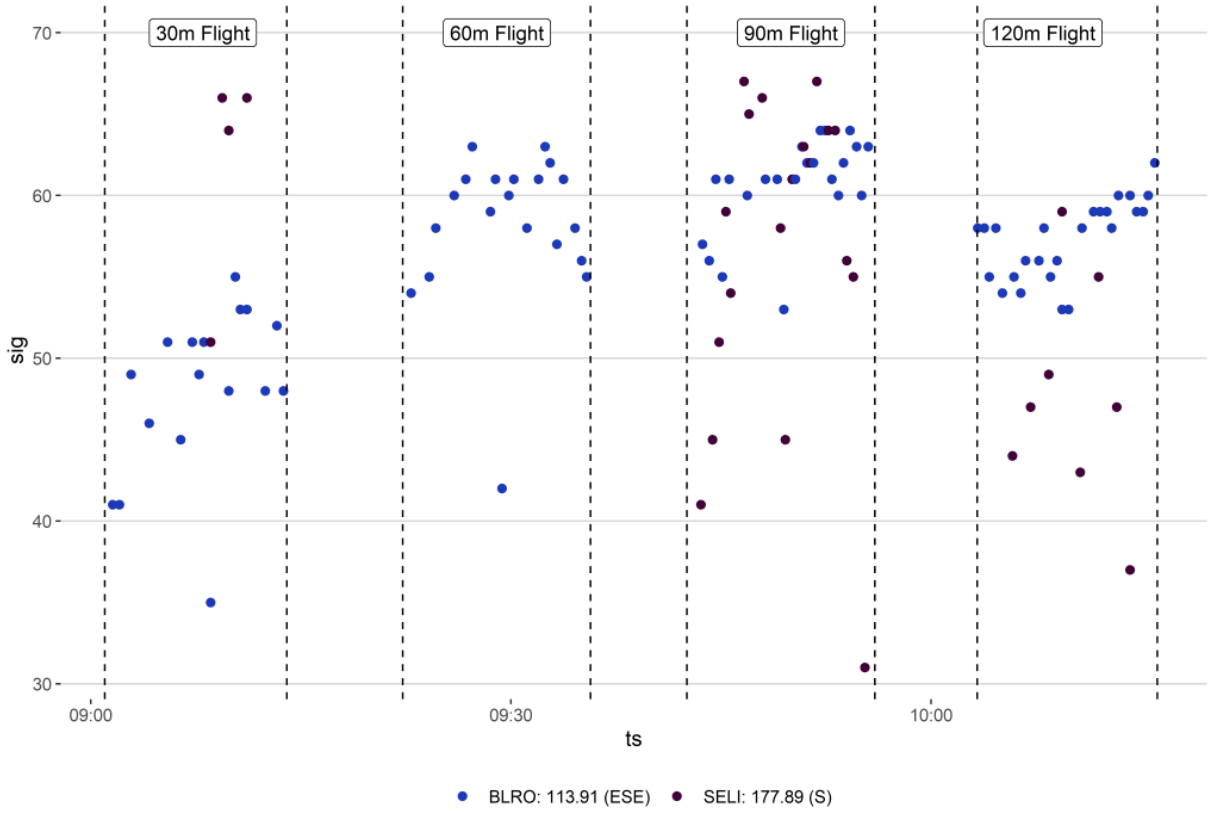

Figure 1.103. Signal strength from a Lotek receiver (scale = 1-255) of a test tag during the 4 calibration survey flights on 9 July 2019. The start and end of each flight is marked by a dashed line. Colors indicate receiver (Black Rock = Blue; Southeast Lighthouse = Purple); all Black Rock detections were from the antenna facing 114° and Southeast Lighthouse station from the antenna facing 178°.

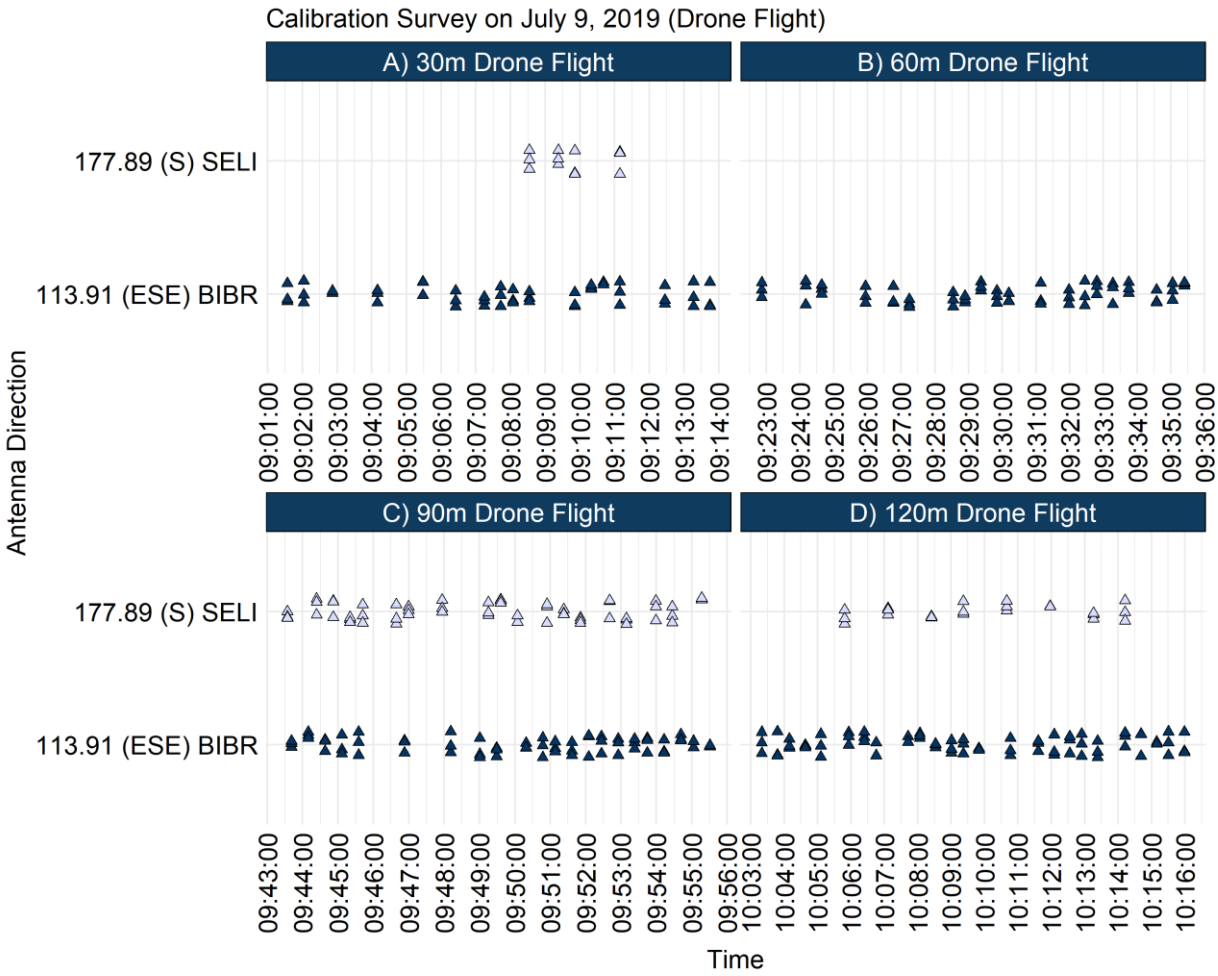

Figure 1.104. Probability of obtaining near-simultaneous detections from two VHF tracking stations on Block Island during calibration surveys with a quadcopter drone on 9 July 2019. The drone was flown at 4 altitudes (30 m (top left), 60 m (top right), 90 m (bottom left) and 120 m (bottom right) along 6 km of transects at 10 m per second. The 5-element Yagi antenna at Black Rock (blue triangles) had high detection rates, while the 5-element Yagi at Southeast Lighthouse (purple circles) had much lower detection rates of test tag, with no detections when the drone was flying at 60 m above sea level

Based on the beam radiation patterns of the 6 5-element Yagi antennas at the Black Rock and SE Lighthouse stations, the antenna facing south at SE Lighthouse (Figure 1.105, SEBI-3 panel) and the antenna facing SE at Black Rock (BRBI-2 panel) were the ones most likely to have simultaneous detections (Figures 1.105, 1.106, 1.107, 1.108). What is clear from the radiation patterns is that the beam patterns increased as a function of estimated test tag altitude.

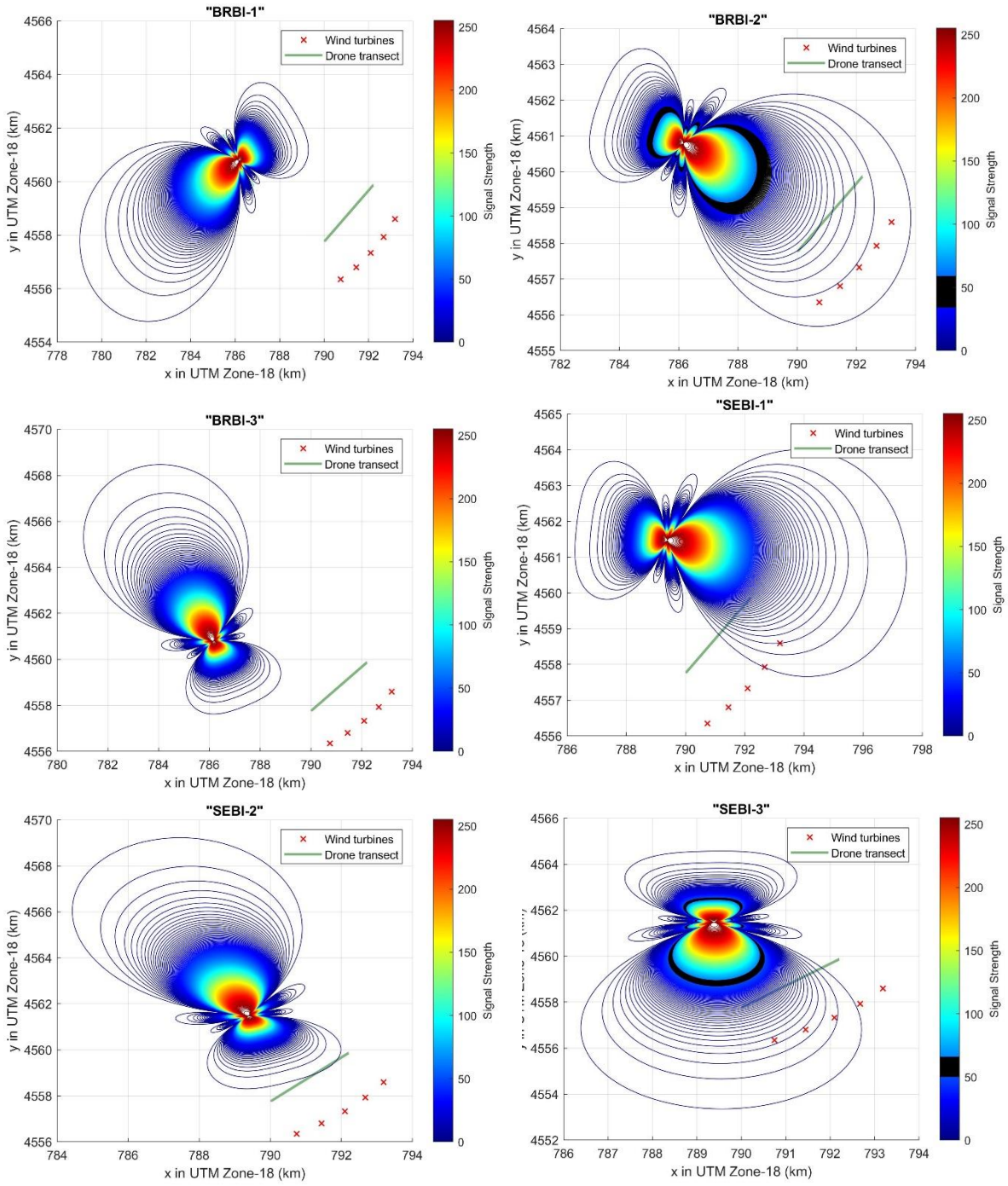

Figure 1.105. Estimated signal strength radiation pattern on 9 July 2019 for 5-element Yagi antennas at Black Rock (BRBI) and the Southeast Lighthouse station (SEBI) in 2019 assuming the test tag was flying at **30 m altitude**. Based on signal strength (between ~30-60) of the test tag, it was assumed to be located within the black zone. The transect the drone was flown on is shown as the green line. The 5 turbines at the Block Island Wind Farm are shown as red X's. UTM grids cells are 1 km by 1 km.

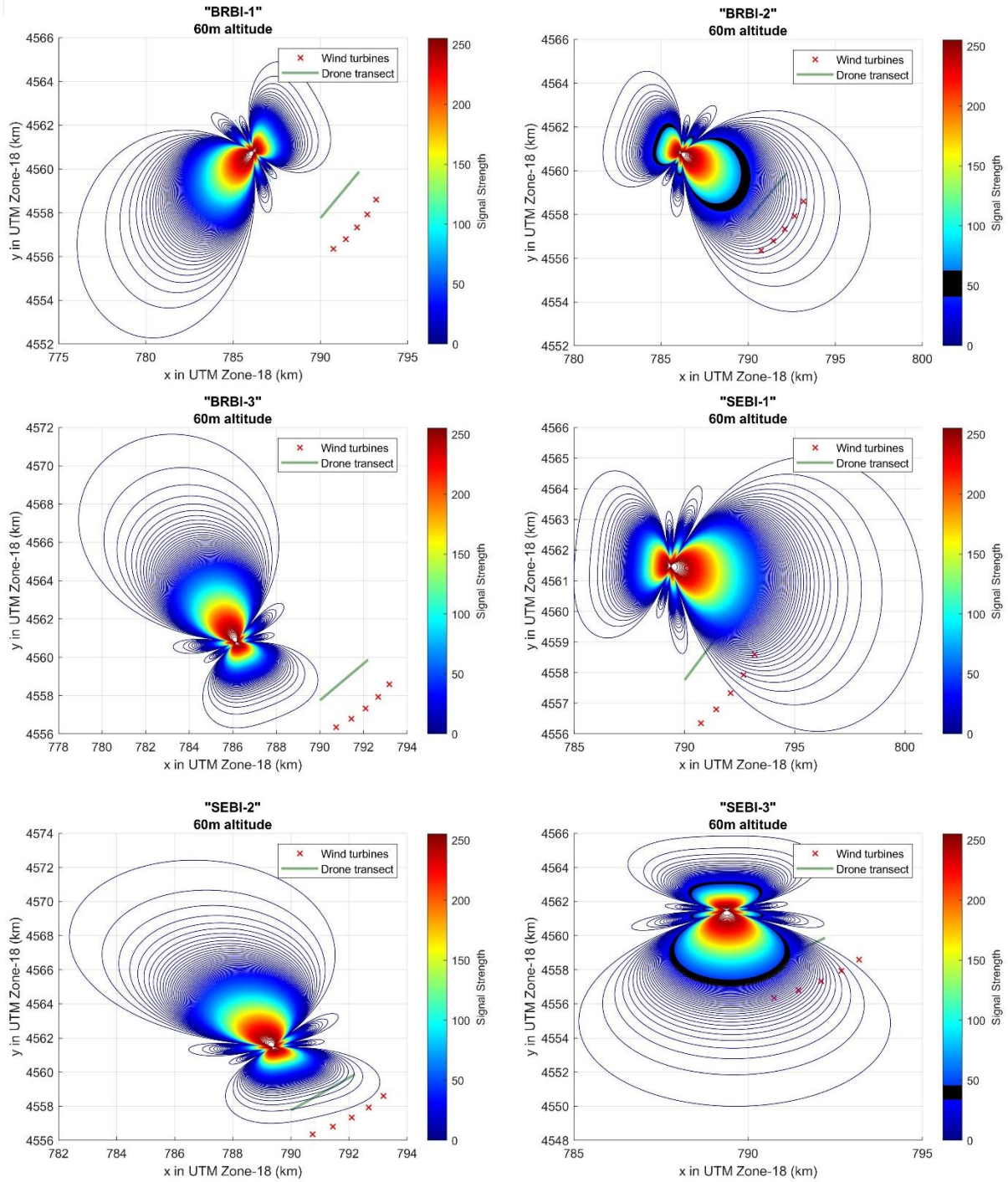

Figure 1.106. Estimated signal strength radiation pattern on 9 July 2019 for 5-element Yagi antennas at Black Rock (BRBI) and the Southeast Lighthouse station (SEBI) in 2019 assuming the test tag was flying at **60 m altitude**. Based on signal strength (between ~30-60) of the test tag, it was assumed to be located within the black zone. The transect the drone was flown on is shown as the green line. The 5 turbines at the Block Island Wind Farm are shown as red X's. UTM grids cells are 1 km by 1 km.

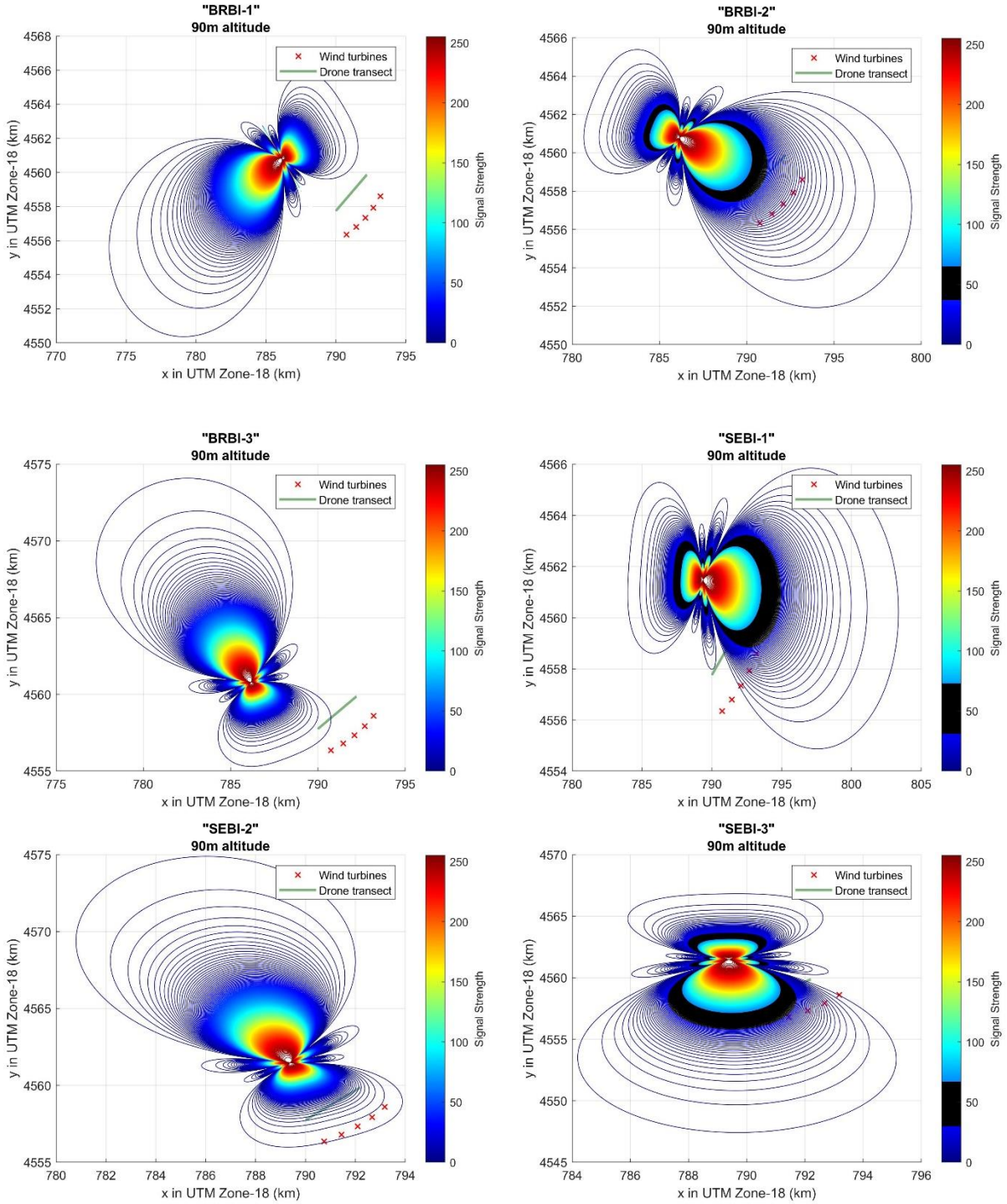

Figure 1.107. Estimated signal strength radiation pattern 9 July 2019 for 5-element Yagi antennas at Black Rock (BRBI) and the Southeast Lighthouse station (SEBI) in 2019 assuming the test tag was flying at **90 m altitude**. Based on signal strength (between ~30-60) of the test tag, it was assumed to be located within the black zone. The transect the drone was flown on is shown as the green line. The 5 turbines at the Block Island Wind Farm are shown as red X's. UTM grids cells are 1 km by 1 km.

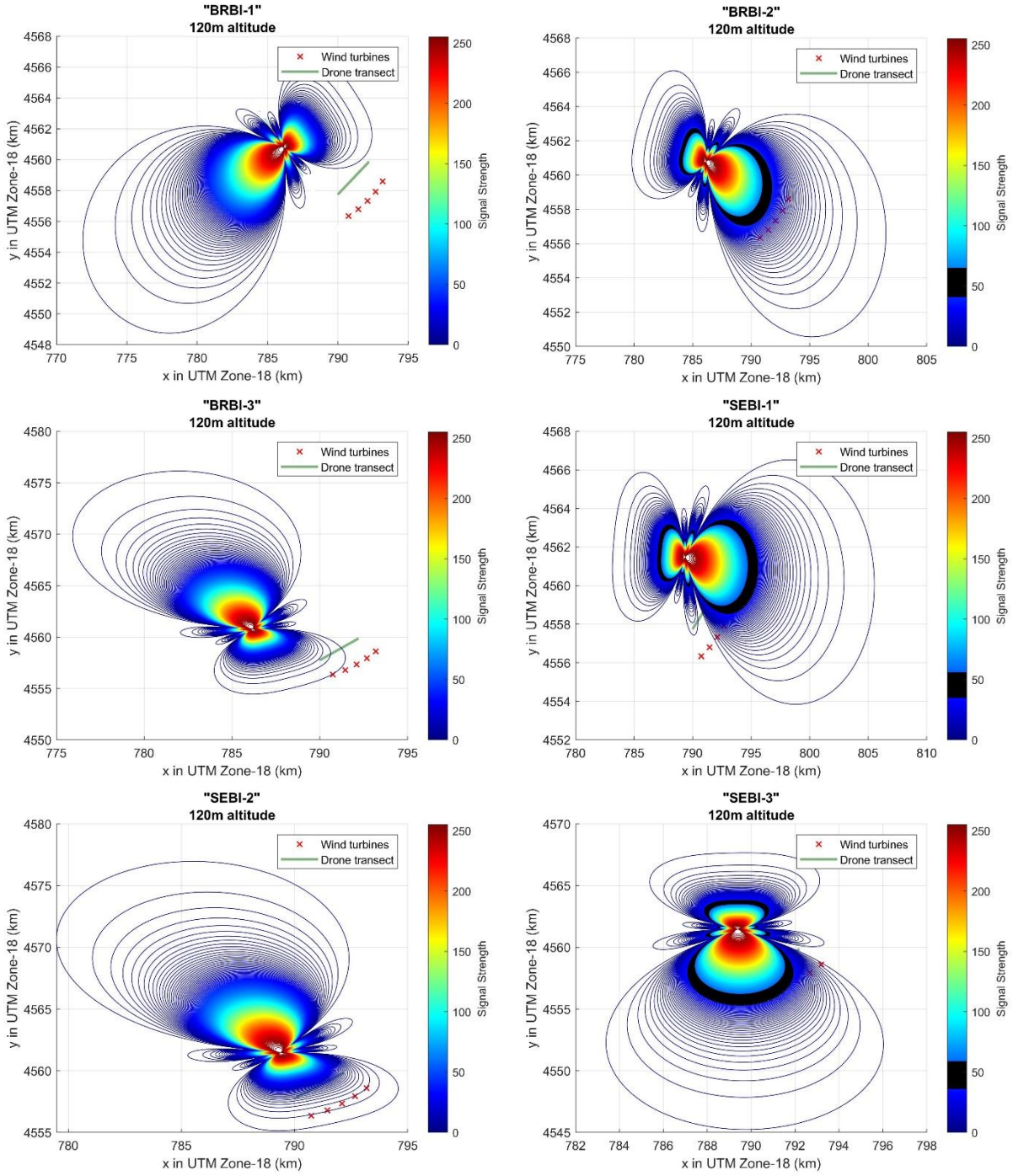

Figure 1.108. Estimated signal strength radiation pattern on 9 July 2019 for 5-element Yagi antennas at Black Rock (BRBI) and the Southeast Lighthouse station (SEBI) in 2019 assuming the test tag was flying at **120 m altitude**. Based on signal strength (between ~30-60) of the test tag, it was assumed to be located within the black zone. The transect the drone was flown on is shown as the green line. The 5 turbines at the Block Island Wind Farm are shown as red X's. UTM grids cells are 1 km by 1 km

1.5.1.5.1 9 July 2019 Drone Flight Model Results

There were statistically significant differences (H= 23.9, P < 0.001) in the accuracy of the model depending on the known flight altitude of the drone (Figures 1.109 & 1.110). There was a great deal of inaccuracy of model predictions when the drone was flying ≤60 m altitude, whereas when the drone was at a higher altitude accuracy was under 1 km. At 30 m asl altitude the difference between the actual and predicted location of the drone was 5,145 m (2,405 – 6,113; median, 25th% -75th%) and at 60 m asl, the difference between the actual and estimated location was 3,841 (1,800 – 5,700 m). At 90 m, the median difference was 958 m (246 – 1,855 m), while at 120 m the median difference was 826 m (633- 1,548 m).

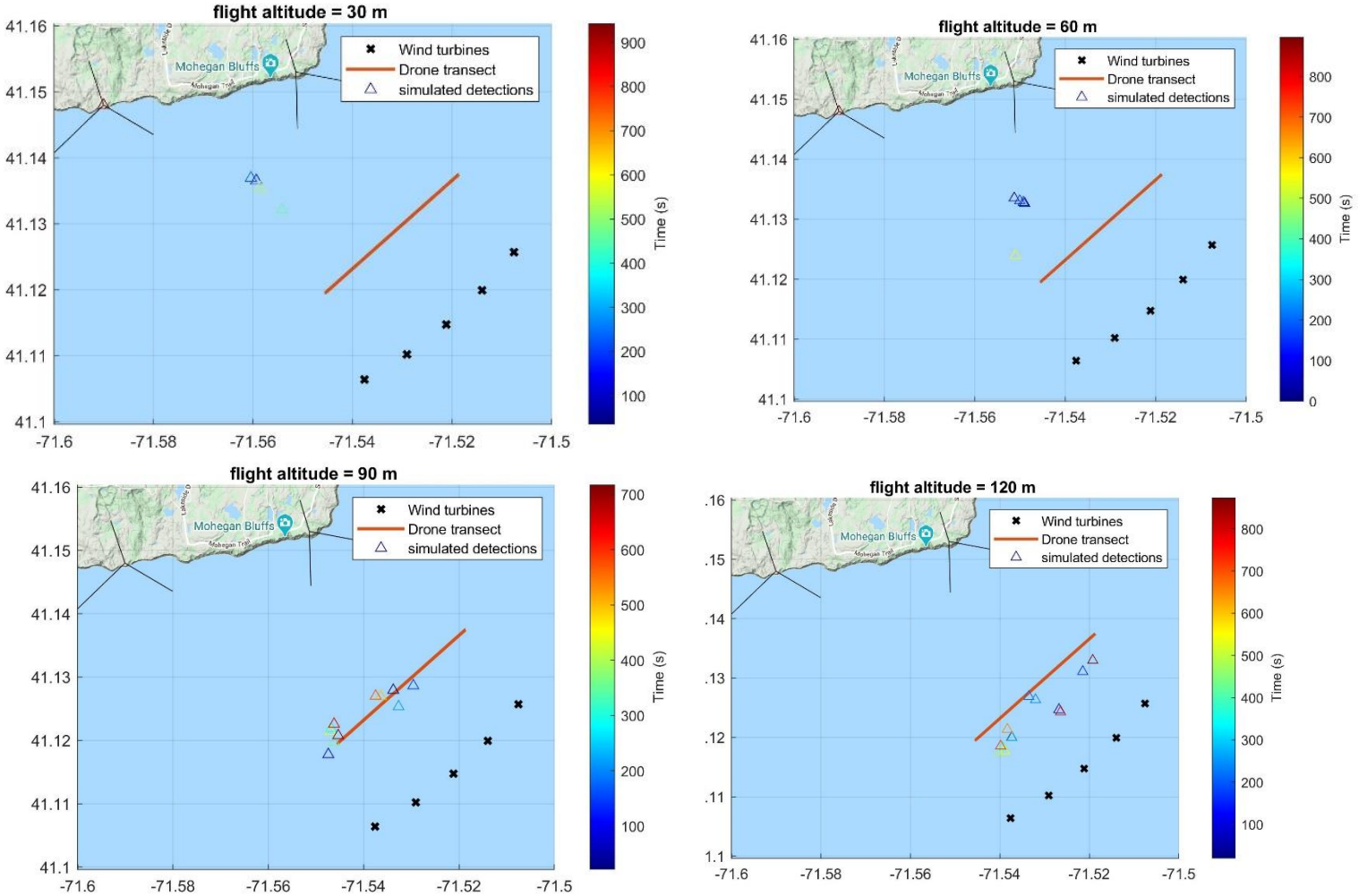

Figure 1.109. Calibration survey results for flight on 9 July 2019. Predicted locations of a test tag (colored triangles) based on simultaneous detections from automated telemetry stations located at Black Rock and SE Lighthouse on Block Island in relationship to the actual transect flown by a drone (orange line) at four different flight altitude: 30 m (upper left panel), 60 m (upper right panel), 90 m (lower left panel) and 120 m (lower right panel). The 5 turbines of the Block Island Wind Farm are shown (black squares). The drone flew at a constant speed of 10 m per sec

during these test flights. Model predictions were poor when the tag was flown at altitudes of 30 and 60 m, whereas the model was more accurate when the test tag was flown >60 m altitude.

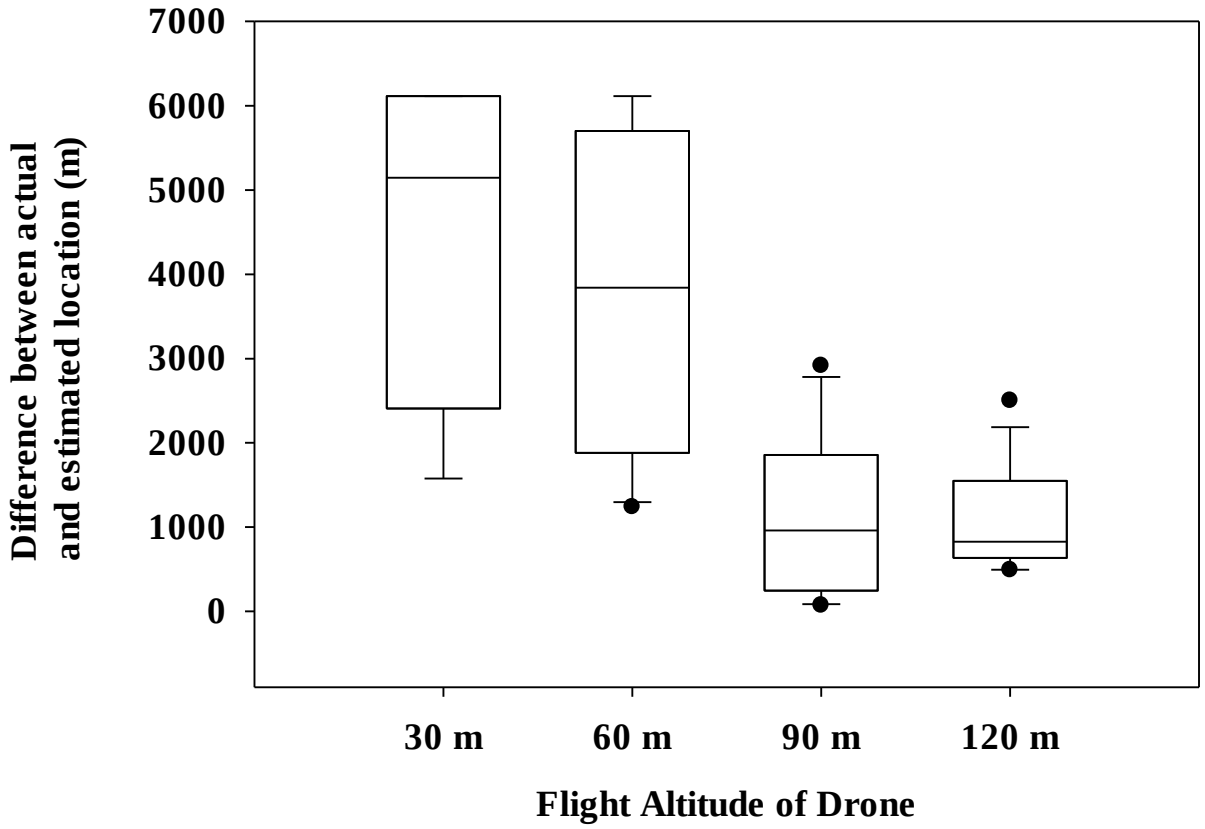

Figure 1.110. Accuracy and precision of model predictions to estimate the location of a test tag located on a moving drone flown at 4 altitudes during calibration survey on 9 July 2018 (see Figure 1.80). Model predictions were poor when drone was flown at altitudes of 30 m (median accuracy = 5,145 m) and 60 m (3,841 m), and more accurate when flown at 90 m (1,501 m) and 120 m (922 m).

1.5.2 Predicting locations of Wild Birds

From 2017 to 2019, the automated tracking stations on Block Island at Black Rock and Southeast Lighthouse detected a total of 157 tagged individuals from 15 different species (Table 1.18). We tagged Common and Roseate terns with digital VHF transmitters at mixed-species tern colonies in Long Island Sound (Great Gull Island, NY, and Falkner Island, CT), and Piping Plovers in southern Rhode Island from 2017 to 2019. We were most effective at detecting Common Terns, as we detected 79% of the 80 Common Terns we had tagged, with detection occurring either during the breeding or post-breeding seasons (Table 1.18). We also detected 24% of the 50

Roseate Terns that we had tagged, and 33% of the 58 Piping Plovers that we had tagged.

The major advantage of being part of the Motus network is that individuals tagged by other researchers were also detected by our automated telemetry towers. We detected 12 species (6 species of shorebirds, and 6 species of passerines) tagged by other researchers (Table 1.18). Many of these detected were the tower located at Southeast Lighthouse in 2017, which was a station constructed and operated by a previous BOEM funded study (Loring et al. 2019). It is unclear whether more tagged birds were available in 2017 to be detected, or if the increased tower height and antenna gain at the Southeast Lighthouse tower in 2017 affected detection rates.

Table 1.18. Summary of the total number of individual tagged birds detected by two automated tracking stations on Block Island, Black Rock and Southeast Lighthouse, from 2017 – 2019. We present the overall percentage of individuals that we tagged were detected by towers on Block Island.

	Cumulative number of individuals (% birds banded)			
Species	**2017**	**2018**	**2019**	**Total**
Common Tern	16 (80.0%)	14 (36.8%)	33 (82.5%)	63 (78.9%)
Roseate Tern	2 (10.0%)	10 (33.3%)		12 (24.0%)
Piping Plover	10 (50.0%)	5 (25.0%)	4 (22.2%)	19 (32.8%)
Semipalmated Plover	8	1	4	13
Sanderling	3	1		4
Red Knot	2	2	3	7
Least Sandpiper	1			1
Semipalmated Sandpiper	14	2		16
White-rumped Sandpiper	9			9
Gray-cheeked Thrush	2			2
Tree Swallow	2			2
Blackpoll Warbler			5	5
Nelson's Sparrow	1			1
Saltmarsh Sparrow	2			2
Ipswich Savannah Sparrow			1	1

One of the keys to predicting location of tagged wild birds is obtaining simultaneous detections from two or more automated telemetry stations to triangulate positions (Kenward 2001). However, obtaining simultaneous detections from the Black Rock and Southeast Lighthouse stations turned out to be much more challenging than expected in 2018 and 2019 (Table 1.19). In

our network of two towers on the southern coast of Block Island, most birds tended to be detected by only one tower.

Table 1.19. Percent of tagged individuals that were simultaneously detected at both the Black Rock and Southeast Lighthouse automated tracking stations in 2018 and 2019. Individuals that were not detected simultaneously were only detected at either the Black Rock or Southeast Lighthouse stations.

	% detected by both tracking stations?		Sample size
Year - Species	**No**	**Yes**	**N**
2018			
Common Tern	69.2	30.8	13
Piping Plover	100.0		5
Roseate Tern	81.8	18.2	11
2019			
Common Tern	72.7	27.3	33
Piping Plover	50.0	50.0	2

Another way to look at this issue is to look at the relationship between total detections in the overall network, the proportion of detections that were on Block Island, and finally the proportion of Block Island detections that were simultaneous (Table 1.20). We have summarized some examples from some birds we monitored in 2019. Across the entire network, these individuals averaged over 21,000 total detections, with most detections at their breeding colonies. However, these same individuals only averaged 225 detections at stations on Block Island, or ~3% of their total detections. Finally, simultaneous detections averaged 7.6 (SD = 8.9) per individual, which represents on average 7% of their detection when near Block Island. Thus, the odds of obtaining simultaneous detections with the network of towers we had operating on Block Island in 2019 was relatively poor, particularly given that the station on the Block Island Wind Farm was not active. Presumably if this station had been active, it would have improved the simultaneous detection rate due to additional antenna coverage.

Table 1.20. Examples of the probability of obtaining simultaneous detections of a tagged bird at tracking stations located on Block Island

Species	Tag ID	Total number of detections from stations			% of total detections at Block Island	% on Block Island that were simultaneous
		Total	Block Island	Simultaneous		
COTE	23	6518	43	3	0.7	7.0
COTE	24	28858	151	22	0.5	14.6
COTE	25	36955	41	1	0.1	2.4
COTE	27	59652	93	0	0.2	0.0
COTE	146	2164	165	18	7.6	10.9
COTE	176	17324	1155	24	6.7	2.1
ROST	253	37582	450	3	1.2	0.7
COTE	474	28381	52	0	0.2	0.0
PIPL	468	128	18	6	14.1	33.3
COTE	11	38128	105	0	0.3	0.0
COTE	15	10153	457	0	4.5	0.0
COTE	120	4277	210	0	4.9	0.0
ROST	17	3805	119	13	3.1	10.9
COTE	16	42319	222	7	0.5	3.2
COTE	20	4273	89	17	2.1	19.1

1.5.2.1 Tracks of actual tagged birds

We provide the tracks of two wild birds to provide evidence of the issues with estimating fine-scale movements of tagged birds. The first is a Common Tern (tag 25, Figure 1.111). We modeled movements based on flight altitudes of 20, 30, 60 and 90 m asl. As modeled flight altitude increased, the predicted locations of the bird came closer to the BIWF. Given that terns typically fly under 30 m altitude, it suggests that models showing movements <30 m asl are most realistic showing movements closer to Block Island. Johnston et al. (2014) modelled typical flight heights of Common Terns <30 m.

We also modeled the flight path of a Piping Plover, also at four different altitudes (tag 468, Figure 1.108). Depending on actual flight altitude, this bird was either flying close to the BIWF (altitudes of 20 and 30 m), or farther south of the BIWF. Thus, one of the critical challenges with this approach is determining flight altitude, as it had major implications for the predicted flight path of a bird.

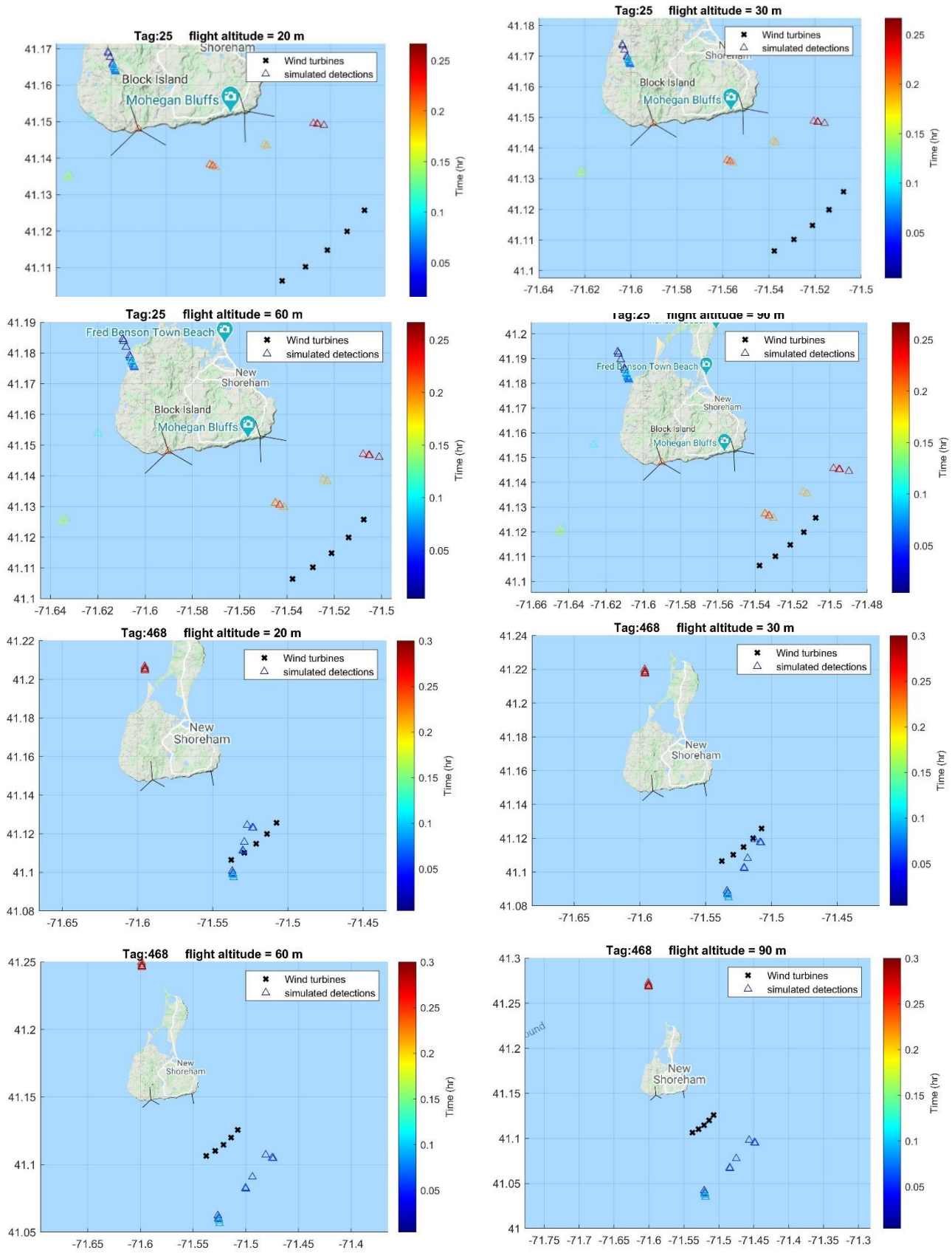

Figure 1.111. Predicted movements of a Common Tern (tag 25) and Piping Plover (tag 468).

1.6 DISCUSSION

We are entering the golden age of animal tracking science (Kays et al. 2015). Technology continues to become more miniaturized, thus allowing researchers to collect more accurate data on smaller species of wildlife throughout their annual cycle, while simultaneously being less invasive (McKinnon and Love 2018). Digitally coded radio transmitters monitored by automated telemetry stations (Taylor et al. 2017) are one recent advance that provides a unique opportunity to potentially monitor offshore movements of volant wildlife (Loring 2016, Dowling et al. 2017, Smetzer et al. 2017, Baldwin et al. 2018, Loring et al. 2019). The advantage of these miniature tags (as small as 0.2 g) is that they will emit a signal at short time intervals (e.g., every 5 second) thus have a high probability of being detected when moving past a specific point (e.g., using receiving stations within range of active or planned offshore wind energy facilities; Loring et al. 2018, 2019, Lefevre and Smith 2020). However, a major limitation of VHF and UHF transmitters is that receivers can only detect the signals of transmitters that are within detection range and line of sight (Kenward 2001), thus the geographic coverage of radio telemetry is limited relative to global-scale tracking technology such as satellite transmitters such as Argos- based Platform Transmitter Terminal (PTT) tags (Nicholls et al. 2007) or GPS tags (Fijn et al. 2017, Owen et al. 2019).

We used automated receiving stations with horizontally polarized Yagi-Uda antennas on the southern coast of Block Island to track the offshore movements of three focal species (Common and Roseate terns and Piping Plovers). Our goal was to model fine-scale movements of tagged volant wildlife using bi-angulation and triangulation from two or more automated radio telemetry stations as they flew near the Block Island Wind Farm. This was a unique opportunity as the Block Island Wind Farm was the first active offshore wind energy facility in North America, and it is relatively close to land (~5 km [3 miles]), thus Block Island's coastline provides sites to construct other automated radio telemetry stations to establish a tracking network. The only other offshore wind farm in the United States is Coastal Virginia Offshore Wind, which now has two 6-MW turbines located 42 km (27 miles) off the coast of Virginia Beach , thus is too far offshore to track tagged wildlife from land except for individuals flying at high altitudes.

As Kenward (2001) outlined, three types of automated telemetry stations have been developed. Cochran et al. (1965) designed and implemented a system of two rotating twin Yagi antennas placed on 20-30 m tall towers, which was an intriguing approach but far beyond the scope of this project (see also Řeřucha et al. 2015). The second approach is an array of fixed vertical dipole antennas to detect Doppler-effect frequency shifts but required high gain tags that would be impractical on small birds (Angerbjorn and Becker 1992; see also Ripperger et al. 2020). The third approach, and one we selected, utilized an array of fixed directional Yagi antennas (Larkin et al. 1996, Gottwald et al. 2019). This was the

approach that Loring et al. (2018, 2019) used along the Atlantic Coast to monitor offshore movements of birds.

The Motus network is a series of several hundred automated tracking stations designed to monitor digitally coded VHF transmitters on a specific frequency allowing thousands of individuals from multiple species to be tracked (166.380 MHz in North America; Taylor et al. 2017; Lefevre and Smith 2020). Most of the research using data collected at Motus stations has focused the chronology of regional movements (Crysler et al. 2016, Brown et al. 2017, Smetzer and King 2018, Anderson et al. 2019) rather than fine-scale movements. Some researchers have used Motus stations to assess factors affecting the timing and specific departure direction of movements, but they did not attempt to develop spatially explicit models of movements (Smolinsky et al. 2013, Deppe et al. 2015). Loring et al. (2018, 2019) used digitally-coded VHF tags to track the offshore movements of four species (Red Knots, Common and Roseate terns, and Piping Plovers), with a focus of modeling regional movements throughout the Atlantic OCS where offshore wind energy are in various stages of planning. In contrast, our goal was to assess the feasibility of using digital VHF transmitters to assess macro-movements near Block Island Wind Farm to assess potential exposure risk (Burger et al 2012).

Our intention at the outset of this project was to design a network of three stations to bi-angulate or tri-angulate the flight pathways of birds flying near the Block Island Wind Farm. Unfortunately, due to technical issues, the station on Block Island Wind Farm rarely worked, so we had to rely on simultaneous detections from the two stations on Block Island to model movements. The two automated towers located on the southern shore of Block Island were effective at detecting the three focal species we targeted for this investigation. In particular, the automated tracking stations detected 79% of the 80 Common Terns we had tagged at breeding colonies in Long Island Sound. This was not entirely unexpected as Loring et al. (2019) found that Common Terns routinely embarked on long foraging flights during the breeding season from Great Gull Island and Falkner towards Block Island Sound between Block Island and Montauk, NY. In addition, at the end of the breeding season, many Common Terns disperse from breeding colonies to Cape Cod, MA, where they stage for a month or more before migrating south generally far offshore to reach their wintering grounds (Nisbet and Mostello 2015, Loring et al. 2019, Althouse et al. 2019). In contrast, Roseate Terns were less likely to be detected south of Block Island, as we detected only 24% of the birds we tagged on Great Gull and Falkner.

We were moderately successful detecting Piping Plovers (i.e., 33% of 58 tagged birds were detected) as they dispersed from their breeding areas in coastal Rhode Island to stopover sites farther south. In fact, the 12-m tall tower in 2017 had higher detection rates of Piping Plovers than shorter towers (6 and 3 m, respectively) in 2018 and 2019. This may be because Piping

Plovers probably migrate north and west of Block Island as they travel east and south of Montauk, NY to migrate directly to coastal New Jersey or areas farther south (Loring et al. 2020). Therefore, shorter towers were less likely to detect this migratory pattern that does not have a major flyway south of Block Island where the radiation pattern of shorter towers were focused.

The major advantage of being part of the Motus network is that individuals tagged by other researchers were also detected by our automated telemetry towers. For example, Lefevre and Smith (2020) documented 35 species detected at Motus tracking stations in Florida. Similarly, we were able to detect the offshore movements of species of birds that were tagged by other Motus researchers. In fact, we detected 12 other species of birds (6 shorebirds and 6 passerines) and theoretically we could have detected tagged bats if they flew within detection range of our towers (Dowling et al. 2017), as all digital VHF transmitters are on the same frequency (Taylor et al. 2017). Of interest were the detections of federally threatened Red Knots, as this species is in decline and there is considerable interest in their offshore movements (Loring et al. 2018). We also detected Semipalmated Plovers all three years, as well as Sanderlings and Semipalmated Sandpipers in two years. This approach is highly dependent on other researchers tagging relevant wildlife. Although an investigation into how many different individuals were tagged each year of our study by others was outside the scope of this study, it would be possible to analyze Motus network data to determine if annual variation in detection rates reflected the pool of available tags, or if the fewer tags detected in 2018 and 2019 reflected actual movement patterns.

When we did detect tagged individuals, we were able to track them for relatively long time periods. The average run length was 11.9 min (SE = 0.8 min; median = 6.9 min; 25^{th}-75^{th} percentiles = 3.2 – 14.3 min; range = 0.4 to 110.5 min; N = 335 runs). This was encouraging, as it meant we had a high likelihood of modeling their movements. Somewhat surprisingly, we did not detect statistically significant differences in run length among species groups, which suggests that this type of monitoring is suitable for a wide range of species that may be detected flying past offshore wind energy facilities with active receiving stations.

One of the key aspects of this study was our work with calibration surveys which gave us insights into the detection rates of tags under various conditions. During calibration surveys, often stations were not able to detect the test tag (e.g., 10 and 27 June 2019), suggesting that under certain conditions the stations can perform poorly. In addition, our field tests suggested that the omnidirectional antenna performed extremely poorly, even though it had relatively high gain (6.5 m tall omni with 10 dB gain). Thus, we recommend that omnidirectional antennas not be used on offshore platforms, as they are not effective at detecting VHF transmitters.

Not unexpectedly, we found high variability in tag detection rates among different

configurations of receiving stations. This most likely was a function of the infrastructure and landscape characteristics near tower. Generally, the Southeast Lighthouse (SELI) Station had lower detection rates compared to the Black Rock (BLRO) Station. The tower at SELI had number of large structures, including the historic lighthouse 100m to the north of the station, a brick garage with a metal fog horn within 20 m to the west, and at least 4 other omnidirectional antennas within a 100 m radius that presumably had a major impact on detection rates of VHF signals from the relatively weak tags on the birds we were tracking. In contrast, Black Rock was on small hill with no immediate infrastructure nearby to interfere with the detection of VHF signals. In addition, the tower on Block Island used in 2019 were relatively short at ~3.3 m tall. Keward (2001) recommended placing antennas at least 2 wavelengths of the transmitter's frequency above the ground. Wavelength of the nanotag transmitters (166.380 MHz) is calculated by using the formula 300/166.380 = 1.8 m, therefore the antennas should have been at least 3.6 m above the ground. On the other hand, there were few sites on the southern shore of Block Island where we could construct telemetry towers, so we had limited options to place stations away from infrastructure or objects that could interfere with signals.

A key concern with our project was our inability to get all antennas to collect data continuously throughout the day for some receivers in some years. This happened at receivers we were monitoring on Block Island (Black Rock and Southeast Lighthouse [except 2017]), as well as the receiver placed on Turbine #1 on the Block Island Wind Farm. In 2018, we found that the Sensorgnome receivers with a raspberry pi were extremely challenging to operate continuously. We found that the external on-off switch on the Sensorgnome receiver was prone to hardware/software issues and would sometimes not work. As a result, we switched to Lotek receivers in 2019, which were used successfully by other BOEM funded studies (Loring et al. 2018, 2019).

We suggest that future research projects located on offshore wind energy facilities attempt to use receivers that utilize newly available, satellite-based data acquisition technology. When we originally contacted Deepwater Wind in 2017 to place a receiver on one of their turbines on the Block Island Wind Farm, we were hoping to utilize a receiver that could download data off the cell phone network, but this was not feasible as no reliable receivers had this capability that we were aware of. Thus, we had to ask Deepwater staff to manually download data. Due to security concerns, WIFI and Bluetooth were not viable options for monitoring receivers on offshore turbines. The new satellite-based data acquisition technology will allow receivers to be monitored remotely in real-time to determine if the receivers are actively collecting data and can upload data remotely. In addition, OSHA regulations are extremely stringent and require extensive training to work on offshore wind turbines, thus only staff working for offshore wind energy companies will have the qualifications to install and service receiving stations. Because trained staff working on offshore turbines have numerous responsibilities, utilizing newly available receiving stations with satellite-based data acquisition is highly recommended.

Projects that have been successfully develop movement models using detection of VHF or UHF transmitters have required multiple stations with directional antennas to ensure multiple simultaneous detections to triangulate positions (e.g., Řeřucha et al. 2015, Gottwald et al 2019), One of the weaknesses of our project was that although we attempted to have three stations to triangulate movements tracks of birds near the Block Island Wind Farm, we often did not have simultaneous detections from more than one station, which limited application of our movement models. Thus, future efforts should be focused on developing a network of tracking stations to obtain simultaneous detections to model fine-scale movements near offshore wind energy facilities should be the goal.

Designing a network of automated radio telemetry stations located on offshore turbines to track movements of volant wildlife with VHF or UHF transmitters will be challenging. The primary goal should be at a minimum to estimate exposure risk (Burger et al. 2011) or even more difficult will be to estimate avoidance (Skov et al. 2018). More advanced models can estimate the altitude of the bird; it starts with an initial altitude for the bird to find the horizontal location of the bird. Then, the intersection of the projected horizontal contours of each antenna results in the location of the bird. If there is no intersection between the contours in the initial altitude, the altitude automatically increases by a specified value until the intersection of the contours are achieved (Janaswamy et al. 2018).

The key to designing a successful network to track movement trajectories of volant wildlife is to have multiple stations place in the correct configuration based on the predicted radiation patterns of Yagi antennas (Janaswamy et al 2018), such as we utilized for this project. We have provided the code to estimate radiation patterns that future planners could utilize for planned offshore wind energy projects. For example, there are three major projects planned for Rhode Island Sound (e.g., Revolution Wind: 704 MW project, 88 turbines; South Fork: 132 MW, 15 turbines; Vineyard Wind: 800 MW, 84 turbines) have numerous offshore turbines that could be used place automated radio telemetry receiving stations. When automated radio telemetry receivers (either VHF or UHF) are placed on offshore turbines in the future, we suggest that receivers are placed on multiple turbines and constructed in a configuration to maximize the probability of estimating exposure risk by tracking the meso-scale movements via triangulation. This means that each receiver should have at least 4 Yagi antennas to maximize coverage in all directions from each offshore turbine where a receiver is located. Finally, we recommend that omnidirectional antennas should be avoided on offshore turbines due to low detection rates.

PART II: TRACKING MIGRATORY BIRDS: APPLYING A PASSIVE TRACKING TECHNIQUE USING DIRECTION OF ARRIVAL FROM VHF RADIO TAGS

Section II Authors:

Jesse Moore, Department of Ocean Engineering, University of Rhode Island
James Miller, Department of Ocean Engineering, University of Rhode Island
Gopu Potty, Department of Ocean Engineering, University of Rhode Island
Peter W.C. Paton, Department of Natural Resources Science, University of Rhode Island

2.1 Introduction: Using Phase to estimate locations of transmitter

Wildlife biologists have been tracking organisms with radio transmitters (hereafter tags) in the very high frequency (VHF) band since the 1950s (Cochran et al. 1965, White and Garrott 1990, Kenward 2001). VHF is the designation of radio waves with wavelengths ranging from 1 to 10 m that correspond to radio frequency electromagnetic waves that range from 30 to 300 megahertz (MHz). Tracking organisms within the VHF band requires a

transmitter (hereafter tag) that emits a signal (e.g., ~166.380 MHz), some type of attachment system to mount the tag on the organism(s) of interest that minimizes impact to the organism (Barron et al. 2010, Geen et al. 2019), an antenna, and a receiver to process the signal detection (Kenward 2001). VHF works on a "line of sight" detection, that is there cannot be a land barrier (e.g. hill) between the receiving station and the transmitter emitting the signal.

Radio Direction Finding (RDF) requires a passive receiving system that extracts information from passing electromagnetic radio waves from a very high frequency (VHF) transmitter to estimate the bearing angle from the receiver to the VHF transmitter. There are three RDF approaches that researchers typically use to estimate the position of the tag from two or more receiving stations: amplitude response, phase response, and time of arrival (Jenkins 1991, Kenward 2001). Most avian ecologists use the amplitude response to estimate the location of tagged individuals (White and Garrott 1990, Kenward 2001), which infers location based on a combination of signal strength and compass bearing (Desrochers et al 2008, Gottwald et al. 2019). Biologists typically estimate the compass bearing of a tag from the receiver by rotating a directional antenna, either a Yagi or H-Adock, to detect the maximum signal strength or the null signal, respectively. (Cochran et al. 1965, White and Garrott 1990, Kenward 2001). The receiving stations must be known locations, but they can either be a series of temporary locations or fixed locations.

An alternative approach to estimate the bearing from the receiving station to the tagged organism is using phase delay measurements, which requires a minimum of two fixed dipole antennas, which are omnidirectional in the horizontal plane. The two antennas should be separated by distance, *d*, which should be ½ the wavelength (λ) of the VHF transmitter being tracked are calculated using Equation 1 below:

$$\tau = \frac{2\pi d}{\lambda} sin(\phi) \qquad (1)$$

As an incident plane wave arrives at angle, φ, it first reaches antenna 1. The wave then travels the distance of $dsin(\varphi)$ before reaching antenna 2. The voltages induced at antenna 1 and 2 are $V_1 \exp j\omega t$ and $V_2 \exp j\omega t$, respectively. Therefore, the bearing angle φ is a function of phase delay (Figure 2.1).

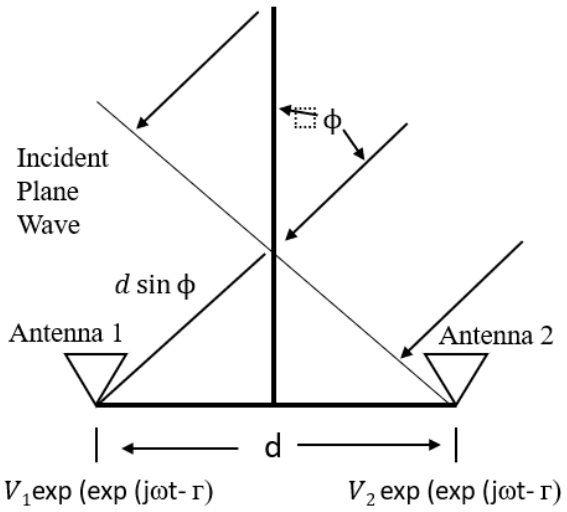

Figure 2.1.Schematic showing Radio Detection Finding based on phase delay measurements based on Jenkins (1991).

2.1.2 Calculating Phase with Two Antennas

When designing a phase delay system, the spacing between antennas is critical and they must have a maximum distance of $\lambda/2$, where λ is the wavelength of the transmitter signal, limiting the maximum phase shift δ to be within π radians (Jenkins 1991). For this study, the frequency of the digitally-coded VHF transmitters was 166.380 MHz which equals a wavelength was 1.80185 m. The bearing precision is estimated as a function of $\Delta\delta/\Delta\varphi$, phase delay over the bearing, with a unit of degrees per degrees.

$$\theta = \arcsin \sqrt{\delta_1^2 + \delta_2^2} \frac{\lambda}{2\pi d} \qquad (2)$$

Equation 2 depicts calculations needed to obtain azimuth angle, where $\delta_{1 \text{ and }} \delta_2$ is phase delay for the respective antenna, d is distance between antennas and λ is wave- length.

The process of estimating the phase delay is described in depth by Jenkins (1991). When passive radio waves are detected by 2 antennas, they are first processed by a dual-channel receiver and then processed by a phase detector (Figure 2.2). The phase detector can output either: (1) analog measurements by summing the analog vectors, (2) digital versions of the sine and cosine waves or (3) passed to a phase comparator (CRT) for a visual output. Typically, the analog phase measurement accuracy decreases when there are frequency variations and a low signal-to- noise ratio (SNR), while digital phase measurements tend to be more stable (Jenkins 1991).

To minimize phase errors, the unmodulated carrier frequency should be set to the center frequency. Phase errors are introduced to the system when there are frequency-shift-keyed signals, where a Fast Fourier Transform (FFT) would show asymmetrical spectral features for both antennas but with differently shifted signals (Jenkins 1991) (Figure 2.3). Phase averaging can be implemented to reduce these phase errors.

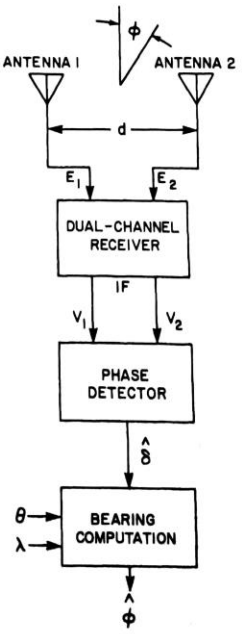

Figure 2.2. Schematic showing the steps needed to obtain a bearing from a remote VHF transmitter using a dual-channel two antenna system using phase measurements (Jenkins 1991)

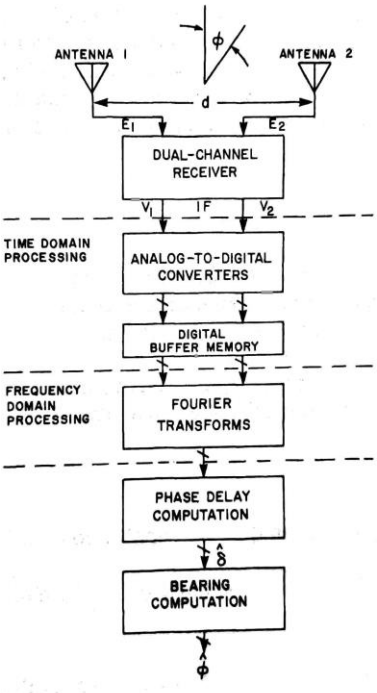

Figure 2.3. Steps needed to estimate signal bearing using the Fast Fourier Transform method (Jenkins 1991).

Step 1 consists of converting the analog signal to digital signal conversion and then storing digital samples, which then are used for performing a Fast Fourier Transform. Then the real and imaginary components can be used to calculate phase using the Equation 3.

$$\gamma = \arctan(i/r) \tag{3}$$

The Fourier transform method has many advantages including (1) reduced signal amplitude variations, (2) improved sensitivity (i.e., up to 30 dB), (3) options for frequency and phase corrections, (4) ideally suited for short duration bursts, (5) interference can be limited by eliminating the undesired spectral components, and (6) digital can be stored and adapted through extra post-processing. This technique is adept for short duration uncooperative transmissions in dense electromagnetic environments (Jenkins 1991).

2.1.3 Calculating Phase using Three Antennas

Phase interferometry typically includes three antenna elements, which are constructed in an equilateral triangle (the spacing between antennas must have a maximum distance of $\lambda/2$, where λ is the wavelength of the transmitter signal), and attached to a triple-channel receiver (Jenkins 1991). For this approach, each antenna is connected to the same receiver to maintain system coherence, which eliminates antenna switching and produces phase measurements and bearing calculations in real time (Figure 2.4a).

This three-antenna array can estimate both azimuth and elevation of the target with similar accuracy of a two-antenna system with the Fourier transform method implemented. However, the three-antenna system requires a highly intensive computational capability for calculating the phase and a signal calibration injected into the system (Jenkins 1991) based on three calculations in equations 4a – 4c:

$$\delta_{1-2} = (2\pi d/\lambda)cos(\phi)sin(\theta) \tag{4a}$$

$$\delta_{3-1} = (2\pi d/\lambda)cos(\phi - 120^{\circ})sin(\theta) \tag{4b}$$

$$\delta_{2-3} = (2\pi d/\lambda)cos(\phi - 240^{\circ})sin(\theta) \tag{4c}$$

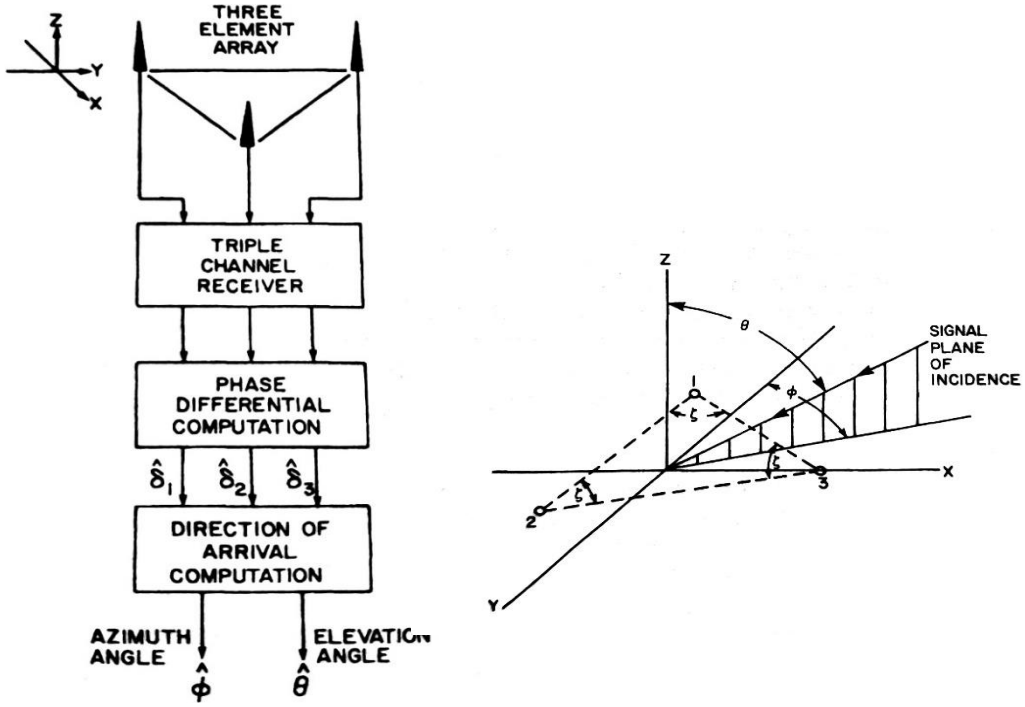

(a) Process to estimate a bearing using the Fourier transform method.

(b) Geometry of triple channel receiver, showing azimuth, elevation and relative angles of antennas $\zeta = 60$

Figure 2.4. Schematics for understanding the processing and geometry of a triple-channel receiver (Jenkins 1991).

Both azimuth and elevation can be estimated using three calculated azimuths angles referenced to the three baselines seen in Equations 5a - 5d, where θ is elevation and φ is azimuth as shown in Figure 4b.

$$\theta = \arcsin\left(\sqrt{\delta_{1-2}^2 + \delta_{3-1}^2 + \delta_{2-3}^2}/[(2\pi d/\lambda)(\sqrt{(3/2)})]\right) \tag{5a}$$

$$\phi_{1-2} = \arctan\left(2\delta_{2-3} + \delta_{1-2}\right)/[(\sqrt{(3)})(\delta_{1-2})] \tag{5b}$$

$$\phi_{1-3} = \arctan\left(2\delta_{3-1} + \delta_{1-2}\right)/[(\sqrt{(3)})(\delta_{1-2})] \tag{5c}$$

$$\phi_{2-3} = \arctan\left(2\delta_{2-3} + \delta_{3-1}/[(\sqrt{(3)})(\delta_{2-3} + \delta_{3-1})\right] \tag{5d}$$

With the φ_{i-j} values, summing them estimates the azimuth bearing using Equation 6.

$$\phi = \arctan\frac{\cos(\phi_{1-2}) + \cos(\phi_{1-3}) + \cos(\phi_{2-3})}{\sin(\phi_{1-2}) + \sin(\phi_{1-3}) + \sin(\phi_{2-3})} \tag{6}$$

Three methods of reducing error are using (1) three antenna systems to remove random measurement errors, (2) utilizing a calibration source to provides a common local oscillator among the antennas to identify phase mismatch errors, and (3) create correction tables based on errors from scattering and coupling (Jenkins 1991).

2.1.4 SNR Phase Degradation

In order to obtain near-field direction of arrival estimation, one could apply phase differences between multiple signals (David et al 2016). One approach is using a quadrature phase detector which works in the digital domain after being converted using an ADC converter (David et al. 2016). Salido-Monzú et al. (2016) focused their research on factors affecting on the degradation of the phase value. Sampling radio signals can be intensive on an acquisition system. Salido-Monzú et al. (2016) chose to purposefully under sample a signal to reduce those requirements on the acquisition and concluded that it can be beneficial but causes some phase estimation uncertainty. The phase degradation results from noise aliasing that causes low signal to noise ratio (SNR) and instabilities in the frequency response. To reduce the noise aliasing effects, David et al (2016) proposed a more restrictive anti-aliasing filtering of the analog signal. However, this would cause more phase uncertainty due to drifts.

Variations in f_0 are greatly affected by the phase sensitivity based on Q, the quality factor of the filter (see Equation 7 below), while the quality factor is affected by the relationship between the quality factor and relative frequency deviation (see Equation 8). By assuming that $f \approx f_0$, the sensitivity of phase, can be related to the quality factor directly. With these equations the minimum stability of components and maximum quality value can be used to design the band-pass filter.

$$\Delta\phi_{H(jf)}\Big|_{\Delta f_0, f\approx f_0} \approx 2Q\frac{\Delta f_0}{f_0} \tag{7}$$

$$\Delta\phi_{H(jf)}\Big|_{\Delta Q, f\approx f_0} \approx 2Q\frac{f_0 - f}{f_0}\frac{\Delta Q}{Q} \tag{8}$$

The designed filter results in a constant phase shift for every received signal where the difference between the two signals is the relative phase difference between them and is a constant (Figure 2.5). Overall Salido-Monzú et al. (2016) found that a bandpass filter, rather than a low pass filter, reduces the sampling speed by 60% with <29% loss of precision. This is important for reducing digitization system cost and computing load, which reduce loss of precision.

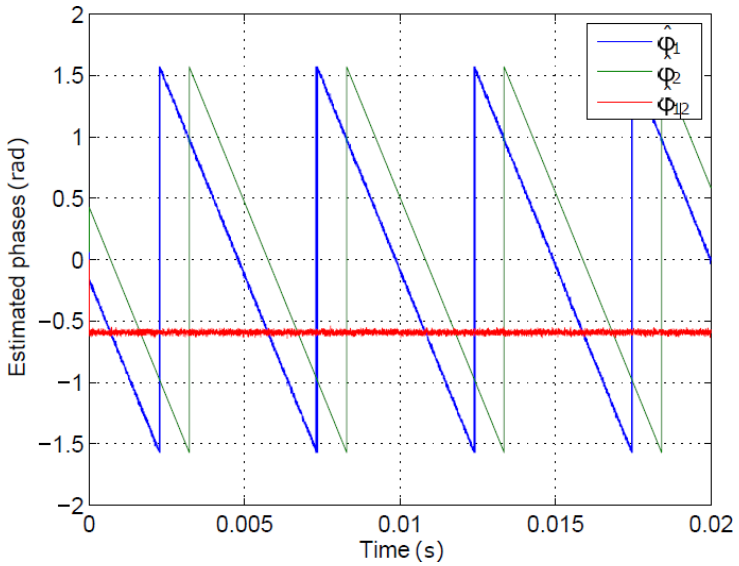

Figure 2.5.Output of phase meters from David et al. (2016).

2.2.0 Methods

2.2.1 Transmitter

The transmitter we used for this project was the digitally-coded VHF with a carrier frequency of 166.380 MHz and 7 sec burst intervals (www.Lotek.com, nanotag; hereafter test tag). This test tag had a lifespan of approximately 280 days, weighed 0.9 g, and a transmission power of -30 dBm (Figure 2.6). Note that other tags, such as the plover and tern tags, typically are programmed to emit a signal every 5-6 sec (Loring et al. 2019).

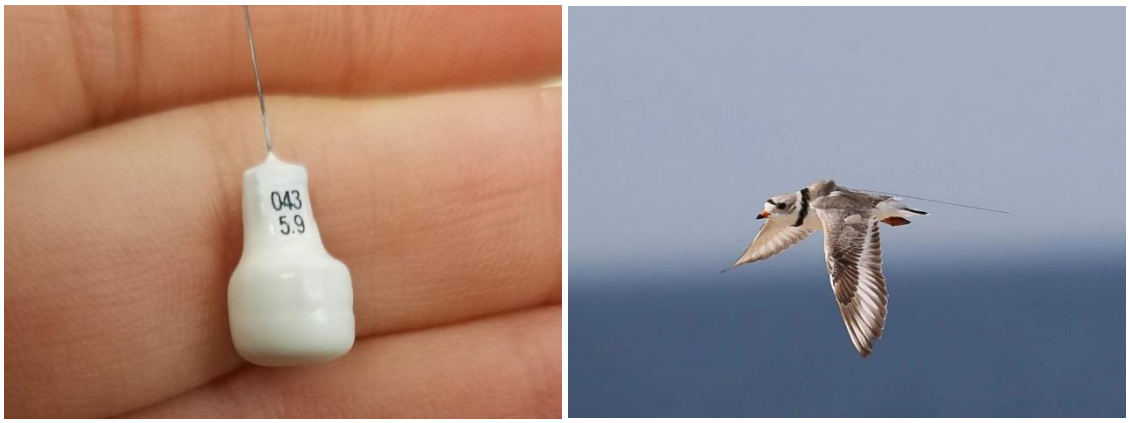

(a) Nanotag used for testing. Photographed

(b) Tagged Piping Plover.

Figure 2.6. Digitally coded VHF transmitter used for this study and tagged Piping Plover in flight.

2.2.2 Receiver Design

The list of materials needed to construct the three-element antenna array, including the receiver, and associated equipment are available in Moore (2020; Appendix A).

2.2.3 Antennas for phase delay array

We used three Shakespeare 476 Classic VHF antennas to construct the phase array (Figure 2.7). These antennas were 6.4 m tall, omnidirectional in azimuth, and have a gain of 10 dB. These antennas are collinear arrays, specifically Franklin arrays, that consist of a meander-line phase reversal.

Figure 2.7. System using three Shakespeare 476 Classic VHF antennas 6.4 m omnidirectional antennas used for phase delay estimation of bearing from receiver to a tagged organism. Dr Jim Miller (r), Fred Pease (l), and Jesse Moore (c – kneeling) are shown during construction.

In order to calculate bearing using phase, the distance between the antennas must be less than or equal to half the wavelength of the incoming electronic pulse (for a 166.38 MHz – 0.9015 m) to limit the ambiguity of the signal bearing. Thus, we spaced the three antennas at ~0.5 wavelength, or 0.889 m, for this experiment.

The estimated beam pattern for each of the three omnidirectional antennas is shown in Figure 2.8. The main beam of the antenna was directed horizontally and was omnidirectional in azimuth. Each antenna had sidelobes: -13.3 dB at 24.2˚, -17.9 dB at 44.3˚, and -21.0 dB at 90.0˚ above and below the horizontal. These sidelobes are also omnidirectional in azimuth

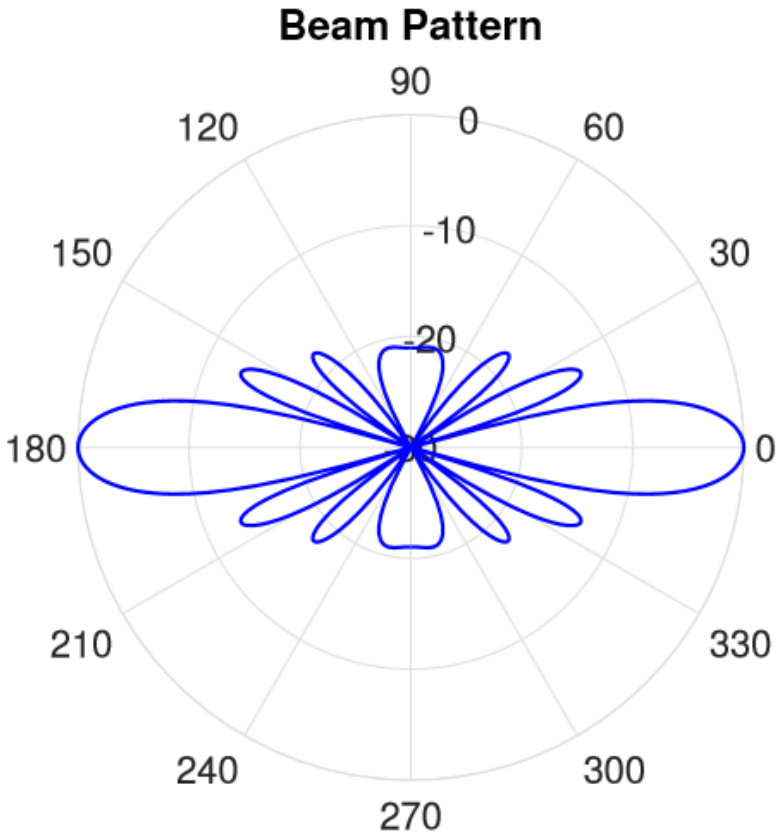

Figure 2.8. Estimated beam pattern for omnidirectional antennas used for this experiment.

2.2.4 Phase Delay Antenna Design

Fred Pease, URI Staff, designed and constructed the antenna array (Figures 2.9 and 2.10). The main constraints were that the system was stable and durable enough to handle harsh weather, uneven land, wind and being elevated high enough above the ground to optimize the beam pattern, as well as the possibility of placing the system on uneven terrain. In addition, the three antennas had to remain equidistant and vertical.

The array consisted of a welded base center set into the group, 2" x 6" pieces of wood for extra surface tension (Figure 2.9b), galvanized metal clamps securing the antennas 0.889 m equidistantly from the metal poles with PVC spacers (Figure 2.9c). The PVC spacers were placed 3.4 and 4.8 m up the antennas using custom-milled 4" diameter PVC discs insert over the antennas and attached with 1" diameter PVC rods. For stability in uneven terrain, we added three leveling rods. The final step for the installing of this structure includes three guy wires to ensure stability of the system.

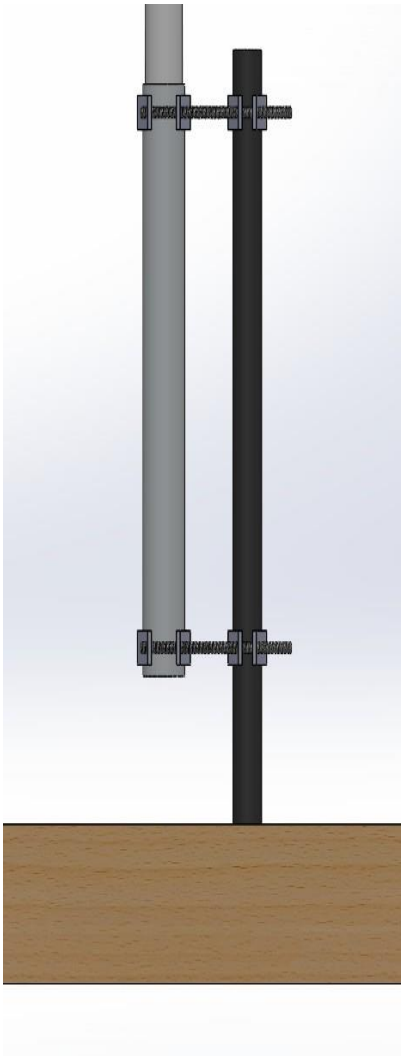

(a) Galvanized antenna clamps with adjustable threaded rod.

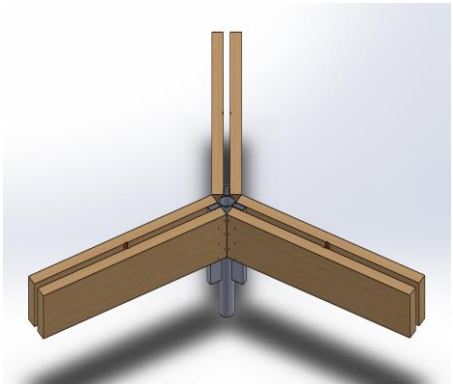

(b) Base of the antenna structure, including a welded metal piece with wooden 2x6 screwed in.

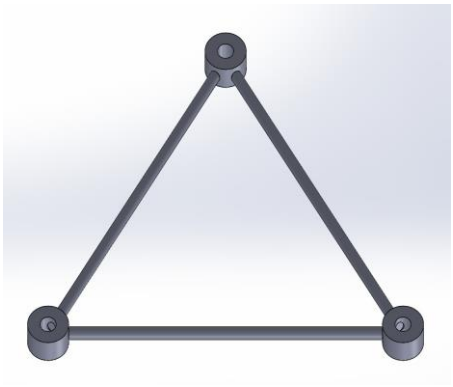

(c) Spacers: PVC rods and milled PVC glued together.

Figure 2.9. Components of the phase array antenna system in Figure 2.7

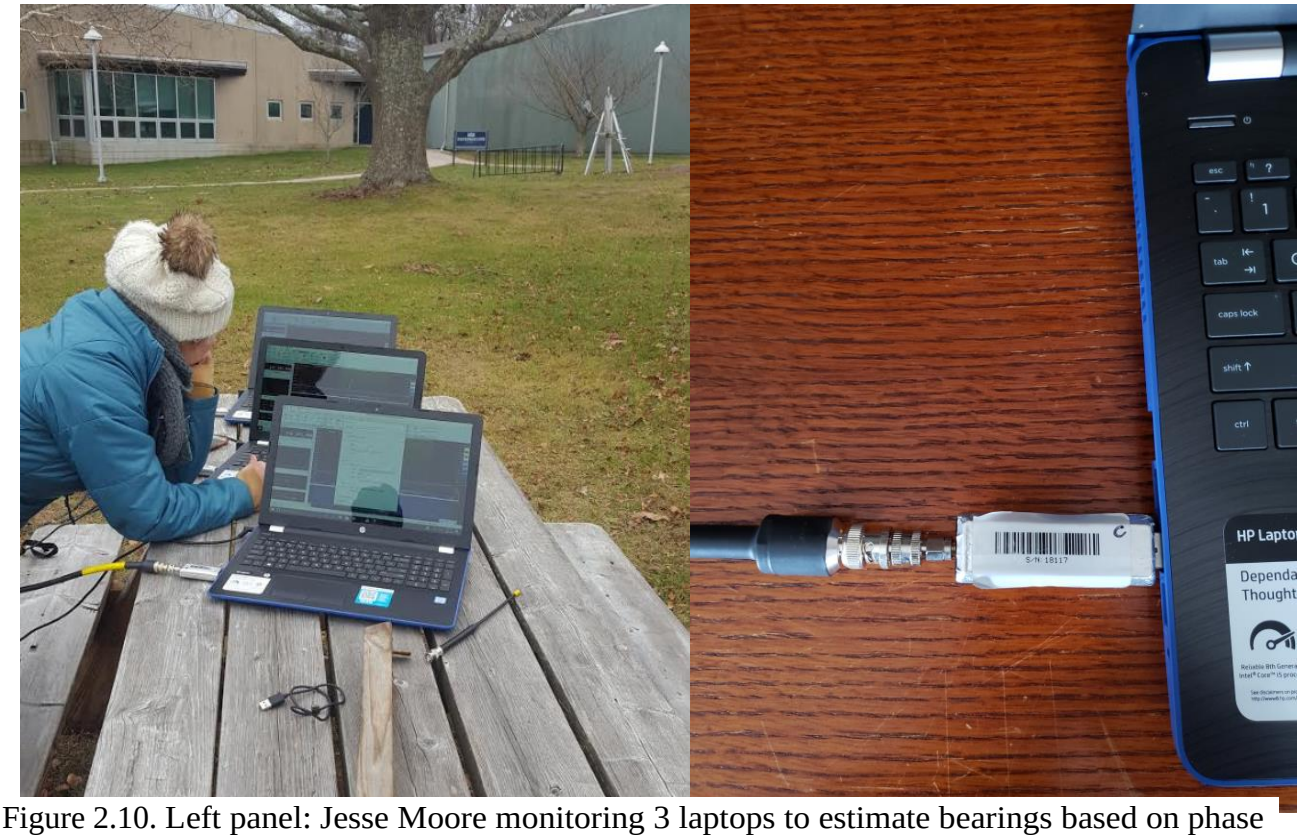

Figure 2.10. Left panel: Jesse Moore monitoring 3 laptops to estimate bearings based on phase delays, Right panel: coaxial cable connected each 6.4 m omnidirectional antenna to a FUNCube Dongle to convert the analog signals to digital for the SDR software.

2.2.5 Data Collection

2.2.5.1 Hardware components of phase delay array

Each of the three antennas was connected to a USB FUNCube Dongle (FCD) using a coaxial cable (TWS400-15 - 15' Jumper with TWS400 3/8", 50-ohm braided cable with BNC Male and UHF Male Installed) (Moore 2020: Appendix A; Figure 2.10). We then connected the FCD via the USB port to a laptop, which ran Software Defined Radio (SDR) (Moore 2020: Appendix B) to capture data collected during the experiment.

The antennas received the electromagnetic plane waves and send the voltage to the FCD (Wickert 2000). The received signal, $r(t)$, was passed through a low-noise amplifier (LNA) and a radio frequency (RF) tuner connected to a local oscillator to grant the user tuning control for the center frequency. The RF mixer had three ports, two of which are inputs and one output. These ports are referred to as the RF input port, local oscillator (LO) input port and the RF output port. The output is the two signals $r(t)\pm$LO, where the signal from LO is usually a sinusoidal continuous wave or square wave. The purpose of the RF mixer is to change the frequency of the electromagnetic signal while maintaining original characteristics such as phase and amplitudes. By doing this the signal can be amplified at a

baseband frequency (Nickolas 2011).

$$A(t)\cdot\sin[2\pi ft+\phi(t)] = A(t)\cdot\sin(2\pi ft)\cdot\cos[\phi(t)] + A(t)\cdot\sin(2\pi ft+\frac{\pi}{2})\cdot\sin[(\phi(t))] \quad (10)$$

This process is known as demodulation (Equation 10), where $A(t)$ is amplitude, $\varphi(t)$ is phase, partly due to propagation. The demodulated signal is then filtered by the low-pass filter (LPF) and then to the variable gain amplifier (VGA) to help increase SNR before being output through the analog-to-digital converter (ADC). The control box shows that the through SDR software, the LNA and VGA can be adjusted (Figure 2.11).

The accuracy of the output signal, $r[n]$ was dependent on the ADC bit depth, ADC sample rate, local oscillator quality and RF mixer stability. In this case, the FCD has a stability of ±1.5*ppm* **Error! Hyperlink reference not valid.**. When applied to the test tag frequency, the frequency has a variation of ± 249.57 Hz (www.funcubedongle.com). Also, the ADC bit depth affected the noise floor. To reduce noise and increase dynamic range a larger bit depth is necessary (VonEhr et al. 2016).

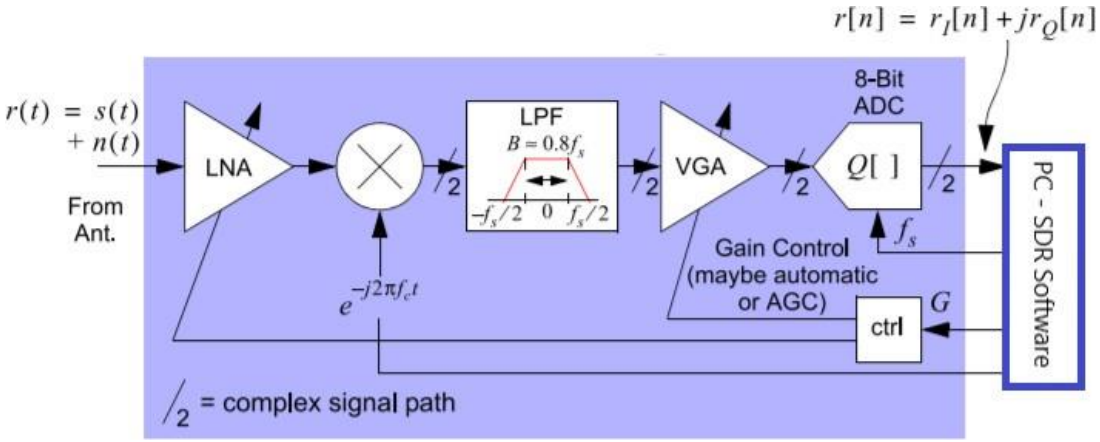

Figure 2.11. Behavior level model of RTL-SDR, comparable to the FUNCube Dongle. Adapted from Wickert 2000.

Figure 2.12.SG 380 series Rf signal generator used generate ultra-high frequency resolution (1 *u*Hz) used a precise calibration source generator with rubidium timebase.

During the summer of 2018, the system included a RF Explorer (Digi-Key Electronics 1597-1173-ND, Thief River Falls, MN) as the calibration source. The generator has a frequency stability of ±0.5 ppm and a frequency accuracy of ±1 ppm (RF Explorer Signal Generator 2019).. After preliminary analysis of the data, we determined the accuracy for the RF Explorer was not suitable for phase processing for this research project.

During the 2019 field season , to reduce errors and synchronize the three antennas, we used a precise RF signal generator (Stanford Research Systems SG380, Sunnyvale, California; Figure 2.12) with a rubidium timebase provided a stability of <±0.0001ppm (166.38 MHz ± 0.016 Hz) . We set the signal generator to propagate a continuous 166.385 MHz sine wave (5,000 Hz above the nanotag carrier signal) through a 5.8 GHz rubber duck omnidirectional antenna. We placed the calibration source antenna equidistant from the three antennas in the center of the phase delay array.

Once the array was constructed, we recorded data with the SDR software at specific time intervals for a set duration on the three computers. The down converted signal was then saved into a .wav file for post-processing. For this experiment, we selected a sample rate of 44.1 kHz with a center frequency of 166.385 MHz's The two channels of the .wav file contained the inphase and quadrature components of the tag signal complex envelope (Proaskis 2006).

2.3.0 Results

During the summers of 2018 and 2019, we conducted both stationary testing and drone testing.

2.3.1 Fixed Tests

In the summer of 2018, we performed a series of experiments to determine the precision of the recording systems by placing a stationary nanotag near the phase delay array. FUNcube dongles (FCD) were labeled as A, B and C to estimate the variation in their clocks. In this test, the original calibration source (RF Explorer) was turned on after a few seconds. A snippet of the recorded data (Figure 2.13) shows the magnitude after filtering and the corresponding unwrapped phase values. This visually shows the time differences of the computer clocks and respective amplitude differences. The time of arrival differences from the antenna 1 to antenna 2 and 3 recording systems were 36 and 6 ms respectively, and had amplitude differences of 0.011, and 0.023. The magnitude inconsistencies could be attributed to the filtering process within the FCD or antenna cable connections having different percentages of physical contact. In other words, the SO-239 type connector on the bottom of the antenna and the UHF connector from the coaxial cable potential affected the results. On the bottom panel in Figure 2.13, the unwrapped phase is shown with and without the calibration source on. At first there were small variations in the phase, but when calibration source was turned on, the phase values began to drift. By having the calibration source equidistant from each antenna, phase values should have been nearly equal. The unwrapped phase values from antenna 1 exhibited a negative differential fringe, because the wrapped phase values jumped from $-\pi$ to π. In contrast the antennas 2 and 3 that have phase jumps from π to $-\pi$. The differentials for antennas 1 through 3 are -838, 670, 343 rad/s respectively.

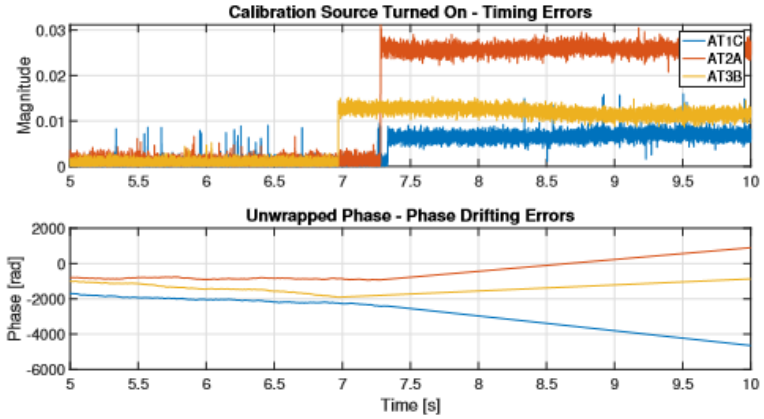

Figure 2.13.Test to determine timing errors (upper panel) and phase drifting errors (lower panel) at 3 omni antennas (blue = Ant. 1, red = Ant. 2, yellow = Ant. 3).

2.3.2 Moving Drone Tests

To test the ability of the phase delay array to accurately track a moving transmitter, we attached a test nanotag to the support struts of a DJI Phantom 3 quadcopter unmanned aerial vehicle (hereafter drone). The drone was flown by Greg Bonynge, a FAA-certified drone pilot in the Department of Natural Resources Science at the University of Rhode Island. All flights had to be pre-approved by the URI Office of Emergency Management. The tests occurred on 9 August 2019; the weather ranged from 78 to 83˚F with sunny skies and low winds, which was important because technology has temperature ratings for both operation and measurement stability. For example, the nanotag operates best within 32 - 95° F (www.lotek.com) and although temperature stability was not rated for the calibration source, the specifications indicate the rubidium timebase improves with temperature stability (www.thinksrs.com). Additionally, higher wind speeds could affect the antennas spacing and the noise floor by shaking the system.

The drone was programmed to record the GPS coordinates (accuracy ± 1m) after hovering for 15 seconds to estimate the test tag location. The hovering points were set before the drone changed direction to aid in both GPS stability and to record two fixes at the same bearing.

Mr. Bonynge flew a total on six flights on 9 August 2019 (Moore 2020: Appendix C). During Flight 1 the drone flew a diamond pattern around the antenna system to test a full 360˚ bearing estimations to check for consistency twice. The first time around the drone was set to fly at 60 m altitude and 2 m/sec and the second time for 120 m altitude and 13 m/sec. Flight 2 is described below, Flight 3 and 4 included a west to east transect at 2 m/sec at altitudes 60 and 120 m respectively. Finally, Flights 5 and 6 were a triangular shaped pattern over the bay where the drone flew at 3 m/sec to check the relation between distance and bearing estimation.

We also flew a stationary altitude test where the drone stayed at a fixed location and only increased in the z-direction. However, there were cable connection during that test making the data unusable. We were able analyze data collected during the North-South Flight 2 surveys at two altitudes, 60 and 120 m, and the transects directly over the antenna system were enough to assess beam pattern. The speed variations were based on file recording lengths and were slow enough to obtain many fixes on the test tag. However, due to the limitations and lack of coherency of the equipment, the data processing shifted to focus specifically Flight 2. Flight 2 began at 11:32 AM, the wind was north westerly and somewhere between 4 and 5.3 m/sec (Figure 2.14).

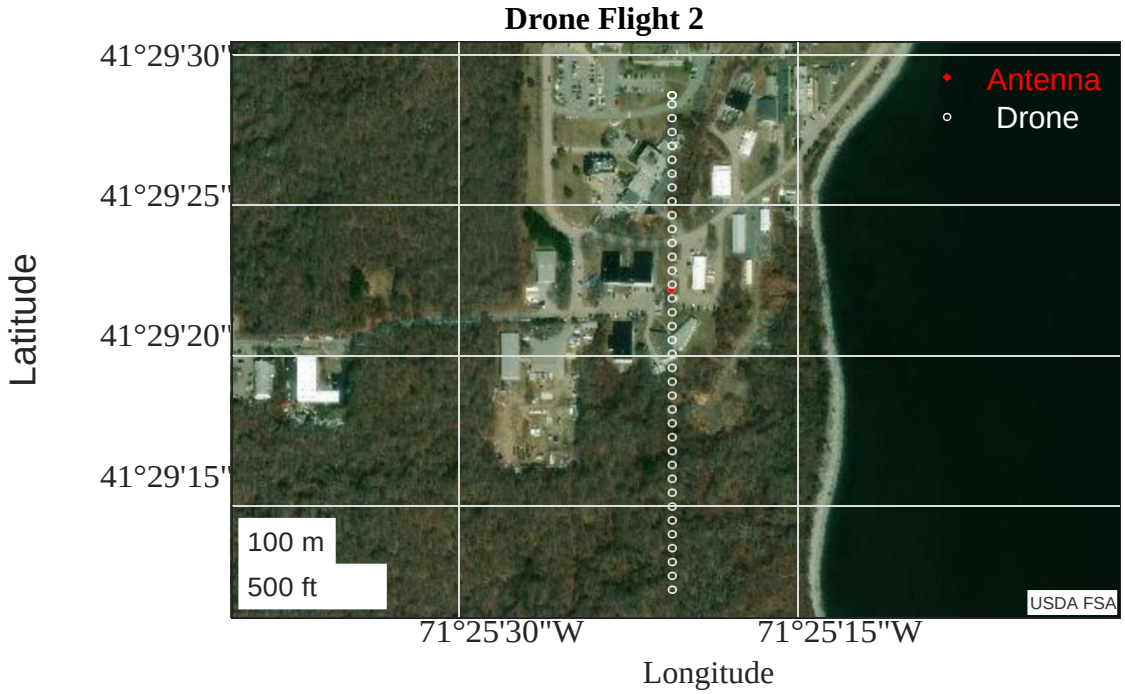

Figure 2.14. Flight pattern 2 (white dots) of a drone on 9 August 2019 over phase delay array flown at 60 and 120 m altitudes.

2.3.2 Processing Methods

2.3.3.1 Theory

This section summarizes the theory necessary to calculate signal bearing using a phase delay array.

A continuous wave (CW) signal from a source, such as a digitally coded VHF bird tag, is $y(t) = A\sin(2\pi f_c t + \theta)$ transmitted from a location $\mathbf{r_b}$ assuming plane wave propagation in the x-y plane.

$$y(t, \mathbf{r}) = A \sin\left[2\pi f_c \left(t - \frac{\hat{n} \cdot (\mathbf{r} - \mathbf{r}_b)}{c}\right) + \theta\right] \tag{11}$$

Equation 11 shows the radio frequency (RF) signal radiating from the source located at $\mathbf{r}_b$

c

with $\mathbf{k} = k\hat{n} = k(u\hat{x} + v\hat{y})$, where k is the wavenumber and is $\frac{2\pi f_c}{c}$, f_c is the carrier frequency, and c is the speed of light.

$$u = \cos\psi \tag{12a}$$

$$v = \sin\psi \tag{12b}$$

The signal is propagating towards the antennas located near the origin on the x-axis and where u and v are the direction cosines given by Equations 12a and 12b

$$y_2(t) = A\sin\left[2\pi f_c\left(t - \frac{\hat{n}\cdot(-d\hat{x} - \mathbf{r}_b)}{c}\right) + \theta\right] \tag{13b}$$

$$y_1(t) = A\sin\left[2\pi f_c\left(t - \frac{\hat{n}\cdot(0\hat{x} - \mathbf{r}_b)}{c}\right) + \theta\right] \tag{13a}$$

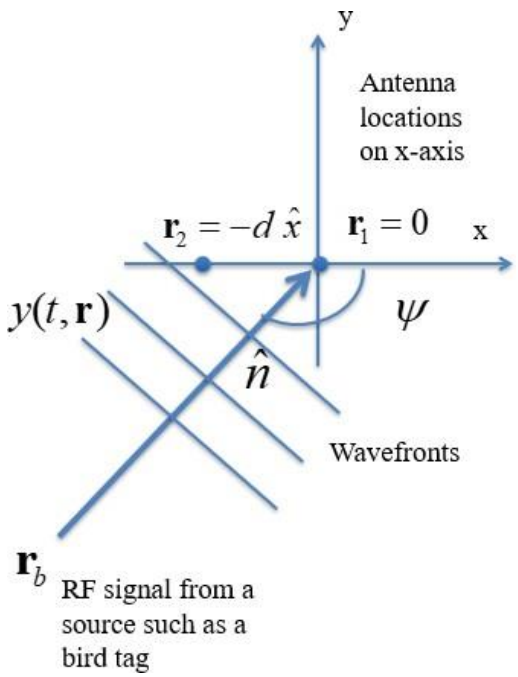

Figure 2.15.Example of frequency differences between the shifted baseband signal and calibration source and their respective bandwidth.

c

The RF signal is received by two antennas located at $\mathbf{r}_1 = 0\hat{x}$ and $\mathbf{r}_2 = -d\hat{x}$, which produces the two signals seen in Equations 13a and 13b (Figure 2.15).

$$y_1(t) = A\sin\left[2\pi f_c\left(t - \frac{(0-R)}{c}\right) + \theta\right] \tag{14a}$$

$$y_2(t) = A\sin\left[2\pi f_c\left(t - \frac{(-d\cos\psi - R)}{c}\right) + \theta\right] \tag{14b}$$

c

These two signals can be simplified using the fact that $\hat{n}\cdot\mathbf{r}_b = R$, this distance from the source such as a bird tag to Antenna 1 and $\hat{n}\cdot d\hat{x} = d\cos\psi$ and are shown in Equations 14a and 14b.

Each signal is then added a small calibration signal, $g(t) = G\sin 2\pi f_g t$, with a frequency near the carrier frequency ($f_g = f_c + \Delta f$) before demodulation so that $z_1(t) = y_1(t) = g(t)$ and $z_2(t) = y_2(t) = g(t)$ (Figure 2.16).

$$y_1(t) = A\sin\left[2\pi f_c(t - \tau_0) + \theta\right] \tag{15a}$$

$$y_2(t) = A\sin\left[2\pi f_c\left(t + \frac{d}{c}\cos\psi - \tau_0\right) + \theta\right] \tag{15b}$$

Further simplifying the expressions for the two signals are given in Equations 15a and 15b where $\tau_0 = \frac{R}{}$, the travel time from the source location to the antenna

$$y_1(t) = A\sin\left[2\pi f_c t + \theta\right] \tag{16a}$$

$$y_2(t) = A\sin\left[2\pi f_c\left(t + \frac{d}{c}\cos\psi\right) + \theta\right] \tag{16b}$$

Note that $2\pi f_c\tau_0$ is a constant phase and can be incorporated into θ, seen in Equations 16a and 16b.

$$y_1(t) = A\sin\left[2\pi f_c t + \theta\right] \tag{17a}$$

$$y_2(t) = A\sin\left[2\pi f_c t + kd\cos\psi + \theta\right] \tag{17b}$$

These expressions can then be simplified into the final forms seen in Equations 17a and 17b, where $k = \frac{2\pi f_c}{c}$ with f_c = 166.380 MHz. This produces a wavenumber of $k = 3.48 rad/m$ and a wavelength of $\lambda = \frac{c}{f} = 1.8m$.

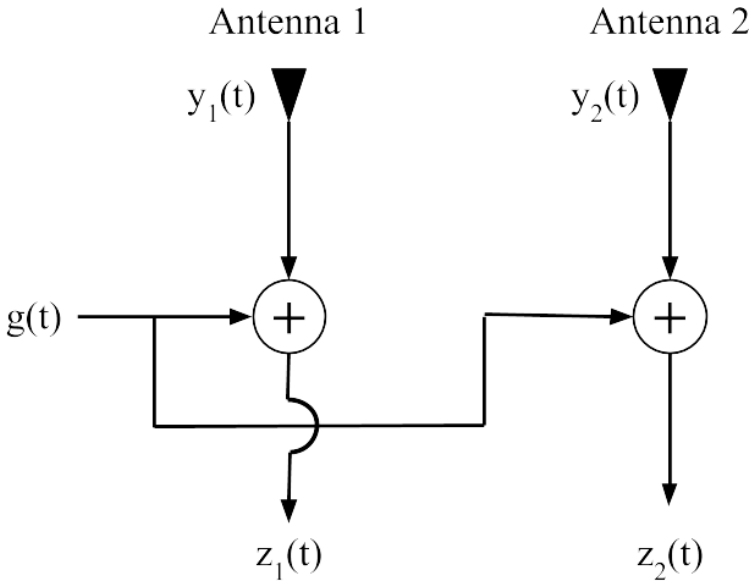

Figure 2.16. Addition of the incoming signals and the calibration source injected through or after the antenna.

Once the calibration source is added, $z_1(t)$ is demodulated at f_1 and $z_2(t)$ at f_2 to compute the respective complex envelops, where f_1 and f_2 are near the carrier frequency f_c.

$$\tilde{z}_1(t) = \tilde{y}_1(t) + \tilde{g}_1(t) = y_{c1}(t) + jy_{s1}(t) + g_{c1}(t) + jg_{s1}(t) \tag{18a}$$

$$\tilde{z}_2(t) = \tilde{y}_2(t) + \tilde{g}_2(t) = y_{c2}(t) + jy_{s2}(t) + g_{c2}(t) + jg_{s2}(t) \tag{18b}$$

Figure 2.17 below shows the demodulation process of channel 1 signal, which would be like channel 2. The combined demodulated equations are shown in Equations 18a and 18b.

$$\tilde{y}_1(t) = A\exp\left[j2\pi\left(f_c - f_1\right)t + j\theta\right] \tag{19a}$$

$$\tilde{y}_2(t) = A\exp\left[j2\pi\left(f_c - f_2\right)t + jkd\cos\psi + j\theta\right] \tag{19b}$$

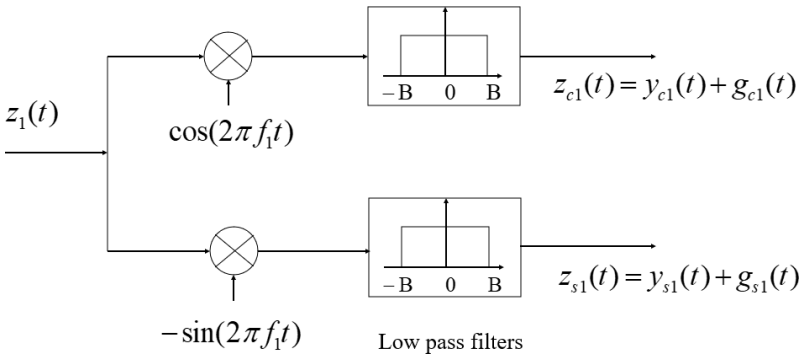

Figure 2.17. Example demodulation of Antenna 1 signal $z_1(t)$ performed by the FUNCube dongle and the resultant output real and imaginary parts.

Further, the complex envelopes of the two RF signals are represented in Equations 19a and 19b which can then be simplified further known that $\exp j\theta$ is a constant and incorporating it into A.

$$\tilde{y}_1(t) = A\exp\left[j2\pi\left(f_c - f_1\right)t\right] \tag{20a}$$

$$\tilde{y}_2(t) = A\exp\left[j2\pi\left(f_c - f_2\right)t + jkd\cos\psi\right] \tag{20b}$$

$$\tilde{g}_1(t) = G\exp\left(j2\pi\left(f_g - f_1\right)t\right) \tag{20c}$$

$$\tilde{g}_2(t) = G\exp\left(j2\pi\left(f_g - f_1\right)t\right) \tag{20d}$$

$$\tilde{z}_1(t) = A\exp\left[j2\pi\left(f_c - f_1\right)t\right] + G\exp\left(j2\pi\left(f_g - f_1\right)t\right) \tag{20e}$$

$$\tilde{z}_2(t) = A\exp\left[j2\pi\left(f_c - f_2\right)t + jkd\cos\psi\right] + G\exp\left(j2\pi\left(f_g - f_2\right)t\right) \tag{20f}$$

The simplified complex envelope signals (Equations 20a and 20b), the complex envelope of the small calibration signal (Equations 20c and 20d), and then complex envelopes of the signal plus the calibration signal (Equations 20e and 20f).

$$\tilde{z}_1(t) = A\exp\left[j2\pi\Delta f_{c1}t\right] + G\exp\left(j2\pi\Delta f_{g1}t\right) \tag{21a}$$

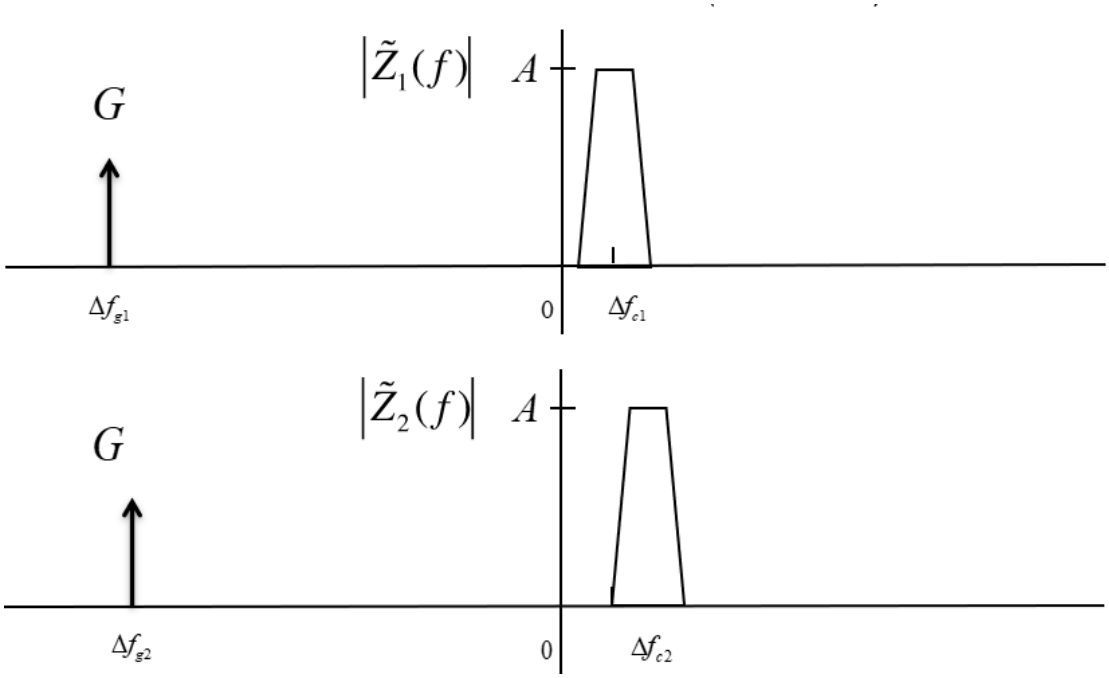

Figure 2.18. Example of frequency differences between the shifted baseband signal and calibration source and their respective bandwidth.

$$\tilde{z}_2(t) = A\exp\left[j2\pi\Delta f_{c2}t + jkd\cos\psi\right] + G\exp\left(j2\pi\Delta f_{g2}t\right) \qquad (21b)$$

By renaming the $(f_c - f_1) = \Delta f_{c1}$, $(f_c - f_2) = \Delta f_{c2}$, $(f_g - f_1) = \Delta f_{g1}$, $(f_c - f_1) = \Delta f_{c1}$, and $(f_g - f_2) = \Delta f_{g2}$, the complex envelops then are can be written as Equations 21a and 21b.

As an example, assume that $|\Delta f_{c1}|, |\Delta f_{c2}| \ll |\Delta f_{g1}|, |\Delta f_{g2}|$ and that $|\Delta f_{c1}|, |\Delta f_{c2}| \sim 1kHz$ and $|\Delta f_{g1}|, |\Delta f_{g2}| \sim 10kHz$.A general schematic can be seen in Figure 21 showing the incoming digitally coded VHF tag signal with a larger bandwidth than the calibration signal. A Fast Fourier Transformation (FFT) can be used to separate these signals.

Overall, the algorithm measures the phase associated with the spatial offset between the two antennas $kd \cos \psi$ and then computes ψ, the direction of arrival. Using an FFT, Δf_{g1} and Δf_{g2} can be estimated from their respective signals. Once found the following parameters are calculated: $f_1 = f_g - \Delta f_{g1}$, $f_2 = f_g - \Delta f_{g2}$, $\Delta f_{c1} = (f_c - f_1)$, $\Delta f_{c2} = (f_c - f_2)$. Finally, the phase difference can be computed between the two signals after shifting the complex envelops to baseband to solve for ψ.

2.3.3.2 Algorithm

In the radio tracking system, the RF signal is first shifted to the baseband in-phase (I) and quadrature (Q) components. These data are then saved digitally into a.wav file which is then loaded into MATLAB for processing (see Moore 2020: Appendix D for all MATLAB code). The *chooseFlight.m* function allows the user to choose which flight they would like to process. The I/Q samples from the .wav file are combined to recreate the received complex signal and window the time block of interest. The complex data goes through a series of functions to eventually estimate the phase values of the received emissions from the test tag.

2.3.3.3 Equations and Code

The processing is subdivided below into the main functions used to estimate the tag bearings (see Figure 2.19).

(b) The command *findpeaks* locates the first transmission after filtering the com- plex data to increase the SNR. For the purpose of solely increasing SNR and not focusing on peak definition yet, the filter for this step has a cut-off frequency that over filters the complex data (i.e., 1,000 Hz).

(c) Once the first emission is located, the function *getInitialBounds.m* determines the start and end index/time the emission exists in and adds a buffer to each side. This windows the data, ideally as small as possible, to reduce the computational load. When the first ping group was a missed detection, the search window shifts over another δt until detections are found.

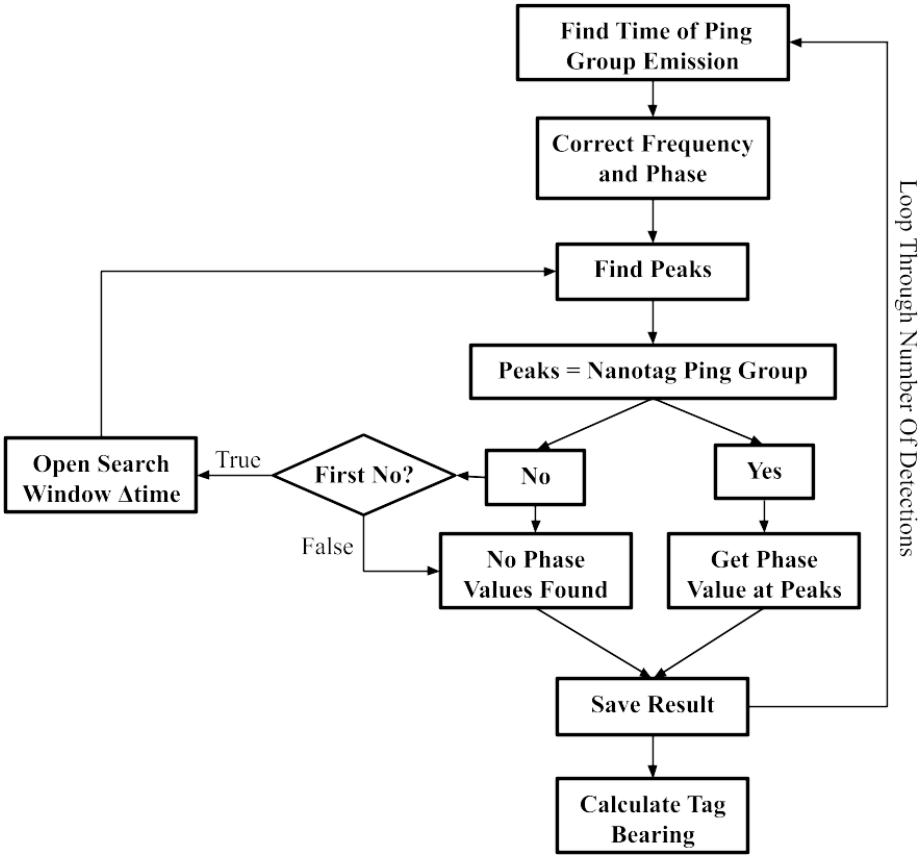

Figure 2.19. Block diagram outlining code process to estimate tag bearing

.

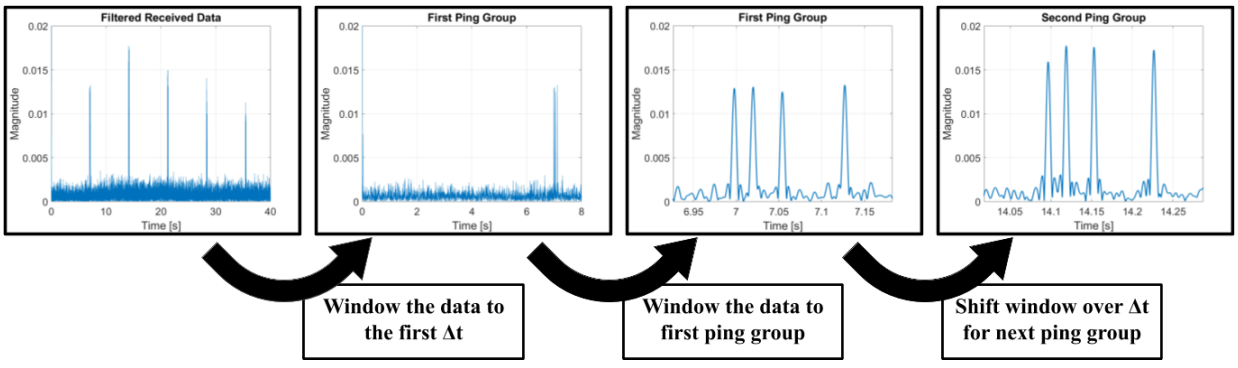

Figure 2 20. Automated ping group detection method

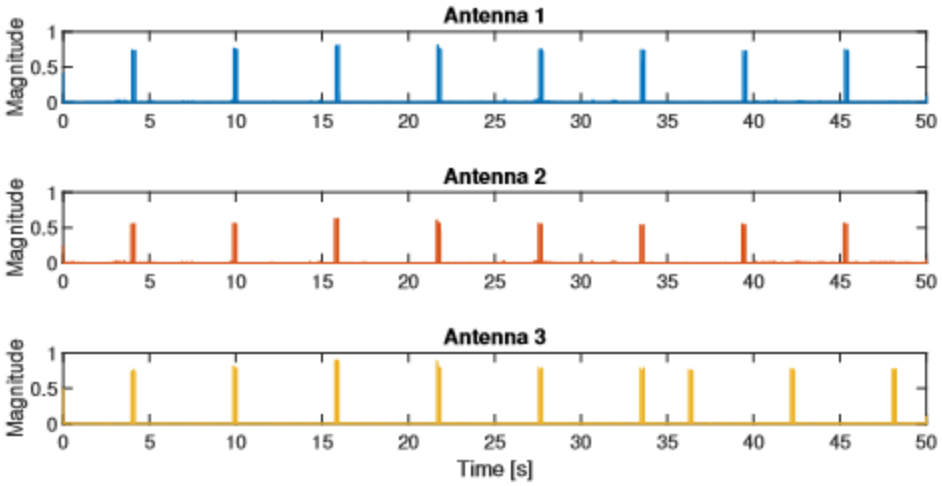

Figure 2.21. An example of filtered signals of fixed location data where there were missing data; see Antenna 3 at time = 36-43 seconds.

Because the test nanotag emitted a signal approximately every 7 seconds, δt was set to this value. The first detection is critical to code automation, as the first ping group determines where the window shifts (Figure 2.20).

If the window shift by δt does not find the 4 pings, the window was then opened to size δt. This allowed the code to find pings that were shifted in time if the data has some missing values (Figure 2.21). In this example. after 35 seconds on Antenna 3 two ping groups occur before a full δt interval had passed, which resulted in the ping groups not lining up with the Antenna 1 or 2 data. However, after searching the full 7 second window the shifted ping group was detected, this becomes the new starting point for the shifting window.

3. Once the ping group is detected from the window, the function *processData.m* processes the data to account for the accumulated errors from using equipment with low precision and accuracy. This step is labeled as ”Correct Frequency and Phase” (Figure 2.21) The script starts by calculating the frequency offset between the calibration source peak and zero. The data were sampled with a center frequency of 166.385 MHz, which was the same frequency of the calibration source. Therefore, an FFT is expected to show the largest peak centered at 0 Hz. This was not the case and varied among FCDs.

$$v = V_c . \exp(-i2\pi f_c t + \theta); \tag{22}$$

The frequency at the peak was then plugged into Equation 22 using the function

demodulateSignal.m. The variables were the demodulated signal as *v*, V_c was the complex signal, f_c was the carrier frequency, *t* was time and θ was phase. After the frequency offset was corrected by shifting the calibration source frequency to zero, the phase also had to be corrected.

Examples of this frequency offset are shown in the FFTs in Figure 2.22. In Figures 2.22a, the FFTs are plotted to show variation among antennae. The calibration source frequency should align with 0 kHz for this shifted FFT.

When looking at the frequency offsets over 300 seconds through multiple FFTs, there was a local oscillator drift due to poor FCD stability. These offsets changed over time (Figure 2.23). The left y axis shows that Antenna 2 offset ranged from 407.5 - 408.3 Hz (variation 0.8 Hz) and right y axis shows that Antenna 3 ranged from 268.5 - 272.3 Hz (variation of 3.8 Hz), with average frequencies seen in Figure 2.22.

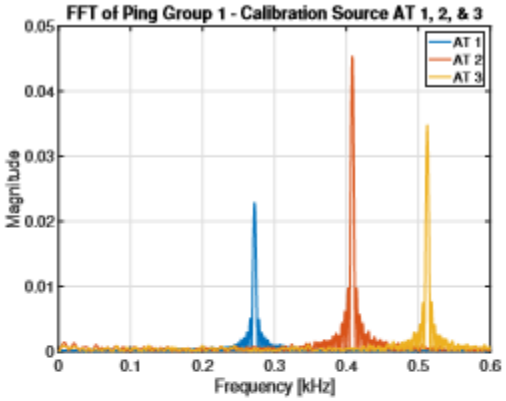

(a) FFT zoomed into the calibration source.

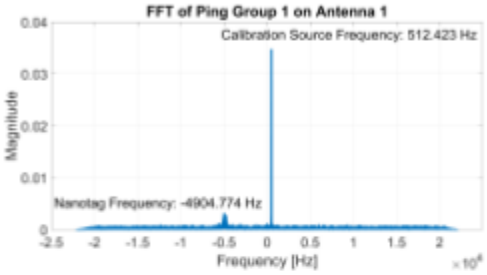

(b) FFT of window for emission 1 from Antenna 1 data.

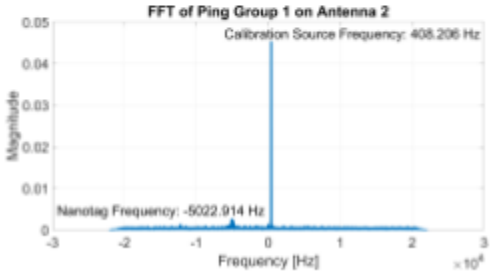

(c) FFT of window for emission 1 from Antenna 2 data.

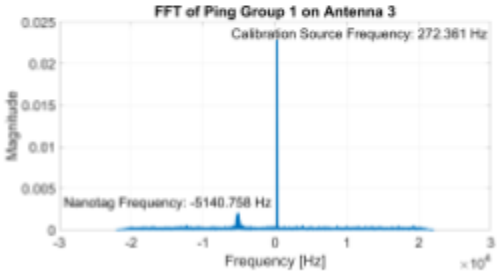

(d) FFT of window for emission 1 from Antenna 3 data.

Figure 2.22.FFT of each Antenna for the first emission in Flight 2.

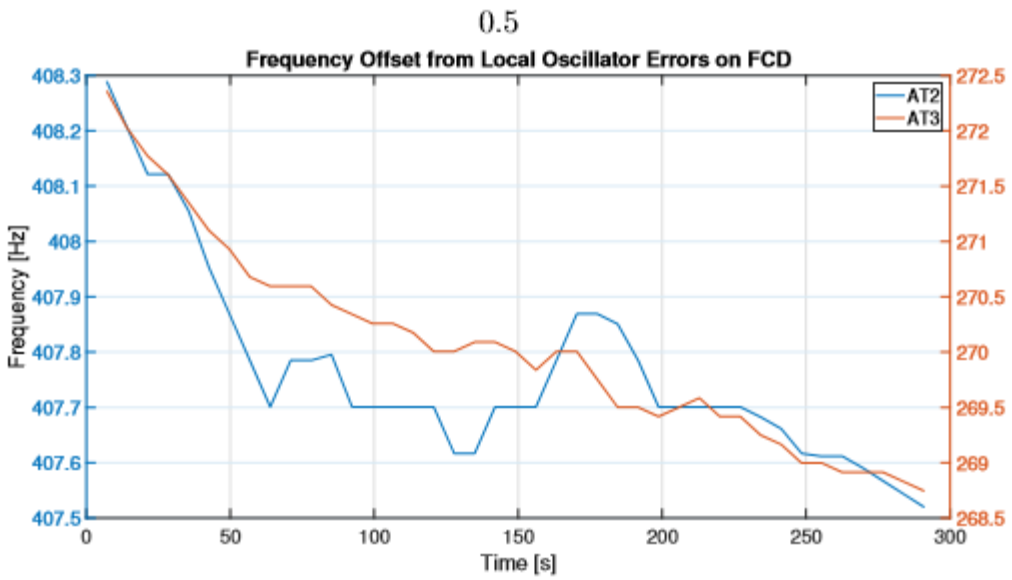

Figure 2.23.Frequency offsets over time as a result of the FCD local oscillators.

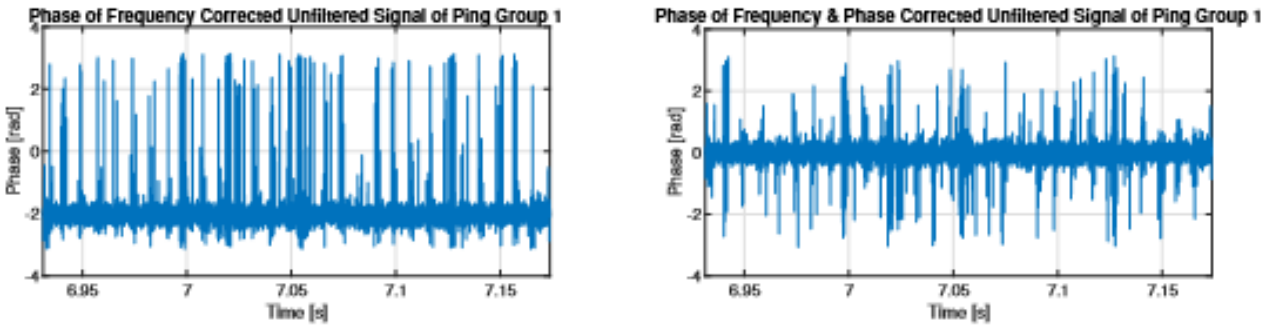

(a) Before phase correction (b) After phase correction.

Figure 2.24. Phase of unfiltered demodulated signal centered at the calibration source frequency

This phase offset is found and corrected by *phaseCorrectedSignal* = *demodulatedSignal* exp $-i(median(demodulatedSignalPhase))$. In Figure 2.24a the offset shows approximately 2 radians. Once the phase was corrected (Figure 2.24b), the demodulated signal was demodulated once more but with the carrier shifted to center the nanotag's carrier frequency. Although the advertised center frequency is 166.380 MHz, the FFT (Figure 2.22) shows that the test tag had a frequency of approximately 166.379.606 Hz. This difference of 394 Hz needs to be accounted for to filter correctly and obtain a clear and distinguished peak from the pings.

The filtering method implemented was a 4th-order low pass Butterworth filter with a cutoff

frequency of 200 Hz using the *butter* command in MATLAB. This command produces the transfer function coefficients to be passed into the *filtfilt* command that filters the data with zero phase distortion by filtering the signal in both the forward and reverse directions. An example of the filtered signal can be seen in Figure 2.25 with the phase values as well. The circles capture the peak time of arrival and magnitude which is used to grab the corresponding phase values. This process is repeated until all the ping groups have been detected.

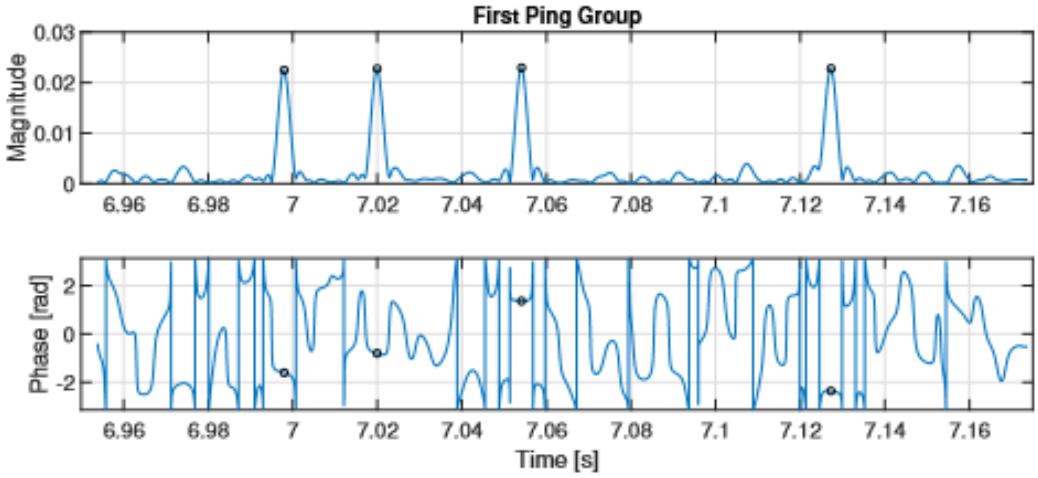

Figure 2.25. Filtered signal showing precise peak detection magnitude (upper panel) and the corresponding undistorted phase values (lower panel).

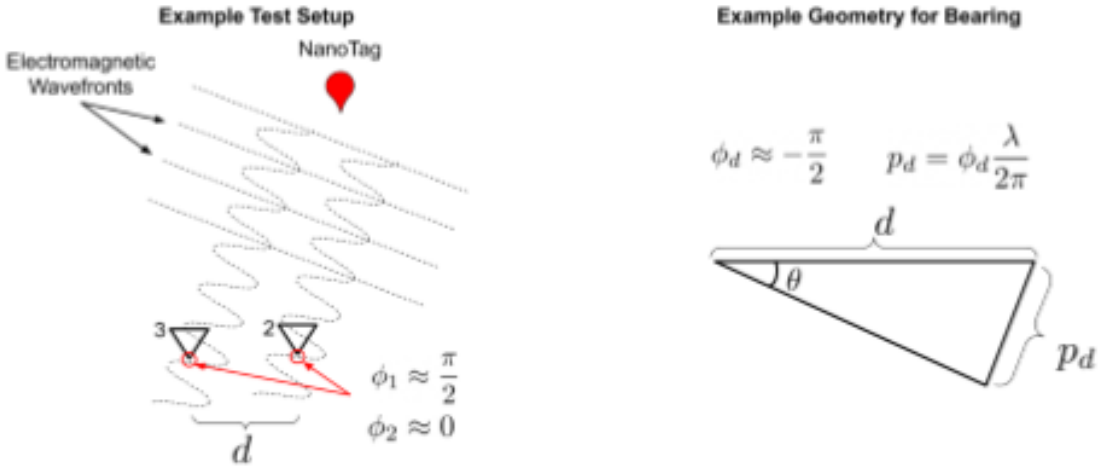

Figure 2.26. Visual representation of obtaining bearing estimations using 2 antennas.

Finally, with all phase values saved, the function *getDOAFrom2Antennas.m* or *getDirectionOfArrival.m* are used to estimate tag bearing. The function *get-DOAFrom2Antennas.m* is implemented for calculations using only two antennas and is used as a benchmark testing method.

$$d_p = \phi_d \frac{\lambda}{2\pi} \tag{23}$$

$$\theta = 90 - \arcsin(d_p/d) \tag{24}$$

$$u = \cos(\alpha)$$
$$v = \cos(\beta)$$
$$w = \cos(\gamma)$$

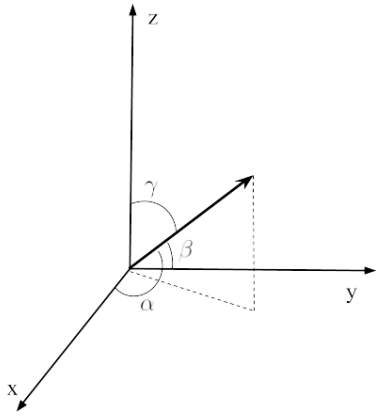

(a) Representation of bearing from direction cosines.

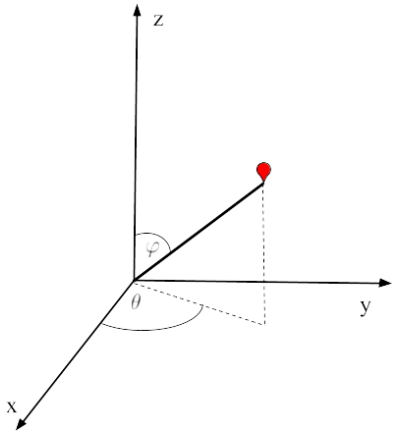

(b) Bearing and elevation angles with spherical angles.

Figure 2.27. Bearing and elevation schematics using direction cosines.

The main equations for function *getDOAFrom2Antennas.m* are outlined in Equations 23 where d_p is path difference and φ_d is phase difference and 24 where d is antenna distance. A visual representation of the process is provided in Figure 2.26 for better understanding.

Function *getDirectionOfArrival.m* uses three antennas and is found by first solving for the direction cosines. Direction cosines are the angles that the vector to the tag in space produces (Figure 2.27a) where the bearing and elevations angles can be calculated (Figure 2.27b).

This is done using the form $Ax = b$. With matrix A representing the geometry of the antenna array, vector b set as the phase differences multiplied by the inverse wave number and x set to the direction cosines. This equation is then solved by multiplying both sides of $Ax = b$ by the inverse of $A^T A$, shown in Equation 26.

$$x = (A^T A)^{-1} A^T b \tag{25}$$

$$\begin{bmatrix} u \\ v \end{bmatrix} = \begin{bmatrix} \delta x_{21} & \delta y_{21} \\ \delta x_{31} & \delta y_{31} \\ \delta x_{32} & \delta y_{32} \end{bmatrix}^{-1} \begin{bmatrix} \delta \phi_{21} \\ \delta \phi_{31} \\ \delta \phi_{32} \end{bmatrix} \frac{\lambda}{2\pi} \tag{26}$$

The inverse tangent of the u and v of the direction cosine, seen in Equation 27, is used to obtain a bearing calculation.

$$\theta = \tan^{-1}(\frac{v}{u}) \tag{27}$$

Once these calculations were done, the bearing estimates were compared to the actual known bearing estimates based on the drone GPS-based location

2.4.1 Estimating the Bearing to a Tag with Two Antennas

2.4.1.1 Methods

Function *getDOAFrom2Antennas.m* (see Moore 2020: Appendix B), uses the phase difference between two antennas (e.g., #2 and 3) to estimate the bearing to a test nanotag. One limitation of using only two antennas is that it is uncertain exactly where the tag is located in relationship to the antenna (Figure 2.28). For example, although the estimated bearing was predicted to be in quadrant I/II, the tag could have been quadrant III/IV. This uncertainty makes a two-antenna system unable to obtain the full 360˚ bearing estimates

without *apriori* knowledge. There were both drone coordinates and notes taken during the drone flights for manually changing the angles to the correct side (see Moore 2020: Appendix A). Although this method is applicable for testing, a two-antenna system would not be practical for bird tracking.

One of the challenges during testing was that the FUNCube dongles drifted in frequency (i.e., ±1.5 ppm). This was evident after performing an FFT on the data recorded using SDR with a center frequency set to 166,385,000 Hz, which was the same frequency as the calibration source. The peak was off center as previously discussed. The test tag frequency also differed from the manufacturer's specifications, but processing accounted for these drifts using the function *getCalibrationSourceFrequencyOffset.m*, (see Moore 2020: Appendix A).

To determine the reliability of the system with two antennas, Flight 2 was used for processing. This was a helpful benchmark as the phase differences were expected to be or close to zero. This aided in the finalization of the code and steps necessary to achieve the correct phase difference for the bearing estimations

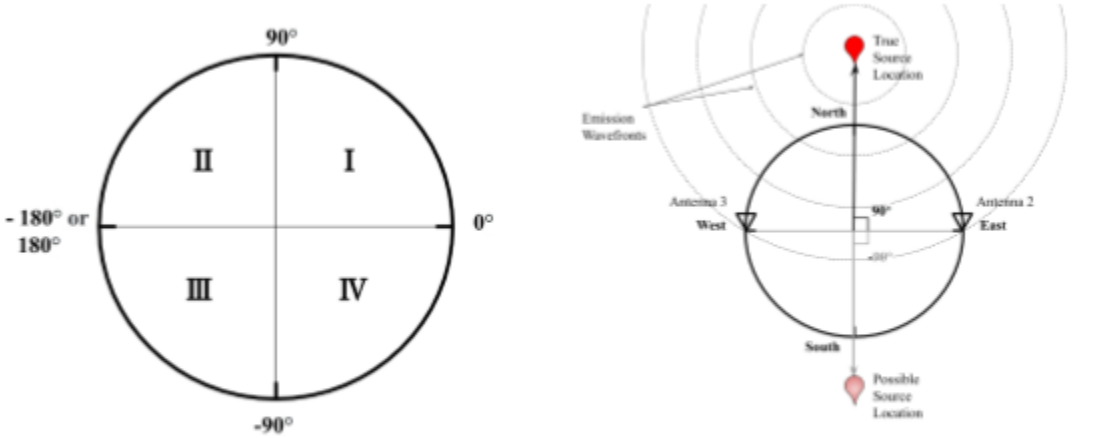

(a) Defining the quadrant space for consistency.

(b) Visual representation of bearing angle uncertainty within the quadrants III and IV.

Figure 2.28. Visual representation of the defining quadrant system and the downside of having a two antenna DF system.

.

2.4.2 Results

With the test tag carrier frequency shifting throughout the recording, different corrections were added to the test tag frequency for demodulation and filtering. However, the peak was difficult to distinguish in the FFT because of the short duration of a transmission and low energy transmissions. As a result, the first correction, 420 Hz, was chosen by manually lining up the test tag frequency ”peak” in energy to zero. After this, a series of FFTs were taken for every emission with a wide windowed moving average filter to catch the upper average limit of the FFT. To ensure that the peak in energy was the test tag and not an unknown transmission, we limited the FFT to a window of 1 kHz around the expected carrier frequency That peak was then recorded and averaged to get the second frequency correction of 394.0903 Hz. These corrections are subtracted from the advertised frequency of 166.380 MHz during processing.

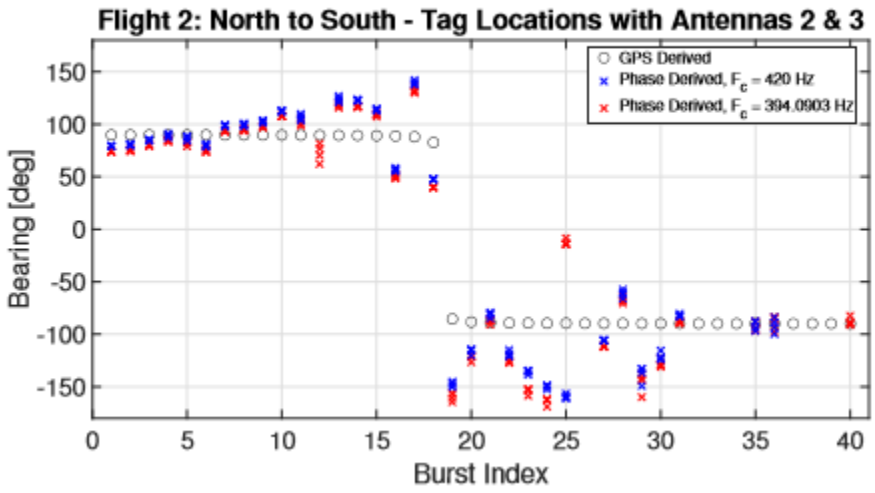

Figure 2.29. Comparison of bearing estimate of the known tag location (drone GPS derived) compared to two estimates based on phase calculations using different carrier frequencies.

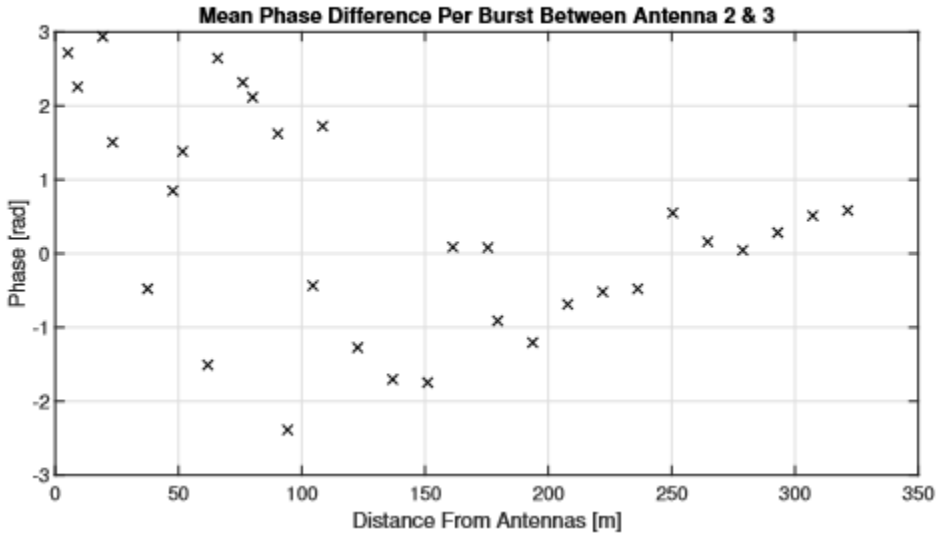

Figure 2.30. Measured error from the mean of the bursts bearing estimations from phase and the drone GPS bearings with respect to distance from antennas.

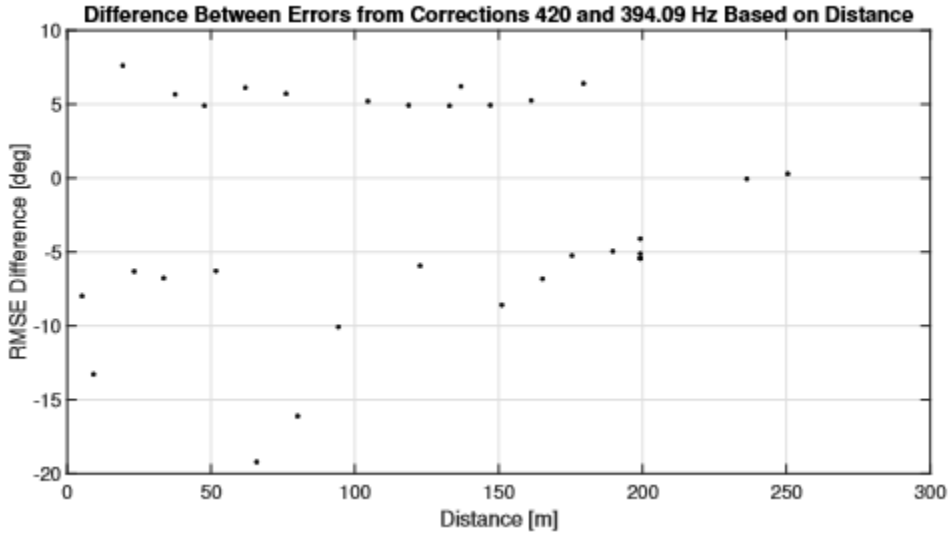

Figure 2.31. Measured error from the mean of the bursts bearing estimations from phase and the drone bearings with respect to distance from antennas.

Figure 2.29 includes the final results from Flight 2, showing the true bearing given by the GPS on the drone and the estimated bearings based on phase values for two different frequency corrections. For this test, it was expected that the phase difference equal zero because for a North to South transect the test tag would be equidistant from antennas 2 and 3. Figure 2.30 includes the phase differences averaged per burst compared to the distance

from the phase delay array to the moving test tag. When the values are close to zero, the errors are small in this case.

By altering the carrier frequency of the test tag, the errors also changed. The two corrected values of 394.0903 Hz and 420 Hz were not consistent in accuracy (Figure 2.31). At some distances, processing with one frequency performed better than the other, but for both corrections the measured errors were largest when the test tag was closer to the antenna. The estimated bearings show an error ranging from of 0.01˚ to 80˚ from the true bearing. At distances over 175 m from the phase delay array to the test tag, the measured errors were less than 20˚. There was no pattern evident in the relationship between errors and distance between the phase delay array and the test tag.

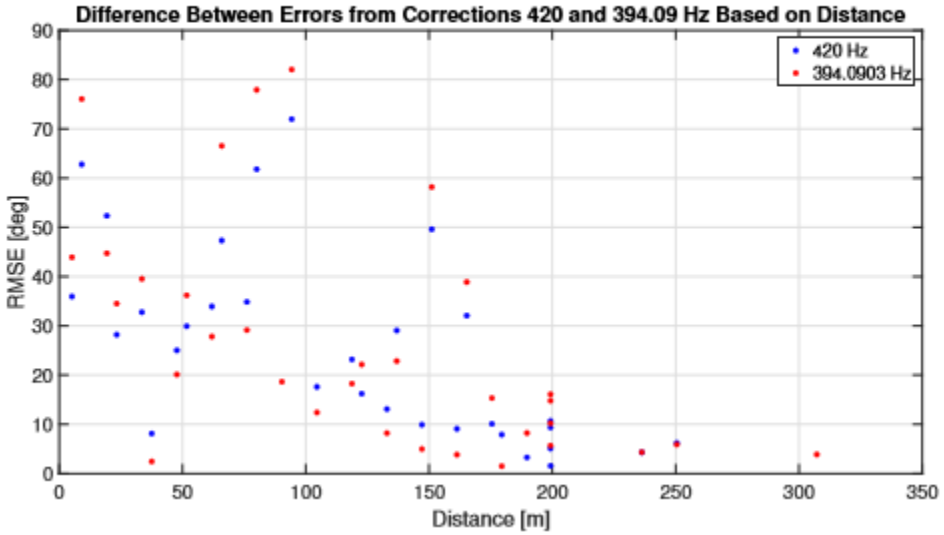

Figure 2.32. Relationship between RMSE values as a function of distance (m) between the test tag and phase delay array antenna system for two correction frequencies.

Using the RMSE values demonstrated the distance and error relationship (Figure 2.32). Most of the root-mean-square error (RMSE) values exhibited a decreasing trend until reaching a threshold distance of 200 m, where the errors began to stabilize to less than 10°. At distances over 175 m, bearing estimates were accurate (e.g., <15° at 225 m and the errors were <6° farther from the antennas), whereas when the tag approaches the antenna error estimates increase dramatically. We assume the errors closer to the phase delay array were because of the beam patterns and proximity to where the electric field became unpredictable (<45 m). Overall, the average RMSE values for 420 and 394.04 Hz were 0.7750° and 0.8250°, respectively.

We compared the errors directly by calculating the difference between the errors for both the measured errors and the RMSE values (Figure 2.33). Except for 177 seconds with a difference of 146°, the RMSE values exhibited a more accurate representation of the differences between the frequency corrections. This is because the bearing estimate differences were based on the mean bearing of each burst, while the RMSE values incorporate the four bearing estimations per burst. Again, there was no obvious relationship between error estimate over time. However, at 120 seconds when the test tag was above the antenna system and the differences in error begin to be more varied rather than the first 100 seconds where errors were relatively level,

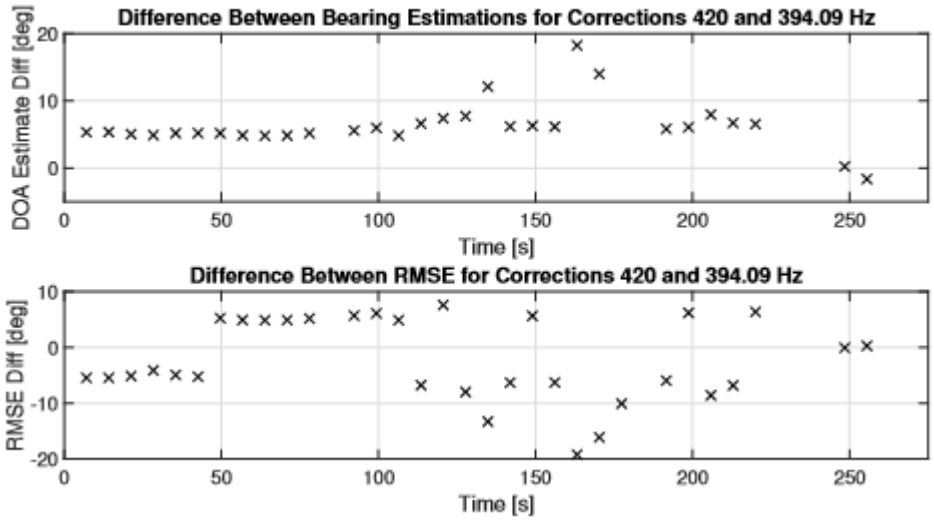

Figure 2.33. Differences in direction of arrival (DOA) bearing estimates (upper panel) and the RMSE errors (lower panel) between frequency corrections 420 and 394.09 Hz. The upper panel excludes an outlier at burst index 25 (t= 177s), where the difference was 146°

Additionally, the FFT estimated carrier frequency varied greatly when there was low SNR (Figure 2.34). The full fluctuations in the carrier frequency are evident when lined up with the ping groups. When the noise flow rose, the variations in the approximations of the test tag carrier frequency increased. As an example, a 55 sec time span from Figure 2.34, which clearly shows large variation in the carrier frequency, which makes estimating tag bearings based on the phase values less accurate (Figure 2.35)

s

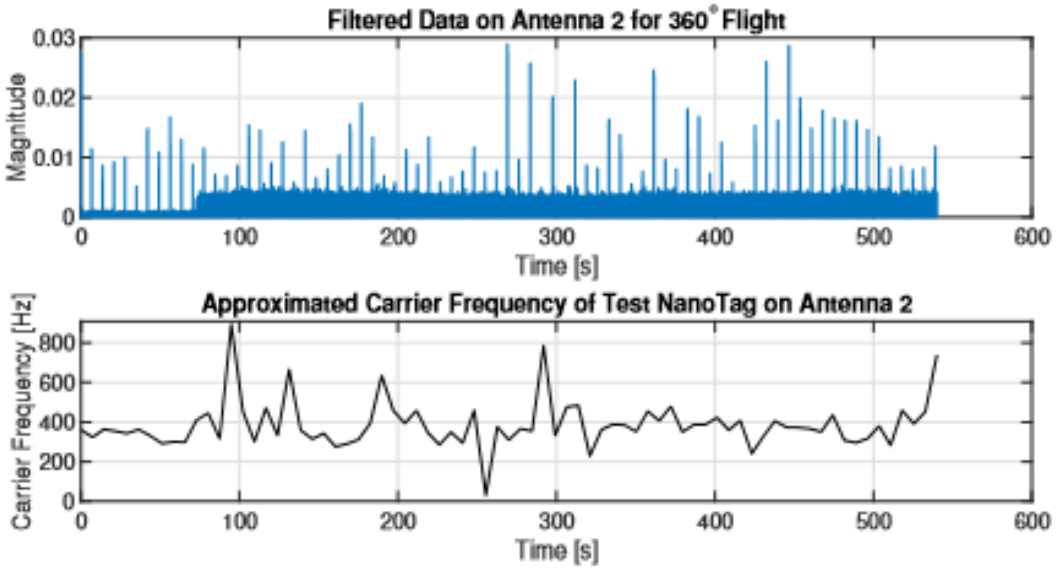

Figure 2.34. Example of the filtered signal on Antenna 2 for Flight 2 with carrier frequency calculations (lower panel) lined up with tag detections (upper panel) over a 55 sec time span.

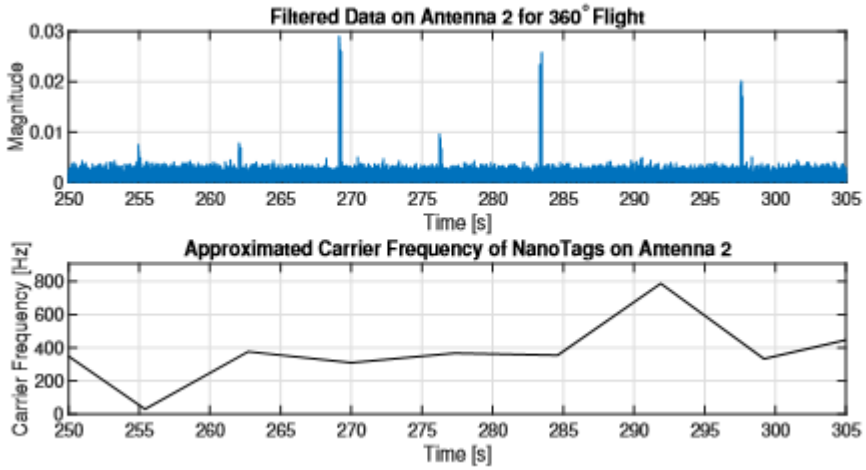

Figure 2.35. Example of the filtered signal on Antenna 2 for Flight 2 with carrier frequency calculations (lower panel) lined up with tag detections over a 55 sec time span.

2.5.1 Conclusions: Sources of Error and Future Work

We were able to estimate the direction of arrival (DOA or bearing) of the test tag using the phase delay antenna array with only two working antennas. We had hoped to test this system with three antennas, but one antenna provided poor quality information and could not be utilized for this experiment.

2.5.1.1 Direction Finding Error Sources

Errors have the ability to accumulate based on the four major categories of error sources: propagation-induced, environmental, instrumental and observational errors (Jenkins 1991). Propagation-induced errors refer to the signal traveling through different mediums, such as the ionosphere, that causes degradation in DOA, signal amplitude and can cause time dispersion effects. For VHF systems these errors are more likely to be a result of surface roughness. The ocean surface can re specifically include radio frequency signal reflections thus causing decreased propagation distance.

Environmental errors can be any natural or man-made obstacle that can cause scattering or redirection of the electromagnetic wavefront causing deviation from the linear path (Jenkins 1991). This error is divided into very near (which is within $\lambda/2\pi$), near (5 - 10 wavelengths), and far region (>5 - 10 wavelengths). Very near errors occur in close proximity to the phase delay antennas and can be caused by local ground conditions that can hold dielectric constant and conductivity variations that can cause DOA errors. Near errors are caused by point and extended re-radiators, including topographic features as well such as seasonal vegetation changes near the array which can affect the antennas received signals.

The far region can consist of re-radiators such as aircraft, and other objects that are far but reflective or also emitting signals. Overall a ground-based phase delay antenna site must consider the following to minimize environmental errors: the array is constructed on a site that is high, level and clear terrain. The ground surrounded the array must be uniform in conductivity and moisture, and not located reradiating features such as man-made buildings, power lines and coastlines. Instrumental errors are derived from imperfections in the equipment or amplitude and phase errors resulting from the use of multiple receivers. Examples and details are summarized in Table 2.1. Observational errors included corrupted data, there tend to be large fluctuations that could be reduced by averaging. It could also be that the human factor caused some error if they are operating the system. In the case of this thesis, observational errors were not considered.

Table 2.1. Equipment imperfections that cause instrumental errors and their effects on the phase detection system (Jenkins 1991:53).

Factor	Reason	Result
Low SNR	Internal receiver noise	Missed detections
Amplitude and phase unbalance	Poor design, Signal: amplitude and bandwidth, Physical: temperature and aging	Difficult to process
Time and frequency inaccuracies	Mistuned RF filters	Time based errors - errors in digital processing, Frequency offsets - mis-matched phase shifts from multiple
Hardware imperfections and aging	Faults in hardware, aging	Limited dynamic range, amplitude and phase instability
Physical misalignment	Imprecise installation	Not optimal antenna setup, dynamic platform, spacing inaccuracy
Digital processing and algorithm imprecision	ADC create quantization noise, Time-sampling errors, Software algorithm imprecision, Software interpolations to reduce memory cost	Invalid assumptions and mathematical errors, Errors in digital data
Calibration inaccuracies	Measurement inaccuracies	Residual errors

Based on the potential sources of error (Table 2.2; Jenkins 1991), it was clear that most of the errors in this experiment were instrumental and environmental errors. The instrumental errors were mostly due to the FUNCube dongles RF mixer and analog to digital converter. These errors are discussed in more depth below. The environmental errors were not as clearly visible but assumed to be there due to the area in which the testing took place. Metal buildings surrounded the phase delay antenna system and re-radiation of the incoming electromagnetic waves are likely have occurred. However, still it is important to keep the other errors in mind when developing a more permanent system.

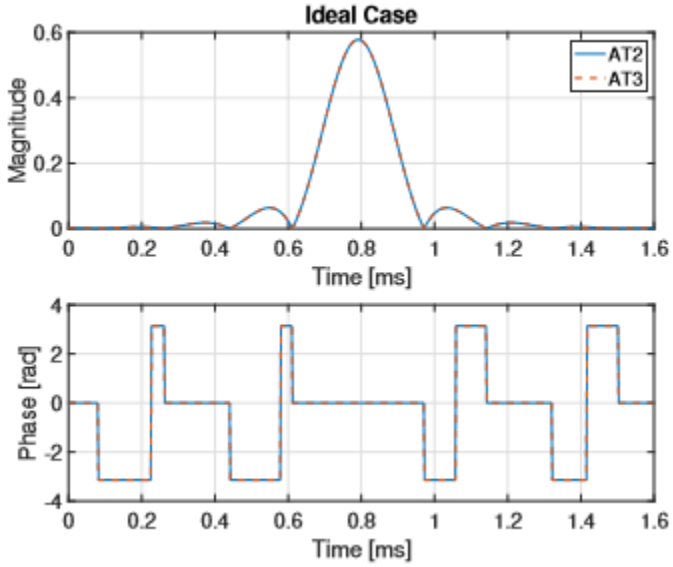

Figure 2.36. Ideal Case.

In addition to understanding common errors based on past research, modeled data of the system was also tested with the same functions developed for processing the test data to ensure that they worked correctly (Figure 2.37). Each of the errors were added to the ideal case data (Figure 2.36) by itself before adding multiple error combinations. This was important to determine which errors had the greatest impact on the accuracy and precision of bearing estimates and how to fix these errors. For this exercise, Antenna 2 modeled data was unaltered, while Antenna 3 data was modeled for errors.

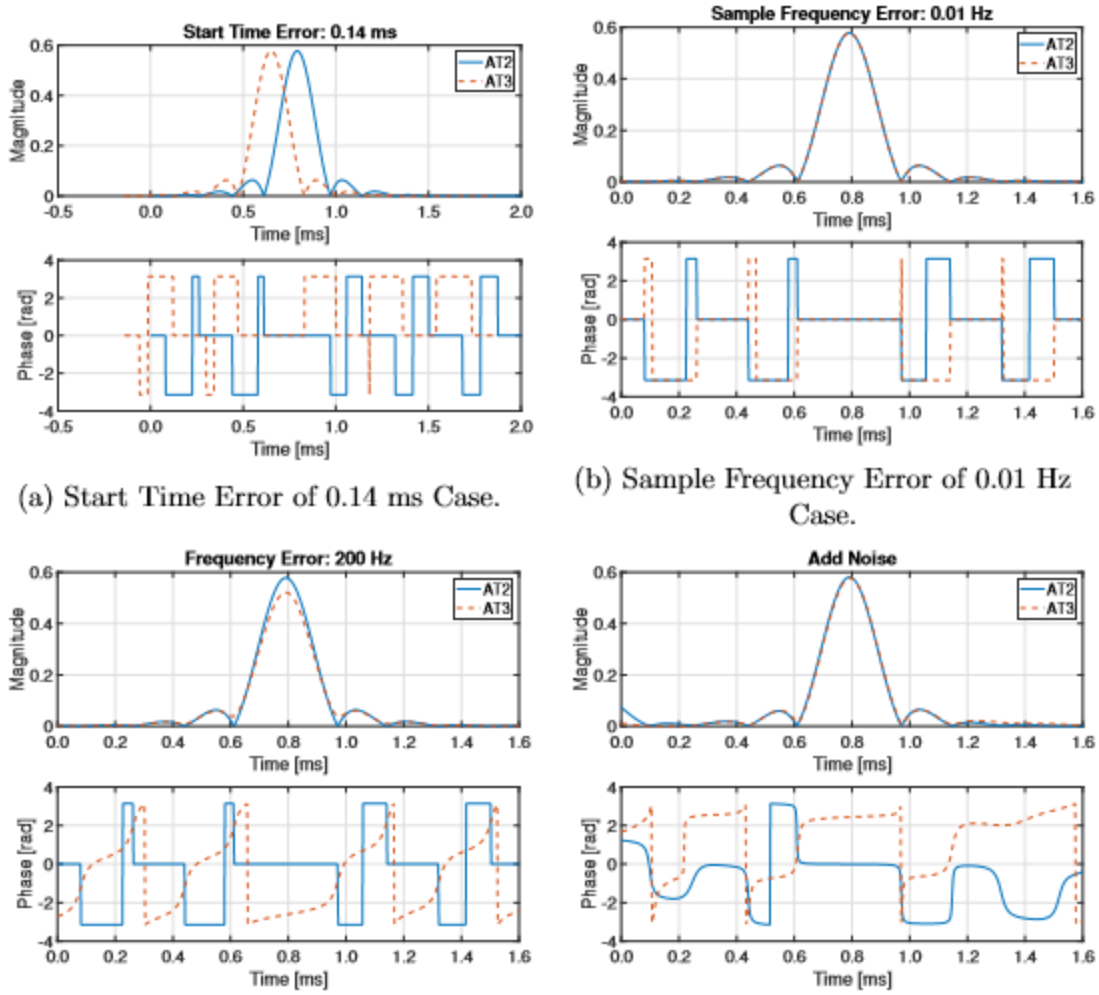

(a) Start Time Error of 0.14 ms Case.

(b) Sample Frequency Error of 0.01 Hz Case.

(c) Frequency Error of 200 Hz Case.

(d) Low SNR Case.

Figure 2.37. Effects of different sources of errors on changes in phase values in modeled data based on a two-antenna system (Antennas 2 and 3). Sources of error include (a) start time (upper left panels), (b) sample frequency errors (upper right panels, (c) frequency error (lower left panels), and (d) SNR (lower right panels).

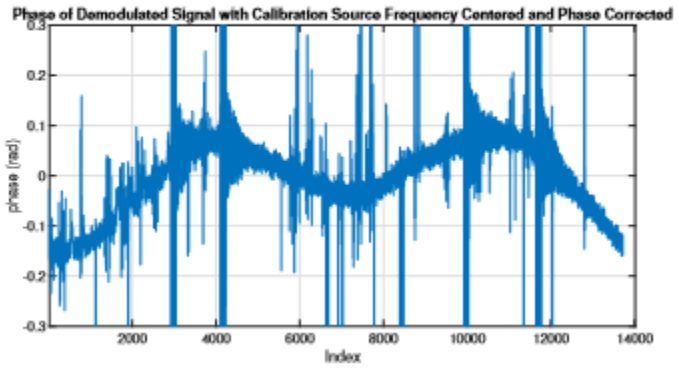

Figure 2.38. Phase of ping group 1 from using the RF Explorer as the calibration source.

The more important errors contributing to phase inconsistencies were frequency errors and SNR (Figures 2.37c and 2.38d). Start time errors did not affect the phase values (Figure 2.37a) or did the sample rate errors (Figure 2.38b). The sample frequency error could create some inaccuracies if phase values of the transmission were sloped or the sample frequency error was much larger. However, the analysis performed here assumed that the error was small.

Finally, the reason that the calculations for two antennas was possible is due to the calibration source stability. In the beginning tests, the RF explorer was a calibration source with a frequency stability of ±0.5 (RF Explorer Signal)Generator 2019). This is evident when looking at the phase inconsistencies (Figure 2.38).

2.6.1 Conclusions

The FUNCube dongles were a major source of large variation. Each FCD had a difference frequency offset by hundreds of hertz, which would change over time, thus needed to be constantly calculated. This source of was accounted for by including a precise calibration source, a rubidium clock with a stability of $<\pm 0.0001 ppm$ (www.thinksrs.som). The more precise calibration source allowed errors in frequency and phase to be corrected, which was critical to this experiment. A primary source of the frequency and phase errors was the FCD local oscillator drifting from the carrier frequency, the ADC timing not being precise enough, and propagation noise. These are errors that were documented in the literature review and were reviewed through modeled data (Figure 2.37).

This research showed that using phase measurements to estimate DOA are sensitive to error, but these errors can be corrected by thorough processing and using higher quality, more accurate and precise equipment. The prime example is that by using the rubidium clock calibration source, most frequency and phase errors from the FUNCube dongle could be corrected. However, the instability of the test digitally coded VHF tag, data dropouts on the Antenna 1 system and general lack of coherency among individual antennas lead to the

calculation of DOA bearings with two antennas. Future design considerations to develop the next generation of this system are summarized in Moore (2020; section 7.3).

Table 2.2. Potential sources of errors and their effects on using a phase delay antenna system to estimate direction of arrival of a radio wave.

Challenges	**Effect**
Clock Differences	Possibly lining up wrong peaks – phase difference errors
Software Memory Usage	Computer freezing – missing data, lining up wrong peaks
FUNCube Dongle Stability	Errors in frequency, affect frequency corrections
Nanotag Frequency Shifts	Frequency correction errors
Frequency Correction	Peak variability and phase correction errors
Peak Variability	Phase value errors
Phase Correction	Large phase errors
Signal-to-Noise-Ratio	Large phase errors
Uncertainties in Antenna and Drone Coordinates	Uncertainties of true bearing angles for phase bearing comparisons

LITERATURE CITED

Althouse, M.A., Cohen, J.B., Karpanty, S.M., Spendelow, J.A., Davis, K.L., Parsons, K.C. and Luttazi, C.F., 2019. Evaluating response distances to develop buffer zones for staging terns. The Journal of Wildlife Management 83:260-271.

Althouse, M.A., Cohen, J.B., Spendelow, J.A., Karpanty, S.M., Davis, K.L., Parsons, K.C. and Luttazi, C.F., 2016. Quantifying the effects of research band resighting activities on staging terns in comparison to other disturbances. Waterbirds 39:417-421.

Anderson, A.M., Duijns, S., Smith, P.A., Friis, C. and Nol, E., 2019. Migration distance and body condition influence shorebird migration strategies and stopover decisions during southbound migration. Frontiers in Ecology and Evolution 7:251.

Angerbjorn, A. and Becker, D. 1992. An automatic location system for wildlife telemetry. In I. G. Priede and S. M. Swift, eds. Wildlife Telemetry Remote Monitoring and Tracking of Animals. Ellis Horwood, New York, N.Y. Pp. 68-75.

Baldwin, J.W., Leap, K., Finn, J.T. and Smetzer, J.R., 2018. Bayesian state-space models reveal unobserved off-shore nocturnal migration from Motus data. Ecological Modelling 386:38-46.

Band, W., Madders, M. and Whitfield, D.P., 2007. Developing field and analytical methods to assess avian collision risk at wind farms. In DeLucas, M. Janss, G. and Ferrer, M. (eds). Birds and wind farms: Risk assessment and mitigation, www.quercus.pt.

Barron, D.G., Brawn, J.D. and Weatherhead, P.J., 2010. Meta-analysis of transmitter effects on avian behaviour and ecology. Methods in Ecology and Evolution 1:180-187.

Becker, P.H., Schmaljohann, H., Riechert, J., Wagenknecht, G., Zajková, Z. and González-Solís, J., 2016. Common Terns on the East Atlantic Flyway: temporal–spatial distribution during the non-breeding period. Journal of Ornithology 157:927-940.

BOEM. 2019. Outer Continental shelf renewable energy leases map book. BOEM Renewable Energy Program, March 2019.

BOEM. 2020. https://www.boem.gov/renewable-energy/state-activities.

Brown, J.M. and Taylor, P.D., 2017. Migratory blackpoll warblers (*Setophaga striata*) make regional-scale movements that are not oriented toward their migratory goal during fall. Movement Ecology *5*:15.

Burger, J. and Gochfeld, M. 1991. The Common Tern: Its breeding biology and social behavior. Columbia University Press, New York. 413pp.

Burger, J., Gordon, C., Lawrence, J., Newman, J., Forcey, G. and Vlietstra, L. 2011. Risk evaluation for federally listed (Roseate Tern, Piping Plover) or candidate (Red Knot) bird species in offshore waters: A first step for managing the potential impacts of wind facility development on the Atlantic Outer Continental Shelf. Renewable Energy 36:338-351.

Critchley, E.J., Grecian, W.J., Bennison, A., Kane, A., Wischnewski, S., Cañadas, A., Tierney, D., Quinn, J.L. and Jessopp, M.J., 2020. Assessing the effectiveness of foraging radius

models for seabird distributions using biotelemetry and survey data. Ecography 43:184-196.

Cochran, W.W., Warner, D.W., Tester, J.R. and Kuechle, V.B., 1965. Automatic radio-tracking system for monitoring animal movements. BioScience 15:98-100.

Cook, A.S., Humphreys, E.M., Bennet, F., Masden, E.A. and Burton, N.H., 2018. Quantifying avian avoidance of offshore wind turbines: current evidence and key knowledge gaps. Marine Environmental Research, 140:278-288.

Crewe, T.L., Crysler, Z., and Taylor, P.D. 2019. Motus R book. Available from: https://motus.org/MotusRBook

Critchley, E.J., Grecian, W.J., Bennison, A., Kane, A., Wischnewski, S., Cañadas, A., Tierney, D., Quinn, J.L. and Jessopp, M.J., 2020. Assessing the effectiveness of foraging radius models for seabird distributions using biotelemetry and survey data. Ecography 43:184-196.

Crysler, Z.J., Ronconi, R.A. and Taylor, P.D., 2016. Differential fall migratory routes of adult and juvenile Ipswich Sparrows (*Passerculus sandwichensis princeps*). Movement Ecology 4:3.

David, S.-M., Meca-Meca, F. J., Martín-Gorostiza, E., and Lázaro-Galilea, J. L., 2016. Snr degradation in undersampled phase measurement systems. Sensor 1: 1772.

Deppe, J.L., Ward, M.P., Bolus, R.T., Diehl, R.H., Celis-Murillo, A., Zenzal, T.J., Moore, F.R., Benson, T.J., Smolinsky, J.A., Schofield, L.N. and Enstrom, D.A., 2015. Fat, weather, and date affect migratory songbirds' departure decisions, routes, and time it takes to cross the Gulf of Mexico. *Proceedings of the National Academy of Sciences*, *112*: E6331-E6338.

Desholm, M., Fox, A., Beasley, P., and Kahlert, J. 2006. Remote techniques for counting and estimating the number of bird–wind turbine collisions at sea:a review. Ibis 148:76–89.

Desholm, M. and Kahlert, J., 2005. Avian collision risk at an offshore wind farm. Biology Letters 1:296-298.

Desrochers, A., Tremblay, J.A., Aubry, Y., Chabot, D., Pace, P. and Bird, D.M. 2018. Estimating wildlife tag location errors from a vhf receiver mounted on a drone. Drones 2:44.

Dowling, Z., Sievert, P.R., Baldwin, E., Johnson, L., von Oettingen, S. and Reichard, J., 2017. Flight Activity and Offshore Movements of Nano-Tagged Bats on Martha's Vineyard, MA. US Department of the Interior, Bureau of Ocean Energy Management, Office of Renewable Energy Programs, Sterling, Virginia. OCS Study BOEM 2017-54, p.39.

Drewitt, A.L. and Langston, R.H., 2006. Assessing the impacts of wind farms on birds. Ibis 148:29-42.

Durkin, M., Ernst, N. and Veale, J. 2019. Piping Plover breeding season monitoring and management report, 2019. Rhode Island National Wildlife Refuge Complex, unpubl. report, Charlestown, RI.

Elliott-Smith, E. and Haig, S.M., 2004. Piping plover (*Charadrius melodus*), version 2.0. The Birds of North America (PG Rodewald, Editor). Cornell Lab of Ornithology, Ithaca, NY,

USA. https://doi. org/10.2173/bna.

Erickson, W.P., Johnson, G.D., Strickland, D.M., Young Jr, D.P., Sernka, K.J. and Good, R.E., 2001. Avian collisions with wind turbines: a summary of existing studies and comparisons to other sources of avian collision mortality in the United States (No. DOE-00SF22100-). Western EcoSystems Technology, Inc., Cheyenne, WY (United States); RESOLVE, Inc., Washington, DC (United States).

Evans, P.G., Bolton, M., Carroll, M., Wakefield, E., Scragg, E., Owen, E., Pinder, S. and Waggitt, J., 2019. Matches and mismatches between seabird distributions estimated from at-sea surveys and concurrent individual-level tracking. Frontiers in Ecology and Evolution 7:333.

Falconer, C.M., Mitchell, G.W., Taylor, P.D. and Tozer, D.C., 2016. Prevalence of disjunct roosting in nesting Bank Swallows (*Riparia riparia*). The Wilson Journal of Ornithology 128: 429-434.

Fijn, R.C., de Jong, J., Courtens, W., Verstraete, H., Stienen, E.W.M. and Poot, M.J.M., 2017. GPS-tracking and colony observations reveal variation in offshore habitat use and foraging ecology of breeding Sandwich Terns. Journal of Sea Research 127:203-211.

Fox, A.D., Desholm, M., Kahlert, J., Christensen, T.K. and Krag Petersen, I.B., 2006. Information needs to support environmental impact assessment of the effects of European marine offshore wind farms on birds. Ibis 148: 129-144.

Fox, A.D. and Petersen, I.K., 2019. Offshore wind farms and their effects on birds. Dansk Ornitologisk Forenings Tidsskrift 113:86-101.

Furness, R.W., Trinder, M., MacArthur, D. and Douse, A., 2016. A theoretical approach to estimating bird risk of collision with wind turbines where empirical flight activity data are lacking. Energy and Power Engineering 8:183-194.

Furness, R.W., Wade, H.M. and Masden, E.A., 2013. Assessing vulnerability of marine bird populations to offshore wind farms. Journal of Environmental Management 119:56-66.

Geen, G.R., Robinson, R.A. and Baillie, S.R., 2019. Effects of tracking devices on individual birds–a review of the evidence. Journal of avian biology 50:e01823.

Goodale, M.W. and Milman, A., 2016. Cumulative adverse effects of offshore wind energy development on wildlife. Journal of Environmental Planning and Management, 59:1-21.

Gottwald, J., Zeidler, R., Friess, N., Ludwig, M., Reudenbach, C. and Nauss, T., 2019. Introduction of an automatic and open-source radio-tracking system for small animals. Methods in Ecology and Evolution, 10:2163-2172.

Goyert, H.F., 2014. Relationship among prey availability, habitat, and the foraging behavior, distribution, and abundance of Common Terns *Sterna hirundo* and Roseate Terns *S. dougallii*. Marine Ecology Progress Series 506:291-302.

Gratto-Trevor, C., Haig, S.M., Miller, M.P., Mullins, T.D., Maddock, S., Roche, E. and Moore,

P., 2016. Breeding sites and winter site fidelity of Piping Plovers wintering in The Bahamas, a previously unknown major wintering area. Journal of Field Ornithology 87:29-41.

Harwood, A.J., Perrow, M.R., Berridge, R.J., Tomlinson, M.L. and Skeate, E.R., 2017. Unforeseen Responses of a Breeding Seabird to the Construction of an Offshore Wind Farm. In Wind Energy and Wildlife Interactions (pp. 19-41). Springer, Cham.

Hedenström, A., Klaassen, R.H. and Åkesson, S., 2013. Migration of the Little Ringed Plover *Charadrius dubius* breeding in South Sweden tracked by geolocators. Bird Study 60:466-474.

Janaswamy, R., Loring, P. and McLaren, J., 2018. A State Space Technique for Wildlife Position Estimation Using Non-Simultaneous Signal Strength Measurements. arXiv:1805.11171.

Jenkins, H.H. 1991. Small-Aperture Radio Direction-Finding. Massachusetts, United States of America: Artech House Inc..

Johnston, A., Cook, A.S., Wright, L.J., Humphreys, E.M. and Burton, N.H., 2014. Modelling flight heights of marine birds to more accurately assess collision risk with offshore wind turbines. Journal of Applied Ecology 51:31-41.

Kays, R., Crofoot, M.C., Jetz, W. and Wikelski, M. 2015. Terrestrial animal tracking as an eye on life and planet. Science 348:6240.

Kays, R., Tilak, S., Crofoot, M., Fountain, T., Obando, D., Ortega, A., Kuemmeth, F., Mandel, J., Swenson, G., Lambert, T. and Hirsch, B., 2011. Tracking animal location and activity with an automated radio telemetry system in a tropical rainforest. The Computer Journal 54:1931-1948.

Kelsey, E.C., Felis, J.J., Czapanskiy, M., Pereksta, D.M. and Adams, J., 2018. Collision and displacement vulnerability to offshore wind energy infrastructure among marine birds of the Pacific Outer Continental Shelf. Journal of Environmental Management 227:229-247.

Kenward, R.E., 2001. A manual for wildlife radio tagging. Academic Press, New York.

Larkin, R.P., Raim, A. and Diehl, R.H., 1996. Performance of a Non-Rotating Direction-Finder for Automatic Radio Tracking. Journal of Field Ornithology 67:59-71.

Larsen, J.K. and Guillemette, M., 2007. Effects of wind turbines on flight behaviour of wintering common eiders: implications for habitat use and collision risk. Journal of Applied Ecology, 44: 516-522.

Lefevre, K.L. and Smith, A.D., 2020. Florida's strategic position for collaborative Automated Telemetry tracking of avian movements across the Americas. Journal of Fish and Wildlife Management 11: 369-375.

Loring, P., Paton, P., McLaren, J., Bai, H., Janaswamy, R., Goyert, H., and Sievert, P. 2019. Tracking offshore occurrence of Common Terns, endangered Roseate Terns, and threatened Piping Plovers with VHF arrays, Sterling (VA): US Department of the Interior, Bureau of Ocean Energy Management. OCS Study BOEM.

Loring, P., Ronconi, R., Welch, L., Taylor, P. and Mallory, M., 2017. Postbreeding dispersal and

staging of Common and Arctic Terns throughout the western North Atlantic. Avian Conservation and Ecology 12:20.

Loring, P.H., McLaren, J.D., Goyert, H.F. and Paton, P.W.C., 2020. Supportive wind conditions influence offshore movements of Atlantic Coast Piping Plovers during fall migration. The Condor 122:1-16.

Loring P.H., McLaren, J.D., Smith, P.A., Niles, L.J., Koch, S.L., Goyert, H.F., Bai, H. 2018. Tracking movements of threatened migratory rufa Red Knots in U.S. Atlantic Outer Continental Shelf Waters. Sterling (VA): US Department of the Interior, Bureau of Ocean Energy Management. OCS Study BOEM 2018-046. 145 p.

Kenward, R. E. 2001. A Manual for wildlife radio tracking. Academic Press, New York

Körner, F., R. Speck, A. H. Göktoğan, and S. Sukkarieh. 2010. Autonomous airborne wildlife tracking using radio signal strength. 2010 Ieee/RSJ International Conference on Intelligent Robots and Systems. Taipei Taiwan

Masden, E.A. and Cook, A.S.C.P., 2016. Avian collision risk models for wind energy impact assessments. Environmental Impact Assessment Review 56:43-49.

Masden, E.A., Fox, A.D., Furness, R.W., Bullman, R. and Haydon, D.T., 2010. Cumulative impact assessments and bird/wind farm interactions: Developing a conceptual framework. Environmental Impact Assessment Review 30: 1-7.

Maxwell, S.M., Conners, M.G., Sisson, N.B. and Dawson, T.M., 2016. Potential benefits and shortcomings of marine protected areas for small seabirds revealed using miniature tags. Frontiers in Marine Science 3:264.

McKinnon, E.A. and Love, O.P., 2018. Ten years tracking the migrations of small landbirds: Lessons learned in the golden age of bio-logging. The Auk: Ornithological Advances 135: 834-856.

Moore, J., 2020. Tracking Migratory Birds: Applying a Passive Tracking Technique Using Direction of Arrival from VHF Radio Tags. M.S. Thesis, University of Rhode Island, Kingston.

Mostello, C.S., Nisbet, I.C., Oswald, S.A. and Fox, J.W., 2014. Non-breeding season movements of six North American Roseate Terns *Sterna dougallii* tracked with geolocators. Seabird 27:1-21.

Neves, V.C., Nava, C.P., Cormons, M., Bremer, E., Castresana, G., Lima, P., Junior, S.M.A., Phillips, R.A., Magalhães, M.C. and Santos, R.S., 2015. Migration routes and non-breeding areas of Common Terns (*Sterna hirundo*) from the Azores. Emu-Austral Ornithology 115:158-167.

Nicholls, D.G., Robertson, C.J.R. and Murray, M.D., 2007. Measuring accuracy and precision for CLS: Argos satellite telemetry locations. Notornis 54:137-157.

Nickolas, C. 2011. Digi-Key Electronics.The basics of mixers.

https://www.digikey.com/en/articles/ the-basics-of-mixers

Nisbet, I. C. T., J. M. Arnold, S. A. Oswald, P. Pyle, and M. A. Patten (2017). Common Tern (*Sterna hirundo*), version 3.0. In The Birds of North America (P. G. Rodewald, Editor). Cornell Lab of Ornithology, Ithaca, NY, USA.

Nisbet, I.C. and Mostello, C.S. 2015. Winter quarters and migration routes of Common and Roseate Terns revealed by tracking with geolocators. Bird Observer 43:222-230.

Nisbet, I.C.T., Szczys, P., Mostello, C.S. and Fox, J.W., 2011. Female Common Terns *Sterna hirundo* start autumn migration earlier than males. Seabird 24:103-106.

Nisbet, I.C., Mostello, C.S., Veit, R.R., Fox, J.W. and Afanasyev, V. 2011. Migrations and winter quarters of five Common Terns tracked using geolocators. Waterbirds 34:32-39.

Paton, P.W.C., Loring, P., Nyameke, A, and Cormons, G. In Press. Effects of nanotags on the behavior of Roseate Terns nesting on Great Gull Island. Transactions of the Linnaean Society of New York.

Perrow, M.R., Skeate, E.R. and Gilroy, J.J., 2011. Visual tracking from a rigid-hulled inflatable boat to determine foraging movements of breeding terns. Journal of Field Ornithology 82:68-79.

Platteeuw, M., Bakker, J., van den Bosch, I., Erkman, A., Graafland, M., Lubbe, S. and Warnas, M., 2017. A framework for assessing ecological and cumulative effects (faece) of offshore wind farms on birds, bats and marine mammals in the southern North Sea. In Wind energy and wildlife interactions (pp. 219-237). Springer, Cham.

Proakis, J.G. 2006. Digital Signal Processing *(*4th Edition*)*. Prentice-Hall, Inc., USA,

Owen, E., Wakefield, E., Hollinrake, P., Leitch, A., Steel, L. and Bolton, M., 2019. Breeding together, feeding apart: sympatrically breeding seabirds forage in individually distinct locations. Marine Ecology Progress Series 620:173-183.

Řeřucha, Š., Bartonička, T., Jedlička, P., Čížek, M., Hlouša, O., Lučan, R. and Horáček, I., 2015. The BAARA (Biological AutomAted RAdiotracking) system: A new approach in ecological field studies. PloS one 19:e0116785.

Ripperger, S.P., Carter, G.G., Page, R.A., Duda, N., Koelpin, A., Weigel, R., Hartmann, M., Nowak, T., Thielecke, J., Schadhauser, M. and Robert, J., 2020. Thinking small: Next-generation sensor networks close the size gap in vertebrate biologging. PLoS Biology 18: p.e3000655.

RF Explorer Signal Generator, Digi-Key Electronics, 2019, updated to Firmware Version 1.31. [Online]. Available: http://j3.rf-explorer.com/40-rfe/article/ 132-rf-explorer-signal-generator-rfe6gen-specification

Safina, C., Wagner, R.H., Witting, D.A. and Smith, K.J., 1990. Prey delivered to Roseate and Common Tern chicks: Composition and temporal variability. Journal of Field Ornithology 61:331-338.

Salido-Monzú, D., Meca-Meca, F.J., Martín-Gorostiza, E. and Lázaro-Galilea, J.L., 2016. SNR Degradation in Undersampled Phase Measurement Systems. Sensors 16:1772.

Schober, F, Bogel, R., Bugnar, W. M., Burchard, D., Fluch, G., and Rohde, N. 1993. Automatic direction finding and location system based on Doppler effect. Pages 327-336 in M. Paolo, F. Sandro, C. Cristina, and B. Remo, editors. Proceedings of the 12th international symposium on biotelemetry. Litografia Felici, Pisa. Italy

Seward, A., Taylor, R.C., Perrow, M.R., Berridge, R.J., Bowgen, K.M., Dodd, S., Johnstone, I. and Bolton, M., 2020. Effect of GPS tagging on behaviour and marine distribution of breeding Arctic Terns *Sterna paradisaea*. Ibis https://doi.org/10.1111/ibi.12849

Skov, H., Heinänen, S., Norman, T., Ward, R.M., Méndez-Roldán, S. and Ellis, I. 2018. ORJIP Bird Collision and Avoidance Study. Final report – April 2018. The Carbon Trust. United Kingdom. 247 pp.

Scottish Natural Heritage (SNH). 2010. Use of Avoidance Rates in the SNH Wind Farm Collision Risk Model. SNH Avoidance Rate information and Guidance Note. Available at: http://www.snh.gov.uk/planning-and-development/renewableenergy/onshore-wind/bird-collision-risks-guidance/.

Smallwood, K.S., Bell, D.A. and Standish, S., 2020. Dogs detect larger wind energy effects on bats and birds. The Journal of Wildlife Management 84:852-864.

Smetzer, J.R. and King, D.I., 2018. Prolonged stopover and consequences of migratory strategy on local-scale movements within a regional songbird staging area. The Auk: Ornithological Advances 135:547-560.

Smetzer, J.R., King, D.I. and Taylor, P.D., 2017. Fall migratory departure decisions and routes of Blackpoll Warblers *Setophaga striata* and Red-eyed Vireos *Vireo olivaceus* at a coastal barrier in the Gulf of Maine. Journal of Avian Biology *48*: 1451-1461.

Smolinsky, J.A., Diehl, R.H., Radzio, T.A., Delaney, D.K. and Moore, F.R., 2013. Factors influencing the movement biology of migrant songbirds confronted with an ecological barrier. Behavioral Ecology and Sociobiology 67:2041-2051.

Spendelow, J.A., Mostello, C.S., Nisbet, I.C., Hall, C.S. and Welch, L., 2010. Interregional breeding dispersal of adult Roseate Terns. Waterbirds 33:242-245.

Stantial, M.L. and Cohen, J.B., 2015. Estimating flight height and flight speed of breeding Piping Plovers. Journal of Field Ornithology 86:369-377.

Stantial, M.L., Cohen, J.B., Darrah, A.J., Iaquinto, K.E., Loring, P.H. and Paton, P.W., 2018. Radio transmitters did not affect daily nest and chick survival of Piping Plovers (*Charadrius melodus*). The Wilson Journal of Ornithology 130:518-524.

Stantial, M.L., Cohen, J.B., Loring, P.H. and Paton, P.W., 2019. Radio Transmitters did not affect apparent survival rates of Adult Piping Plovers (*Charadrius melodus*). Waterbirds 42: 205-209.

Staudinger, M.D., Goyert, H., Suca, J.J., Coleman, K., Welch, L., Llopiz, J.K., Wiley, D.,

Altman, I., Applegate, A., Auster, P. and Baumann, H., 2020. The role of sand lances (*Ammodytes* sp.) in the Northwest Atlantic Ecosystem: A synthesis of current knowledge with implications for conservation and management. Fish and Fisheries 21:522-556.

Taylor, P., Crewe, T., Mackenzie, S., Lepage, D., Aubry, Y., Crysler, Z., Finney, G., Francis, C., Guglielmo, C., Hamilton, D. and Holberton, R., 2017. The Motus Wildlife Tracking System: a collaborative research network to enhance the understanding of wildlife movement. Avian Conservation and Ecology 12:8.

Thaxter, C.B., Buchanan, G.M., Carr, J., Butchart, S.H., Newbold, T., Green, R.E., Tobias, J.A., Foden, W.B., O'Brien, S. and Pearce-Higgins, J.W., 2017. Bird and bat species' global vulnerability to collision mortality at wind farms revealed through a trait-based assessment. Proceedings of the Royal Society B: Biological Sciences 284: 20170829.

Thaxter, C.B., Lascelles, B., Sugar, K., Cook, A.S., Roos, S., Bolton, M., Langston, R.H. and Burton, N.H., 2012. Seabird foraging ranges as a preliminary tool for identifying candidate Marine Protected Areas. Biological Conservation 156:53-61.

Urmy, S.S. and Warren, J.D., 2018. Foraging hotspots of Common and Roseate terns: the influence of tidal currents, bathymetry, and prey density. Marine Ecology Progress Series 590:227-245.

USFWS. 2020a. 2019 Atlantic Coast Piping Plover Abundance and Productivity Estimates https://www.fws.gov/northeast/pipingplover/pdf/2019-Update-Final.pdf

USFWS 2020b. Piping Plover (*Charadrius melodus*) 5-year review: summary and evaluation. https://ecos.fws.gov/docs/five_year_review/doc6378.pdf

VonEhr, K., Hilaski, S., Dunne, B. E., and Ward, J. 2016.Software defined radio for direction-finding in UAV wildlife tracking," in 2016 IEEE International Conference on Electro Information Technology (EIT). IEEE, 2016, pp. 0464– 0469

Wakeling, J.M. and Hodgson, J., 1992. Optimisation of the flight speed of the Little, Common and Sandwich tern. Journal of experimental biology 169:261-266.

Weithman, C.E., Gibson, D., Walker, K.M., Maddock, S.B., Fraser, J.D., Karpanty, S.M. and Catlin, D.H., 2018. Discovery of an important stopover location for migratory Piping Plovers (*Charadrius melodus*) on South Point, Ocracoke Island, North Carolina, USA. Waterbirds 41:56-62.

Wickert, M. A. 2000. Doftware defined radio and the rtl-sdr usb dongle. http://www.eas.ussc.edu/~mwickert/ece4670/lecture_notes/Lab6.pdf.

White, G. C., and R. A. Garrott. 1990. Analysis of wildlife radio-tracking data. Academic Press, New York.

Yoda, K., 2019. Advances in bio-logging techniques and their application to study navigation in wild seabirds. Advanced Robotics 33:108-117.

Zhang, J., Rayner, M., Vickers, S., Landers, T., Sagar, R., Stewart, J. and Dunphy, B., 2019. GPS telemetry for small seabirds: using hidden Markov models to infer foraging behaviour of

Common Diving Petrels (*Pelecanoides urinatrix urinatrix*). Emu-Austral Ornithology 119:126-137.

1.8.1. Appendices

Appendix 1.1. Summary of Common Terns tagged in 2018 and 2019 for this project.

Colony[1]	Date tagged	Status[2]	USGS Band Number	Tag ID[3]	Mass (g)	Culmen (mm)
Falkner	6/13/2018	N	1412-35301	295	130.3	38.79
Falkner	6/13/2018	N	1412-35302	6	118	34.04
Falkner	6/13/2018	N	1412-35303	296	131.2	33.06
Falkner	6/13/2018	N	1412-35304	119	131	36.77
Falkner	6/13/2018	R	1242-00331	9	121.7	35.78
Falkner	6/13/2018	N	1412-35305	258	128.5	36.14
Falkner	6/13/2018	N	1412-35306	10	128.5	33.09
Falkner	6/13/2018	N	1412-35307	254	123	36.33
Falkner	6/13/2018	N	1412-35308	12	116.7	36.38
Falkner	6/13/2018	R	1362-45209	15	120.3	38.79
Falkner	6/13/2018	N	1412-35309	116	112.9	35.06
Falkner	6/13/2018	R	1362-51824	13	124	39.87
Falkner	6/13/2018	N	1412-35310	16	125.9	37.65
Falkner	6/13/2018	R	1322-04429	7	130.2	39.49
Falkner	6/13/2018	N	1412-35311	117	118.5	35.38
Falkner	6/13/2018	N	1412-35312	120	120.2	33.24
Falkner	6/13/2018	N	1412-35313	298	122.3	40.42
Falkner	6/13/2018	R	1362-28024	255	134.3	39.02
GGIS	6/24/2018	R	1362-39440	103	123.8	35.69
GGIS	6/24/2018	R	1362-10074	179	123.4	35.93
GGIS	6/24/2018	R	1242-74582	177	131.8	35.39
GGIS	6/24/2018	R	1242-47890	176	139.8	35.16
GGIS	6/24/2018	R	1362-39037	175	122.1	37.64
GGIS	6/24/2018	R	1242-64580	171	122.9	37.36
GGIS	6/24/2018	U	1242-32888	172	120.1	37.02
GGIS	6/24/2018	U	1367-26997	54	112.2	35.95
GGIS	6/24/2018	U	1362-59222	51	121.7	35.62
GGIS	6/26/2018	U	1172-37502	47	135.4	35.79
GGIS	6/26/2018	U	1242-75693	48	123.7	35.41
GGIS	6/27/2018	U	1362-17940	67	130.3	32.95
GGIS	6/27/2018	U	1382-14492	64	131.3	39.12
GGIS	6/27/2018	U	1242-63911	65	124.4	39.2
GGIS	6/27/2018	U	1362-21024	62	123.9	37.95
GGIS	6/27/2018	U	1362-36086	63	113.9	33.73
GGIS	6/27/2018	U	1402-00727	66	120.1	37.2
GGIS	6/27/2018	U	1362-55796	60	120	36.5
GGIS	6/27/2018	U	1362-17477	21	121.3	34.17
GGIS	6/27/2018	U	1362-44927	20	107.5	34.04
GGIS	6/23/2019	R	1402-00704	28	133.4	38.5
GGIS	6/23/2019	R	1362-48866	15	124.6	34.5
Colony[1]	Date	**Status[2]**	**USGS Band**	**TagID[3]**	**Mass**	**Culmen**

GGIS	6/23/2019	R	1362-39763	14	129.2	36
GGIS	6/23/2019	N	1402-17467	16	127.3	36.4
GGIS	6/23/2019	R	1242-60946	13	117.8	36.14
GGIS	6/23/2019	R	1332-80338	477	108.8	34.9
GGIS	6/23/2019	R	1182-36620	12	120.9	36.1
GGIS	6/23/2019	R	1182-25113	11	115.1	36.1
GGIS	6/23/2019	R	1362-48141	9	113	35.1
GGIS	6/23/2019	R	1332-87650	149	111	33.3
GGIS	6/23/2019	N	1402-17468	510	110.3	35
GGIS	6/23/2019	N	1402-17469	10	110.6	35.1
GGIS	6/23/2019	R	1362-18508	147	120.7	33.1
GGIS	6/23/2019	N	1402-17470	509	115.1	36.1
GGIS	6/23/2019	R	1362-55804	508	112.5	38.3
GGIS	6/23/2019	N	1402-17471	507	106.4	31.6
GGIS	6/23/2019	N	1402-17472	505	105.5	
GGIS	6/23/2019	R	1402-00451	504	106.4	37.83
GGIS	6/23/2019	N	1402-17474	506	119.8	36.4
GGIS	6/23/2019	N	1402-17475	503	109.3	36.9
GGIS	6/23/2019	R	1362-57176	29	109.9	33
GGIS	6/24/2019	R	1402-17171	27	109.1	38.8
GGIS	6/24/2019	R	1382-13387	24	133.6	36.1
GGIS	6/24/2019	N	1402-17481	25	116.8	39.8
GGIS	6/24/2019	R	1382-09008	26	104.6	35.6
GGIS	6/24/2019	N	1402-17482	22	105.9	34.4
GGIS	6/24/2019	R	1332-81826	476	110.3	37.33
GGIS	6/24/2019	R	1332-81265	23	106.5	34.9
GGIS	6/24/2019	N	1402-17485	478	104.8	34.45
GGIS	6/24/2019	N	1402-17527	152	113.5	37.83
GGIS	6/24/2019	N	1402-17528	151	134.3	32.65
GGIS	6/24/2019	R	1362-41690	472	119.5	37.6
GGIS	6/24/2019	R	1402-17482	146	106	35.3
GGIS	6/24/2019	N	1402-17486	474	119.5	34.74
GGIS	6/24/2019	R	1402-17441	475	111.4	36.7
GGIS	6/24/2019	R	1362-41295	473	111.1	35.5
GGIS	6/24/2019	R	1362-38048	148	106.4	30.98
GGIS	6/24/2019	R	1362-28770	145	131.4	37.31
GGIS	6/24/2019	N	1402-17487	150	105.3	33.39
GGIS	6/24/2019	R/N	1402-17488	479	115.8	35.1

[1]Colony: Falkner Island, CT; Great Gull Island, NY (GGIS); 2Status: New capture (N), recapture (R); [3]ID number for tag for Motus system.

Appendix 1.2. Summary of Roseate Terns tagged in 2018 for this project.

Colony[1]	Date	USGS band number	Auxiliary Band[2]	Tag ID[3]	Mass (g)	Culmen (mm)
Falkner	6/16/2018	1392-11001	YE E93	5	114.2	38.88
Falkner	6/16/2018	1182-97001	U0/01	253	122.3	39.12
Falkner	6/16/2018	1362-15297	97/6X	8	122.6	40.53
Falkner	6/16/2018	1322-00778	16/1N	11	114.8	38.34
Falkner	6/16/2018	1182-75981	81/9E	14	118.8	40.32
Falkner	6/16/2018	1392-11002	YE (E95)	115	121	39.33
Falkner	6/16/2018	1242-32755	55/4F	118	110.8	39.6
Falkner	6/16/2018	1322-00863	79/1N	257	120.1	39.99
Falkner	6/16/2018	1392-11003	YE (E96)	300	115.6	40.04
Falkner	6/16/2018	1322-00807	42/1N	297	122.3	40.04
GGIS	6/23/2018	1362-49912	BL EP9	108	120.8	42.89
GGIS	6/23/2018	1362-40729	BL TB9	107	116.6	38.8
GGIS	6/23/2018	1402-16181	BL TA1	106	123.2	38.87
GGIS	6/24/2018	1242-79721	21/8N	102	119.7	39.89
GGIS	6/24/2018	1362-15479	79/4N	105	109.8	36.96
GGIS	6/24/2018	1402-16182	BL (TA2)	104	111.9	39.72
GGIS	6/24/2018	1242-48067	67/OZ	180	112.1	38.47
GGIS	6/24/2018	1242-49658	58/6U	101	125.2	4243
GGIS	6/24/2018	1362-29128	BL (FV2)	178	111.3	41.8
GGIS	6/26/2018	1402-16183	YE (K26)	52	104	39.07
GGIS	6/26/2018	1362-29211	BI (UC1)	53	128.7	40.07
GGIS	6/26/2018	1242-40849	49/8P	49	125	38.73
GGIS	6/26/2018	1402-16184	BL (TA4)	50	119.7	38.47
GGIS	6/27/2018	1362-29020	BL (UC3)	61		
GGIS	6/27/2018	1402-16185	BL (TA5)	23	107	36.56
GGIS	6/27/2018	1402-16186	BL (TA6)	24	123.3	38.78
GGIS	6/27/2018	1402-16187	BL (TA7)	22	109.4	36.99
GGIS	6/27/2018	1362-29063	BL (UC5)	17	117.4	38.48
GGIS	6/27/2018	1402-16188	BL (TA8)	18	119.8	37.78
GGIS	6/27/2018	1362-49411	BL (UC6)	19	120	35.97

[1]Colony: Falkner Island, CT; Great Gull Island, NY (GGIS)

[2]Aux band: band codes: either metal field readable (##/##) or plastic field readable Yellow (YE) with 3 black letters or blue (BL) with 3 white letters

[3]ID number for tag for Motus system.

Appendix 1.3. Summary of Piping Plovers tagged in Rhode Island in 2018 and 2019 for this project.

Beach[1]	Date	Age[2]	Sex	Tag ID[3]	Left Leg[4]	Right leg[5]	Mass (g)	Wing (mm)	Culmen (mm)
NCA1-2	5/24/2018	ASY	M	8	GF (5UK)	BL	52.8	115	12.61
NCA2-2	5/24/2018	ASY	M	9	GF (6UU)	BL	56.6	119	13.13
NNWR-1	5/24/2018	SY	F	26	GF (KE5)	BL	57.5	118	12.23
NCA1-1	5/24/2018	AHY	M	27	GF (UYY)	BL	53.12	120	12.71
NCA2-4	5/24/2018	SY	M	28	GF (N5V)	BL	51.6	118	11.99
NCA1-3	5/24/2018	ASY	U	29	GF (A3M)	BL	61.4	119	13.59
TLD-1	5/24/2018	ASY	M	43	GF (YKK)	BL	53.9	119	12.06
NCA2-1	5/24/2018	ASY	M	NA	2561-89282	GF (319)	53.1	119	13.1
EBWH-2	5/25/2018	ASY	U	10	GF (77K)	BL	56.4	116	13.13
EBWH-3	5/25/2018	ASY	F	11	GF (9M7)	BL	53.8	114	12.86
Q-1	5/25/2018	ASY	F	44	GF (MEU)	BL	55.3	113	12.6
Q-3	5/25/2018	ASY	M	45	GF (MX7)	BL	59.6	123	13.49
Q-2	5/25/2018	SY	F	46	GF (UU4)	BL	60.6	115	13.4
EBWH-4	5/25/2018	ASY	M	97	GF (N7E)	BL	54.8	117	12.63
TP-8	5/29/2018	ASY	M	94	GF (VNC)	BL	55.7	121	13.08
TP-7	5/29/2018	ASY	F	96	GF (N77)	BL	53.9	119	12.5
TP-4	5/29/2018	SY	F	167	GF (V9V)	BL	63.7	120	12.4
TP-5	5/29/2018	SY	M	168	GF (410)	BL	57	116	13.46
TP-2	5/29/2018	ASY	M	169	GF (PV5)	BL	53.7	119	13.64
TP-6	5/29/2018	ASY	F	170	GF (KXM)	BL	60.2	118	13.69
TP-11	5/30/2018	ASY	U	95	GF (P14)	BL	53.9	116	13.22
NCA2-1	5/28/2019	ASY	F	8	GF (5UK)	BL	57.3	115	13.34
NCA2-2	5/28/2019	ASY	F	41	GF (K39)	BL	56.9	119	13.77
NCA1-1	5/28/2019	ASY	M	42	GF (A4J)	BL	60.5	118	12.23
NNWR-1	5/28/2019	ASY	F	468	GF (MPV)	BL	53.6	121	12.21
NCA1-4	5/28/2019	AHY	M	469	GF (M16)	BL	59.3	115	13.95
NCA1-2	5/28/2019	ASY	F	470		GF (PMU)	60	121	13.55
NCA1-3	5/28/2019	ASY	M	471	GF (ALU)	BL	58.4	119	12.74
NCA2-5	5/28/2019	ASY	F	499	GF (KJ9)	BL	54.5	119	12.41
EBWH-7	5/29/2019	ASY	M	5	GF (A6U)	BL	63.8	119	13.26
EBWH-6	5/29/2019	ASY	F	6	GF (U94)	BL	58.7	120	13.49
EBWH-4	5/29/2019	ASY	M	7	GF (EJA)	BL	55	116	13.51
EBWH-1	5/29/2019	ASY	M	32	GF (AE9)	BL	59.8	115	12.98
EBWH-8	5/29/2019	ASY	M	33	GF (N7E)	BL	55.3	118	13.14
EBWH-5	5/29/2019	ASY	M	40	GF (82E)	BL	56.8	115	12.6
Q-2	5/29/2019	ASY	M	501	GF (MKJ)	BL	58.1	121	11.86
Q-4	5/29/2019	ASY	M	502	GF (AC4)	BL	57.6	119	12.24
TP-4	5/30/2019	ASY	M	39	GF (NP7)	BL	52.5	119	13.84
TP-8	5/30/2019	ASY	F	500	GF (U8C)	BL	54.3	118	12.71

[1]Beaches, Ninigret Conservation Area (NCA), Ninigret National Wildlife Refuge (NNWR), Thin Layer Deposition area at Ninigret (TLD), East Beach Watch Hill (EBWH), Quonochontaug (Q),

Trustom Pond NWR (TP)
[2]Age: After Second Year (ASY), Second Year (SY)
[3]Nanotag ID number for Motus network
[4]Band on left tibiotarsus: Green flag (GF), 3 alphanumeric codes in white
[5]Color band on right tibiotarsus: blue (BL), some birds had green flag on right leg

Appendix 1.4. Agreement between DWW and URI to install receiver and antennas on Block Island Wind Farm Turbine #1.

Equipment Installation, Maintenance, Use and Hold Harmless Agreement

This Equipment Installation, Maintenance, Use and Hold Harmless Agreement (the "Agreement") is executed by and between the University of Rhode Island ("URI") and Deepwater Wind, LLC ("DWW"), Deepwater Wind Block Island, LLC ("DWBI") and their respective affiliates of any tier including the f/v Lindsey E and the Atlantic Pioneer, which are currently under charter to DWBI (each a "DWW Party" and collectively "DWW Group").

Whereas, URI has requested DWBI to install and maintain, on behalf of URI, URI owned digital VHF telemetry technology to track the movements of high-priority species as more particularly described in Exhibit A ("URI Equipment") on one of DWBI's wind turbines and platforms located within DWBI's offshore windfarm located in Block Island Sound off the coast of Rhode Island (the "Location");

Whereas, DWBI is prepared to install and maintain the URI Equipment on of its wind turbines and platforms in that Location, as requested by URI, subject to the terms and conditions of this Agreement.

Now Therefore, in consideration of the premises and mutual covenants set forth herein, and for other good and valuable consideration, the parties hereby agree as follows:

1. Term. URI's obligations and agreements in this Agreement shall apply from July 31, 2017 through December 31, 2018 ("Term").

2. Acknowledgement. URI acknowledges and agrees that:

   2.1. URI will provide the URI Equipment to the DWW Parties for installation by the DWW parties on one turbine jacket on one of DWBI's wind turbines in the Location..

   2.2. Data collection will be performed by URI remotely, and the data collected by URI will be shared with the DWW Group upon request.

   2.3. URI personnel, representatives and/or contractors shall not have access to the Block Island Wind Farm at any time, and will not have access to the URI Equipment after URI has provided to the DWW Group for installation.

   2.4. While the DWW Parties will make reasonable efforts to provide power for the URI Equipment at all reasonable times, the DWW Parties make no representation or warranty with respect to the availability of on-board power as described in Exhibit A, or with respect to the quality of the on-board power.

   2.5. While the DWW parties will use reasonable efforts to properly install the URI Equipment (with advice and instructions from URI as needed and appropriate) so that it may be used as intended to collect data, and maintained in reasonable condition to allow its continuing use, the DWW Parties make no warranty with respect to, the proper installation of the URI Equipment, or with respect to the proper maintenance or condition of the URI Equipment once installed. However, the DWW Parties assume full responsibility for the health and safety of all their employees, agents

and representatives who are involved in the installation or maintenance of the URI Equipment (except and to the extent any such employee agent or representative is injured as a result of the negligence of URI or its employees, agents or representatives, or as a result of a known defect in the URI Equipment) and for compliance with OSHA requirements, or other applicable regulatory compliance requirements, relating to the installation or maintenance of the URI Equipment at the Location.

2.6. URI does hereby, on behalf of itself and its affiliates, subcontractors, and the directors, officers, agents, employees, successors and assigns of each of them (collectively, "URI Group") RELEASE, WAIVE, DISCHARGE, AND COVENANT NOT TO SUE the DWW Parties from any and all liability, claims, demands, actions, and causes of action whatsoever for any loss, damage, or destruction of the URI Equipment, REGARDLESS OF WHETHER SUCH LOSS IS CAUSED BY THE NEGLIGENCE OF THE DWW PARTIES, or otherwise and regardless of whether such liability arises in tort, contract, strict liability, or otherwise, to the fullest extent allowed by law.

3. Hold Harmless. URI shall be solely responsible for the safety and protection of the persons and property of URI Group, including the URI Equipment, and shall comply with all applicable federal, state and local safety laws and regulations. URI's liability under this Section shall not be limited notwithstanding anything contained herein to the contrary.

4. Indemnity. URI hereby agrees to indemnify, defend and hold harmless DWW Group from and against any and all claims, judgments, demands, causes of action, losses, liabilities, interest, awards, penalties, costs, fees and expenses (including without limitation, reasonable attorneys' fees and legal costs) (collectively "Claims") for: (i) personal or bodily injury to, sickness, disease or death of any URI employees of or individuals in the URI Group arising from, relating to, or in connection with this Agreement (for example in connection with data collection); (ii) any physical loss, loss of use of, or damage to the URI Equipment, whether owned, leased or chartered; and (iii) any fines and penalties imposed by any governmental authority on account of any violation of any applicable laws to be complied with by URI or the URI Group in connection with this Agreement.

5. Indemnity Scope. The indemnity obligations and releases set forth above shall apply to all Claims, regardless of whether caused or contributed to by negligence or other fault (including sole, joint or concurrent) of any of the parties indemnified or released, or any theory of legal liability, including strict liability, defect in premises, materials or equipment, "ruin", or any other anticipated or unanticipated event or condition and regardless of whether pre-existing the execution of this Agreement.

6. Indemnity Defense. When URI is required to indemnify a DWW Party in accordance with this Agreement for a claim brought by a third party, URI shall assume on behalf of such DWW Party, and conduct with due diligence and in good faith, the defense of any claim against such Party, whether or not URI shall be joined therein, and the DWW Party shall cooperate with URI in such defense. URI shall be in charge of the defense and settlement of such claim; provided, however, that without relieving URI of its obligations hereunder or impairing URI's right to control the defense or settlement thereof, the DWW Party may elect to participate through separate counsel in the defense of any such claim, but the fees and

expenses of such counsel shall be at the expense of such DWW Party; except in the event that (i) the DWW Party shall have reasonably concluded that there exists a material conflict of interest between URI and the DWW Party in the conduct of the defense of such claim (in which case URI shall not have the right to control the defense or settlement of such claim, on behalf of such DWW Party), or (ii) URI shall not have employed counsel to assume the defense of such claim within a reasonable time after notice of the commencement of an action thereon, in which case the reasonable fees and expenses of counsel shall be paid by URI. URI shall not settle any such claims or actions in a manner which would require any action or forbearance from action by any DWW Party without the prior written consent of the DWW Party.

7. Indemnity Survival. THE INDEMNITY OBLIGATIONS AND RELEASES THAT APPLY TO AN EVENT OR CONDITION THAT OCCURS DURING THE TERM OF THIS AGREEMENT SHALL SURVIVE AND NOT BE AFFECTED BY THE EXPIRATION OR TERMINATION OF THIS AGREEMENT.

8. Insurance. URI agrees that it shall procure and maintain insurance as require by law and as otherwise specified in this Section. Prior to the commencement of the Term and thereafter for the duration of the Term, URI shall at its own expense, procure and maintain in effect, or cause to be procured and maintained, the minimum insurance coverages specified in Appendix 1 with carriers acceptable to DWW. The insurance coverages shall not include (i) any claims made insurance policies or (ii) any self-insured retention or deductible amount greater than $250,000, unless approved by DWW in writing. All insurance policies, with the exception of workers' compensation, Employer's Liability and automobile liability, shall be primary to any other insurance or self-insurance maintained by DWW. All insurance policies (other than worker's compensation insurance) shall provide for a waiver of subrogation against each DWW Party by URI and its insurers. All insurance policies, with the exception of workers' compensation and Employer's Liability, shall name the DWW Parties as additional insureds. Prior to the commencement of the Term, URI shall deliver to DWW evidence of the required insurance coverage in the form of Certificates of Insurance acceptable to DWW. The insurance policies shall contain a provision that coverage cannot be cancelled, allowed to expire or the limits materially reduced, until at least thirty (30) days (ten (10) days in the case of nonpayment of premium) after written notice has been given to the DWW. All insurance coverages shall be provided by insurance companies acceptable to DWW and having ratings of A-/VII or better in the best Key Rating Insurance Guide (latest edition in effect at the latest date stated in the Certificates of Insurance provided in accordance with paragraph 5 above). Failure to maintain the insurance required under this Agreement shall constitute a material breach of this Agreement and URI shall be liable for any resulting costs, liabilities and damages (including attorneys' fees and settlement expenses) incurred by DWW in connection with such breach. The insurance provided shall in no manner relieve or release URI, its agents, subURIs and invitees from, or limit their liability as to, any obligations assumed under this Agreement.

9. Governing Law. This Agreement, any disputes or claims arising out of or relating to this Agreement, and any questions concerning its validity, construction or performance shall be governed by the substantive laws of the State of New York without regard to its conflict of law principles (other than Section 5-1401 of the New York General Obligations Law). Each of the Parties hereby irrevocably waives,

to the fullest extent permitted by law, any and all right to trial by jury in any legal proceeding arising out of or in connection with this Agreement.

10. Miscellaneous. The terms and provisions of this Agreement, including any appendix, may only be modified, amended or supplemented by written agreement duly executed by each party. No failure or delay by a DWW Party in exercising any right hereunder and no course of dealing between the parties shall operate as a waiver thereof. No waiver of any breach of the terms of this Agreement shall be effective unless such waiver is in writing and signed by DWW. No waiver of any breach shall be deemed to be a waiver of any other or subsequent breach. If any provision of this Agreement for any reason shall be held invalid, illegal or unenforceable by any governmental authority or court having jurisdiction over the interpretation or enforcement of this Agreement, then such holding shall not invalidate or render unenforceable any other provision hereof and such portions shall remain in full force and effect as if this Agreement had been executed without the invalid, illegal or unenforceable portion. If any provision of this Agreement is declared invalid, illegal or unenforceable, then the Parties shall promptly renegotiate to restore this Agreement as near as possible to its original intent and effect. This Agreement may be executed electronically and in more than one counterpart, each of which shall be deemed to be an original, but all of which together shall constitute one and the same document. This Agreement supersedes all prior agreements and understandings among the parties with respect to the subject matter hereof. An original of this executed Agreement may be imaged or scanned and stored on computer tapes and disks. If such an image of this Agreement is introduced as evidence in any judicial, arbitration, mediation or administrative proceedings, no party shall object to the admissibility of the imaged Agreement on the basis that it was not originated or maintained in documentary form under the hearsay rule, the best evidence rule or other rule of evidence.

In Witness Whereof, URI has caused this Agreement to be duly executed and delivered by the undersigned duly authorized representative.

University of Rhode Island

By: _____
Name:
Title:

Deepwater Wind, LLC
Deepwater Wind Block Island, LLC

By: _____
Name: Jeffrey Grybowski
Title: CEO

APPENDIX 1

Type of Coverage	Limits of Liability	Minimum Coverage
Workers' Compensation Insurance	Workers' compensation insurance in accordance with all applicable laws in the state(s) in which the Services are to be performed. The policy shall contain an "All States" endorsement, a "Voluntary Compensation" endorsement and include coverage for Alternate Employer.	Statutory
Employers' Liability Insurance	Employer's liability insurance, for the URI's liability arising out of injury to or death of its employees.	Employer's liability shall be written with minimum limits of $1,000,000 each accident; $1,000,000 disease policy limit and $1,000,000 disease each employee.
Commercial General Liability Insurance	Commercial General Liability Insurance written on an occurrence basis, unless otherwise agreed in writing by the DWW, for bodily injury (including death) and property damage claims to third parties arising from the Services performed by the URI. Said coverage shall include premises/operations, products/completed operations for a period of not less than three (3) years from the date that the Services are completed. The policy shall not include any exclusions for independent URIs, broad form property damage, blanket contractual liability and the policy must be endorsed to include sudden and accidental pollution (30 day discovery / 60 day reporting clause).	$1,000,000 each occurrence and $3,000,000 in the aggregate as respects products liability and completed operations and a $3,000,000 general aggregate.
Automobile Liability Insurance	Automobile Liability insurance providing coverage for all owned, non-owned and hired vehicles used in connection with the Services performed under this Agreement.	$1,000,000 per accident for bodily injury and property damage.
Umbrella/Excess Liability Insurance	Umbrella/Excess Liability Insurance. Such coverage shall be on an occurrence basis, unless otherwise agreed by the DWW, providing coverage over and above the Employer's Liability, Commercial General Liability, and Automobile Liability, insurance policies specified above.	$10,000,000 each occurrence and in the aggregate. The limits required herein may be satisfied by any combination of primary, umbrella or excess liability policies.

EXHIBIT A

Antennas: System would utilize four 6-element antennas per turbine, mounted on each side of one turbine platform with approximately 90-degree separation of main beams. Each antenna is 64-in. long and weighs approximately 7 lbs. The antennas are tuned to 166 MHz and are receive-only (do not transmit). URI will provide mounting hardware provided by the manufacturer.

Receiver: 'Sensorgnome' made by Compudata (https://compudata.ca/sensorgnome/). Contained within pelican case (13-in. x 12-in. x 6-in.) and stored inside an additional, slightly larger waterproof case (16-in x 15-in x 9-in).

Power requirements:
Power draw of the receiver is ~15.5 amp hrs/day (with WIFI data or cell data uplink). Receiver will be powered by onboard power source (if available).

Data download procedures:
Download data remotely through cellular data stick (requires cellular reception)

Appendix 1.5. Instructions for Ørsted staff on how to install Lotek SRX800DI receiver on Block Island Wind Farm turbine #1, and how to download data for 2019 field season on BIWF Turbine #1

Installing Lotek receiver:

1) hook up power cable on back of black box, connect to power supply with alligator clips in yellow otter box, run outlet to outside of otter box to connect to extension cord to plug into 110 v system
2) hook up GPS (in pouch in black receiver box) to back plug on receiver – put GPS on outside of otter box
3) turn on power supply (red light should go on), then turn on receiver – **mode** light should blink green every 3 sec if downloading data
5) plug in antennas into BNC ports 1-4 on receiver, please record which antenna is in which port (e.g., east facing antenna is in port 1) below
6) **Optional** - to verify receiver is working, connect USB cable (in pouch in back of receiver) to laptop.
7) turn on laptop, open to desktop (password is **Birder123,** capital **B**)
8) click on **Desktop icon** (left column, URI stadium)
9) Click on **SRX800 Host shortcut Lotek icon** (right hand column)
10) Click "**USB**" on connect icon, 2nd column from left, this will connect laptop to receiver, it should state in lower right: **Connection: USB, MODEL SRX800 D1**
11) Click **Live View,** every 10 sec a new antenna should show up, and Tag ID 30 show up**.**
12) If working, click on Live View to turn it off, then (shut down SRTX800 host – red X upper right; then shut off laptop – mouse to upper left windows icon, then shut down icon upper right), just make sure receiver still has **green light flashing on Mode**

Antenna port on receiver	Direction antenna facing
1	
2	
3	
4	

Peter Paton
Cell 401-XXX-XXXX
1 Greenhouse Rd
Dept of Natural Resources Science
Univ of Rhode Island
Kingston RI 02881

Appendix 1.5 continued:
Download data from Lotek bird receiver

1) Make sure receiver is on (mode light should blink green if collecting data)
2) hook up tan cable (in pouch inside black Lotek receiver first letter is box) from receiver to USB port in laptop
3) turn on laptop, open to desktop (password is **Birder123,** capital **B**)
4) click on **Desktop icon** (left column, URI stadium)
5) Click on **SRX800 Host shortcut Lotek icon** (right hand column)
6) Click "**USB**" on connect icon, 2nd column from left, this will connect laptop to receiver, it should state in lower right: **Connection: USB, MODEL SRX800 D1**
7) Click Select **Download type** "**Everything since last download**"
8) click **Download** in receiver data column (3rd from right)
9) SRX data download panel should open up, click "**Download**" button –right column
10) Enter file name "BIWF date" (e.g., BIWF 13 May 2019) – then click **Save**
11) High-speed file receive box should open up - blue bar filling screen shows data download down**, then click "Done" then click "OK' on next screen**
12) Back at SRX data download screen, if free memory is low (e.g, <100,000 bytes (upper left)**,** then click **Log On (lower right),** then click **Reset Data Memory** then click **Yes**
13) **Click Exit (lower right), you should be back on SRX host screen**
14) you can disconnect cable, shut down laptop (shut down SRTX800 host – red X upper right; then shut off laptop – mouse to upper left windows icon, then shut down icon upper right), just make sure receiver still has green light flashing on Mode

Appendix 1 6. Matlab code used to estimate the location of a test tag during kite surveys (2017 and 2018) or drone surveys (2019) from automated tracking stations on Block Island.

I: Calibration and Bird Tracking, kite survey 2017

```
% close all;
% clear all;
clc; clear;%close all
z=15; % the height of the bird
t_size=20; % change the value here to adjust the window size(unit:second)
time_mode=2; % 1: the previsou time window; 2: the time window which is overlapped with last one
% different case by how many antennas
G0 = 0; % Gain for conversion from sensorgnome to lotek
gain = 8; % Gain of antenna based on the number of elements
% a=801.59; b=30.273; % two constants
p0=4.89*10^-11;% 2.55271649539568e-12;

b=0.3013;%0.5752/2;
ZM=255;Zm=0;
lambda=1.8; % wavelength in free space
le=4.6; % the effective length of the overall array
k0=2*pi/lambda; % wavenumber in freespace
beta0=-(k0+2.94/le);
p=beta0*le/2; q=k0*le/2;
psi=0:pi/200:2*pi;
g_psi=cos(pi/2*sin(psi))./cos(psi).*sinc((p+q*cos(psi))/pi);

% Used to find the intersection points
%
delta_psi=pi/3;
g_psi_delta=cos(pi/2*sin(psi-delta_psi))./cos(psi-delta_psi).*sinc((p+q*cos(psi-delta_psi))/pi);
[psi_inter,r_inter]=polyxpoly(psi,abs(g_psi),psi,abs(g_psi_delta),'unique');
% polar(psi,abs(g_psi),'--r');
% hold on;
% polar(psi,abs(g_psi_delta),'--g');
% polar(psi_inter,r_inter,'o');

%[name,mainbeam,t_lat,t_lon,t_y,t_x,t_h,g_h] = csvimport('Allstation.csv', 'columns',
[1,2,3,4,5,6,7,8],'noHeader', true);
[time,signal,a_detect,date] = csvimport('direction_file_BI_2017.csv', 'columns', [1,2,3,4],'noHeader', true);
[name,mainbeam,t_y,t_x,t_h,g_h] = csvimport('Allstations_2017.csv', 'columns', [1,2,3,4,5,6],'noHeader', true);

tim_start = 1;
tim_last = 5000;
time = time(tim_start:tim_last);
signal = signal(tim_start:tim_last);
a_detect = a_detect(tim_start:tim_last);
% for i = 1:length(time)-1
% tim_test(i) = time(i+1) - time(i);
% end
% plot(tim_test)
%%%%%% converting signal of Sensorgnome to Lotek %%%%%%
% for 2017 BI wind farm and BI black rock are Sensorgnome
signal0 = signal;
SR = ismember(a_detect,{'BIBR-1','BIBR-2','BIBR-4','BIWF-1','BIWF-3','BIWF-5','BIWF-7'}); %find sensorgnomes;
signal(SR) = (40*G0 + 44*signal(SR) + 4565)/11;


%%%%%

index=zeros(1,size(a_detect,1));
for i = 1:size(a_detect,1)
   indexc=strfind(name, a_detect{i});
   index(i)=find(not(cellfun('isempty', indexc)));
end
HT=t_h(index)+g_h(index); % elevation of tower + elevation of ground
theta=mainbeam(index);  % beam of each bearing


g_delta=10^-((11.1-gain)/10); %for TE14-0 and GG14&15, the gain should be adjusted (9dbi for them, 11.1dbi for
others)
sp_antenna=ismember(a_detect,{'BIWF-1','BIWF-3','BIWF-5','BIWF-7'}); %find the special antenna whose gain is 9
dbi;

% convert the displaying number to the received power
xi=sqrt(p0*(((ZM-2*Zm+signal)./(ZM-signal)).^(1/(2*b))-1));
%-----------------------------------------------------------------
% get the radar range with the given
r=sqrt(HT./xi*z*sin(p+q)/(p+q)).*(~sp_antenna)...
```

```
    + g_delta*sqrt(HT./xi*z*sin(p+q)/(p+q)).*sp_antenna;
tower_x=t_x(index);
tower_y=t_y(index);
global_x=r.*sind(theta)+t_x(index); % to my understanding these are locations of signal(bird) if they are
global_y=r.*cosd(theta)+t_y(index); % we assume they are exactly in the direction of antenna

% Used to plot the signal above the value-------
%
indexsignal=find(signal>0);  % you can change the value
global_x=global_x(indexsignal);
global_y=global_y(indexsignal);
time=time(indexsignal);
tower_x=tower_x(indexsignal);
tower_y=tower_y(indexsignal);

% global t n;
n=1;
t=1;

if time_mode==1
  global_x_new=zeros(1,1000);global_y_new=zeros(1,1000);time_new=zeros(1,1000);
   while t <= length(time) %length(time)
        temp_diff=time(t:end)-time(t);
        temp_index=find(abs(temp_diff)<=(t_size));
          switch length(temp_index)
            case 1
                global_x_new(n)=global_x(t);
                global_y_new(n)=global_y(t);
                time_new(n)=time(t);
                n=n+1;
                t=t+1;
            case 2
                 if isequal(a_detect{t},a_detect{t+1})
                     global_x_new(n:n+1)=global_x(t-1+temp_index);
                     global_y_new(n:n+1)=global_y(t-1+temp_index);
                     time_new(n:n+1)=time(t-1+temp_index);
                     n=n+2;
                     t=t+2;

                 elseif (strncmpi(a_detect{t},a_detect{t+1},4) && ...
                         ismember(abs(str2num(a_detect{t}(6))-str2num(a_detect{t+1}(6))),[1,5]))  % special
case xxx-1 and xxx-6
                     r1_delta_psi=theta(t)/180*pi;r2_delta_psi=theta(t+1)/180*pi;
                     r1_g_psi=cos(pi/2*sin(psi-r1_delta_psi))./cos(psi-r1_delta_psi).*sinc((p+q*cos(psi-
r1_delta_psi))/pi);
                     r2_g_psi=cos(pi/2*sin(psi-r2_delta_psi))./cos(psi-r2_delta_psi).*sinc((p+q*cos(psi-
r2_delta_psi))/pi);
                     r1r2_sp=ismember({a_detect{t:t+1}},{'BIWF-1','BIWF-3','BIWF-5','BIWF-7'}); %find the
special antenna whose gain is 9 dbi;
                     xi1=sqrt(p0*(((ZM-2*Zm+signal(t))/(ZM-signal(t)))^(1/(2*b))-1));
                     xi2=sqrt(p0*(((ZM-2*Zm+signal(t+1))/(ZM-signal(t+1)))^(1/(2*b))-1));
                     r1=sqrt(HT(t)/xi1*z*abs(r1_g_psi))*(~r1r2_sp(1))...
                         +g_delta*sqrt(HT(t)/xi1*z*abs(r1_g_psi))*(r1r2_sp(1));
                     r2=sqrt(HT(t+1)/xi2*z*abs(r2_g_psi))*(~r1r2_sp(2))...
                         +g_delta*sqrt(HT(t+1)/xi2*z*abs(r2_g_psi))*(r1r2_sp(2));
                     [temp_psi_int,temp_r]=polyxpoly(psi,r1,psi,r2,'unique');
                     if abs(str2num(a_detect{t}(6))-str2num(a_detect{t+1}(6)))==1
                       int_index=find(temp_psi_int>min([r1_delta_psi,r2_delta_psi]) &
temp_psi_int<max([r1_delta_psi,r2_delta_psi]));
                     else
                       int_index=find(temp_psi_int>max([r1_delta_psi,r2_delta_psi]) &
temp_psi_int<(min([r1_delta_psi,r2_delta_psi])+2*pi));
                     end
                     psi_int=temp_psi_int(int_index);
                     r_int=temp_r(int_index);
                     global_x_new(n)=mean(r_int.*sin(psi_int))+tower_x(t);
                     global_y_new(n)=mean(r_int.*cos(psi_int))+tower_y(t);
                     time_new(n)=mean(time(t-1+temp_index));
                     n=n+1;
                     t=t+2;
                 else
                     global_x_new(n)=mean(global_x(t-1+temp_index));
                     global_y_new(n)=mean(global_y(t-1+temp_index));
                     time_new(n)=mean(time(t-1+temp_index));
                     n=n+1;
                     t=t+2;
                 end
            otherwise
                  if sum(strncmpi(a_detect{t-1+temp_index(1)},a_detect(t-1+temp_index(1):t-
1+temp_index(end),1),4)==0)==0
%                     global_x_new(n)=tower_x(t);
```

```
%                       global_y_new(n)=tower_y(t);
%                       time_new(n)=mean(time(t-1+temp_index));
%                       n=n+1;
%                       t=t+length(temp_index);
                    else
                       global_x_new(n)=mean(global_x(t-1+temp_index));
                       global_y_new(n)=mean(global_y(t-1+temp_index));
                       time_new(n)=mean(time(t-1+temp_index));
                       n=n+1;
                       t=t+length(temp_index);
                    end
            end
    end
 global_x_new=global_x_new(1:n-1);global_y_new=global_y_new(1:n-1);time_new=time_new(1:n-1);

elseif time_mode ==2
  n=1;
  global_x_new=zeros(1,1000);
  global_y_new=zeros(1,1000);
  time_new=zeros(1,1000);
  for t = t_size/2:t_size/2:time(end)+t_size/2
      temp_diff=time-t;
      temp_index=find(abs(temp_diff)<=(t_size/2));
      if ~isempty(temp_index)
           switch length(temp_index)
              case 1  % if one detection is smaller time stamp
                 global_x_new(n)=global_x(temp_index);
                 global_y_new(n)=global_y(temp_index);
%                  time_new(n)=time(temp_index);
                 time_new(n)=t;
                 n=n+1;
              case 2 % If two detections are smaller time stamp
                   if isequal(a_detect{temp_index(1)},a_detect{temp_index(2)})
                    global_x_new(n)=mean(global_x(temp_index));
                    global_y_new(n)=mean(global_y(temp_index));
                    %time_new(n)=mean(time(temp_index));
                    time_new(n)=t;
                    n=n+1;
                  elseif (strncmpi(a_detect{temp_index(1)},a_detect{temp_index(2)},4) && ...
                        ismember(abs(str2num(a_detect{temp_index(1)}(6))-
str2num(a_detect{temp_index(2)}(6))),[1,5]))  % special case xxx-1 and xxx-6
                    r1_delta_psi=theta(temp_index(1))/180*pi; % convert bearing to radian
                    r2_delta_psi=theta(temp_index(2))/180*pi;

                    r1_g_psi=cos(pi/2*sin(psi-r1_delta_psi))./cos(psi-r1_delta_psi).*sinc((p+q*cos(psi-
r1_delta_psi))/pi);
                    r2_g_psi=cos(pi/2*sin(psi-r2_delta_psi))./cos(psi-r2_delta_psi).*sinc((p+q*cos(psi-
r2_delta_psi))/pi);

                    r1r2_sp=ismember({a_detect{temp_index(1):temp_index(2)}},{'BIWF-1','BIWF-3','BIWF-
5','BIWF-7'}); %find the special antenna whose gain is 9 dbi;

                    xi1=sqrt(p0*(((ZM-2*Zm+signal(temp_index(1)))/(ZM-signal(temp_index(1))))^(1/(2*b))-1));
                    xi2=sqrt(p0*(((ZM-2*Zm+signal(temp_index(2)))/(ZM-signal(temp_index(2))))^(1/(2*b))-1));

                    r1=sqrt(HT(temp_index(1))/xi1*z*abs(r1_g_psi))*(~r1r2_sp(1))...
                        +g_delta*sqrt(HT(temp_index(1))/xi1*z*abs(r1_g_psi))*(r1r2_sp(1));
                    r2=sqrt(HT(temp_index(2))/xi2*z*abs(r2_g_psi))*(~r1r2_sp(2))...
                        +g_delta*sqrt(HT(temp_index(2))/xi2*z*abs(r2_g_psi))*(r1r2_sp(2));

%                     r1=sqrt(HT(temp_index(1))*exp(-(signal(temp_index(1))-a)/(2*b))*z*abs(r1_g_psi));
%                     r2=sqrt(HT(temp_index(2))*exp(-(signal(temp_index(2))-a)/(2*b))*z*abs(r2_g_psi));
                    [temp_psi_int,temp_r]=polyxpoly(psi,r1,psi,r2,'unique');
                    if abs(str2num(a_detect{temp_index(1)}(6))-str2num(a_detect{temp_index(2)}(6)))==1
                      int_index=find(temp_psi_int>min([r1_delta_psi,r2_delta_psi]) &
temp_psi_int<max([r1_delta_psi,r2_delta_psi]));
                    else
                      int_index=find(temp_psi_int>max([r1_delta_psi,r2_delta_psi]) &
temp_psi_int<(min([r1_delta_psi,r2_delta_psi])+2*pi));
                    end
                    psi_int=temp_psi_int(int_index);
                    r_int=temp_r(int_index);
                    global_x_new(n)=mean(r_int.*sin(psi_int))+tower_x(temp_index(1));
                    global_y_new(n)=mean(r_int.*cos(psi_int))+tower_y(temp_index(1));
                    %time_new(n)=mean(time(temp_index));
                    time_new(n)=t;
                    n=n+1;
                  else
                    global_x_new(n)=mean(global_x(temp_index));
                    global_y_new(n)=mean(global_y(temp_index));
                    %time_new(n)=mean(time(temp_index));
```

```
                    time_new(n)=t;
                    n=n+1;

                end
            otherwise % for 3 and more detections which are smaller than time stamp
                if sum(strncmpi(a_detect{temp_index(1)},a_detect(temp_index(1):temp_index(end),1),4)==0)==0
% All are from one tower
%                         global_x_new(n)=tower_x(temp_index(1));
%                         global_y_new(n)=tower_y(temp_index(1));
%                         %time_new(n)=mean(time(temp_index));
%                         time_new(n)=t;
%                         n=n+1;
                    else
                        global_x_new(n)=mean(global_x(temp_index));
                        global_y_new(n)=mean(global_y(temp_index));
                        %time_new(n)=mean(time(temp_index));
                        time_new(n)=t;
                        n=n+1;
                    end


          end

      end

  end
 global_x_new=global_x_new(1:n-1);
 global_y_new=global_y_new(1:n-1);
 time_new=time_new(1:n-1);

end

col=time_new;
xplot=global_x_new;
yplot=global_y_new;
zplot=zeros(size(xplot));
% figure('position',[-1800 300 600 400])
% for i = 1:length(xplot)
% plot(xplot(i),yplot(i),'x')
% hold on
% pause(0.05)
% end
% static_tra=surface([xplot;xplot],[yplot;yplot],[zplot;zplot],[col;col],...
%         'facecol','no',...
%         'edgecol','interp',...
%         'LineStyle','--',...
%         'linewidth',0.5,...
%         'Marker','o',...
%         'MarkerSize',11 );

% h=colorbar;

%%%%%%%%%%%% plotting in google map
kite = readtable('track2017.csv'); % Greg's coordinates
kite_tim = datenum(kite.Var2)*3600*24;
kite_delta_tim = kite_tim - kite_tim(1);

% Wind turbines locations
BITU_lat = [41.125733, 41.119933,41.114767, 41.110200, 41.106383];
BITU_lon = [-71.507567, -71.513950, -71.521133, -71.529117, -71.537650];

% reciever's location
BR_lon = -71.5901; BR_lat = 41.148;
SE_lon = -71.5514; SE_lat = 41.153;
BR_bearing = [102;152;200]; BR_unit_circle = 360 + 90 - BR_bearing;
SE_bearing = [0;60;120;180;240;300];  SE_unit_circle = 360 + 90 - SE_bearing;
BR_desire_lon = [BR_lon + 0.02; BR_lon + 0.005; BR_lon - 0.005];
SE_desire_lon = [SE_lon; SE_lon + 0.01; SE_lon + 0.01; SE_lon;SE_lon - 0.01;SE_lon - 0.01];

BR_desire_lat = tand(BR_unit_circle).*(BR_desire_lon - BR_lon) + BR_lat;
SE_desire_lat = tand(SE_unit_circle).*(SE_desire_lon - SE_lon) + SE_lat;
SE_desire_lat(1) = SE_lat + 0.01; SE_desire_lat(4) = SE_lat - 0.01;


figure('position',[-1000 300 600 400])
zone    = repmat('18 N',length(xplot),1);
[lat1,lon1] = utm2deg(xplot,yplot,zone);
scatter(lon1,lat1,[],time_new,'^')
hold on
scatter(kite.Var3(1:end),kite.Var4(1:end),10,kite_delta_tim,'.')
hold on
```

```
for i = 1:length(BR_bearing)
    plot([BR_lon;BR_desire_lon(i)],[BR_lat;BR_desire_lat(i)],'k')
    hold on
end
for i =1:length(SE_bearing)
    plot([SE_lon;SE_desire_lon(i)],[SE_lat;SE_desire_lat(i)],'k')
    hold on
end
hold on
scatter(BITU_lon,BITU_lat,'x','k','LineWidth',2)
% text(-71.45,41.27,'x   Block Island Wind Turbines')
grid on
colormap(jet)
cc = colorbar;cc.Label.String = 'Time (s)'
% title(['Gain = ' num2str(gain) ' dB '])
plot_google_map('MapType','terrain')
print output2017 -djpeg -r300

%% creating table for prediction versus actual kite
tim_start = datenum(date(1))*24*3600;
tim_new1  = tim_start + time_new';
for i = 1:length(tim_new1)
     [diff(i),index_tim(i)] = min(abs(kite_tim - tim_new1(i)));
end

kite_time    = kite.Var2(index_tim);
kite_lat_sel = kite.Var4(index_tim);
kite_lon_sel = kite.Var3(index_tim);
[kite_x_sel,kite_y_sel] = wgs2utm(kite_lat_sel,kite_lon_sel,18,'N');

x_diff = xplot' - kite_x_sel;
y_diff = yplot' - kite_y_sel;

figure('position',[-1800 200 600 400])
plot(x_diff);hold on
plot(y_diff)
legend('xdiff','ydiff')

table1 = table(kite_time,kite_x_sel,kite_y_sel,xplot',yplot',
'VariableNames',{'time','x_kite','y_kite','x_predict','y_predict'});
writetable(table1,'simulation_data_2017.csv')
```

II: Calibration and Bird tracking Code: kite survey 2018

```
% close all;
% clear all;
clc; clear
z=20; % the height of the bird
month_filename = 'Aug'; %Aug or July
time_mode=2; % 1: the previsou time window; 2: the time window which is overlapped with last one
% different case by how many antennas
t_size=30; % change the value here to adjust the window size(unit:second)
G0 = 0; % Gain of conversion from sensorgnome to lotek
gain =8; % GAin of antenna based on the number of elements

% a=801.59; b=30.273; % two constants

p0= 4e-12; %4.89*10^-11;2.55271649539568e-12;
b=0.3013;%0.5752/2;
ZM=255;Zm=0;
lambda=1.8; % wavelength in free space
le=2; % the effective length of the overall array
k0=2*pi/lambda; % wavenumber in freespace
beta0= -(k0+2.94/le);
p=beta0*le/2; q=k0*le/2;
psi=0:pi/200:2*pi;
g_psi=cos(pi/2*sin(psi))./cos(psi).*sinc((p+q*cos(psi))/pi);

% Used to find the intersection points
%
delta_psi=pi/3;
g_psi_delta=cos(pi/2*sin(psi-delta_psi))./cos(psi-delta_psi).*sinc((p+q*cos(psi-delta_psi))/pi);
[psi_inter,r_inter]=polyxpoly(psi,abs(g_psi),psi,abs(g_psi_delta),'unique');
% polar(psi,abs(g_psi),'--r');
% hold on;
% polar(psi,abs(g_psi_delta),'--g');
% polar(psi_inter,r_inter,'o');
```

```
% Done

%[name,mainbeam,t_lat,t_lon,t_y,t_x,t_h,g_h] = csvimport('Allstation.csv', 'columns',
[1,2,3,4,5,6,7,8],'noHeader', true);
[time,signal,a_detect,date] = csvimport(['direction_file_BI_2018_no_WF_no_omni_' month_filename '.csv'],
'columns', [1,2,3,4],'noHeader', true);
[name,mainbeam,t_y,t_x,t_h,g_h] = csvimport('Allstations_2018.csv', 'columns', [1,2,3,4,5,6],'noHeader', true);

% tim_start = 1;
% tim_last = 1500;
% time = time(tim_start:tim_last);
% signal = signal(tim_start:tim_last);
% a_detect = a_detect(tim_start:tim_last);
%%%%%% converting signal of Sensorgnome to Lotek %%%%%%
% for 2018 all receivers are sensorgnome

signal = (40*G0 + 44*signal + 4565)/11;


%%%%%

index=zeros(1,size(a_detect,1));
for i = 1:size(a_detect,1)
   indexc=strfind(name, a_detect{i});
   index(i)=find(not(cellfun('isempty', indexc)));
end
HT=t_h(index)+g_h(index); % elevation of tower + elevation of ground
theta=mainbeam(index);  % beam of each bearing


g_delta=10^-((11.1-gain)/10); %for TE14-0 and GG14&15, the gain should be adjusted (9dbi for them, 11.1dbi for
others)
sp_antenna=ismember(a_detect,{'BIBR-1','BIBR-2','BIBR-3','BIBR-4','BIWF-1','BIWF-3','BIWF-5','BIWF-7','SELI-
2','SELI-3'}); %find the special antenna whose gain is 9 dbi;

% convert the displaying number to the received power
xi=sqrt(p0*(((ZM-2*Zm+signal)./(ZM-signal)).^(1/(2*b))-1));
%-----------------------------------------------------------------
% get the radar range with the given
r=sqrt(HT./xi*z*sin(p+q)/(p+q)).*(~sp_antenna)...
    + g_delta*sqrt(HT./xi*z*sin(p+q)/(p+q)).*sp_antenna;
tower_x=t_x(index);
tower_y=t_y(index);
global_x=r.*sind(theta)+t_x(index);
global_y=r.*cosd(theta)+t_y(index);

% Used to plot the signal above the value-------
%
indexsignal=find(signal>0);  % you can change the value
global_x=global_x(indexsignal);
global_y=global_y(indexsignal);
time=time(indexsignal);
tower_x=tower_x(indexsignal);
tower_y=tower_y(indexsignal);
% figure
% plot(global_x,global_y,'.')
% hold on
% plot(tower_x,tower_y,'x')

%
% done--------------------

% global t n;
n=1;
% time_window=[];global_xwindow=[];global_ywindow=[];
t=1;


if time_mode==1
  global_x_new=zeros(1,1000);global_y_new=zeros(1,1000);time_new=zeros(1,1000);
   while t <= length(time) %length(time)
        temp_diff=time(t:end)-time(t);
        temp_index=find(abs(temp_diff)<=(t_size));
          switch length(temp_index)
            case 1
                global_x_new(n)=global_x(t);
                global_y_new(n)=global_y(t);
                time_new(n)=time(t);
                n=n+1;
                t=t+1;
            case 2
```

```
                if isequal(a_detect{t},a_detect{t+1})
                    global_x_new(n:n+1)=global_x(t-1+temp_index);
                    global_y_new(n:n+1)=global_y(t-1+temp_index);
                    time_new(n:n+1)=time(t-1+temp_index);
                    n=n+2;
                    t=t+2;

                elseif (strncmpi(a_detect{t},a_detect{t+1},4) && ...
                        ismember(abs(str2num(a_detect{t}(6))-str2num(a_detect{t+1}(6))),[1,5]))  % special
case xxx-1 and xxx-6
                    r1_delta_psi=theta(t)/180*pi;r2_delta_psi=theta(t+1)/180*pi;
                    r1_g_psi=cos(pi/2*sin(psi-r1_delta_psi))./cos(psi-r1_delta_psi).*sinc((p+q*cos(psi-
r1_delta_psi))/pi);
                    r2_g_psi=cos(pi/2*sin(psi-r2_delta_psi))./cos(psi-r2_delta_psi).*sinc((p+q*cos(psi-
r2_delta_psi))/pi);
                    r1r2_sp=ismember({a_detect{t:t+1}},{'BIBR-1','BIBR-2','BIBR-3','BIBR-4','BIWF-1','BIWF-
3','BIWF-5','BIWF-7','SELI-2','SELI-3'}); %find the special antenna whose gain is 9 dbi;
                    xi1=sqrt(p0*(((ZM-2*Zm+signal(t))/(ZM-signal(t)))^(1/(2*b))-1));
                    xi2=sqrt(p0*(((ZM-2*Zm+signal(t+1))/(ZM-signal(t+1)))^(1/(2*b))-1));
                    r1=sqrt(HT(t)/xi1*z*abs(r1_g_psi))*(~r1r2_sp(1))...
                        +g_delta*sqrt(HT(t)/xi1*z*abs(r1_g_psi))*(r1r2_sp(1));
                    r2=sqrt(HT(t+1)/xi2*z*abs(r2_g_psi))*(~r1r2_sp(2))...
                        +g_delta*sqrt(HT(t+1)/xi2*z*abs(r2_g_psi))*(r1r2_sp(2));
                    [temp_psi_int,temp_r]=polyxpoly(psi,r1,psi,r2,'unique');
                    if abs(str2num(a_detect{t}(6))-str2num(a_detect{t+1}(6)))==1
                      int_index=find(temp_psi_int>min([r1_delta_psi,r2_delta_psi]) &
temp_psi_int<max([r1_delta_psi,r2_delta_psi]));
                    else
                      int_index=find(temp_psi_int>max([r1_delta_psi,r2_delta_psi]) &
temp_psi_int<(min([r1_delta_psi,r2_delta_psi])+2*pi));
                    end
                    psi_int=temp_psi_int(int_index);
                    r_int=temp_r(int_index);
                    global_x_new(n)=mean(r_int.*sin(psi_int))+tower_x(t);
                    global_y_new(n)=mean(r_int.*cos(psi_int))+tower_y(t);
                    time_new(n)=mean(time(t-1+temp_index));
                    n=n+1;
                    t=t+2;
                else
                    global_x_new(n)=mean(global_x(t-1+temp_index));
                    global_y_new(n)=mean(global_y(t-1+temp_index));
                    time_new(n)=mean(time(t-1+temp_index));
                    n=n+1;
                    t=t+2;
                end
            otherwise
                 if sum(strncmpi(a_detect{t-1+temp_index(1)},a_detect(t-1+temp_index(1):t-
1+temp_index(end),1),4)==0)==0
                    global_x_new(n)=tower_x(t);
                    global_y_new(n)=tower_y(t);
                    time_new(n)=mean(time(t-1+temp_index));
                    n=n+1;
                    t=t+length(temp_index);
                 else
                    global_x_new(n)=mean(global_x(t-1+temp_index));
                    global_y_new(n)=mean(global_y(t-1+temp_index));
                    time_new(n)=mean(time(t-1+temp_index));
                    n=n+1;
                    t=t+length(temp_index);
                 end
          end
   end
 global_x_new=global_x_new(1:n-1);global_y_new=global_y_new(1:n-1);time_new=time_new(1:n-1);

elseif time_mode ==2
  n=1;
  global_x_new=zeros(1,1000);
  global_y_new=zeros(1,1000);
  time_new=zeros(1,1000);
  for t = t_size/2:t_size/2:time(end)+t_size/2
      temp_diff=time-t;
      temp_index=find(abs(temp_diff)<=(t_size/2));
      if length(temp_index)>=3
          temp_index=temp_index(2:3);
      end
      if ~isempty(temp_index)
           switch length(temp_index)
              case 1
                 global_x_new(n)=global_x(temp_index);
                 global_y_new(n)=global_y(temp_index);
%                  time_new(n)=time(temp_index);
```

```
                time_new(n)=t;
                n=n+1;
            case 2
                if isequal(a_detect{temp_index(1)},a_detect{temp_index(2)})
                  global_x_new(n)=mean(global_x(temp_index));
                  global_y_new(n)=mean(global_y(temp_index));
                  %time_new(n)=mean(time(temp_index));
                  time_new(n)=t;
                  n=n+1;
                elseif (strncmpi(a_detect{temp_index(1)},a_detect{temp_index(2)},4) && ...
                     ismember(abs(str2num(a_detect{temp_index(1)}(6))-
str2num(a_detect{temp_index(2)}(6))),[1,5]))  % special case xxx-1 and xxx-6
                  r1_delta_psi=theta(temp_index(1))/180*pi;r2_delta_psi=theta(temp_index(2))/180*pi;
                  r1_g_psi=cos(pi/2*sin(psi-r1_delta_psi))./cos(psi-r1_delta_psi).*sinc((p+q*cos(psi-
r1_delta_psi))/pi);
                  r2_g_psi=cos(pi/2*sin(psi-r2_delta_psi))./cos(psi-r2_delta_psi).*sinc((p+q*cos(psi-
r2_delta_psi))/pi);
                  r1r2_sp=ismember({a_detect{temp_index(1):temp_index(2)}},{'BIBR-1','BIBR-2','BIBR-
3','BIBR-4','BIWF-1','BIWF-3','BIWF-5','BIWF-7','SELI-2','SELI-3'}); %find the special antenna whose gain is 9
dbi;
                  xi1=sqrt(p0*(((ZM-2*Zm+signal(temp_index(1)))/(ZM-signal(temp_index(1))))^(1/(2*b))-1));
                  xi2=sqrt(p0*(((ZM-2*Zm+signal(temp_index(2)))/(ZM-signal(temp_index(2))))^(1/(2*b))-1));
                  r1=sqrt(HT(temp_index(1))/xi1*z*abs(r1_g_psi))*(~r1r2_sp(1))...
                      +g_delta*sqrt(HT(temp_index(1))/xi1*z*abs(r1_g_psi))*(r1r2_sp(1));
                  r2=sqrt(HT(temp_index(2))/xi2*z*abs(r2_g_psi))*(~r1r2_sp(2))...
                      +g_delta*sqrt(HT(temp_index(2))/xi2*z*abs(r2_g_psi))*(r1r2_sp(2));

%                   r1=sqrt(HT(temp_index(1))*exp(-(signal(temp_index(1))-a)/(2*b))*z*abs(r1_g_psi));
%                   r2=sqrt(HT(temp_index(2))*exp(-(signal(temp_index(2))-a)/(2*b))*z*abs(r2_g_psi));
                  [temp_psi_int,temp_r]=polyxpoly(psi,r1,psi,r2,'unique');
                  if abs(str2num(a_detect{temp_index(1)}(6))-str2num(a_detect{temp_index(2)}(6)))==1
                    int_index=find(temp_psi_int>min([r1_delta_psi,r2_delta_psi]) &
temp_psi_int<max([r1_delta_psi,r2_delta_psi]));
                  else
                    int_index=find(temp_psi_int>max([r1_delta_psi,r2_delta_psi]) &
temp_psi_int<(min([r1_delta_psi,r2_delta_psi])+2*pi));
                  end
                  psi_int=temp_psi_int(int_index);
                  r_int=temp_r(int_index);
                  global_x_new(n)=mean(r_int.*sin(psi_int))+tower_x(temp_index(1));
                  global_y_new(n)=mean(r_int.*cos(psi_int))+tower_y(temp_index(1));
                  %time_new(n)=mean(time(temp_index));
                  time_new(n)=t;
                  n=n+1;
                else
                  global_x_new(n)=mean(global_x(temp_index));
                  global_y_new(n)=mean(global_y(temp_index));
                  time_new(n)=mean(time(temp_index));
                  time_new(n)=t;
                  n=n+1;

                end
             otherwise

                 if sum(strncmpi(a_detect{temp_index(1)},a_detect(temp_index(1):temp_index(end),1),4)==0)==0
%                       global_x_new(n)=tower_x(temp_index(1));
%                       global_y_new(n)=tower_y(temp_index(1));
%                       %time_new(n)=mean(time(temp_index));
%                       time_new(n)=t;
%                       n=n+1;
                  else
                       global_x_new(n)=mean(global_x(temp_index));
                       global_y_new(n)=mean(global_y(temp_index));
                       %time_new(n)=mean(time(temp_index));
                       time_new(n)=t;
                       n=n+1;
                  end


        end

    end
  end
 global_x_new=global_x_new(1:n-1);
 global_y_new=global_y_new(1:n-1);
 time_new=time_new(1:n-1);

end

col=time_new;
xplot=global_x_new;
```

```
yplot=global_y_new;
zplot=zeros(size(xplot));
% figure
% static_tra=surface([xplot;xplot],[yplot;yplot],[zplot;zplot],[col;col],...
%         'facecol','no',...
%         'edgecol','interp',...
%         'LineStyle','--',...
%         'linewidth',0.5,...
%         'Marker','o',...
%         'MarkerSize',11 );
%
% h=colorbar;
% colormap(jet)

%%%%%%%%%%%% plotting
kite_filename = ['Kite_' month_filename '_2018.csv'];%('KITEAUG18_loc.csv');
kite = readtable(kite_filename);% %Kite locations
kite_tim = datenum(strcat(cellstr(kite.Date),{' '},kite.Time))*3600*24 - 4*3600; % 4*3600 is for time
difference in time reference
kite_delta_tim = kite_tim - kite_tim(1);
% Wind turbines locations
BITU_lat = [41.125733, 41.119933,41.114767, 41.110200, 41.106383];
BITU_lon = [-71.507567, -71.513950, -71.521133, -71.529117, -71.537650];

% reciever's location
BR_lon = -71.5901; BR_lat = 41.148;
SE_lon = -71.5514; SE_lat = 41.153;
BR_bearing = [354;234;114]; BR_unit_circle = 360 + 90 - BR_bearing;
SE_bearing = [166];  SE_unit_circle = 360 + 90 - SE_bearing;
BR_desire_lon = [BR_lon - 0.001; BR_lon - 0.008; BR_lon + 0.008];
SE_desire_lon = [SE_lon + 0.002];

BR_desire_lat = tand(BR_unit_circle).*(BR_desire_lon - BR_lon) + BR_lat;
SE_desire_lat = tand(SE_unit_circle).*(SE_desire_lon - SE_lon) + SE_lat;

figure('position',[-1000 300 600 400])
zone    = repmat('18 N',length(xplot),1);
[lat1,lon1] = utm2deg(xplot,yplot,zone);
scatter(lon1,lat1,[],time_new,'^');
colorbar
colormap(jet)
hold on
scatter(kite.Longitude,kite.Latitude,10,kite_delta_tim,'.')
for i = 1:length(BR_bearing)
    plot([BR_lon;BR_desire_lon(i)],[BR_lat;BR_desire_lat(i)],'k')
    hold on
end
for i =1:length(SE_bearing)
    plot([SE_lon;SE_desire_lon(i)],[SE_lat;SE_desire_lat(i)],'k')
    hold on
end
hold on
scatter(BITU_lon,BITU_lat,'x','k','LineWidth',2)
text(-71.45,41.27,'x   Block Island Wind Turbines')
grid on
colormap(jet)
cc = colorbar;cc.Label.String = 'Time (s)';
title([kite_filename],'Interpreter','none')
plot_google_map('MapType','terrain')
print output2018 -djpeg -r300


%% %% creating table for prediction versus actual kite

tim_start = datenum(date(1))*24*3600;
tim_new1  = tim_start + time_new';
for i = 1:length(tim_new1)
     [diff(i),index_tim(i)] = min(abs(kite_tim - tim_new1(i)));
end

kite_date    = kite.Date(index_tim);
kite_time    = kite.Time(index_tim);
kite_lat_sel = kite.Latitude(index_tim);
kite_lon_sel = kite.Longitude(index_tim);
[kite_x_sel,kite_y_sel] = wgs2utm(kite_lat_sel,kite_lon_sel,18,'N');

x_diff = xplot' - kite_x_sel;
y_diff = yplot' - kite_y_sel;

figure('position',[-1800 100 600 400])
plot(datenum(kite_time),x_diff);hold on
```

```
plot(datenum(kite_time),y_diff)
legend('xdiff','ydiff')

figure ('position',[-1800 500 600 400])
scatter(kite_x_sel,xplot)
xlabel('actual x')
ylabel('predicted x')

table1 = table(kite_date,kite_time,kite_x_sel,kite_y_sel,xplot',yplot',
'VariableNames',{'Date','time','x_kite','y_kite','x_predict','y_predict'});
writetable(table1,'simulation_data_2018Aug.csv')
```

III: Calibration and Brid Tracking : drone survey 2019

```
% close all;
% clear all;
clc; clear
z=[120]; % the height of the bird
drone1 = readtable(['flight_' num2str(z) 'm_AGL_sor.csv']); % Greg's coordinates
[time,signal,a_detect,date] = csvimport(['direction_file_combined_' num2str(z) 'm.csv'], 'columns',
[1,2,3,4],'noHeader', true);
time_mode=1; % 1: the previsou time window; 2: the time window which is overlapped with last one
t_size=60; % change the value here to adjust the window size(unit:second)
% a=801.59; b=30.273; % two constants
gain = 8;

p0=100*10^-11;% 20*10^-11;% for 30and 60; 40 for 90; 60 for 120 2.55271649539568e-12;
b=0.3013;%0.5752/2;
ZM=255;Zm=0;
lambda=1.8; % wavelength in free space
le=2; % the effective length of the overall array
k0=2*pi/lambda; % wavenumber in freespace
beta0=-(k0+2.94/le);
p=beta0*le/2; q=k0*le/2;
psi=0:pi/200:2*pi;
g_psi=cos(pi/2*sin(psi))./cos(psi).*sinc((p+q*cos(psi))/pi);

% Used to find the intersection points
%
% delta_psi=pi/3;
% g_psi_delta=cos(pi/2*sin(psi-delta_psi))./cos(psi-delta_psi).*sinc((p+q*cos(psi-delta_psi))/pi);
% [psi_inter,r_inter]=polyxpoly(psi,abs(g_psi),psi,abs(g_psi_delta),'unique');
% polar(psi,abs(g_psi),'--r');
% hold on;
% polar(psi,abs(g_psi_delta),'--g');
% polar(psi_inter,r_inter,'o');

% Done

%[name,mainbeam,t_lat,t_lon,t_y,t_x,t_h,g_h] = csvimport('Allstation.csv', 'columns',
[1,2,3,4,5,6,7,8],'noHeader', true);
[name,mainbeam,t_y,t_x,t_h,g_h] = csvimport('Allstations_2019.csv', 'columns', [1,2,3,4,5,6],'noHeader', true);

index=zeros(1,size(a_detect,1));
for i = 1:size(a_detect,1)
   indexc=strfind(name, a_detect{i});
   index(i)=find(not(cellfun('isempty', indexc)));
end
HT=t_h(index)+g_h(index); % elevation of tower + elevation of ground
theta=mainbeam(index);  % beam of each bearing


g_delta=10^-((11.1-gain)/10); %for TE14-0 and GG14&15, the gain should be adjusted (9dbi for them, 11.1dbi for
others)
sp_antenna=ismember(a_detect,{'BRBI-1','BRBI-2','BRBI-3','SEBI-1','SEBI-2','SEBI-3','TE14-0','GG14-1','GG14-
2','GG14-3','GG15-1','GG15-2','GG15-3','GG15-4','TE15-0'}); %find the special antenna whose gain is 9 dbi;

% convert the displaying number to the received power
xi=sqrt(p0*(((ZM-2*Zm+signal)./(ZM-signal)).^(1/(2*b))-1));
%-----------------------------------------------------------------
% get the radar range with the given
r=sqrt(HT./xi*z*sin(p+q)/(p+q)).*(~sp_antenna)...
    + g_delta*sqrt(HT./xi*z*sin(p+q)/(p+q)).*sp_antenna;
tower_x=t_x(index);
tower_y=t_y(index);
global_x=r.*sind(theta)+t_x(index);
global_y=r.*cosd(theta)+t_y(index);

% Used to plot the signal above the value-------
%
```

```
indexsignal=find(signal>0);  % you can change the value
global_x=global_x(indexsignal);
global_y=global_y(indexsignal);
time=time(indexsignal);
tower_x=tower_x(indexsignal);
tower_y=tower_y(indexsignal);
%
% done--------------------

% global t n;
n=1;
% time_window=[];global_xwindow=[];global_ywindow=[];
t=1;
% different case by how many antennas

if time_mode==1
  global_x_new=zeros(1,1000);global_y_new=zeros(1,1000);time_new=zeros(1,1000);
   while t <= length(time) %length(time)
        temp_diff=time(t:end)-time(t);
        temp_index=find(abs(temp_diff)<=(t_size));
          switch length(temp_index)
            case 1
                global_x_new(n)=global_x(t);
                global_y_new(n)=global_y(t);
                time_new(n)=time(t);
                n=n+1;
                t=t+1;
            case 2
                 if isequal(a_detect{t},a_detect{t+1})
                     global_x_new(n:n+1)=global_x(t-1+temp_index);
                     global_y_new(n:n+1)=global_y(t-1+temp_index);
                     time_new(n:n+1)=time(t-1+temp_index);
                     n=n+2;
                     t=t+2;

                 elseif (strncmpi(a_detect{t},a_detect{t+1},4) && ...
                         ismember(abs(str2num(a_detect{t}(6))-str2num(a_detect{t+1}(6))),[1,5]))  % special
case xxx-1 and xxx-6
                     r1_delta_psi=theta(t)/180*pi;r2_delta_psi=theta(t+1)/180*pi;
                     r1_g_psi=cos(pi/2*sin(psi-r1_delta_psi))./cos(psi-r1_delta_psi).*sinc((p+q*cos(psi-
r1_delta_psi))/pi);
                     r2_g_psi=cos(pi/2*sin(psi-r2_delta_psi))./cos(psi-r2_delta_psi).*sinc((p+q*cos(psi-
r2_delta_psi))/pi);
                     r1r2_sp=ismember({a_detect{t:t+1}},{'BRBI-1','BRBI-2','BRBI-3','SEBI-1','SEBI-2','SEBI-
3','TE14-0','GG14-1','GG14-2','GG14-3','GG15-1','GG15-2','GG15-3','GG15-4'}); %find the special antenna whose
gain is 9 dbi;
                     xi1=sqrt(p0*(((ZM-2*Zm+signal(t))/(ZM-signal(t)))^(1/(2*b))-1));
                     xi2=sqrt(p0*(((ZM-2*Zm+signal(t+1))/(ZM-signal(t+1)))^(1/(2*b))-1));
                     r1=sqrt(HT(t)/xi1*z*abs(r1_g_psi))*(~r1r2_sp(1))...
                         +g_delta*sqrt(HT(t)/xi1*z*abs(r1_g_psi))*(r1r2_sp(1));
                     r2=sqrt(HT(t+1)/xi2*z*abs(r2_g_psi))*(~r1r2_sp(2))...
                         +g_delta*sqrt(HT(t+1)/xi2*z*abs(r2_g_psi))*(r1r2_sp(2));
                     [temp_psi_int,temp_r]=polyxpoly(psi,r1,psi,r2,'unique');
                     if abs(str2num(a_detect{t}(6))-str2num(a_detect{t+1}(6)))==1
                       int_index=find(temp_psi_int>min([r1_delta_psi,r2_delta_psi]) &
temp_psi_int<max([r1_delta_psi,r2_delta_psi]));
                     else
                       int_index=find(temp_psi_int>max([r1_delta_psi,r2_delta_psi]) &
temp_psi_int<(min([r1_delta_psi,r2_delta_psi])+2*pi));
                     end
                     psi_int=temp_psi_int(int_index);
                     r_int=temp_r(int_index);
                     global_x_new(n)=mean(r_int.*sin(psi_int))+tower_x(t);
                     global_y_new(n)=mean(r_int.*cos(psi_int))+tower_y(t);
                     time_new(n)=mean(time(t-1+temp_index));
                     n=n+1;
                     t=t+2;
                 else
                     global_x_new(n)=mean(global_x(t-1+temp_index));
                     global_y_new(n)=mean(global_y(t-1+temp_index));
                     time_new(n)=mean(time(t-1+temp_index));
                     n=n+1;
                     t=t+2;
                 end
            otherwise
                  if sum(strncmpi(a_detect{t-1+temp_index(1)},a_detect(t-1+temp_index(1):t-
1+temp_index(end),1),4)==0)==0
%                     global_x_new(n)=tower_x(t);
%                     global_y_new(n)=tower_y(t);
%                     time_new(n)=mean(time(t-1+temp_index));
%                     n=n+1;
```

```
%                     t=t+length(temp_index);
                  else
                     global_x_new(n)=mean(global_x(t-1+temp_index));
                     global_y_new(n)=mean(global_y(t-1+temp_index));
                     time_new(n)=mean(time(t-1+temp_index));
                     n=n+1;
                     t=t+length(temp_index);
                  end
          end
   end
 global_x_new=global_x_new(1:n-1);global_y_new=global_y_new(1:n-1);time_new=time_new(1:n-1);

elseif time_mode ==2
  n=1;
  global_x_new=zeros(1,1000);
  global_y_new=zeros(1,1000);
  time_new=zeros(1,1000);
  for t = t_size/2:t_size/2:time(end)+t_size/2
      temp_diff=time-t;
      temp_index=find(abs(temp_diff)<=(t_size/2));
      if ~isempty(temp_index);
           switch length(temp_index)
              case 1
                 global_x_new(n)=global_x(temp_index);
                 global_y_new(n)=global_y(temp_index);
%                  time_new(n)=time(temp_index);
                 time_new(n)=t;
                 n=n+1;
              case 2
                   if isequal(a_detect{temp_index(1)},a_detect{temp_index(2)})
                     global_x_new(n)=mean(global_x(temp_index));
                     global_y_new(n)=mean(global_y(temp_index));
                     %time_new(n)=mean(time(temp_index));
                     time_new(n)=t;
                     n=n+1;
                   elseif (strncmpi(a_detect{temp_index(1)},a_detect{temp_index(2)},4) && ...
                         ismember(abs(str2num(a_detect{temp_index(1)}(6))-
str2num(a_detect{temp_index(2)}(6))),[1,5]))  % special case xxx-1 and xxx-6
                     r1_delta_psi=theta(temp_index(1))/180*pi;r2_delta_psi=theta(temp_index(2))/180*pi;
                     r1_g_psi=cos(pi/2*sin(psi-r1_delta_psi))./cos(psi-r1_delta_psi).*sinc((p+q*cos(psi-
r1_delta_psi))/pi);
                     r2_g_psi=cos(pi/2*sin(psi-r2_delta_psi))./cos(psi-r2_delta_psi).*sinc((p+q*cos(psi-
r2_delta_psi))/pi);
                     r1r2_sp=ismember({a_detect{temp_index(1):temp_index(2)}},{'BRBI-1','BRBI-2','BRBI-
3','SEBI-1','SEBI-2','SEBI-3','TE14-0','GG14-1','GG14-2','GG14-3','GG15-1','GG15-2','GG15-3','GG15-4'}); %find
the special antenna whose gain is 9 dbi;
                     xi1=sqrt(p0*(((ZM-2*Zm+signal(temp_index(1)))/(ZM-signal(temp_index(1))))^(1/(2*b))-1));
                     xi2=sqrt(p0*(((ZM-2*Zm+signal(temp_index(2)))/(ZM-signal(temp_index(2))))^(1/(2*b))-1));
                     r1=sqrt(HT(temp_index(1))/xi1*z*abs(r1_g_psi))*(~r1r2_sp(1))...
                         +g_delta*sqrt(HT(temp_index(1))/xi1*z*abs(r1_g_psi))*(r1r2_sp(1));
                     r2=sqrt(HT(temp_index(2))/xi2*z*abs(r2_g_psi))*(~r1r2_sp(2))...
                         +g_delta*sqrt(HT(temp_index(2))/xi2*z*abs(r2_g_psi))*(r1r2_sp(2));

%                      r1=sqrt(HT(temp_index(1))*exp(-(signal(temp_index(1))-a)/(2*b))*z*abs(r1_g_psi));
%                      r2=sqrt(HT(temp_index(2))*exp(-(signal(temp_index(2))-a)/(2*b))*z*abs(r2_g_psi));
                     [temp_psi_int,temp_r]=polyxpoly(psi,r1,psi,r2,'unique');
                     if abs(str2num(a_detect{temp_index(1)}(6))-str2num(a_detect{temp_index(2)}(6)))==1
                       int_index=find(temp_psi_int>min([r1_delta_psi,r2_delta_psi]) &
temp_psi_int<max([r1_delta_psi,r2_delta_psi]));
                     else
                       int_index=find(temp_psi_int>max([r1_delta_psi,r2_delta_psi]) &
temp_psi_int<(min([r1_delta_psi,r2_delta_psi])+2*pi));
                     end
                     psi_int=temp_psi_int(int_index);
                     r_int=temp_r(int_index);
                     global_x_new(n)=mean(r_int.*sin(psi_int))+tower_x(temp_index(1));
                     global_y_new(n)=mean(r_int.*cos(psi_int))+tower_y(temp_index(1));
                     %time_new(n)=mean(time(temp_index));
                     time_new(n)=t;
                     n=n+1;
                   else
                     global_x_new(n)=mean(global_x(temp_index));
                     global_y_new(n)=mean(global_y(temp_index));
                     %time_new(n)=mean(time(temp_index));
                     time_new(n)=t;
                     n=n+1;

                   end;
               otherwise
                    if sum(strncmpi(a_detect{temp_index(1)},a_detect(temp_index(1):temp_index(end),1),4)==0)==0
%                         global_x_new(n)=tower_x(temp_index(1));
```

```
%                           global_y_new(n)=tower_y(temp_index(1));
%                           %time_new(n)=mean(time(temp_index));
%                           time_new(n)=t;
%                           n=n+1;
                    else
                         global_x_new(n)=mean(global_x(temp_index));
                         global_y_new(n)=mean(global_y(temp_index));
                         %time_new(n)=mean(time(temp_index));
                         time_new(n)=t;
                         n=n+1;
                    end


           end

      end

  end
 global_x_new=global_x_new(1:n-1);
 global_y_new=global_y_new(1:n-1);
 time_new=time_new(1:n-1);

end

col=time_new;
xplot=global_x_new;
yplot=global_y_new;
zplot=zeros(size(xplot));
% figure
% static_tra=surface([xplot;xplot],[yplot;yplot],[zplot;zplot],[col;col],...
%         'facecol','no',...
%         'edgecol','interp',...
%         'LineStyle','--',...
%         'linewidth',0.5,...
%         'Marker','o',...
%         'MarkerSize',11 );
%
% h=colorbar;

%%%%%%%%%%% plotting in google map
drone_tim = datenum(cellstr(drone1.DateTime),'yyyy:mm:dd HH:MM:SS')*3600*24;
drone_delta_tim = drone_tim - drone_tim(1);

% Wind turbines locations
BITU_lat = [41.125733, 41.119933,41.114767, 41.110200, 41.106383];
BITU_lon = [-71.507567, -71.513950, -71.521133, -71.529117, -71.537650];

% reciever's location
BR_lon = -71.5901; BR_lat = 41.148;
SE_lon = -71.5514; SE_lat = 41.153;
BR_bearing = [234;114;336]; BR_unit_circle = [216;336;114];
SE_bearing = [98;338;178];  SE_unit_circle = [352;112;272];
BR_desire_lon = [BR_lon - 0.01; BR_lon + 0.01; BR_lon - 0.003];
SE_desire_lon = [SE_lon + 0.011; SE_lon - 0.002; SE_lon + 0.0003];

for i = 1:3
    BR_desire_lat(i) = tand(BR_unit_circle(i))*(BR_desire_lon(i) - BR_lon) + BR_lat;
    SE_desire_lat(i) = tand(SE_unit_circle(i))*(SE_desire_lon(i) - SE_lon) + SE_lat;
end

figure('position',[-1000 500 600 400])
scatter(BITU_lon,BITU_lat,'x','k','LineWidth',2)
hold on
plot(drone1.lon,drone1.lat,'linewidth',2)

zone    = repmat('18 N',length(xplot),1);
[lat1,lon1] = utm2deg(xplot,yplot,zone);
scatter(lon1,lat1,[],time_new,'^')
hold on

% scatter(drone1.lon,drone1.lat,[],drone_delta_tim)
for i = 1:3
    plot([BR_lon;BR_desire_lon(i)],[BR_lat;BR_desire_lat(i)],'k')
    hold on
    plot([SE_lon;SE_desire_lon(i)],[SE_lat;SE_desire_lat(i)],'k')
    hold on
end

grid on
colormap(jet)
cc = colorbar;cc.Label.String = 'Time (s)'
```

```
legend('Wind turbines','Drone transect','simulated detections')
title(['flight altitude = ' num2str(z) ' m '])
plot_google_map('MapType','terrain')
print output2019 -djpeg -r300

%% %% creating table for prediction versus actual drone

drone_tim = datenum(drone1.DateTime,'yyyy:mm:dd HH:MM:SS')*3600*24 + 4*3600;
tim_start = datenum(date(1))*24*3600;
tim_new1  = tim_start + time_new';
for i = 1:length(tim_new1)
     [diff(i),index_tim(i)] = min(abs(drone_tim - tim_new1(i)));
end

drone_time    = drone1.DateTime(index_tim);
drone_lat_sel = drone1.lat(index_tim);
drone_lon_sel = drone1.lon(index_tim);
[drone_x_sel,drone_y_sel] = wgs2utm(drone_lat_sel,drone_lon_sel,18,'N');

x_diff = xplot' - drone_x_sel;
y_diff = yplot' - drone_y_sel;

figure('position',[-1800 100 600 400])
plot(datenum(drone_time,'yyyy:mm:dd HH:MM:SS'),x_diff);hold on
plot(datenum(drone_time,'yyyy:mm:dd HH:MM:SS'),y_diff)
legend('xdiff','ydiff')

figure ('position',[-1800 500 600 400])
scatter(drone_x_sel,xplot)
xlabel('actual x')
ylabel('predicted x')

table1 = table(drone_time,drone_x_sel,drone_y_sel,xplot',yplot',
'VariableNames',{'time','x_drone','y_drone','x_predict','y_predict'});
writetable(table1,['simulation_data_2019_' num2str(z) 'm.csv'])
```

Appendix 1.7. Matlab code used to estimate antenna radiation patterns for automated tracking stations located on Block Island from 2017-2019.

IV: Antenna Patterns, 2017

```
clc; clear;

BI0 = readtable('direction_file_BI_2017.csv');
antenna_index = ismember(BI0.Var3,{'BIWF-1'}); %filtering the antenna
signal = BI0.Var2(antenna_index);
a_detect = BI0.Var3(antenna_index);
G0=0;
signal0 = signal;
SR = ismember(a_detect,{'BIBR-1','BIBR-2','BIBR-4','BIWF-1','BIWF-3','BIWF-5','BIWF-7'}); %find sensorgnomes;
signal(SR) = (40*G0 + 44*signal(SR) + 4565)/11;

kite_filename = 'track2017.csv';
kite = readtable(kite_filename);% %Kite locations

%%
stationFile = 'Allstations_2017.csv';
stationData=readtable(stationFile,'Delimiter',',','ReadVariableNames',true);


gain =11;
antenna = {'"BIBR-1"','"BIBR-2"','"BIBR-4"','"SELI-1"','"SELI-2"','"SELI-3"','"SELI-4"','"SELI-5"','"SELI-
6"','"BIWF-1"','"BIWF-3"','"BIWF-5"','"BIWF-7"'}; % 2017 antennas

index = 10; % desire or desired antennas
r1r2_sp = false; %for 2017, this should be false
altitude = 20;
le      = 4.6; % the effective length of the overall array
 p0   = 4.89*10^-11;
% p0   = 2.55271649539568e-12;
b    = 0.3013; % the values from rama's paper
ZM   = 255;
Zm   = 0;
zz = 255;
Z_display = 1:1:zz; % lotek scale signal
```

```
xi  = p0*(((ZM-2*Zm+Z_display)./(ZM-Z_display)).^(1/(2*b))-1);
lambda = 1.8; % wavelength in free space
k0     = 2*pi/lambda; % wavenumber in freespace
beta0  = -(k0+2.94/le);
p      = beta0*le/2;
q      = k0*le/2;
psi    = 0:pi/400:2*pi;


beam=stationData.beam;
bearing=stationData.bearing;
tower_x=stationData.x_m;
tower_y=stationData.y_m;
tower_h=stationData.mast_height_m;
ground_h=stationData.ground_elevation_m;

    for i = 1:length(antenna)
        indexc=strfind(beam, upper(strrep(antenna(i),'"','''))); %remove the double quote in the antenna
        index_st=find(not(cellfun('isempty', indexc)));
        detect.beam(i)=beam(index_st);
        detect.bearing(i)=bearing(index_st);
        detect.tower_x(i)=tower_x(index_st);
        detect.tower_y(i)=tower_y(index_st);
        detect.tower_h(i)=tower_h(index_st);
        detect.ground_h(i)=ground_h(index_st);
    end
%----  get the height of the antenna ------
HT=detect.tower_h+detect.ground_h;
theta=detect.bearing;
beam=detect.beam;
towerx=detect.tower_x;
towery=detect.tower_y;

col = jet(zz);
col(min(round(signal)):max(round(signal)),:) = 0;
figure
for i = 1:length(xi)
z = altitude;
%------------------------------

%----get the certain radiation pattern in polar coord. --------
g_delta=10^-((11.1-gain)/10); %for TE14-0 and GG14&15, the gain should be adjusted (9dbi for them, 11.1dbi for
others)
r1_delta_psi=theta(index)/180*pi;

r1_g_psi=cos(pi/2*sin(psi-r1_delta_psi))./cos(psi-r1_delta_psi).*sinc((p+q*cos(psi-r1_delta_psi))/pi);

%r1r2_sp=ismember(detect.beam(index),{'TE14-0','GG14-1','GG14-2','GG14-3','GG15-1','GG15-2','GG15-3','GG15-
4'}); %find the special antenna whose gain is 9 dbi;
r1=sqrt(HT(index)/sqrt(xi(i))*z*abs(r1_g_psi))*(~r1r2_sp(1)) +
g_delta*sqrt(HT(index)/sqrt(xi(i))*z*abs(r1_g_psi))*(r1r2_sp(1));

r1_x=r1.*sin(psi)+towerx(index);
r1_y=r1.*cos(psi)+towery(index);


zone    = repmat('18 N',length(r1_x),1);
[lat1,lon1] = utm2deg(r1_x,r1_y,zone);

% [towery_lat,towerx_lon]  = utm2deg(towerx(index),towery(index),'18 N');
% t1=plot(towerx_lon,towery_lat,'r','Marker','x','MarkerSize',11 );
% t2=plot(towerx(c(i,2)),towery(c(i,2)),'g','Marker','x','MarkerSize',11 );

% pattern1=plot(lon1,lat1,'Color', col(z,:));
pattern1=plot(r1_x/1000,r1_y/1000,'Color', col(i,:));


hold on

end
colormap(col)
cc = colorbar;cc.Label.String = 'Signal Strength';

caxis([0 255])

% drone        = readtable(['flight_' num2str(altitude) 'm_AGL.csv']); % drone's coordinates
% [x_drone,y_drone] = wgs2utm(drone.lat,drone.lon,18,'N'); % converting from lat/long to UTM 18N

BITU_lat = [41.125733, 41.119933,41.114767, 41.110200, 41.106383];
BITU_lon = [-71.507567, -71.513950, -71.521133, -71.529117, -71.537650];
```

```
[BITU_x,BITU_y] = wgs2utm(BITU_lat,BITU_lon,18,'N');

% hold on
% scatter(BITU_lon,BITU_lat,'x','k','LineWidth',2)
scatter(BITU_x/1000,BITU_y/1000,'x','r','LineWidth',1)

hold on
[kite_x,kite_y] = wgs2utm(kite.Var4,kite.Var3,18,'N');
scatter(kite_x/1000,kite_y/1000,5,'.')
% text(-71.45,41.27,'x   Block Island Wind Turbines')
% xlim([min(min(lon1))-0.05 max(max(lon1))+0.05]);
% ylim([min(min(lat1))-0.05 max(max(lat1))+0.05]);
% plot_google_map('MapType','terrain')
%

% hold on
% scatter(x_drone/1000,y_drone/1000,'o','k','LineWidth',1)

grid on

% text(8e5/1000,4.585e6/1000,'x   Block Island Wind Turbines')
% text(8e5/1000,4.58e6/1000,'o   drone position')
% text(8e5/1000,4.5750e6/1000,['      Flight Altitude:' num2str(altitude) 'm'])
% if r1r2_sp == 0
%     title(['antenna effective length: ' num2str(le) ' m'])
% else
%     title(['antenna effective length: ' num2str(le) ' m and adjusted Gain'])
% end
title([antenna(index)])
% xlim([7.6e5 8.5e5]/1000);
% ylim([4.52e6 4.59e6]/1000);
xlabel('x in UTM Zone-18 (km)')
ylabel('y in UTM Zone-18 (km)')
filename = ['radiation_patt2017_' num2str(index)];
print (filename,'-djpeg','-r300')

% xlim([min(min(lon1))-0.25 max(max(lon1))+0.25]);
% ylim([min(min(lat1))-0.25 max(max(lat1))+0.25]);
% get_google_map('MapType','terrain')
% print radiation_pattern1 -djpeg -r300
```

V: Antenna Patterns, 2018

```
clc; clear;

BI0 = readtable('direction_file_BI_2018_no_WF_no_omni_July.csv');
antenna_index = ismember(BI0.Var3,{'BIBR-2'}); %filtering the antenna
signal = BI0.Var2(antenna_index);
G0 = 0;
signal = (40*G0 + 44*signal + 4565)/11;

month_filename = 'July';% or Aug
kite_filename = ['Kite_' month_filename '_2018.csv'];%('KITEAUG18_loc.csv');
kite = readtable(kite_filename);% %Kite locations

%%
stationFile = 'Allstations_2018.csv';
stationData=readtable(stationFile,'Delimiter',',','ReadVariableNames',true);


gain =8;
antenna = {'"BIBR-1"','"BIBR-2"','"BIBR-3"','"SELI-2"'}; % 2018 antennas
index = 2; % desire or desired antennas
altitude = 20;
r1r2_sp = true; %for 2018, this should be ture as all antennas are 5 element

le     = 2; % the effective length of the overall array
p0= 4e-12; %4.89*10^-11;2.55271649539568e-12;
% p0  = 2.55271649539568e-12;
b   = 0.3013; % the values from rama's paper
ZM  = 255;
Zm  = 0;
zz = 255;
Z_display = 1:1:zz; % lotek scale signal
xi  = p0*(((ZM-2*Zm+Z_display)./(ZM-Z_display)).^(1/(2*b))-1);
lambda = 1.8; % wavelength in free space
k0     = 2*pi/lambda; % wavenumber in freespace
beta0  = -(k0+2.94/le);
p      = beta0*le/2;
```

```
q      = k0*le/2;
psi    = 0:pi/400:2*pi;


beam=stationData.beam;
bearing=stationData.bearing;
tower_x=stationData.x_m;
tower_y=stationData.y_m;
tower_h=stationData.mast_height_m;
ground_h=stationData.ground_elevation_m;

    for i = 1:length(antenna)
        indexc=strfind(beam, upper(strrep(antenna(i),'"','')); %remove the double quote in the antenna
        index_st=find(not(cellfun('isempty', indexc)));
        detect.beam(i)=beam(index_st);
        detect.bearing(i)=bearing(index_st);
        detect.tower_x(i)=tower_x(index_st);
        detect.tower_y(i)=tower_y(index_st);
        detect.tower_h(i)=tower_h(index_st);
        detect.ground_h(i)=ground_h(index_st);
    end
%----  get the height of the antenna ------
HT=detect.tower_h+detect.ground_h;
theta=detect.bearing;
beam=detect.beam;
towerx=detect.tower_x;
towery=detect.tower_y;

col = jet(zz);
col(min(round(signal)):max(round(signal)),:) = 0;
figure
for i = 1:length(xi)
z = altitude;
%-----------------------------

%----get the certain radiation pattern in polar coord. --------
g_delta=10^-((11.1-gain)/10); %for TE14-0 and GG14&15, the gain should be adjusted (9dbi for them, 11.1dbi for
others)
r1_delta_psi=theta(index)/180*pi;

r1_g_psi=cos(pi/2*sin(psi-r1_delta_psi))./cos(psi-r1_delta_psi).*sinc((p+q*cos(psi-r1_delta_psi))/pi);

%r1r2_sp=ismember(detect.beam(index),{'TE14-0','GG14-1','GG14-2','GG14-3','GG15-1','GG15-2','GG15-3','GG15-
4'}); %find the special antenna whose gain is 9 dbi;
r1=sqrt(HT(index)/sqrt(xi(i))*z*abs(r1_g_psi))*(~r1r2_sp(1)) +
g_delta*sqrt(HT(index)/sqrt(xi(i))*z*abs(r1_g_psi))*(r1r2_sp(1));

r1_x=r1.*sin(psi)+towerx(index);
r1_y=r1.*cos(psi)+towery(index);


zone    = repmat('18 N',length(r1_x),1);
[lat1,lon1] = utm2deg(r1_x,r1_y,zone);

% [towery_lat,towerx_lon]  = utm2deg(towerx(index),towery(index),'18 N');
% t1=plot(towerx_lon,towery_lat,'r','Marker','x','MarkerSize',11 );
% t2=plot(towerx(c(i,2)),towery(c(i,2)),'g','Marker','x','MarkerSize',11 );

% pattern1=plot(lon1,lat1,'Color', col(z,:));
pattern1=plot(r1_x/1000,r1_y/1000,'Color', col(i,:));


hold on

end
colormap(col)
cc = colorbar;cc.Label.String = 'Signal Strength';

caxis([0 255])

% drone        = readtable(['flight_' num2str(altitude) 'm_AGL.csv']); % drone's coordinates
% [x_drone,y_drone] = wgs2utm(drone.lat,drone.lon,18,'N'); % converting from lat/long to UTM 18N

BITU_lat = [41.125733, 41.119933,41.114767, 41.110200, 41.106383];
BITU_lon = [-71.507567, -71.513950, -71.521133, -71.529117, -71.537650];

[BITU_x,BITU_y] = wgs2utm(BITU_lat,BITU_lon,18,'N');

% hold on
% scatter(BITU_lon,BITU_lat,'x','k','LineWidth',2)
scatter(BITU_x/1000,BITU_y/1000,'x','r','LineWidth',1)
```

```
hold on
[kite_x,kite_y] = wgs2utm(kite.Latitude,kite.Longitude,18,'N');
scatter(kite_x/1000,kite_y/1000,10,'.')
% text(-71.45,41.27,'x   Block Island Wind Turbines')
% xlim([min(min(lon1))-0.05 max(max(lon1))+0.05]);
% ylim([min(min(lat1))-0.05 max(max(lat1))+0.05]);
% plot_google_map('MapType','terrain')
%

% hold on
% scatter(x_drone/1000,y_drone/1000,'o','k','LineWidth',1)

grid on

% text(8e5/1000,4.585e6/1000,'x   Block Island Wind Turbines')
% text(8e5/1000,4.58e6/1000,'o   drone position')
% text(8e5/1000,4.5750e6/1000,['      Flight Altitude:' num2str(altitude) 'm'])
% if r1r2_sp == 0
%     title(['antenna effective length: ' num2str(le) ' m'])
% else
%     title(['antenna effective length: ' num2str(le) ' m and adjusted Gain'])
% end
title([antenna(index)])
% xlim([7.6e5 8.5e5]/1000);
% ylim([4.52e6 4.59e6]/1000);
xlabel('x in UTM Zone-18 (km)')
ylabel('y in UTM Zone-18 (km)')
filename = ['radiation_patt2018_' month_filename '_' num2str(index)];
print (filename,'-djpeg','-r300')

% xlim([min(min(lon1))-0.25 max(max(lon1))+0.25]);
% ylim([min(min(lat1))-0.25 max(max(lat1))+0.25]);
% get_google_map('MapType','terrain')
% print radiation_pattern1 -djpeg -r300
```

V: Antenna Patterns, 2019

```
clc; clear;
altitude = 120;
BI0 = readtable(['direction_file_combined_' num2str(altitude) 'm.csv']);
signal = BI0.Var2;
antenna_index = ismember(BI0.Var3,{'BRBI-3'}); %filtering the antenna
signal = BI0.Var2(antenna_index);
%%
stationFile = 'Allstations_2019.csv';
stationData=readtable(stationFile,'Delimiter',',','ReadVariableNames',true);

gain = 8;
antenna = {'"BRBI-1"','"BRBI-2"','"BRBI-3"','"SEBI-1"','"SEBI-2"','"SEBI-3"'}; % 2019 antennas

index =3; % desire or desired antennas
le     = 2; % the effective length of the overall array
p0=100*10^-11;% 4.89*10^-11;
% p0= 2.55271649539568e-12;
b   = 0.3013; % the values from rama's paper
ZM  = 255;
Zm  = 0;
zz = 255;
Z_display = 1:1:zz; % lotek scale signal
xi  = p0*(((ZM-2*Zm+Z_display)./(ZM-Z_display)).^(1/(2*b))-1);
lambda = 1.8; % wavelength in free space
k0     = 2*pi/lambda; % wavenumber in freespace
beta0  = -(k0+2.94/le);
p      = beta0*le/2;
q      = k0*le/2;
psi    = 0:pi/400:2*pi;

r1r2_sp = true;

beam=stationData.beam;
bearing=stationData.bearing;
tower_x=stationData.x_m;
tower_y=stationData.y_m;
tower_h=stationData.mast_height_m;
ground_h=stationData.ground_elevation_m;

    for i = 1:length(antenna)
```

```
        indexc=strfind(beam, upper(strrep(antenna(i),'"','')); %remove the double quote in the antenna
        index_st=find(not(cellfun('isempty', indexc)));
        detect.beam(i)=beam(index_st);
        detect.bearing(i)=bearing(index_st);
        detect.tower_x(i)=tower_x(index_st);
        detect.tower_y(i)=tower_y(index_st);
        detect.tower_h(i)=tower_h(index_st);
        detect.ground_h(i)=ground_h(index_st);
    end
%----  get the height of the antenna ------
HT=detect.tower_h+detect.ground_h;
theta=detect.bearing;
beam=detect.beam;
towerx=detect.tower_x;
towery=detect.tower_y;

col = jet(zz);
col(min(round(signal)):max(round(signal)),:) = 0;
figure
drone        = readtable(['flight_' num2str(altitude) 'm_AGL.csv']); % drone's coordinates
[x_drone,y_drone] = wgs2utm(drone.lat,drone.lon,18,'N'); % converting from lat/long to UTM 18N

BITU_lat = [41.125733, 41.119933,41.114767, 41.110200, 41.106383];
BITU_lon = [-71.507567, -71.513950, -71.521133, -71.529117, -71.537650];

[BITU_x,BITU_y] = wgs2utm(BITU_lat,BITU_lon,18,'N');

% hold on
% scatter(BITU_lon,BITU_lat,'x','k','LineWidth',2)
scatter(BITU_x/1000,BITU_y/1000,'x','r','LineWidth',1)


% text(-71.45,41.27,'x   Block Island Wind Turbines')
% xlim([min(min(lon1))-0.05 max(max(lon1))+0.05]);
% ylim([min(min(lat1))-0.05 max(max(lat1))+0.05]);
% plot_google_map('MapType','terrain')
%
hold on
plot(x_drone/1000,y_drone/1000,'col',[0.5 0.7 0.5],'LineWidth',2)

grid on

% text(8e5/1000,4.585e6/1000,'x   Block Island Wind Turbines')
% text(8e5/1000,4.58e6/1000,'o   drone position')
% text(8e5/1000,4.5750e6/1000,['      Flight Altitude:' num2str(altitude) 'm'])
% if r1r2_sp == 0
%     title(['antenna effective length: ' num2str(le) ' m'])
% else
%     title(['antenna effective length: ' num2str(le) ' m and adjusted Gain'])
% end


for i = 1:length(xi)
z = altitude;
%-----------------------------

%----get the certain radiation pattern in polar coord. --------
g_delta=10^-((11.1-gain)/10); %for TE14-0 and GG14&15, the gain should be adjusted (9dbi for them, 11.1dbi for
others)
r1_delta_psi=theta(index)/180*pi;

r1_g_psi=cos(pi/2*sin(psi-r1_delta_psi))./cos(psi-r1_delta_psi).*sinc((p+q*cos(psi-r1_delta_psi))/pi);

%r1r2_sp=ismember(detect.beam(index),{'TE14-0','GG14-1','GG14-2','GG14-3','GG15-1','GG15-2','GG15-3','GG15-
4'}); %find the special antenna whose gain is 9 dbi;
r1=sqrt(HT(index)/sqrt(xi(i))*z*abs(r1_g_psi))*(~r1r2_sp(1)) +
g_delta*sqrt(HT(index)/sqrt(xi(i))*z*abs(r1_g_psi))*(r1r2_sp(1));

r1_x=r1.*sin(psi)+towerx(index);
r1_y=r1.*cos(psi)+towery(index);


zone    = repmat('18 N',length(r1_x),1);
[lat1,lon1] = utm2deg(r1_x,r1_y,zone);

% [towery_lat,towerx_lon]  = utm2deg(towerx(index),towery(index),'18 N');
% t1=plot(towerx_lon,towery_lat,'r','Marker','x','MarkerSize',11 );
% t2=plot(towerx(c(i,2)),towery(c(i,2)),'g','Marker','x','MarkerSize',11 );

% pattern1=plot(lon1,lat1,'Color', col(z,:));
pattern1=plot(r1_x/1000,r1_y/1000,'Color', col(i,:));
```

```
hold on

end
colormap(col)
cc = colorbar;cc.Label.String = 'Signal Strength';
caxis([0 255])

title0 = [num2str(z) 'm altitude'];
title([antenna(index) title0]);
% xlim([7.6e5 8.5e5]/1000);
% ylim([4.52e6 4.59e6]/1000);
xlabel('x in UTM Zone-18 (km)')
ylabel('y in UTM Zone-18 (km)')
legend('Wind turbines','Drone transect')

filename = ['radiation_patt2019_' num2str(altitude) 'm_' num2str(index)];
print (filename,'-djpeg','-r300')
% xlim([min(min(lon1))-0.25 max(max(lon1))+0.25]);
% ylim([min(min(lat1))-0.25 max(max(lat1))+0.25]);
% get_google_map('MapType','terrain')
% print radiation_pattern1 -djpeg -r300
```

Endpiece – Block Island Wind Farm taken by drone during calibration survey